THE UNIVERSITY OF
WARWICK

AUTHOR: **Chen SI** DEGREE: **Ph.D.**

TITLE: **The Quantitative Analysis of Optical Phase Measurement and its Application to the determination of Corneal Birefringence**

DATE OF DEPOSIT: .....

I agree that this thesis shall be available in accordance with the regulations governing the University of Warwick theses.

I agree that the summary of this thesis may be submitted for publication.

I **agree** that the thesis may be photocopied (single copies for study purposes only).

Theses with no restriction on photocopying will also be made available to the British Library for microfilming. The British Library may supply copies to individuals or libraries. subject to a statement from them that the copy is supplied for non-publishing purposes. All copies supplied by the British Library will carry the following statement:

> "Attention is drawn to the fact that the copyright of this thesis rests with its author. This copy of the thesis has been supplied on the condition that anyone who consults it is understood to recognise that its copyright rests with its author and that no quotation from the thesis and no information derived from it may be published without the author's written consent."

AUTHOR'S SIGNATURE: .....

USER'S DECLARATION

1. I undertake not to quote or make use of any information from this thesis without making acknowledgement to the author.
2. I further undertake to allow no-one else to use this thesis while it is in my care.

DATE SIGNATURE ADDRESS

.....

.....

.....

.....

.....

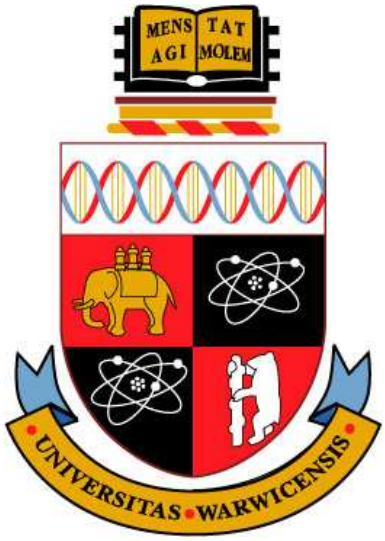

The Quantitative Analysis of Optical Phase Measurement and its Application to the determination of Corneal Birefringence

by

Chen SI

Thesis

Submitted to the University of Warwick

for the degree of

Doctor of Philosophy

School of Engineering

February 2011

THE UNIVERSITY OF WARWICK

Contents

List of Tables

List of Figures

Acknowledgments

I would like to give special thanks to Professor Peter Bryanston-Cross, my supervisor, for his advice throughout the planning and production of this project. I have learned a lot from him to be a good researcher. I would like to acknowledge the help and support of the other members of our research team; Dr. Joe Nawasra, for his technical support on the optical devices arrangement in experiment; Mr. R. H. Edwards for their technical support.

I would like to thank surgeon Mr. Gary Misson (Warwick Hospital), for his consultant and advice concerning the corneas, and cornea specimens provided.

I would also like to thank Dr. David Clifton (Oxford University, Engineering Department)and Dr.Daciana Iliescu (Warwick University, Engineering Department) who aided in prove reading this thesis, and gave suggestions and support.

I would also like to thank my parents for the financial support of the study, and Warwick University for the study and research support.

Special thanks to my family and fiancee. Without their support it would not have happened.

Declarations

This thesis is presented in accordance with the regulations for the degree of Doctor of Philosophy. It has been composed by myself and has not been submitted in any previous application for any degree. The work described in this thesis is the results of my own investigations except where stated otherwise.

Signature:

To Mum, Dad, and Queena

Abstract

In this thesis, a phase sensitive interferometer is successfully implemented to perform birefringent object surface-profile measurement, based on a polarisation adjustment approach. Using monochromatic light, a novel polarization interferometric method is developed, incorporating the birefringence technique and a waveplate. In our experiments, a birefringent wedge is designed for generating carrier fringes in the polariscope. Retardance is calculated from phase shifting using a phase matching technique. The accuracy of the method has been demonstrated to have an error of less than 0.02 radians. The accuracy and resolution quantitative analysis presented in this thesis can be used to determine accurately the phase-shifting interferometry for high-precision surface profile and bio-structure, such as fibre and collagen measurements with low cost.

FFT technique and phase-stepping methods are described to determine birefringence within the cornea. The distribution of human corneal lamellar collagen is determined through a microscopic technique using the combination of a circular polariser and a quarter-wave retarder. A quantitative measure of corneal birefringence is achieved by phase unwrapping. The experimental findings of elliptic and hyperbolic populations of collagen fibrils may explain the optical phenomena of central corneal retardation with biaxial-like behaviour in more peripheral areas.

A low cost, simple, and direct approach has been developed to make the required microscopic measurement. The traditional transmission system is improved by applying a reflection system with an *LED* light source and is suitable for the analysis of the birefringent cornea structures in vivo.

A further instrument based upon a synthetic aperture approach has been created with the purpose of measuring the three dimensional birefringence structure of the cornea. The concept of the instrument is a combination of the parallax between individual lenses and the numerically generated planes of focus to visualise the phase structure.

Key words: *phase sensitivity, monochromatic light source, retardance, phase shifting accuracy, phase stepping method, Fast Fourier transform (FFT)technique, polarisation, phase unwrapping, multi-camera, birefringence structure.*

Chapter 1

Introduction

Optical engineering covers many fields, prominent subfields of these include illumination engineering, photonics, and optoelectronics with practical applications like lens design, fabrication and testing of optical components, and image processing. There has been a rapid development of optical materials and their applications in the field of communications. In other important areas, optical measurement and diagnostics have played an important role. Examples include a variety of medical and mechanical uses. Some of these will be investigated and discussed in this thesis. However, there are still many important issues in this field to be resolved.

Birefringence measurement is important in this study. The technology used for measuring phase shifting is based on the property of most transparent birefringent material. The quantitative analysis is described by this thesis as one of the main points. There are also some novel designs for experiments, which have been successfully implemented. In the main application, the three dimensional optical phase measurement of cornea birefringence has been studied and explored using a novel approach.

1.1 Background

1.1.1 Optical Birefringence

Birefringence is an optical phenomenon where a ray of light decomposes into two rays, known as the ordinary ray ($o-ray$)and the extraordinary ray ($e-ray$). It occurs when the ray passes through certain types of transparent material that possesses two refractive indices. The phenomenon of *birefringence* occurs in optically anisotropic media. This media has optical properties that depend on directions of propagation of each ray. The phenomenon of birefringence is also referred to as *double refraction*[3]. The "double" or "bi" in the name of this effect refers to the two different directions of propagation that a given incident ray can take in such media. The directions of propagation are dependent on the direction of polarisation.

The optical path difference is a classical optical concept related to *birefringence*. It is defined by the relative phase shift between the ordinary and extraordinary rays as they emerge from an anisotropic material. A simple method of optical phase shifting requires a parallel slab of birefringent material. If the optic axis lies parallel to the surface and light falls on the slab at normal incidence, both *o* and *e* rays continue to propagate in the same direction, but with different velocities. The phase change produced by propagation through the material will be different for the two rays.

If a normally isotropic glass plate is compressed, it is found to act like a negative uniaxial crystal. The optic axis is in the direction of the stress. This means that for light incident perpendicular to this direction, the glass acts like a retardation plate. This stress induced *birefringence* is called *photoelasticity*. For most purposes it can be assumed that *birefringence* is linearly proportional to the stress, with the constant of proportionality being the stress-optical co-efficient. A quantitative measure of both the stress and phase can be obtained by adding a retarding material between the polarisers in a polariscope.

1.1.2 Polariscope

Photoelasticity is a nondestructive, whole-field, graphic stress-analysis technique based on the opto-mechanical property of *birefringence*, which is possessed by many transparent polymers. When combined with other optical elements and illuminated with an ordinary light source, a loaded photoelastic specimen (or a photoelastic coating applied to an ordinary specimen) exhibits fringe patterns. These fringe patterns are determined by the difference between the principal stresses, in a plane normal to the light propagation direction. This method is used primarily for analyzing two dimensional plane problems, which is the main focus on this thesis.

A polariscope is an optical instrument that allows the birefringence in transparent specimens to be analysed. It consists of a light source, a polariser, an optional quarter-wave plate, a specimen, another optional quarter-wave plate, and a second polarizer called the analyser. Two types of polariscope are commonly employed the plane polariscope and the circular polariscope. [4].

Photoelasticity uses circular polariscope to measure retardation. The sample is placed between crossed polarisers and is thus illuminated by linearly polarised light, whereas in a circular polariscope quarter wave plates are added before and after the sample, so it is illuminated with circularly polarized light. Measuring the transmitted intensity allows the determination of the sample retardation. The overall accuracy of the method depends on the accuracy with which the transmitted intensity can be measured. When using circular polariscopes, the measurement is subject to errors due to the quarter wave plates, especially when white light source is used.

Phase-stepping photoelasticity is a development of conventional photoelasticity methods. It uses non-conventional polariscopes which are a combination of plane and circular polariscopes. The retardation magnitude and fast/slow axis orientations of a sample are measured by recording a number of transmitted intensities for various relative orientations of the optical elements in the polariscope.

1.1.3 History of birefringence and Phase Measurements

The shift towards the wave theory of light began at the beginning of the 19th century.The first clues to the existence of polarised light surfaced around 1669, when Erasmus Bartholin discovered that crystals of the mineral Iceland spar (more commonly referred to as calcite) produce a double image when objects are viewed through the crystals in transmitted light. In 1801 Thomas Young discovered the interference of light from adjacent pinholes and established the wave theory of light. Ridiculed in England, *Young's* theory was championed in France by Fresnel and Arago who faced the opposition of senior scientists, such as Laplace, Fourier and Poisson, who supported the corpuscular theory. The polarisation of light by reflection had been discovered in 1808 by Malus and the polarising angle discovered by Brewster in 1811. Fresnel was able to explain polarisation using $Youngs$ suggestion that light was a transverse vibration and his analysis of diffraction effects were convincing. However, the final evidence in support of the wave theory depended on experimental proof that light travelled more slowly in denser media; since the corpuscular theory required the reverse [5].

With the theoretical understanding established, it becomes possible to develop a linear birefringent polariser. The most renowned birefringent polariser was introduced in 1828 by the Scottish physicist William Nicol (1768-1851). The Nicol prism is now mainly of historical interest, having long been superseded by other, more effective polarisers. Double refraction in a phenomenon is explained by the laws of electromagnetism, proposed by British mathematician James Clerk Maxwell in the 1860s [6].

1.1.4 Reasons for Measurement

In 1816 Sir David Brewster discovered that normally transparent isotropic substances could be made optically anisotropic by the application of mechanical stress. This phenomenon is known as mechanical birefringence, photoelasticity, or stress birefringence. Under compression or tension, the material takes on the properties

of a negative or positive uniaxial crystal, respectively. In either case, the effective optic axis is in the direction of the stress, and the induced birefringence is proportional to the stress [7]. If the stress is not uniform over the sample, neither is the birefringence or the retardance imposed on a transmitted wave.

Birefringence causes the transmitted wave front to have different optical path for the vertical and horizontal orientations of linear polarisation. Subtracting these profiles reveals the amount of phase difference between the fast and slow axes of the material. As a result, birefringence can be calculated. Phase-measurement techniques using a computer-controlled interferometer employing a variable liquid-crystal retarder provide a fully automated instrument for measuring stress birefringence [8].

Knowing the polarisation state of the light incident upon a sample, the detection and analysis of the polarisation state of the transmitted light allows the determination of the samples birefringence distribution. This requires the development of quantitative techniques which enable the accurate measurement of the retardation magnitude and fast/slow axis orientations, leading to the determination of the sample's physical properties.

The polarising effect by reflection can also be used in the study of surface structure. This is particularly useful on materials which usually absorb light but can also be optically polished. The reflection of linearly or circularly polarised light is accompanied by a change in phase of components, giving an elliptically polarised reflected beam. Instruments called ellipsometers are used that can measure the refractive index and the thickness of transparent films.

In transparent materials such as glass and plastic, birefringence may be induced by residual stress. Using the stress-optic effect, stress-induced birefringence measurements can be used for quality control and quality enhancement by monitoring the amount of stress in selected locations of the material.

In biology, birefringence imaging has become a powerful tool for the dynamic observation of the growth cones of developing neuritis and bundled microtubules

in living cells. More recently, birefringence of retinal nerve fiber layer in the human eye and its measurement has been used to determine the shape of the cornea and for early detection of glaucoma [9].

In my application, the birefringence measurement was successful implemented into industrial components, the previous research work proved the methodology and algorithm qualitatively. For the purpose to measure the complicated biomedical structure of cornea which has small size compared with industrial specimen, not only the feasibility needs to be confirmed by simulation and test, but also the accuracy of the measurement needs to be analysed. Based on the previous algorithms which are about phase measurement, both Fourier Transform (*FFT*) and Phase stepping methods were implemented into the data processing and compared for accuracy.

1.1.5 Interferometry Technology of Fringe Analysis

By using interferometry techniques, a valid and calibrated system can be used for measuring the surface of specimen with high precision. Holographic interferometry has proven to be a powerful non-destructive testing tool for the measurement of displacement and its derivatives. With the aid of fringe analysis, holographic interferometry is extensively implemented. The quantitative evaluation of holographic interferometer fringes for the determination of components of three-dimensional deformation requires the accurate measurement of many fringe patterns [10]. The use of image analysis techniques plays an important role in achieving a high resolution interferogram.

This thesis describes the development of a diagnostic system. The Fourier transform method was used in the evaluation of the retardation by using a fringe carrier system. In photoelasticity, the light intensity from the analyzer in a circular polariscope depends on both the retardation (isochromatic) and the isoclinic parameter. A fast Fourier transform (FFT) method is then used to process the complete photoelastic fringe image over the whole surface of the model. The experiment also uses a minimum spanning tree phase unwrapping strategy to create a continuous

map of the whole stress field. Finally, the whole principal stress difference field is calculated and plotted from one single exposure showing the methods' potential for use as a reflection analysis system, suitable for application to non-stationary objects and complicated stress patterns. Interferometric surface topography based on two-dimensional Fourier transform (2D FFT) has been compared to a phase stepping technique. A new self-calibrating phase stepping method has been developed and reported. An optimal filtering algorithm for 2D FFT has been described. Both methods have been applied in determining the topography of a steel auxiliary plate (platen) using a Michelson interferometer. The standard deviation of the difference between these two methods has been found. Micro-meter level resolution in surface topography is shown to be feasible with new-designed hardware.

The application of phase-shifting photoelasticity to a real-time dynamic event involves simultaneous recording of the four phase-shifted images. An instrument, believed to be novel, has been developed for this purpose. The Multispec Imager was introduced into digital photoelasticity to enable the splitting of the optical path of an object into four identical paths, thus permitting the recording of the required four phase-shifted images. Experimental demonstration is provided for validation.

This study also investigated the change in corneal curvature and corneal wave-front aberrations with accommodation. The advent of computerised corneal topography analysis (through videokeratoscopes) has changed our level of understanding of the shape of the corneal surface. Just as it is difficult to get a good idea of the topography of a land surface with a two-dimensional map, so it is with the corneal topography map. It is much easier to visualise the corneal surface by showing it in a 3D (perspective) map. The 3D map can graphically show even small changes in the shape of topography and thus give a better, solid object view' of what is happening.

1.2 Structure

This thesis concerns the development of analysis strategies, aiming at quantitative analysis of four image related subclasses in optical engineering. The first subclass being interferometric images; the second subclass being phase stepping measurement with rotator and multi-camera methods; the third subclass being phase analysis with different types of cameras and light sources; the last subclass being high resolution images and reconstruction of a three-dimensional phase object. It has been necessary to apply techniques from the field of digital image processing and more general computer science to carry out the analysis.

In the development of the complete system, the design of the experiments and the analysis technique are interdependent. The following is intended to provide an overview of the organization of the thesis. In this thesis, the phase stepping and Fourier transforms techniques have been used to provide quantitative data comparative approaches. Their results are compared to determine the most accurate method for the measurement of cornea birefringence.

Chapter 2 summarizes the common methodologies used in this area and it is intended as a theory basis for subsequent chapters. Phase measurement and interferometry technology are explained and the settings up procedure are described. However, the discussion of the advantages and disadvantages of these techniques which are used experimentally is left until chapter 3.

Chapter 3 presents the design of the experiment and diagnostic equipment. The data is derived from experiments using different light sources, light-emitting diode, fluorescent, infrared, light-emitting diode array and laser illumination. The experimental results obtained have been used to refine the diagnostic for contrast, illumination intensity and spectral content with respect to the quality of the phase contrast observed. Charge Coupled Device (CCD) and Complementary Metal Oxide Semiconductor (CMOS) techniques have been tested in preparation for the subsequent experiments. The details of each step are considered in depth with the aim of obtaining accurate measurements. As the study develops the miniature po-

lariscope and synchronized triggering camera-array are introduced. For the test of photoelasticity and interferometry analysis, they have been modified considerably. With the aid of the multi-camera, it is possible to achieve high-resolution image, depth of field detection, image stitching and dynamic range measurement.

In Chapter 4, the main aims of the thesis are developed comparing phase stepping, carrier fringe and FFT technique quantitative analysis in phase measurement and photoelasticity stress analysis. There have been several impediments to the quantitative analysis of images using optical techniques. The 1-D and 2-D Fourier transform fringe analysis is given in this chapter, and the phase unwrapped algorithm is implemented for accuracy analysis with phase mapping. Chapter 5 focuses on the structure and optical system of the human eye. There is some testing using polarised light to study the cornea and retina. Interferometry and phase-stepping techniques are used in this application.

The eye measurement platform is introduced in chapter 6. Here the traditional laser light source is replaced and monochromatic LED and infrared are advocated. The normal photoelasticity transmission system is improved to a reflection system. This set up is designed to be as flexible and be adaptive for as many applications as possible. The cornea phase structure and surface information are successfully explored and reconstructed by three-dimensional measurement. The micro-level structure is studied by a polarised microscope.

The aim of chapter 7 is to present 3D phase object reconstruction based on the method and equipment described above, and to construct a future plan.

The Fig.1.1 shows the structure of the thesis,

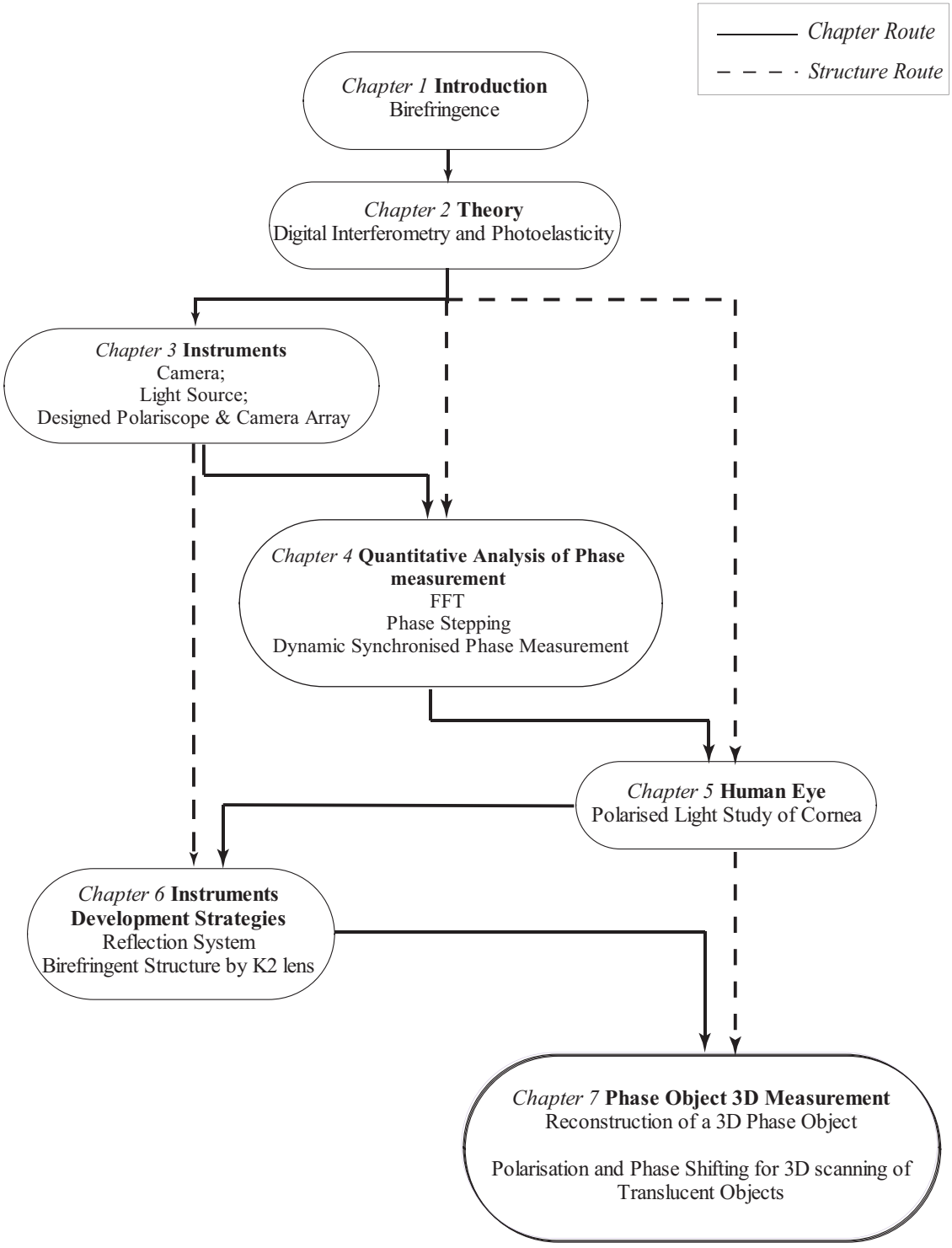

Figure 1.1 Main structure and content of thesis.

Chapter 2

Birefringence Measurement and Optical Interferometry Technology

Birefringence spectroscopy is a measurement of orientation in an optically anisotropic sample from the retardation of polarized light passing through the specimen. In order to view the birefringence in a sample, polarised light must be used. It is important that the polariser is oriented so that it is neither parallel nor perpendicular to the principle axis of the sample, as will be discussed further[11].

Phase measurement interferometry can be used to directly measure wavefront phase in an interferometer corresponding to the relative difference between the test and reference optical paths [12].When a detector is used to sense fringes, and a known phase change is induced between the object and reference beams, the phase of a wavefront may be directly calculated from changes in the recorded intensity data [13]. The data are then passed to a computer where the phase at each point is calculated. Information about the test surface is geometrically related to the calculated wavefront phase.

Spatial phase measurement methods represent a separate class of phase measurement methods distinct from temporal methods. In spatial methods, the phase information is separated out in space and is recorded in one time frame, which is in contrast to the temporal methods that separate phase information into a time sequence of interferograms. The spatial techniques can be further subdivided

into phase stepped methods and spatial carrier methods. Both approaches have particular advantages in different areas of application [14].

Photoelasticity is a method for stress analysis of specimens subject to load. The standard methods rely on the technique of making a model which is a copy (often on a reduced scale) of the specimen under investigation.

This model, usually made from plastics such as epoxy or polyester resins, becomes birefringent when subject to loads. Thus, a two-dimensional photoelastic model exerted by forces in its own plane will behave as a general retarder, the retardance and the direction of the retardation axes being continuous variables across the model plane. When this loaded model is placed in a polariscope which consists of a light source and properly arranged polarising elements, a system of fringes is observed.

2.1 Literature Review

Two methods are commonly used for digital phase measurements. In one method, *phase shifting* , the optical path difference between the interfering beams is varied linearly with time. In another method, *phase stepping*, the optical path difference between the interfering wavefronts is changed in equal steps. The two methods are theoretically equivalent. Four measurements at each point can be used conveniently to calculate the original phase difference between the wavefronts at that point. A charge-coupled detector (CCD) array can be used to make measurements simultaneously at a very large number of points (typically, 512×512), which obtains high resolution (3272×2469 pixels) covering the interference pattern. An advanced camera could obtain an image with very high resolution, and a powerful computer could process the data easily. Since the phase calculation algorithm only yields phase data to modulo 2π, subsequent processing is usually necessary to link adjacent points and remove discontinuities in phase.

2.2 Fringe Pattern Analysis

A fringe pattern can be considered as a sinusoidal signal fluctuation in a two-dimensional space, where the intensity distribution of the interference pattern $I(x, y)$ can be described by:

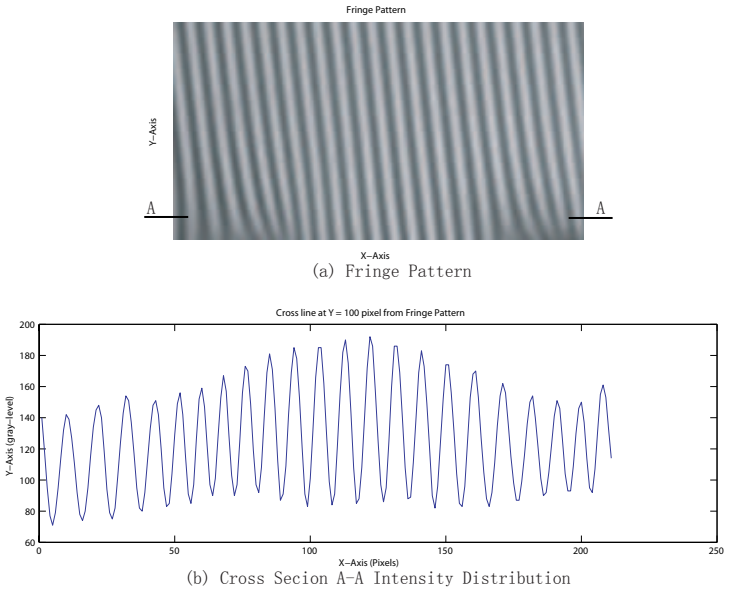

(a) Fringe Pattern

(b) Cross Secion A-A Intensity Distribution

Figure 2.1 A Fringe Pattern as a Sinusoidal signal Fluctuation in Space.

$$I(x, y) = a(x, y) + b(x, y)\cos[\phi(x, y) + \phi_{ref}] \tag{2.1}$$

here $a(x, y)$ and $b(x, y)$ are background illumination and local contrast respectively; and $\phi(x, y)$ is the phase function obtained when an interferometer, moire system, or other device produces a continuous map which is an analogue of the physical quantity being measured; and ϕ_{ref} is a reference phase. In all partial cases the reference function and noise are introduced in an additive or multiplicative manner.

In Fig.2.1, (a) is a standard fringe pattern which generates by a crystal quartz wedge. Line AA is a raster line, it presents intensity distribution curve in (b). The background contrast functions contain the intensities of interfering fields and the various disturbances. Generally, $a(x, y)$ contains all additive contributions, while $b(x, y)$ comprises all multiplicative influences.

The main analysis of the fringe pattern is computing the phase $\phi(x, y)$ by measuring intensity values. The general process is shown in Fig.2.2 [15].

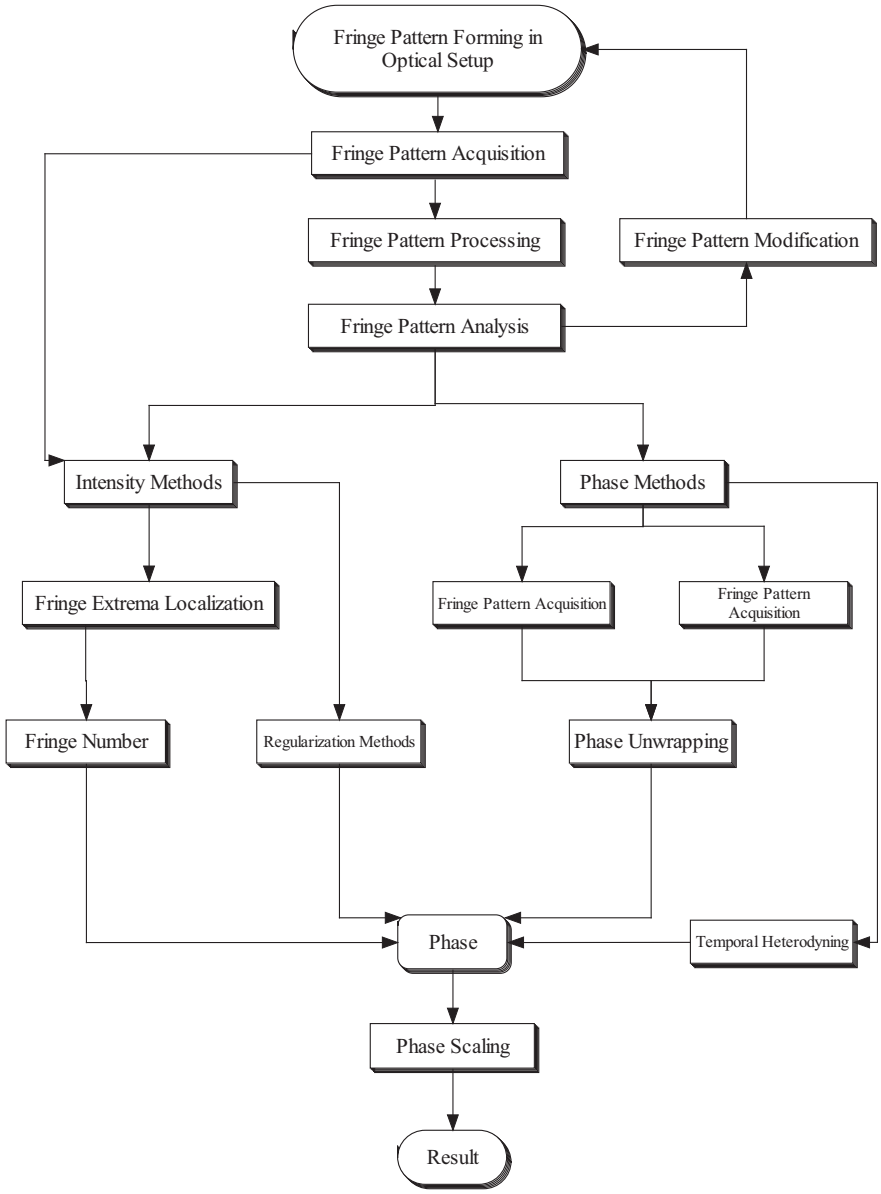

Figure 2.2 The general scheme of the fringe pattern analysis process.

These procedures finalize the fringe measurement stage, which reduces a fringe pattern to a continuous phase map. It converts the phase map into a physical intensity mapping and measures, in a form which enables further information processing.

2.2.1 Temporal Phase-Stepping Interferometry (PSI)

Phase-Stepping Interferometry (PSI) is the most common technique used to detect the modulating phase of interferograms. In the PSI technique, an interference pattern is phase stepped under computer control and spatially digitized over several phase steps.

To detect the phase value $\phi(x, y)$, the phase is correlated with the sinusoidal and cosine signal of the same frequency and averaged over many periods of oscillation. The phase $\phi(x, y)$ can be calculated using

$$\phi(x,y) = \arctan\left(\frac{\int_{-\infty}^{\infty} I(t)\sin(\omega t)dt}{\int_{-\infty}^{\infty} I(t)\cos(\omega t)dt}\right) = \arctan\left(\frac{(b/2)\sin(\phi)}{(b/2)\cos(\phi)}\right) \tag{2.2}$$

In a similar manner to the integrated case, the intensity of interference fringes can be expressed using Fourier series and the phase can be described by[16][17][18][19]

$$\phi = \arctan\left(\frac{\sum_{i=1}^{N} I_i(x,y)\sin\delta_i}{\sum_{i=1}^{N} I_i(x,y)\cos\delta_i}\right) \tag{2.3}$$

The effective reference phase in the measurements is also affected by the surrounding disturbance. A method which evaluates the actual phase difference between the interfering beams at the same time as the data are read was proposed in[20].

The phase-stepping technique allows one to measure the interference phase with an accuracy of 1/100 of a fringe at any point in the image [21]. The following shows different algorithms for the phase-stepping method of phase measurements.

Three-Step Technique

It is known that three recorded interferograms with different phase steps are basically needed to calculate the phase in the general equation of interference fringe pattern. For three recorded intensity distributions with the phase shifts $\gamma_i = \pi/4$, $3\pi/4$ and $5\pi/4$ [15][22]. The equations are:

$$
\begin{aligned}
I_1(x,y) &= I_0(x,y)\left\{1+\gamma\cos\left[\phi\left(x,y\right)+\tfrac{\pi}{4}\right]\right\}\\
I_2(x,y) &= I_0(x,y)\left\{1+\gamma\cos\left[\phi\left(x,y\right)+\tfrac{3\pi}{4}\right]\right\}\\
I_3(x,y) &= I_0(x,y)\left\{1+\gamma\cos\left[\phi\left(x,y\right)+\tfrac{5\pi}{4}\right]\right\}
\end{aligned}
\tag{2.4}
$$

The phase at each point in the interferogram is simplified as

$$
\phi(x,y)=\arctan\left[\frac{I_3(x,y)-I_2(x,y)}{I_1(x,y)-I_2(x,y)}\right] \tag{2.5}
$$

where the numerator and denominator of equation 2.5 are:

$$
I_3(x,y)-I_2(x,y)=\sqrt{2}I_0(x,y)\gamma\sin\phi \tag{2.6}
$$

$$
I_1(x,y)-I_2(x,y)=\sqrt{2}I_0(x,y)\gamma\cos\phi \tag{2.7}
$$

and the detected fringe visibility is

$$
\gamma=\frac{\sqrt{\left(I_3(x,y)-I_2(x,y)\right)^2+\left(I_1(x,y)-I_2(x,y)\right)^2}}{\sqrt{2}I_0} \tag{2.8}
$$

When the phase shift $\Delta\phi$ is used, the three intensities become

$$
\begin{aligned}
I_1(x,y) &= I_0(x,y)\left\{1+\gamma\cos\left[\varphi\left(x,y\right)-\delta\right]\right\}\\
I_2(x,y) &= I_0(x,y)\left\{1+\gamma\cos\left[\varphi\left(x,y\right)\right]\right\}\\
I_3(x,y) &= I_0(x,y)\left\{1+\gamma\cos\left[\varphi\left(x,y\right)+\delta\right]\right\}
\end{aligned}
\tag{2.9}
$$

and the phase can be calculated using

$$
\phi(x,y)=\arctan\left[\left(\frac{1-\cos\phi(x,y)}{\sin\phi(x,y)}\right)\frac{I_1(x,y)-I_3(x,y)}{2I_2-I_1(x,y)-I_3(x,y)}\right] \tag{2.10}
$$

The detected fringe visibility for the general phase shift $\Delta\phi$ is

$$
\gamma=\frac{\sqrt{\left[\left(1-\cos\delta\right)\left(I_1-I_3\right)\right]^2+\left[\sin\delta\left(2I_2-I_1-I_3\right)\right]^2}}{2I_0\sin\delta(1-\cos\delta)} \tag{2.11}
$$

Four-Step Technique

The Four-Step method is a common algorithm for phase calculations. The four recorded sets of intensity measurements can be written as below in this case

[15][22].

$$\begin{aligned}
I_1(x,y) &= I_0(x,y)\left[1+\gamma\cos\phi(x,y)\right] \\
I_2(x,y) &= I_0(x,y)\left\{1+\gamma\cos\left[\phi\left(x,y\right)+\tfrac{\pi}{2}\right]\right\} = I_0\left[1-\gamma\sin\phi(x,y)\right] \\
I_3(x,y) &= I_0(x,y)\left\{1+\gamma\cos\left[\phi\left(x,y\right)+\pi\right]\right\} = I_0\left[1-\gamma\cos\varphi(x,y)\right] \\
I_4(x,y) &= I_0(x,y)\left\{1+\gamma\cos\left[\phi\left(x,y\right)+\tfrac{3\pi}{2}\right]\right\} = I_0\left[1+\gamma\sin\phi(x,y)\right]
\end{aligned} \tag{2.12}$$

where $\delta = 0$, $\pi/2$, π and $3\pi/2$ respectively. The phase at each point is

$$\phi(x,y) = \arctan\left[\frac{I_4(x,y)-I_2(x,y)}{I_1(x,y)-I_3(x,y)}\right] \tag{2.13}$$

and where the detected fringe visibility is calculated from

$$\gamma = \frac{\sqrt{\left(I_4-I_2\right)^2+\left(I_1-I_3\right)^2}}{2I_0} \tag{2.14}$$

Five-Step Technique

The Five-Step method uses $\pi/2$ phase shifts to minimize phase calibration errors. This algorithm is designed to reduce the possibility of having the numerator and denominator tend to zero, and thereby reduces the uncertainty in the calculation[15][22]. The five frames of intensity with relative phase shifts of δ are,

$$\begin{aligned}
I_1(x,y) &= I_0(x,y)\left\{1+\gamma\cos\left[\phi(x,y)+\pi\right]\right\} = I_0\left[1-\gamma\cos\phi(x,y)\right] \\
I_2(x,y) &= I_0(x,y)\left\{1+\gamma\cos\left[\phi\left(x,y\right)-\tfrac{\pi}{2}\right]\right\} = I_0\left[1+\gamma\sin\phi(x,y)\right] \\
I_3(x,y) &= I_0(x,y)\left\{1+\gamma\cos\phi\left(x,y\right)\right\} \\
I_4(x,y) &= I_0(x,y)\left\{1+\gamma\cos\left[\phi\left(x,y\right)+\tfrac{\pi}{2}\right]\right\} = I_0\left[1-\gamma\sin\phi(x,y)\right] \\
I_5(x,y) &= I_0(x,y)\left\{1+\gamma\cos\left[\phi\left(x,y\right)+\pi\right]\right\} = I_0\left[1-\gamma\cos\phi(x,y)\right]
\end{aligned} \tag{2.15}$$

where the phase shifts are $-\pi$, $-\pi/2$, 0, $\pi/2$ and π. The phase calculated from this set is given by

$$\phi(x,y) = \arctan\left\{\frac{2\left[I_2(x,y)-I_4(x,y)\right]}{2I_3(x,y)-I_5(x,y)-I_1(x,y)}\right\} \tag{2.16}$$

For this technique, the detected fringe visibility is given by

$$\gamma = \frac{\sqrt{2\left(I_2 - I_4\right)^2 + \left(2I_3 - I_5 - I_1\right)^2}}{4I_0} \tag{2.17}$$

This algorithm may get high accuracy of phase measurement, but it needs more acquisition time than others and may be susceptible to random environmental errors.

Fourier Transform Method

The Fourier Transform and inverse transform can be defined as

$$G(u) = \int_{-\infty}^{\infty} g(x) e^{-j2\pi ux} \tag{2.18}$$

$$g(x) = \int_{-\infty}^{\infty} G(u) e^{j2\pi ux} \tag{2.19}$$

If $g(x)$ is continous and integrable and $G(u)$ is integrable in the equations above, the Discrete Fourier Transform (DFT) is defined as [23]

$$G(n) = \frac{1}{N} \sum_{k=0}^{N-1} g(k) e^{(-j2\pi nk)/N}, \qquad \text{for} \quad n = 0, 1, 2, 3, ..., N-1 \tag{2.20}$$

$$g(k) = \sum_{n=0}^{N-1} G(n) e^{(j2\pi nk)/N}, \qquad \text{for} \quad n = 0, 1, 2, 3, ..., N-1 \tag{2.21}$$

A two dimensional function $g(x, y)$ has a two dimensional Fourier transform $G(u, v)$ given by

$$G(u, v) = \int_{-\infty}^{\infty} \int_{-\infty}^{\infty} g(x, y) e^{-j2\pi(ux+uy)} dxdy \tag{2.22}$$

and where the two dimensional inverse Fourier transform is

$$g(x, y) = \int_{-\infty}^{\infty} \int_{-\infty}^{\infty} G(u, v) e^{-j2\pi(ux+uy)} dudv \tag{2.23}$$

Equations2.22 and 2.23 are analogous to the one dimensional case, and the two dimensional $G(u, v)$ can be expressed as a one dimensional case. The two dimensional Discrete Fourier Transform is defined as

$$G(u,v) = \frac{1}{MN}\sum_{x=0}^{M-1}\sum_{y=0}^{N-1} g(x,y)e^{-j2\pi(\frac{ux}{M}+\frac{vy}{N})}, \quad \text{for} \quad u = 0,1,2,3,...,M-1 \quad \text{and} \quad v = 0,1,2,3,...,N-1 \tag{2.24}$$

$$g(x,y) = \sum_{x=0}^{M-1}\sum_{y=0}^{N-1} G(u,v)e^{j2\pi(\frac{ux}{M}+\frac{vy}{N})}, \quad \text{for} \quad u = 0,1,2,3,...,M-1 \quad \text{and} \quad v = 0,1,2,3,...,N-1 \tag{2.25}$$

The Fast Fourier Transform (FFT) technique is employed to extract phase information. The carrier frequency interferogram can be written based on $Takeda's$ method

$$g(x,y) = a(x,y) + c(x,y)e^{2\pi f_0 jx} + c^*(x,y)e^{-2\pi f_0 jx} \tag{2.26}$$

with

$$c(x,y) = \frac{b(x,y)}{2}e^{j\phi(x,y)} \tag{2.27}$$

and where $*$ denotes the complex conjugate.

The recorded intensity distribution of the fringe pattern shown is Fourier transformed with respect to x, which gives:

$$g(f,y) = A(f_x,y) + C(f_x - f_0,y) + C^*(f_x + f_0,y) \tag{2.28}$$

where the upper case quantities denote the Fourier spectra, and where f_x is the spatial frequency in the x direction. Since the spatial variations of $a(x,y)$, $b(x,y)$ and $\phi(x,y)$ are slow compared to the spatial carrier frequency f_0, the Fourier spectra in equation2.26 are separated by f_0, as is shown in Fig.(2.3).

Using a quadrature bandpass filter, the function $H(f_x - f_0,y)$ in the frequency plane, the function $C(f_x - f_0,y)$ can be isolated and translated by f_0 toward the origin to remove the carrier and obtain $C(f_x,y)$ as it is shown in Fig.2.3, therefore,

$$C(f_x - f_0,y) = H(f_x - f_0,y)g(x,y) \tag{2.29}$$

where $H(f_x - f_0,y)$ represents a quadrature bandpass filter centered at $-\omega_0$ and with a bandwidth large enough to contain the spectrum of $C(f_x - f_0,y)$. Then the

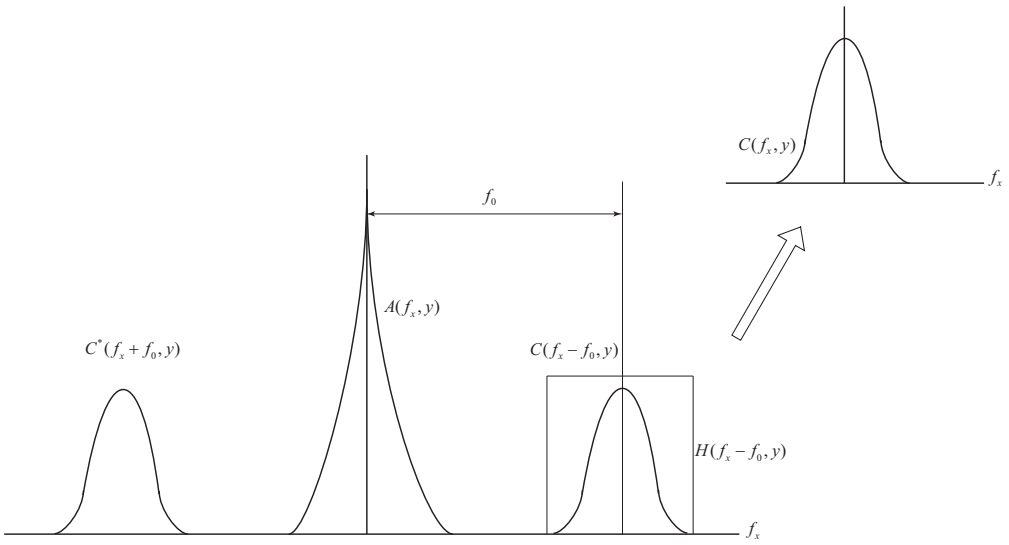

Figure 2.3 Separated Fourier spectra of a tilted fringe pattern.

following step either translates the information peak toward the origin to remove the carrier frequency f_0 to obtain $C(f_x, y)$ or Fourier transform it to find directly the inverse Fourier transforms of the filtered signal, so the phase is obtained from equation:

$$\phi(x, y) = \arctan\left(\frac{\mathrm{Im}[c(x, y)]}{\mathrm{Re}[c(x, y)]}\right) \tag{2.30}$$

where Im and Re represent the imaginary and real parts of $c(x, y)$, respectively.

Since phase calculation by computer gives principal values ranging from $-\pi$ to π, the phase distribution is wrapped into this range and consequently has discontinuities with 2π phase jumps for variations greater than 2π. These phase distributions have to be corrected by using a phase unwrapping algorithm.

As an example of the two dimensional FFT for fringe analysis, Fig. 2.4 shows the fringe pattern obtained by using a fringe carrier. The resulting interference phase distribution modulo 2π is given in Fig. 2.5, and the unwrapped phase map is shown in Fig. 2.6.

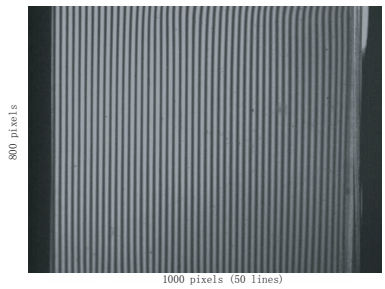

Figure 2.4 Interference pattern of carrier fringe by crystal quartz wedge.

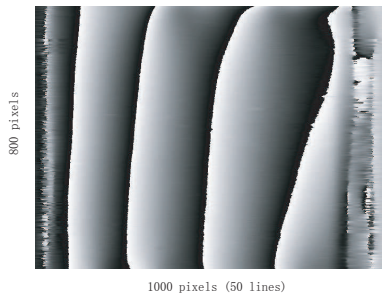

Figure 2.5 Interference phase modulo 2π.

2.2.2 Phase Unwrapping Method

Phase unwrapping is the process by which the absolute value of the phase angle of a continuous function that extends over a range of more than 2π is recovered. This absolute value is lost when the phase term is wrapped upon itself with a repeat distance of 2 π due to the fundamental sinusoidal nature of the wave functions used in the measurement of physical properties.

The relationship between the wrapped phase and unwrapped phase may be stated as

$$\phi_w(x, y) = \phi_u(x, y) + 2\pi k(x, y) \tag{2.31}$$

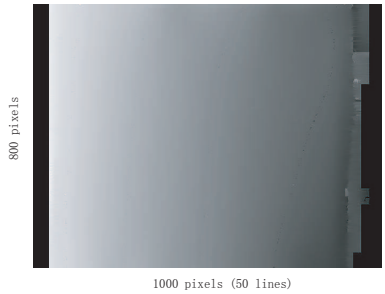

Figure 2.6 Unwrapped phase map of interference fringes.

where $\phi_w(x, y)$ is the wrapped phase, $\phi_u(x, y)$ is the unwrapped phase, and $k(x, y)$ is an integer-valued correcting field.

The phase calculations in phase-shifting interferometry can be expressed normally as following shown:

$$\phi = \arctan(I_\alpha / I_\beta) \tag{2.32}$$

where I_α and I_β are functions of the recorded intensity. It gives the principle phase values ranging from $-\pi$ to π due to the feature of arctangent function, so that the phase distribution is wrapped and has 2π phase jumps. The result from the direct calculation of arctangent function is called *wrapped phase*.

The wrapped phase is a sawtooth function and discontinuities occur when it changes by 2π. These discontinuities can be corrected by adding or subtracting 2π according to the direction of the phase jump, which gives unwrapped phase. When phase jumps from π to $-\pi$, we get the result by adding 2π. If the change is from $-\pi$ to π, then we subtract 2π. In practice, phase jumps are not exactly equal to 2π due to the errors caused by the resolution and noise of data.

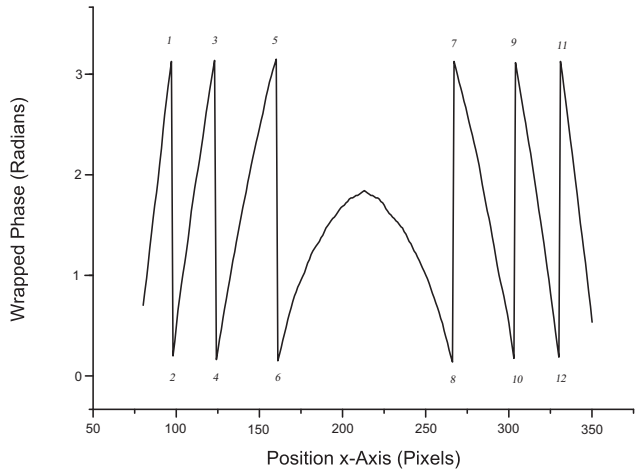

Figure 2.7 Wrapped phase distribution of centre raster in a wrapped phase map .

Fig.2.7 and Fig.2.8 show an example of the phase unwrapping process. In Fig. 2.7, the 2π phase jumps occur at points $1, 3, 5, 7, 9$ and 11. At points $1, 3$ and 5, the phase change is from π to $-\pi$, so that 2π is added to the phase from points $2, 4$ and 6 to the end of the lines. 2π is subtracted from the phase along the path from points $8, 10$ and 12 to the end of the lines at the points $7, 9$ and 11. The

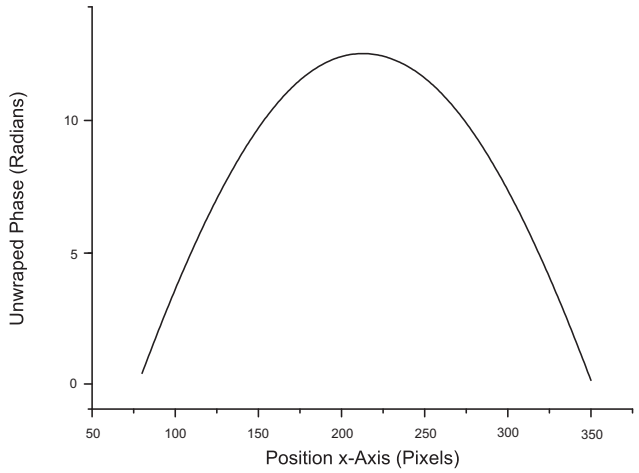

Figure 2.8 Unwrapped phase distribution of centre raster obtained from the wrapped phase data .

unwrapped map which is obtained from the phase data is shown in Fig.2.8, where the unwrapped phase distribution is shown as a continuous function.

Another phase unwrapping method was proposed by Judge [24]. This method uses the minimum spanning tree approach for phase unwrapping. The minimum spanning tree is a mechanism for comparing the consistency of possible phase unwrapping routes.

The minimum spanning tree is a product of graph theory. The Fig. 2.9 is an example of a weighted directed graph, which consists of vertices and edges. A graph is connected if it is possible to reach any vertex from any other vertex by traveling along the edges. A graph G is said to be connected if there is at least one path between every pair of vertices in G. Otherwise, G is disconnected. Fig. 2.9 shows a connected graph.

A spanning tree of a graph G is a minimal subgraph connecting all the vertices of G. If graph G is a weighted graph ($i.e.$, if there is a real number associated with each edge of G), then the weight of a spanning tree T is defined as the sum of the weights of all the branches in T. Among all of the spanning trees of G, those with the smallest weight are called Minimum Spanning Trees. Fig.2.10 shows the minimum spanning tree of the graph in Fig.2.9 [25].

The minimum spanning tree may be constructed using various algorithms. Prim's

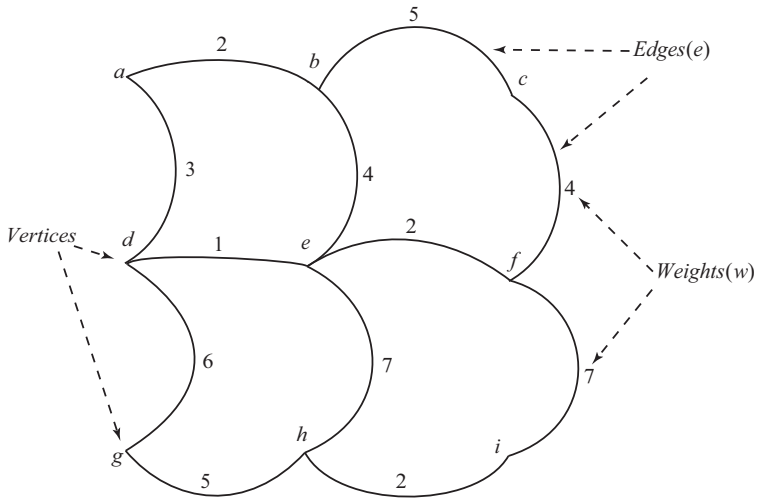

Figure 2.9 Example of a weighted undirected connected Graph.

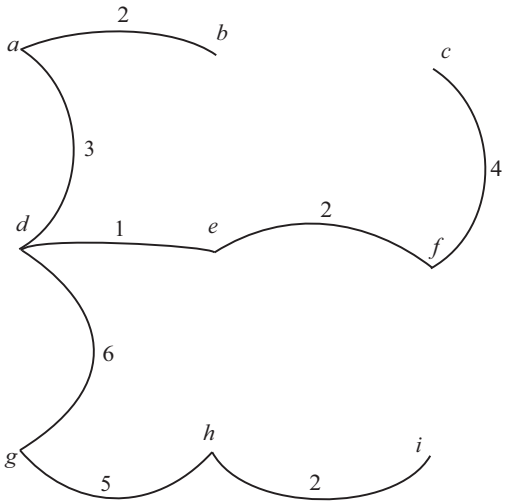

Figure 2.10 A Minimum Spanning Tree of the Weighted Graph.

algorithm presents an efficient solution. The four edge weights are tabulated for each pixel. Unwrapping begins at the pixel which holds the lowest edge weight.

On each iteration of Prim's algorithm a new edge e is added to the growing spanning tree T. The edge e is the edge of least weight connecting a vertex in the remainder of graph with those in T.

The initial procedures of our methods include the steps of computation of the wrapped phase map, fringe edge detection, and then row-by-row, column by column unwrapping of phase.

The aim of the process is to automatically produce a displacement map of the

surface described by the phase fringe field. The processed output will contain a displacement value for each pixel of the captured field relative to some single origin.

2.3 Digital Photoelasticity

The electromagnetic field is a vector quantity which is perpendicular to the direction of propagation and with a defined orientation in space. This property is known as the polarisation of light. Jones vectors and matrices are used to describe polarisation. The control and measurement of the state of polarization by some methods are treated in this chapter.

2.3.1 Polarised Light

The theory of photoelasticity is based on the wave nature of light. For ordinary light, the orientation of the amplitude vector in the plane perpendicular to the propagation direction is random.

If the amplitude vectors of all light rays emanating from a source are restricted to a single plane, the light is said to be plane polarised, as shown in Fig.2.11

Viewing the light wave head-on, the wave can be seen with its amplitude vector restricted to a single plane, which is called the $plane\ of\ polarisation.$

If two waves are propagating in the same direction, vector algebra may be applied to the wave amplitudes to determine the resultant wave amplitude. Consider first the addition of two plane polarised waves that are in phase, but that have different planes of polarization, as is shown in Fig.2.12

The vector addition of these two waves produces a new plane-polarized wave which has the same frequency, wavelength, and phase as the component waves.

When two plane-polarized waves of arbitrary amplitude and different phase are combined, the figure is shown as below in Fig.2.13:

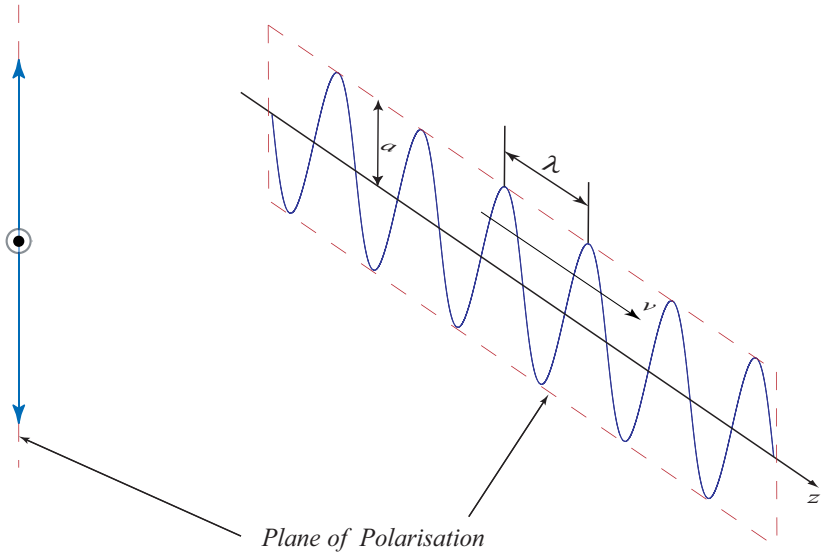

Figure 2.11 Plane-Polarised Light.

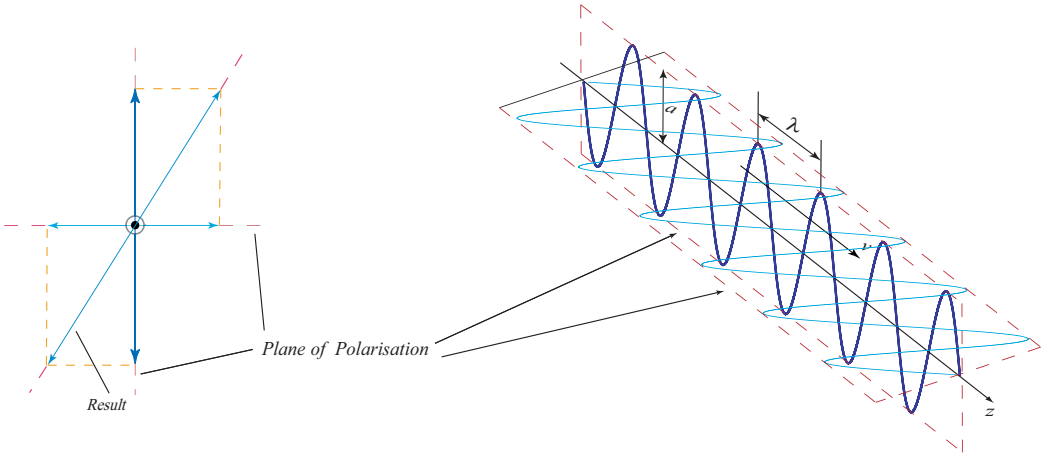

Figure 2.12 Addition of two plane-polarized light waves that are in phase.

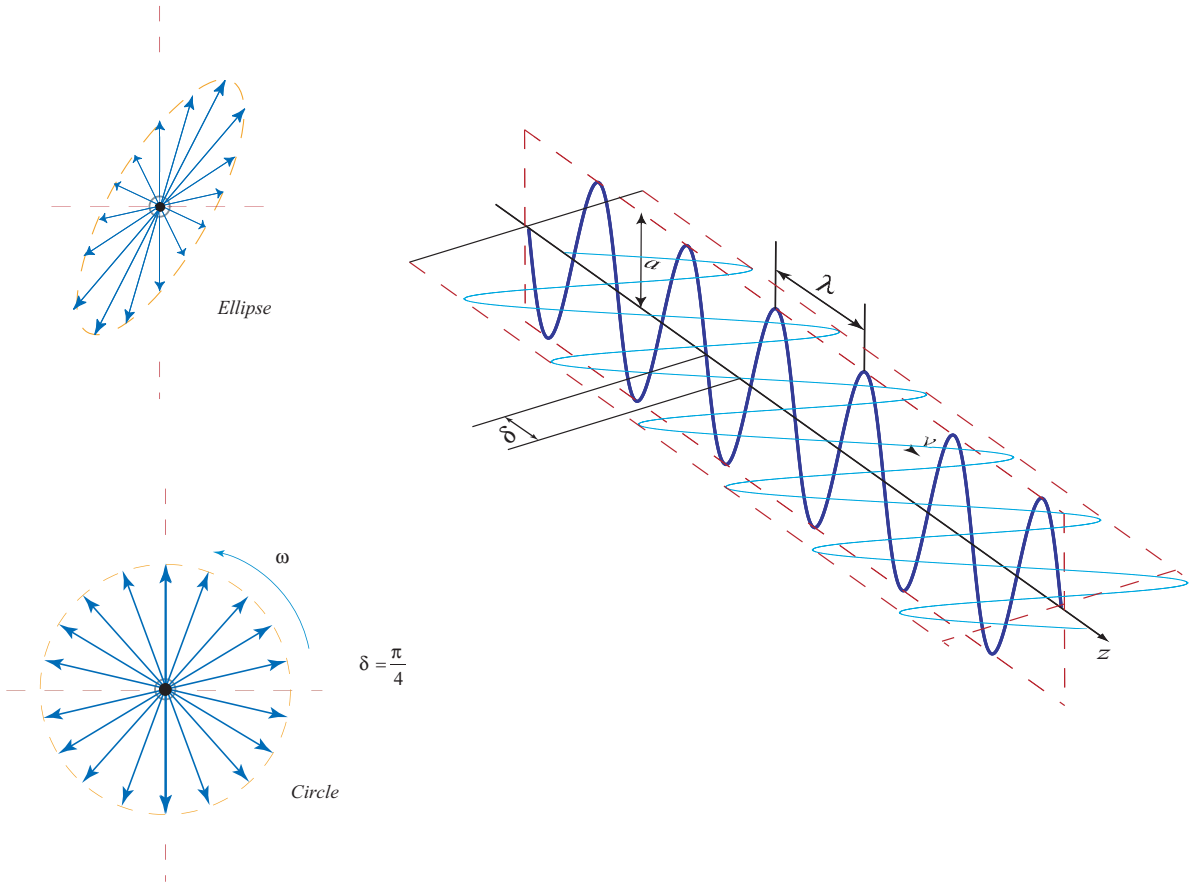

Figure 2.13 Elliptically and Circularly Polarized Light.

The horizontally polarized wave is ahead of the vertically polarized wave by a distance δ. At the instant shown, at the leading edge of the wave, the horizontal component is negative and the vertical component vanishes; therefore, the resultant is in the negative horizontal direction. A short time later, the horizontal component becomes slightly more negative and the vertical component rapidly becomes negative; therefore, the resultant is in the fourth quadrant as viewed backwards along the +z axis. With increasing time, an elliptical path is traced by the amplitude vector of the resultant wave, as shown. Thus the result of adding two plane-polarized waves that are neither in phase nor in the same plane is a special kind of rotating wave, called an $elliptically\ polarized\ wave$. This wave has the same frequency as the component waves, but is not restricted to a single plane.

An important special case of elliptically polarized light is circularly polarized light. This can be (and usually is) created by combining orthogonal plane-polarized waves of equal amplitude that are out of phase by exactly one-quarter of a wavelength ($\delta = \pi/4$). The resultant wave is a rotating wave of constant amplitude and constant angular frequency ω.

2.3.2 The Jones Matrix of Polarised Light

Considering a plane wave propagating in the z-direction, the components along the x and y axes of the field amplitude vector are

$$\begin{aligned} U_x &= U\cos\phi \\ U_y &= U\sin\phi \end{aligned} \tag{2.33}$$

and so we have

$$\begin{aligned} u &= (U_x e^{i\delta_x} e_x + U_y e^{i\delta_y} e_y) e^{ikz} \\ &= e^{i\beta/2}(U_x e^{-i\delta/2} e_x + U_y e^{i\delta/2} e_y) \\ &= e^{i\beta/2}(u_x e_x + u_y e_y) \end{aligned} \tag{2.34}$$

where e_x and e_y are the unit vectors along the $x-$ and $y-$ axis respectively. δ_x

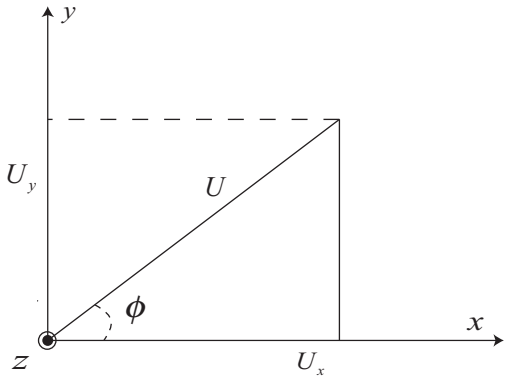

Figure 2.14 x and y axes vector of field amplitude.

and δ_y are phase constants. $\beta = \delta_x + \delta_y$, $\delta = \delta_y - \delta_x$, $e^{i\beta/2}$ is a common phase factor which can be omitted since it does not affect the orientation of u.

Equation 2.34 can be written as,

$$|U\rangle = e^{i\beta/2} \begin{pmatrix} u_x \\ u_y \end{pmatrix} \tag{2.35}$$

where $u_x = U_x e^{-i\delta/2}$, $u_y = U_y e^{i\delta/2}$, $|U\rangle$ is called Jones vector or state vector, representing the state of polarization of the wave[26]. Equation 2.35 can be decomposed as

$$|U\rangle = U_x e^{-i\delta/2} |P_x\rangle + U_y e^{i\delta/2} |P_y\rangle \tag{2.36}$$

where

$$|P_x\rangle = \begin{pmatrix} 1 \\ 0 \end{pmatrix}, \qquad |P_y\rangle = \begin{pmatrix} 0 \\ 1 \end{pmatrix} \tag{2.37}$$

are base vectors representing waves, linearly polarized in the $x-$ and $y-$ directions, respectively. Equation 2.36 is a general expression for an arbitrary state of polarization decomposed into the orthogonal basis $|P_x\rangle$ and $|P_y\rangle$.

As discussed in the above section, equation 2.36 represents a wave, linearly polarised at an angle ϕ to the $x-$ axis, and is termed a $P-$ state, when $\delta = 0$ and $U_x = \cos\phi$, $U_y = \sin\phi$, which yields

$$|P\rangle = \cos\phi |P_x\rangle + \sin\phi |P_y\rangle \tag{2.38}$$

For circularly polarized states, we have $\delta = \pm\pi/2$ and $U_x = U_y = 1/\sqrt{2}$ (normalized intensity).

Right circularly polarised wave (an $R-$state) is given by

$$|R\rangle = \frac{1}{\sqrt{2}}(e^{-i\pi/4}\,|P_x\rangle + e^{i\pi/4}\,|P_y\rangle) \tag{2.39}$$

and a left circularly polarised wave (an $L-$state) is

$$|L\rangle = \frac{1}{\sqrt{2}}(e^{i\pi/4}\,|P_x\rangle + e^{-i\pi/4}\,|P_y\rangle) \tag{2.40}$$

It is easily verified that the Jones matrix for a linear polarizer with its transmission direction along the $x-$axis represented in the $|P_x\rangle$ and $|P_y\rangle$ basis, must be

$$P_x = \begin{pmatrix} 1 & 0 \\ 0 & 0 \end{pmatrix} \tag{2.41}$$

and that of a retarder with retardance δ with its fast axis along the $x-$axis must be

$$M_x = \begin{pmatrix} e^{-i\delta/2} & 0 \\ 0 & e^{i\delta/2} \end{pmatrix} \tag{2.42}$$

To find the general expressions of these matrices when their axes are oriented at an arbitrary angle ϕ to the $x-$axis, we proceed as follows. First rotate the coordinate system through an angle ϕ such that the $x'-$ axis coincides with the filter axis, then apply the matrix of the filter and finally rotate the coordinate system back to its original position. This is expressed mathematically as,

for the polariser

$$P = R^{-1}P_xR \tag{2.43}$$

for the retarder

$$M = R^{-1}M_xR \tag{2.44}$$

where

$$R = \begin{pmatrix} \cos\phi & \sin\phi \\ -\sin\phi & \cos\phi \end{pmatrix} \tag{2.45}$$

is the rotation matrix and

$$R^{-1} = \begin{pmatrix} \cos\phi & -\sin\phi \\ \sin\phi & \cos\phi \end{pmatrix} \tag{2.46}$$

is its inverse.

This gives

$$P = \begin{pmatrix} \cos^2\phi & \sin\phi\cos\phi \\ \sin\phi\cos\phi & \sin^2\phi \end{pmatrix} \tag{2.47}$$

and

$$M = \begin{pmatrix} e^{-i\delta/2}\cos^2\varphi + e^{i\delta/2}\sin^2\varphi & -2i\sin(\delta/2)\sin\varphi\cos\varphi \\ -2i\sin(\delta/2)\sin\varphi\cos\varphi & e^{-i\delta/2}\sin^2\varphi + e^{i\delta/2}\cos^2\varphi \end{pmatrix} \tag{2.48}$$

As useful examples which are normally used in experiments, by putting $\delta = \pi/2$ and $\delta = \pi$, we find the matrixes for the $\lambda/4$ and $\lambda/2$ plates, respectively[27].

2.4 Advantage and Disadvantage of Methods

Spatial and Temporal techniques

The spatial and temporal techniques described above are based on the same principle of synchronous detection, however, they offer different possibilities as measuring techniques. The temporal methods are better suited for high accuracy measurements while the spatial techniques are designed for testing dynamic events, pulsed wavefront sensing and measurements under adverse conditions. Relative advantages and disadvantages of the main spatial techniques comparison with the temporal techniques are as follows[28], and Fig.2.15 shows a table which is about the comparison of advantages and disadvantages between the measurement by using spatial carrier (FFT) and phase stepping methods.

Problems with the Fast Fourier Transform (FFT) technique

The Fourier Transform analysis based on the FFT algorithm is suitable for automated fringe pattern analysis. The advantage of this technique is that only a single frame of irradiance data is required, and that phase-shift elements are not needed. Furthermore, background intensity variations and speckle noise can be reduced.

	Spatial Carrier	Phase-Steped
Advantages	Only one nterferogram.	*n* phase shifted interferograms are produced simultaneously.
	No special devices for carrier generation, whereas the temporal techniques require a frequency or phase-shifting device.	Enables analysis in one frame time.
	Allows analysis of dynamic events, pulsed wavefront sensing.	
	The measurements may be performed in adverse conditions.	
Disadvantages	Requires more sophisticated processing.	Requires additional calibration procedures and high quality imaging optics.
	In a general case it is more difficult to fully automate.	
	Detector array must have a higher spatial resolution or multiple detectors are required.	
	Spatial distribution of detector sensitivities must be uniform over the array.	

Figure 2.15 Comparison of Advantage and Disadvantages between Spatial Phase Measurement and Phase-Stepping Method.

However. there are some problems with the FFT based algorithm, such as aliasing, the ripple effect and spectral leakage. An infinite sequence of equidistant impulses can be described with a sample wave form and a sample interval, if the sample interval is too large, aliasing occurs. To avoid this problem, a sample interval has to be selected to be higher than one-half of the reciprocal of the highest frequency component ($\text{one sample interval} \leq 1/2 \times \text{highest frequency component}$).

It is necessary to truncate the sample wave form using the discrete Fourier transform so that only a finite number of points are considered. The cause of the ripple effect is that the truncation interval is insufficiently wide. To reduce it, if the Fourier transform of the truncation function approaches an impulse, there will be less error introduced by the convolutions in the results from truncation.

Finally, the leakage problem arises from the digitisation of data and truncation. An appropriate time-domain truncation or weighting function which has suitable frequency domain side-lobe characteristics has to be chosen in order to reduce the leakage. The leakage affects the results depending on the side lobes of the function FFT, where smaller side lobes can reduce spectral leakage. A weighting function is applied to the N-point sampling function before the FFT is computed, and this also reduces leakage.

The FFT method requires that there are sufficient carrier fringes to give a monotonic change in fringe field. This might be not guaranteed for an unknown fringe field in experiments. Incorrect filtering in the frequency domain, the influence of random noise, and the presence of spurious transients must be considered as sources of error in the FFT. Even an inappropriate selection of the carrier fringe frequency will result in error.

Chapter 3

Diagnostic Instrument and Design

In this chapter, CCD and $CMOS$ cameras are introduced. The characteristics of them are compared from their theories and parameters. Their results are compared and analysed. Then the camera which could obtain better performance will be used in experiments.

To pursue better accuracy, the light source needs to be selected carefully. Light source of different wavelengths are used and analysed in the experiments. The special and expensive light sources, such as infrared, laser diode and laser, are tested and compared, but not implemented in the instrument. The fluorescent light, red, blue and green LED were chosen based on their wavelength and bandwidth for evaluation in the instrument design.

Both of the camera and light sources are important factors in the experiment for accuracy analysis.

The last section of this chapter introduces a novel multi-camera design of the hardware. Two variations were constructed but not demonstrated for cornea application. The first, a multi-lens single camera construction. The second, an array of 9 individual cameras; the objective being to create a multi-step phase stepping measurement and analysis of the cornea. The potential application of this work is described in the further work chapter. Only a limited photoelastic evaluation has been possible, shown as an example of the application at the end of the chapter.

3.1 Type of Camera

Charge Coupled Device(CCD) and Complementary Metal Oxide Semiconductor($CMOS$) image sensors are two kinds of technologies.

The $CMOS$ sensors are cheaper and less power consuming than CCD. However, CCD's have better resolution but have some errors such as smearing.

"*In a CCD device, the charge is actually transported across the chip and read at one corner of the array. An analog-to-digital converter turns each pixel's value into a digital value. In most $CMOS$ devices, there are several transistors at each pixel that amplify and move the charge using more traditional wires. The $CMOS$ approach is more flexible because each pixel can be read individually*" [29].

3.1.1 Charge-Coupled Device(CCD) Camera

Both CCD and $CMOS$ senor cameras are used in experiments. With the advantage of CCD sensor, high resolution sensitivity data are collected. Due to the $CMOS$ sensor architecture, and sensor's characteristics, the multiple camera system is set up by using $CMOS$ sensor cameras. The details of description and parameters of two types of sensors are introduced in following sections.

High accuracy and resolution of image are an important focus in scientific and industrial imaging applications. The $AVT - Oscar\ CCD$ camera is used in our experiments, where the active area of the sensor (2/3 inch) consists of 3288×2470 pixels, and the pixel size is 2.7 micron, which can produce accurate data.

The essential idea behind the charge-coupled device (CCD) is the way the image is read from the array. The basic building block of this technique is the metal-oxide-semiconductor (MOS) capacitor [30]. The charge coupling is easily visualised as a "bucket bridge" of transferred charge, where the charge in one bucket is poured or moved into the adjacent bucket by the external manipulation of voltages. The quantity of the stored charge depends on the applied voltages and on the capacitance of the storage element.

3.1.2 Comparison

"*Because of these manufacturing differences, there have been some noticeable differences between CCD and $CMOS$ sensors*" [31].

- CCD sensors, as mentioned above, create high-quality, low-noise images. CMOS sensors, traditionally, are more susceptible to noise.

- Because each pixel on a CMOS sensor has several transistors located next to it, the light sensitivity of a CMOS chip tends to be lower. Many of the photons hitting the chip hit the transistors instead of the photodiode.

- CMOS traditionally consumes little power. Implementing a sensor in CMOS yields a low-power sensor.

- CCDs use a process that consumes lots of power. CCDs consume as much as 100 times more power than an equivalent CMOS sensor.

- CMOS chips can be fabricated on just about any standard silicon production line, so they tend to be extremely inexpensive compared to CCD sensors.

- CCD sensors have been mass produced for a longer period of time, so they are more mature. They tend to have higher quality and more pixels.

"*Based on these differences, CCDs tend to be used in cameras that focus on high-quality images with lots of pixels and excellent light sensitivity. CMOS sensors traditionally have lower quality, lower resolution and lower sensitivity. CMOS sensors are just now improving to the point where they reach near parity with CCD devices in some applications. CMOS cameras are usually less expensive and have greater battery life*" [31].

Feature	CCD	$CMOS$
Signal out of pixel	Electron Packet	Voltage
Signal out of chip	Voltage (Analog)	Bits (Digital)
Amplifier mismatch	N/A	Moderate
System noise	Low	Moderate
System Complexity	High	Low
Sensor complexity	Low	High
Performance		
Responsivity	Moderate	Slightly better(7.3DN(nj/cm^2))
Dynamic range	High(0.035dB to 20dB)	Moderate(54.6dB)
Speed	Moderate(20μs to 67s)	High(40μs to 60s)
Biasing and Clocking	Multiple High voltage	Single Low voltage

Table 3.1 CCD and $CMOS$ feature and performance comparison (The value are from the camera which are used in experiments (CCD - AVT Oscar 810c; $CMOS$ - PixelLink PL-621)).

$CMOS$ imagers offer superior integration, power dissipation and system size at the expense of image quality (particularly in low light) and flexibility. They are the technology of choice for high-volume, space-constrained applications. CCD offer superior image quality and flexibility at the expense of system size. They remain the most suitable technology for high-end imaging applications, such as digital photography, broadcast television, high-performance industrial imaging, and most scientific and medical applications[29]. Table 3.1 lists the comparison features and performance of *CCD* and *CMOS* cameras, which the models we used in out experiments.

3.2 Monochromatic Light Source

An incoherent monochromatic LED light source has been chosen for the system as it was found to provide excellent results. This design was based and compared with a previous laser based set up. The LED system was lower in cost and did not suffer from dust particle generated diffraction noise. The details are described as below.

The laser is an important source for interferometry, as it is a bright source of

coherent radiation. Lasers are not necessarily monochromatic, because they may have more than one longitudinal mode. It is important to understand the unique temporal coherence properties of a laser in order to obtained high contrast fringes.

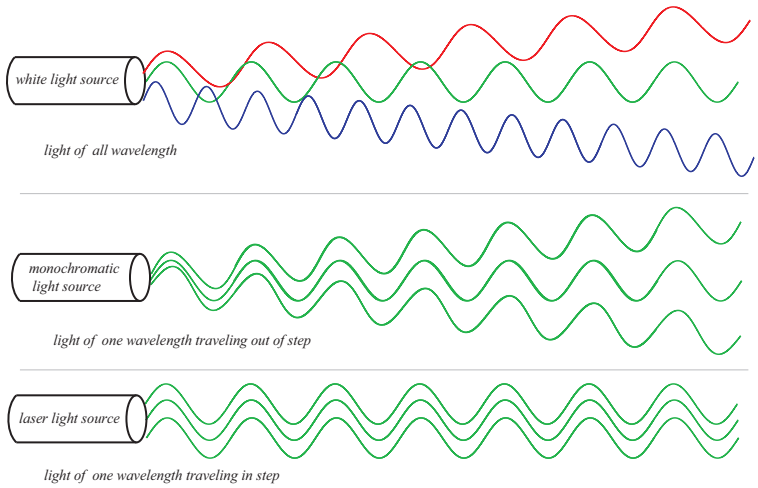

Figure 3.1 Different Light Sources Comparison.

Fig. 3.1 shows the comparison of different light sources of wavelength traveling. The white light source which shows on the top in the Fig. 3.1 presents fluorescent light source in our experiments. Monochromatic light source in the middle of Fig. 3.1 means the *LED* light source in experiment. The bottom light source shows the laser light source.

3.2.1 Coherent Light Source

Perfectly coherent light propagates according to conventional diffraction theory. Perfectly coherent light does not lose coherence as it propagates through any medium which is time-independent. For perfectly coherent light propagating in time-independent media, coherence theory is not needed.

In comparison with other types of lasers, the laser diode has a number of advantages: small size, high efficiency, integrability with electronic components, and ease of pumping and modulation by electric current injection. However, the spectral linewidth of LDs (laser diode) is typically larger than that of other lasers. If the thickness of the active region (the junction) could be reduced, the optical gain would be the same with a far lower current density. This is a problem, however,

because the carriers tend to diffuse out of the region. The solution to this problem is to use a heterostructure device which confines the light within the active medium that acts as an optical waveguide. By comparing LEDs and LDs, we note that LDs produce light even below threshold. When operated below threshold, the LD acts as an edge-emitting LED. In fact, most LEDs are simply edge-emitting double-heterostructure devices. LDs with sufficiently strong injection, so that stimulated emission is much greater than spontaneous emission, but with little feedback so that the lasing threshold is high, are called super-luminescent LEDs.

If the light source has a single spectral line, we say that it is monochromatic. Then it is formed by an infinite sinusoidal wave, or equivalently, it has a long coherence length. On the other hand, a light source with several spectral lines or a continuous spectrum is non-monochromatic. Then its wave or coherence length is short. A light source with a short wave is said to be temporally incoherent and a monochromatic light source is temporally coherent.

3.2.2 Incoherent Light Source

Most light sources are temporally and spatially incoherent, from candle light to the Sun: they all radiate light by spontaneous emission. Light-Emitting Diodes (LED) are both monochromatic and incoherent, making them suitablelight source for the common path nature of birefringence measurement under investigation.

Fluorescent lamps and Light-Emitting Diodes (LED) are mainly used in experiments. Fluorescent lamps are a general kind of lamp that produce a strong mercury line at 253.7 nm from low-pressure mercury gas[32]. This excites a fluorescent material to emit a continuum of visible radiation.

Light-Emitting Diode

Throughout the last decade, LED technology has been developed rapidly not only with regards to illumination but also in other different applications. $LEDs$ have shown energy savings of more than 80% compared with their incandescent

rivals[33]. LEDs are much more efficient in producing monochromatic light. Therefore, we choose this pure colour light source with low cost. However, since LEDs produce much less light per light source compared with additional light sources, several LEDs are assembled into arrays to meet the light level requirements of applications (see Fig. 3.2). The discrete nature of $LEDs$ could potentially create uneven light distributions.

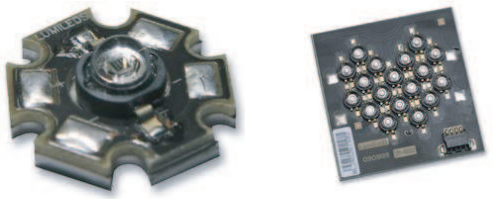

Figure 3.2 $Luxeon$ 18 LED Flood LED - Green Batwing, 540 lm @ 1050mA.

A uniform luminance distribution is important in our applications, and the LED is becoming a viable alternative with luminance uniformity, an important criterion is back-lighted monochromatic signage[34].

In the experiment, a compressive stress frozen circular disk which is epoxy resin of diameter 50 mm and thickness 5 mm is used. Fig.3.3(a), (b) and (c) show the dark field isochromatic fringes at illumination wavelengths of 420, 530 and 632 nm, respectively, mapped over grids of identical size in one quadrant. It can be see that the fringe orders at similar locations on the disk are altered when different wavelengths illumination are implemented.

Table.3.2 gives the distances of the respective nth order fringe from the point P along $X - X$ using the different wavelengths. With the exception of the $0th$ order fringe, all the other higher fringe orders are relatively closer to P when the illumination wavelength is shorter. This is in accordance with the higher sensitivity at lower wavelength behavior outlined in photoelastic stress-optic relationships [35].

In photoelasticity, we used a source with lower spectral bandwidth results in higher accuracy measurements. Nevertheless, bandwidth limits within 100 $nanometer(nm)$ are generally considered sufficient to provide accurate measurements in computer-

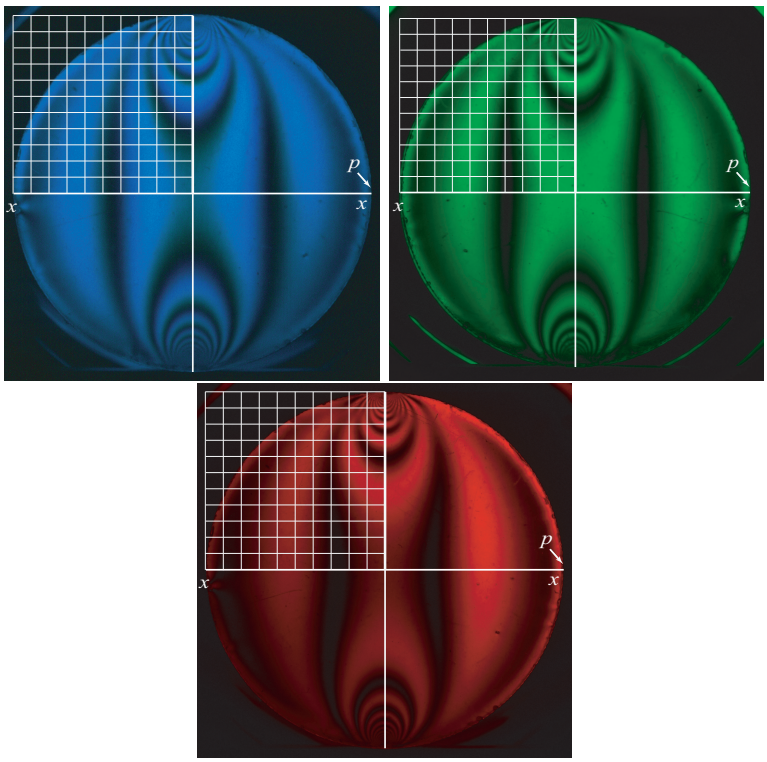

Figure 3.3 Circular polarising photoelectric dark-field fringe pattern of compressive stress frozen epoxy resin disk (a)420 nm wavelength LED illumination (b) 530 nm wavelength LED illumination (c) 632 nm wavelength LED illumination.

aid photoelasticity. The bandwidth of LED emitters which are used in experiments fall within the limit.

LED emitters also provide very fast flash response, on average about 40ns, which make them ideal for use in impact and transient loading studies.

Another outstanding feature of LEDs is their ability to emit light at more than one discrete wavelength. The ability to illuminate with more than one wavelength enhances the versatility of photoelasticity. This is because some birefringent ma-

Fringe Order	Distance from P using 420 nm wavelength light (mm)	Distance from P using 530 nm wavelength light (mm)	Distance from P using 632 nm wavelength light (mm)
0	0	0	0
1	12.50	13.13	14.38

Table 3.2 Distance from P along $X - X$ of the fringe patterns in Fig.3.3 obtained using 420,530 and 632 nm wavelength LED illumination.

terials such as animal and human corneas absorb radiation strongly at a particular bandwidth. Alternatively, with LED devices it is possible to select a type that operates in a bandwidth that yields maximal transmittance. Moreover, it is also now available with a few emitters built-in to produce two or three wavelength outputs selectable by simple electrical switching.

3.2.3 Phase Measurement by using LED Monochromatic Illumination

Monochromatic Components of White Light Fringe Pattern

A photoelastic fringe pattern obtained from a fluorescent lamp is given in Fig.3.4.

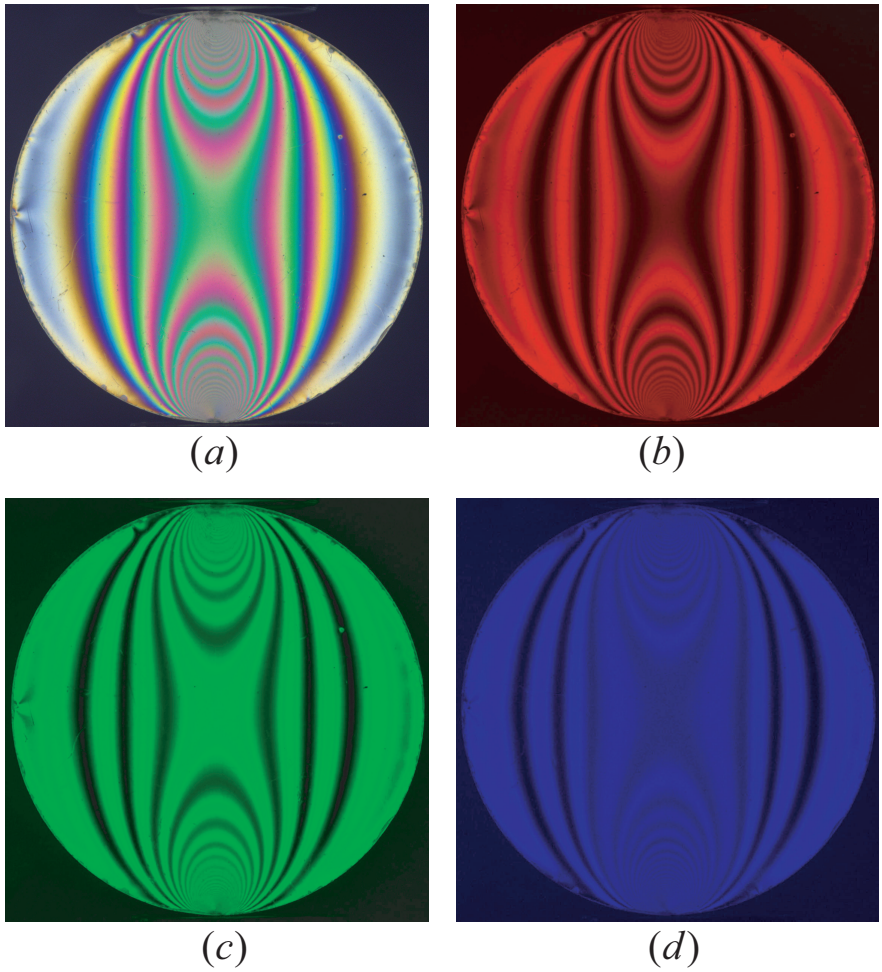

Figure 3.4 Photoelastic fringe patterns obtained under (a) raw image data model, and by three color channels to the (b) red, and (c) green, and (d) blue.

The fringe pattern can be separated into its monochromatic components to enable phase-shifting. The color image is separated into red, green and blue channels.

The respective fringe patterns are shown in Fig.3.4$(b), (c)$ and (d). From these patterns, the red and green channels have higher contrast than the blue channel. The poor contrast of blue fringes pattern maybe due to two reasons. One possibility is the low quantum efficiency of signals handled in the blue channel of the CCD sensor, which is shown in Fig.3.5. It is well known that the overall signal to noise ratio of any color channel in a CCD reduces with intensity.

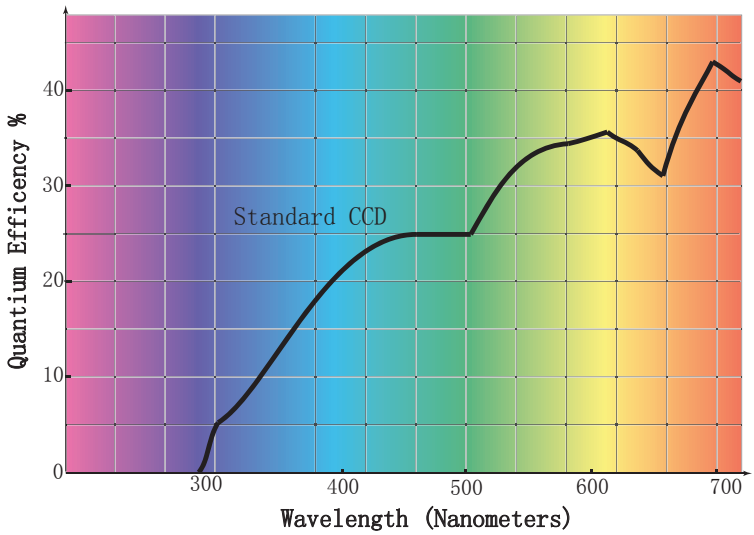

Figure 3.5 Quantum efficiency of a typical CCD sensor in the visible spectrum.

Another possible reason maybe due to the light source itself. As we can see from Fig.3.6, the photon irradiance across the visible spectrum contains certain peaks. Both green and red region experience only one strong peak that is relatively bandwidth limited. This contrasts with the blue region, which experiences two equally strong peaks instead of one. That overall photon irradiance in the blue spectrum is low also exacerbates the quantum efficiency in the blue region.

Processing a series of fringe patterns of the same stress frozen specimen provided the wrapped whole-field phase maps of sample. They are depicted in Fig.3.7 (a) to (d) for the raw, red, green and blue components, respectively.

Fig.3.8 (a) to (d) give plots of the wrapped and unwrapped phase distributions of a horizontal section marked $A - A$ in Fig.3.7 using the red, green, and blue components, respectively. In all cases, it could be seen that the phase distributions were regular with the exception of a small high frequency region for the blue image.

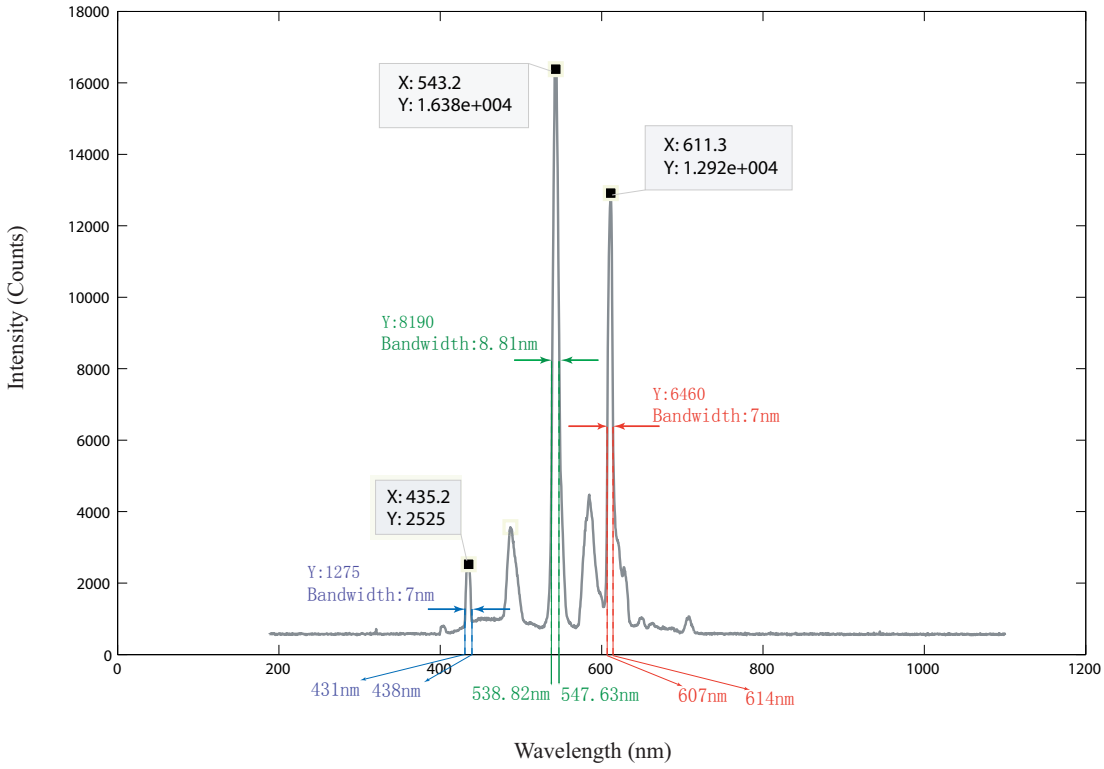

Figure 3.6 Fluorescence spectrum measured by spectrum meter.

Fig.3.8 (d) to (f) give plots of the wrapped phase distributions of a horizontal section marked $B - B$ in Fig.3.7. In this case, we can infer that the phase distributions were again regular for the red and green phase maps. However, the high frequency region was more extensive in the case of the blue component. The low contrast region where present at the top and bottom of the specimen in Fig.3.4 corresponded with areas of high fringe density.

From this result, it can be inferred that any phase-shift operation applied to the blue fringe patterns will result in erroneous phase maps, in particular in the regions where the fringe density is high. It appears that accurate phase shift can only be achieved using the red and green components extracted from the fringe pattern acquired using a white-light source. Despite this limitation, it should be noted that unwrapped phase maps are derivable using one wavelength phase map alone. Unwrapping with multiple wavelength phase maps is important only in cases where discontinuities that extend to more than one wavelength are present.

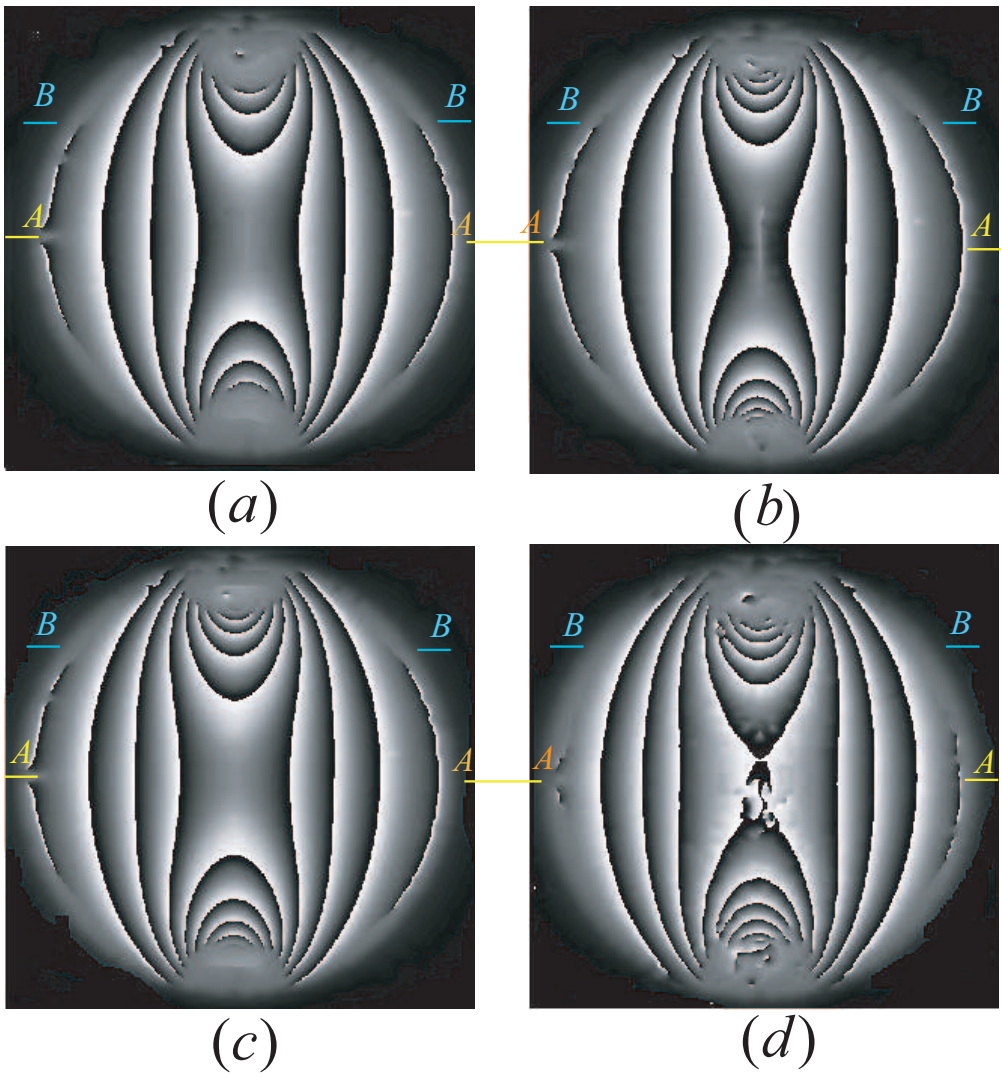

Figure 3.7 Wrapped whole filed isochromatic phase maps obtained using the (a) raw, (b) red, (c) green and (d) blue channels.

It is found that a phase-shift operation can produce whole-field phase maps from the red, green and blue components extracted from the fringe image achieved from the white light. The phase map of this component is noisy at regions of high fringe density because the spectral characteristics of the light source and the relatively poor quantum efficiency in the blue channel of the camera sensor.

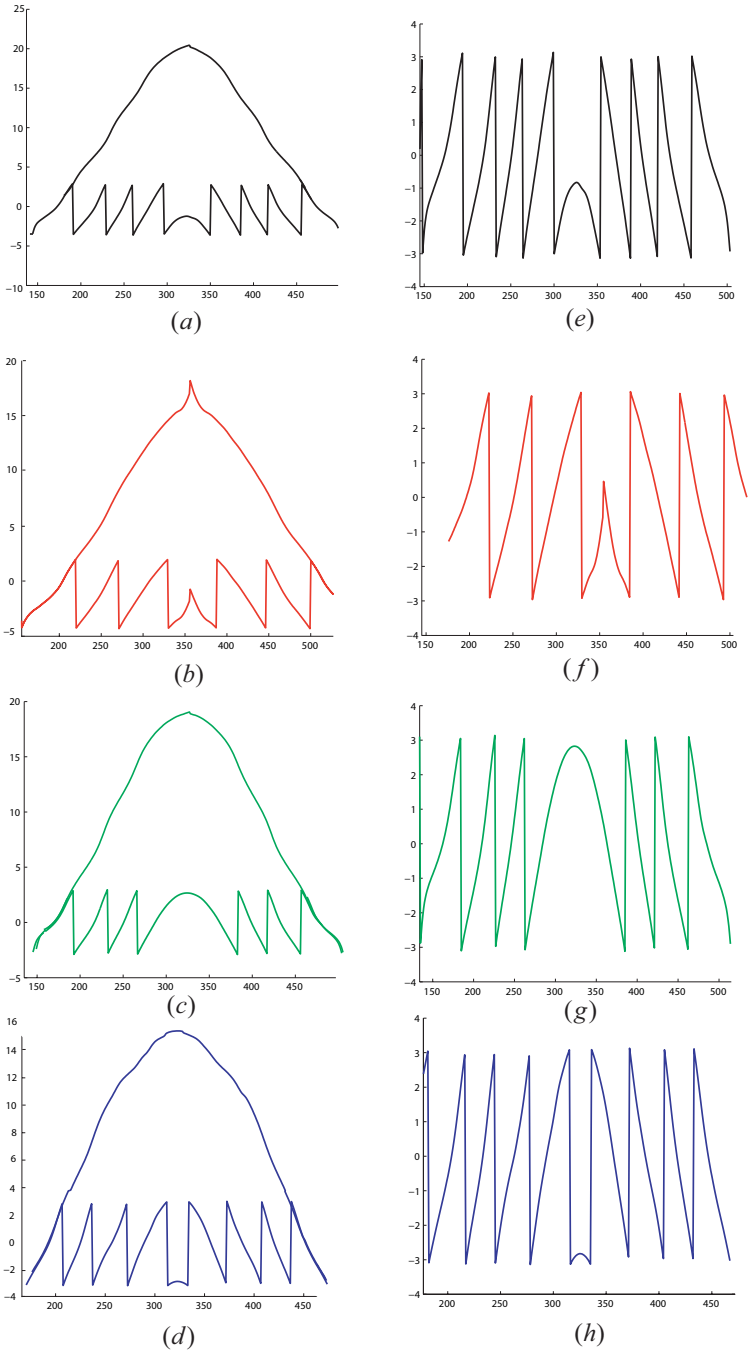

Figure 3.8 Central cross line of wrapped whole filed isochromatic phase maps using the (a) raw, (b) red, (c) green and (d) blue channels.

The phase maps of a quartz wedge, which are solved by phase stepping method are also compared here. All the conditions are same, except for the different kind of light source. The light source are Monochromatic LED light and white light respectively. The results are shown in Fig.3.9 and Fig.3.10,

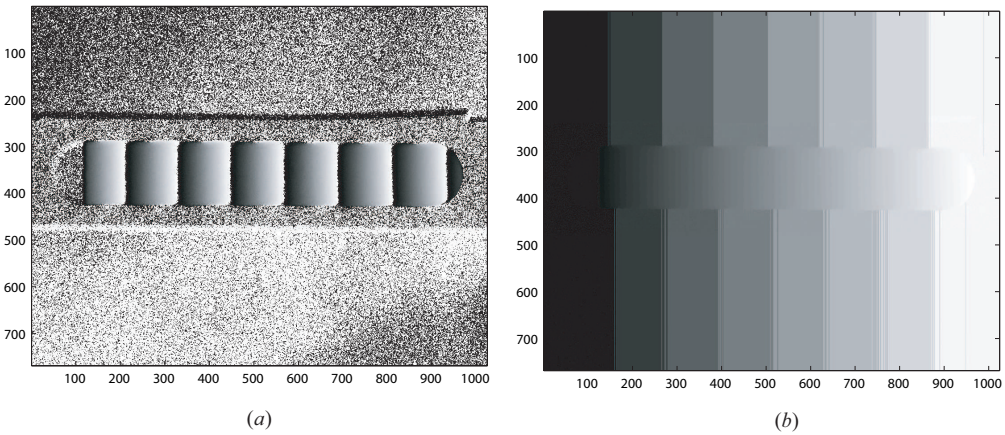

Figure 3.9 Phase map of quartz wedge - Monochromatic Light Source (a)wrapped phase map , (b)unwrapped phase map.

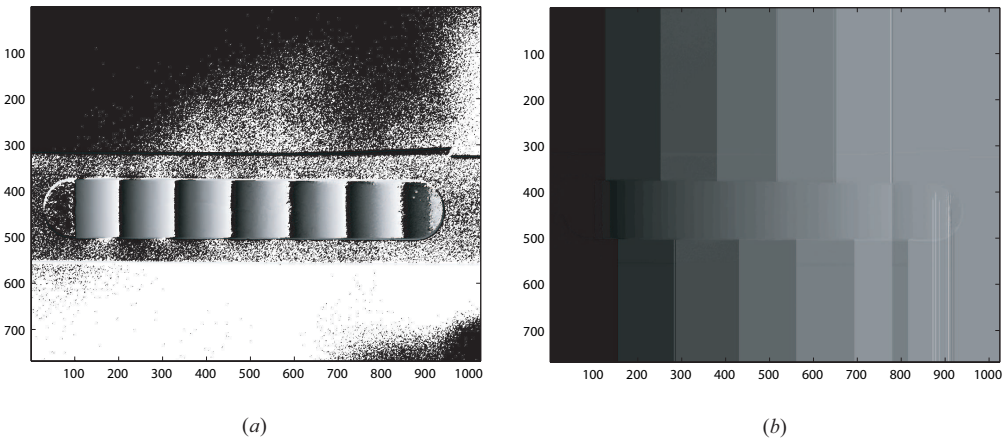

Figure 3.10 Phase map of quartz wedge - White Light Source (a)wrapped phase map , (b)unwrapped phase map.

The Fig.3.9 and Fig.3.10 show a wrapped and unwrapped phase map created by a monochromatic and white light source respectively. The white light sources spectral width resulting in a loss of fringe contrast as the thickness and path-length of the test wedge increases. Whereas, the image made using the monochromatic source does not. As a result an incoherent monochromatic source was considered suitable for the measurement of the cornea. The difference in the resulting fringe contrast is further illustrated in Fig.3.11.

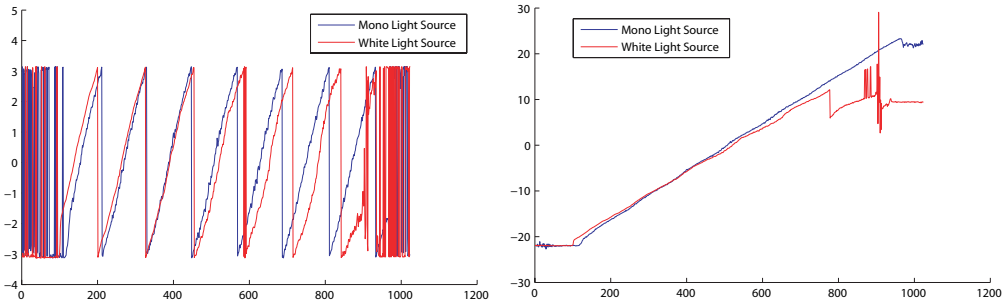

(a) (b)

Figure 3.11 Raster line of phase map of quartz wedge (a)wrapped phase map , (b)unwrapped phase map.

Fig.3.11 shows the comparison of phase between the two light source. The monochromatic light which is shown as blue line result shows better performance than white light source results.

3.3 The Design of a Miniature Polariscope

3.3.1 Structure and Mathematical Modeling of the Miniature Polariscope

Although computerized finite element programs are now able to provide numerical solutions for a wide variety of designs under different loading conditions, experimental methods are crucial in the stages prior to production to confirm the validity of the computational models used.

Photoelasticity is a popular method for experimental stress analysis. Using a direct loading method, the anticipated loads are applied to the sample, the technique is less cumbersome than the stress-freezing method and allows the effect of different loads to be the observed with one specimen.

Photoelasticity can be broadly classified as phase-shifting, carrier-fringe schemes and step-loading. In order for the fringe pattern to be clearly resolved, and for automatic determination of the whole field, an electronic imaging device has to be incorporated into the setup. The most commonly used device is a CCD camera, which processes good imaging characteristics.

The structure of the miniature polariscope is shown in Fig.3.12. The set up in Fig.3.12 presents the laboratory installation on a optical table, which is limited by the instruments we have. For the idea of a portable device, all optical components and light source could be designed and integrated for a minimum size.

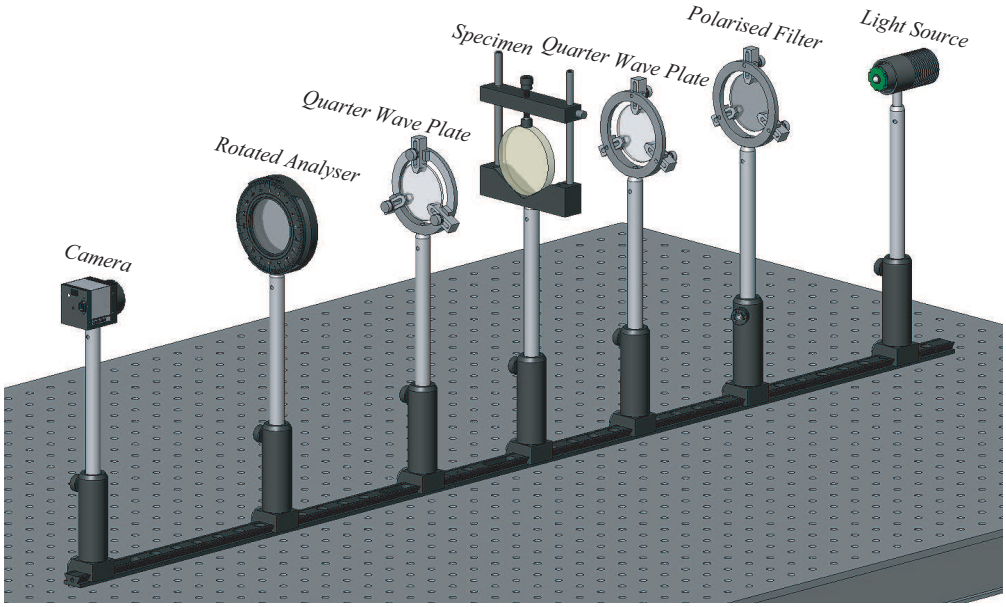

Figure 3.12 Polariscope System.

A stressed model made of temporary birefringent material is inserted into the polariscope. Fringe patterns related to the principal stress difference and the principal stress direction in the specimen are captured by the digital camera and processed and displayed by a computer. The effects of the stressed model in the digital polariscope are revisited using Jones Calculus.

3.3.2 Full Field Automated Fringe Analysis by Phase Stepping Method

A simple polarised phase shifting method for analysing fringe patterns based on the polariscope system is proposed. The system employs a circular polarised beam at the input and a rotating analyser at the output of the system. The simplicity of our approach is proved theoretically and experimentally, also the classical specimens measurement will provide the reference for the applications in the final chapters of this thesis. The basic idea of this method is to exploit the relationship between phase retardation caused by loads applied on the specimen to find directly the

total fringe order at each point. In order obtain results, phase unwrapping is one of the crucial steps in the processing of determine the total fringe orders. The phase unwrapping process is usually performed line by line with prior knowledge of the total fringe order for at least one point after eliminating isoclinic ambiguity. In this research, the processing can automatically perform the phase unwrapping process directly based on the results of phase shifting independent of the status of ambiguity, and no prior knowledge is needed of the total fringe order for at least one point. Experiments on a round disk, ring and "U" shape specimens under compression are provided as demonstrations.

Introduction and Review

Full field birefringent parameters measurement by phase shifting methods have been proposed. This digital image processing techniques have been studied in recent years [36] [37] [38]. However, the birefringent parameters are obtained by solving inverse trigonometric functions with the isoclinic angle being calculated in the range $-\pi/4 < \theta < \pi/4$ and the isochromatic fringe order in the range $0 < \delta < \pi$ or $0 < \delta < 2\pi$ depending on whether a two or four quadrant cotangent function is used with these techniques.

The previous work of phase unwrapping is normally tedious and time-consuming, especially for an irregular fringe, which process line by line with a known value of total fringe order for at least one point. We have implemented automatic phase unwrapping in a simple and straightforward manner. Apart from some novel developments in this area, the capabilities of dynamic measurement and analysis are also possible.

Before the advent of digital processing, the most common method for measuring fractional fringe orders was the $Tardy$ method. It can be used with a normal polariscope, and required no additional equipment. The disadvantage is that it is a point-wise method and thus time-consuming for whole area analysis. To use this method, the axis of the polariser is aligned with the principled direction of the maximum principal stress. All other elements of the polariscope are rotated relative

to the polariser so that a standard dark-field polariscope exists. Substituting $\theta = 0$ into equation 3.1,

$$J_M = \begin{bmatrix} \cos\frac{\delta}{2} - i\cos 2\theta \sin\frac{\delta}{2} & -i\sin 2\theta \sin\frac{\delta}{2} \\ -i\sin 2\theta \sin\frac{\delta}{2} & \cos\frac{\delta}{2} + i\cos 2\theta \sin\frac{\delta}{2} \end{bmatrix} \tag{3.1}$$

and with the analyser is rotated by an amount β to create extinction at the point of interest, the $Jones$ vector is,

$$J_M = \begin{bmatrix} \cos\frac{\delta}{2} + i\sin\frac{\delta}{2} & 0 \\ 0 & \cos\frac{\delta}{2} - i\sin\frac{\delta}{2} \end{bmatrix} \tag{3.2}$$

and

$$\begin{aligned} \begin{Bmatrix} U \\ V \end{Bmatrix} &= \tfrac{1}{2} \begin{bmatrix} 0 & 0 \\ \cos\beta & \sin\beta \end{bmatrix} \begin{bmatrix} 1 & -i \\ -i & 1 \end{bmatrix} \times \\ &\quad \begin{bmatrix} \cos\frac{\delta}{2} - i\sin\frac{\delta}{2} & 0 \\ 0 & \cos\frac{\delta}{2} + i\sin\frac{\delta}{2} \end{bmatrix} \begin{bmatrix} 1 & i \\ i & 1 \end{bmatrix} \begin{bmatrix} 0 \\ 1 \end{bmatrix} ae^{i\omega t} \\ &= \tfrac{1}{2}\left[2\cos\beta\cos\tfrac{\delta}{2} + 2\sin\beta\sin\tfrac{\delta}{2}\right] \end{aligned} \tag{3.3}$$

Giving the dark field intensity as

$$I = |U|^2 = a^2 \sin^2\left(\frac{\delta}{2} + \beta\right) \tag{3.4}$$

extinction occurs when $\delta/2 \pm \beta = n\pi$ where n=0,1,2,3,... and the fractional fringe order N at the point of interest is given by $N = \delta/2\pi = n \pm \beta/\pi$.

This method was a basis for the phase shifting method. Since the method relies on a circular polariscope, only those techniques utilizing a circular polariscope will be mentioned, with the most current technique advanced for comparison.

Based on the $Hecker$ and $Morche$ method [39], which changed the phase by rotation of the second quarter wave plate and the analyser, while the fast axis of the first quarter wave plate was set to 45^o with respect to the axis of polariser, $Patternson$ and $Wang$ used different steps of optical rotation of the second quarter wave plate and analyser for algorithm [36], which used six intensity equations

with the setting that varied as follows:

φ	ϕ	β	Intensity Equation
$3\pi/4$	0	$\pi/4$	$i_1 = i_b + \frac{i_a}{2}(1 + \cos\delta)$
$3\pi/4$	0	$3\pi/4$	$i_2 = i_b + \frac{i_a}{2}(1 - \cos\delta)$
$3\pi/4$	0	0	$i_3 = i_b + \frac{i_a}{2}(1 - \sin 2\theta \sin\delta)$
$3\pi/4$	$\pi/4$	$\pi/4$	$i_4 = i_b + \frac{i_a}{2}(1 + \cos 2\theta \sin\delta)$
$3\pi/4$	$\pi/2$	$\pi/2$	$i_5 = i_b + \frac{i_a}{2}(1 + \sin 2\theta \sin\delta)$
$3\pi/4$	$3\pi/4$	$3\pi/4$	$i_6 = i_b + \frac{i_a}{2}(1 - \cos 2\theta \sin\delta)$

Table 3.3 $Patternson$ and $Wang$'s Algorithm .

From the equations summarized in Table4.3, both the isoclinic angle and the phase retardation can be computed using

$$\begin{aligned} \theta &= \tfrac{1}{2}\tan^{-1}((I_5 - I_3)/(I_4 - I_6)) \\ \delta &= \tan^{-1}(2(I_5 - I_4)/(I_1 - I_2)(\sin 2\theta - \cos 2\theta)) \end{aligned} \tag{3.5}$$

In circular polariscope based phase shifting algorithms, although the phase retardation can be determined in a full range [0,2π] by using the four quadrant arctangent function, its interaction with the isoclinic angle still leads to ambiguity regarding its mathematical sign.

In this method, the phase change is caused by rotation of the output optical elements of the circular polariscope, which requires that the second quarter wave plate and the analyser of the polariscope can be rotated independently. The design requirement of these polariscopes is ease and precision. Thus, the quarter-wave plates were inter-linked with a 45^o maximum rotation capability. So, the device used in this application can not be implemented normally.

Phase Shifting with Birefringent Material Using Fringe Analysis Based on a Polariscope System

The phase stepping method was developed to extract the fractional fringe orders, which is the phase distribution at every pixel of fringe pattern. The four-step algorithm is most widely used, and is adapted in this study. From Table.3.4, the

isoclinic and isochromatic parameters are deduced to be

$$I_b = \frac{1}{2}(I_1 + I_3) \tag{3.6}$$

$$\theta = \frac{1}{2}\tan^{-1}\left(\frac{I_4 - I_b}{I_2 - I_b}\right) \tag{3.7}$$

$$\delta = \tan^{-1}\left(\frac{i_4 - i_2}{i_1 - i_3}\right) \tag{3.8}$$

From equation 3.7, two possible solutions are introduced. One is in the range $[-\pi/4, \pi/4]$, and the other in the range $[-\pi/2, -\pi/4]$ or $[\pi/2, \pi/4]$. When expressed in the range [$-\pi$,π], there will be two values of δ (with opposite mathematical sign of) $sin(2\theta \pm \pi/2)$, but with the same magnitude based on the two solutions above. Without additional information, the phase shifting technique is unable to identify the correct solution for the isoclinic angle. Therefore, the relationships between the actual values of θ, δ and their calculated values can be deduced as follows [40],

$$\theta = \theta_c, \quad -\pi/4 < \theta_c < \pi/4 \tag{3.9}$$

$$\delta = \delta_c, \quad -\pi < \delta_c < \pi \tag{3.10}$$

To solve this problem, the phase shifting combined with load stepping methods could be attempted, but it leads to two major drawbacks. Firstly, it is difficult to achieve three equally-stepped loads. Secondly, in low-stressed regions, the difference in phase retardation between load steps is very small. Hence, results are unreliable and noisy in these regions.

Experiment and Results

The system used in our experiment consists of a CCD camera, and a standard polariscope with a monochromatic LED light source. The plates of the polariscope and rotate each optical element independently.

The photoelastic optical configuration is used for our analysis by the phase shifting method in this experiment, which is shown in Fig.3.13. A monochromatic light passes through a polariser $P_{\pi/4}$ whose polarised axis subtends a right-angle($\pi/2$) with a reference axis x. Then the linear polarised light beam passes through the first quarter wave plate $Q_{\pi/4}$ a birefringent specimen $BS_{\delta,\theta}$, a second quarter-wave plate Q_{γ} and the analyser A_{β} on the optical path.

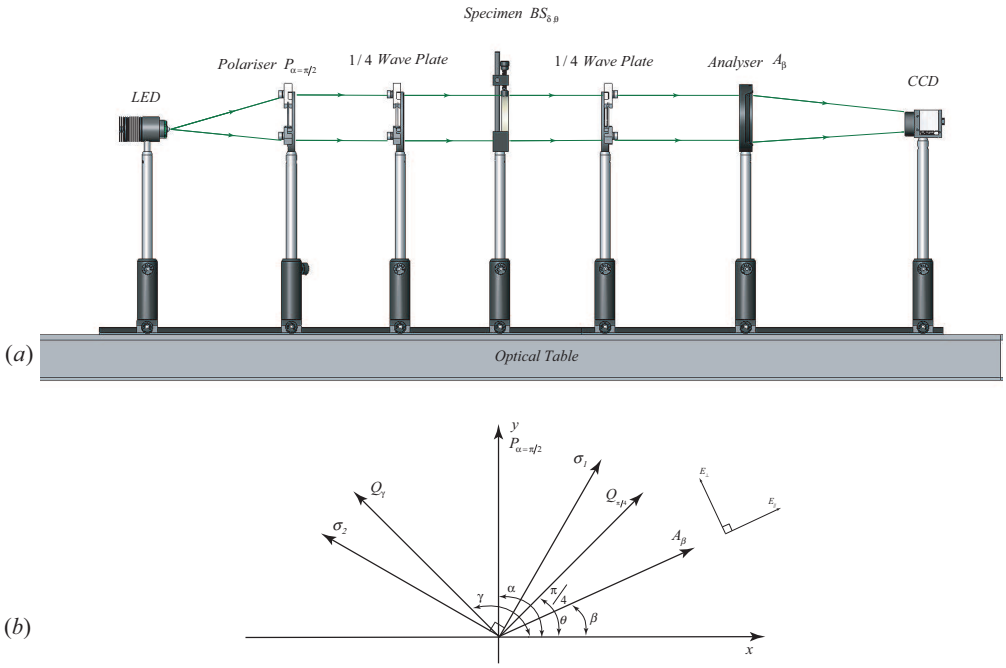

Figure 3.13 (a)Optical set up for phase-stepping photoelasticity and (b) sketch map of light vectors through optical path.

The principle is that when rotating the polariser, the intensity of the passing light will changed periodically, from maximum to vanishing and then back again. So by the intensity changing, we can determine the light axes of the polarisers which are related to the maximum intensity. The angle difference between the light axes of the polarisers and the axis of the assigned polariser is the actual phase shifting step of the recorded fringe pattern by the CCD camera. The test procedure uses the experimental system shown in Fig.3.14.

To demonstrate the method, a round disk specimen under vertical compression has been studied. The light source is monochromatic LED at $530nm$. Following

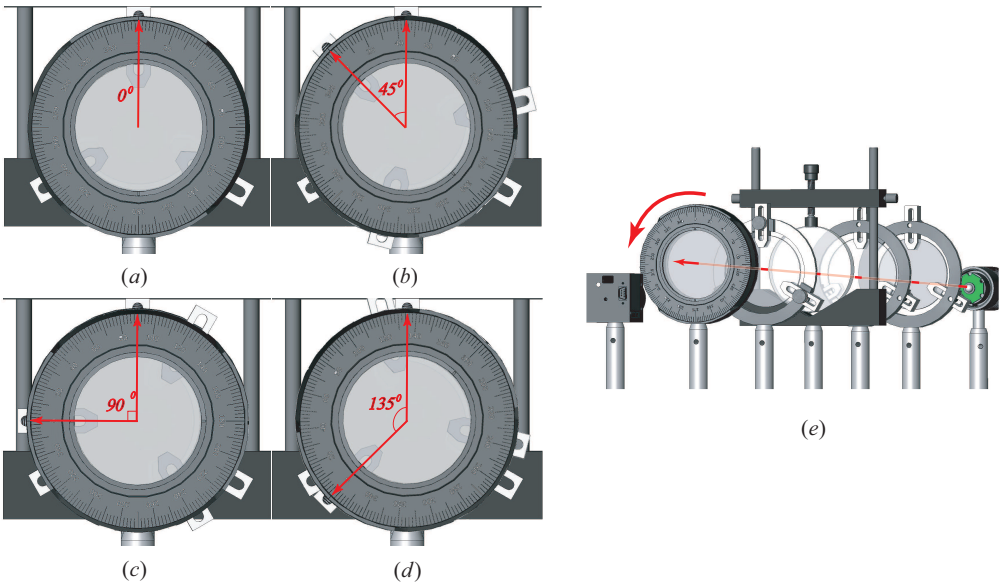

Figure 3.14 (a),(b),(c) and (d) are shown the angles configuration of the analyser rotation, (e) shows the analyser rotation in polariscope system.

Table3.4, four images are captured at each angle as shown in Fig.3.15.

Number	Analyser angle β	Intensity equation	Fringe patterns interpretation
1	0	$i_1 = i_b + i_a \sin^2 \frac{\delta}{2}$	Circular polariscope dark field
2	$\pi/4$	$i_2 = i_b + \frac{i_a}{2}(1 + \sin \delta)$	None
3	$\pi/2$	$i_3 = i_b + i_a \cos^2 \frac{\delta}{2}$	Circular polariscope bright field
4	$3\pi/4$	$i_4 = i_b + \frac{i_a}{2}(1 - \sin \delta)$	None

Table 3.4 Summary of intensity equations used in $Asundi's$ algorithm.

The wrapped phase map using the phase stepping method are shown in Fig.3.16. The unwrapped phase map are shown in Fig.3.17. The contour map of unwrapped map are shown in Fig.3.18. The unwrapped phase map of isochromatic is shown in Fig.3.19.

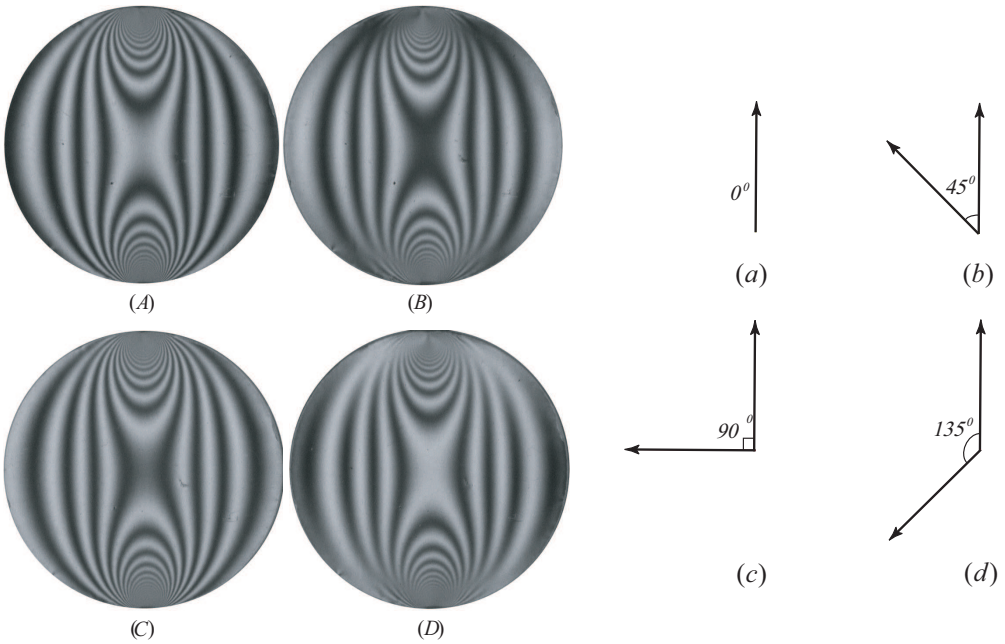

Figure 3.15 (A),(B),(C) and (D) show the intensity distribution on the round disk specimen under compression at each analyser angle position; (a),(b),(c) and (d) show the angles configuration of the analyser rotation.

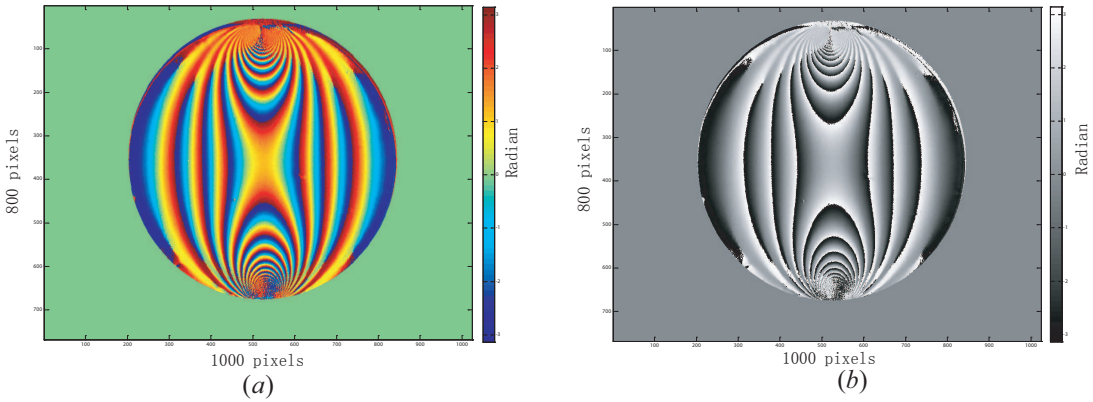

Figure 3.16 (a) and (b) show the color and monochromatic wrapped phase map of circular disk under diametral load (image size 1000×800 pixels).

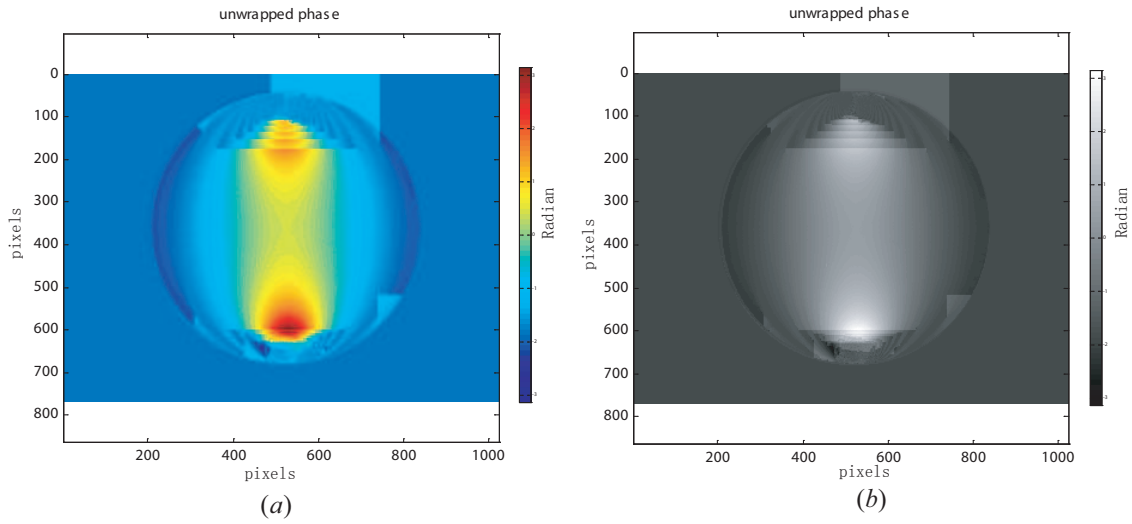

(a) (b)

Figure 3.17 (a) and (b) show the color and monochromatic unwrapped phase map of circular disk under diametral load (image size 1000×800 pixels).

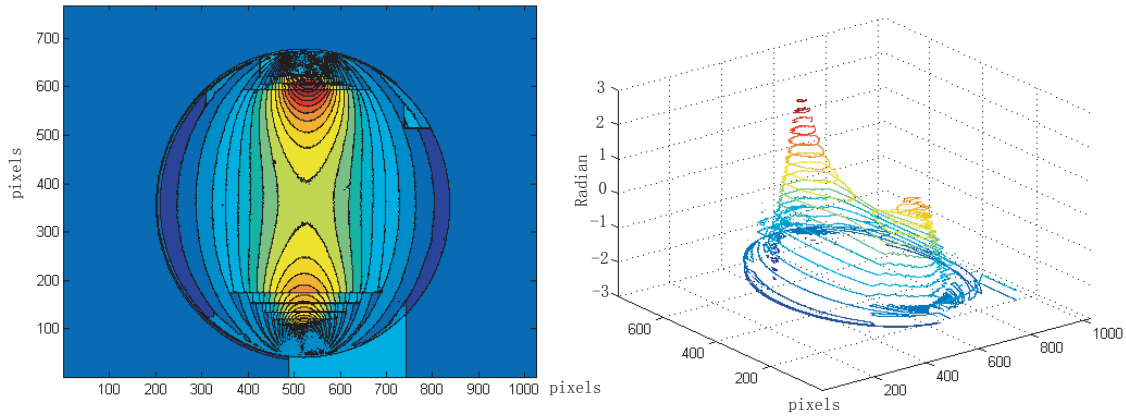

(a) (b)

Figure 3.18 (a) 2D contour map from unwrapped map (b) 3D contour map from unwrapped map of the round disk.

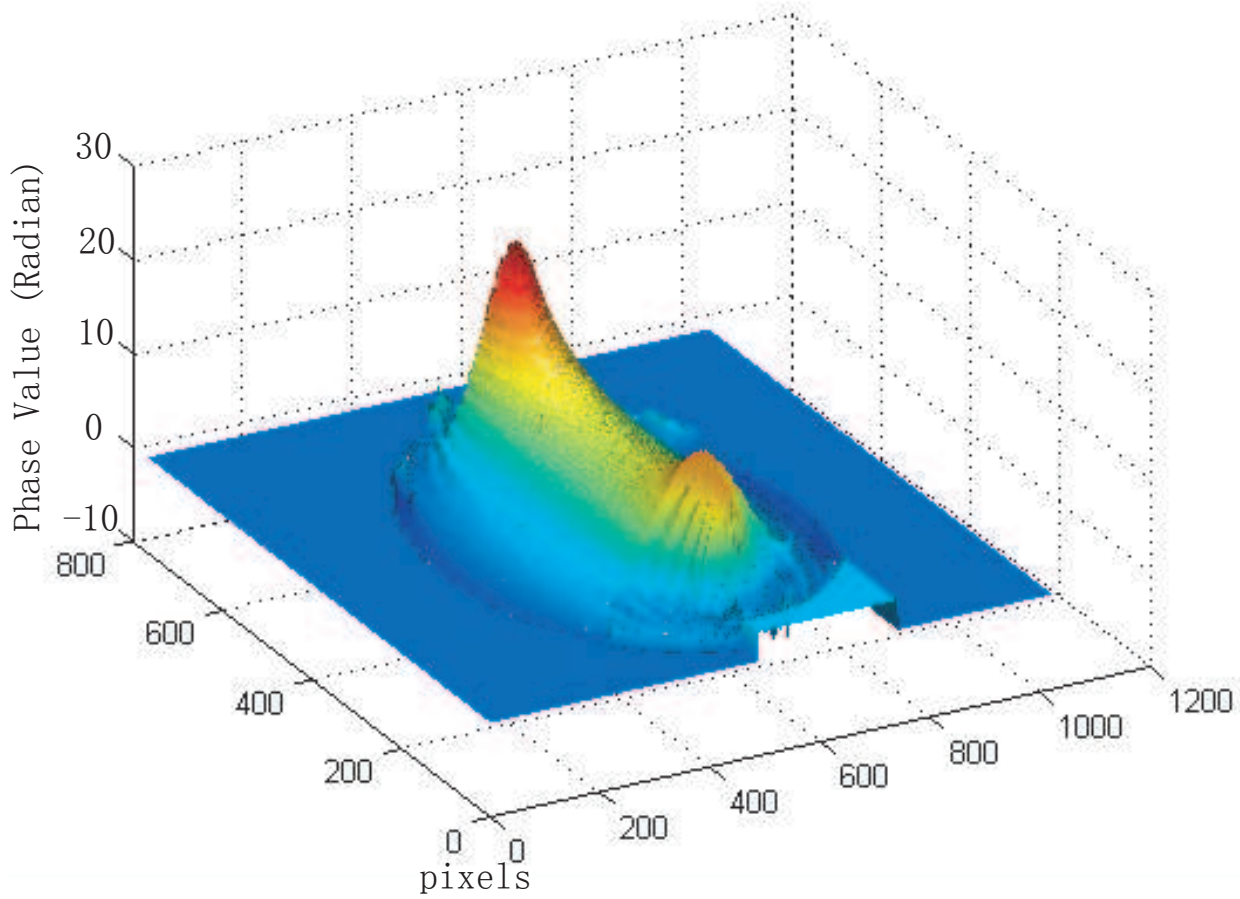

Figure 3.19 The three dimensional expression of unwrapped phase map of the round disk.

Error Analysis for Phase-Stepping Method

The phase changes depend on the rotations of the plate of the polariscope. As shown in the results, the intensity distributions become comparable to a simple phase function distribution and the errors of the phase stepping method decrease. The errors have been qualitatively analysed here.

The error in the fringe order is demonstrated for the polariscope system; the unwrapped phase map is shown in Fig. 3.20. The fringe orders are determined along the horizontal line, which is at the *y*-axis pixel 384.

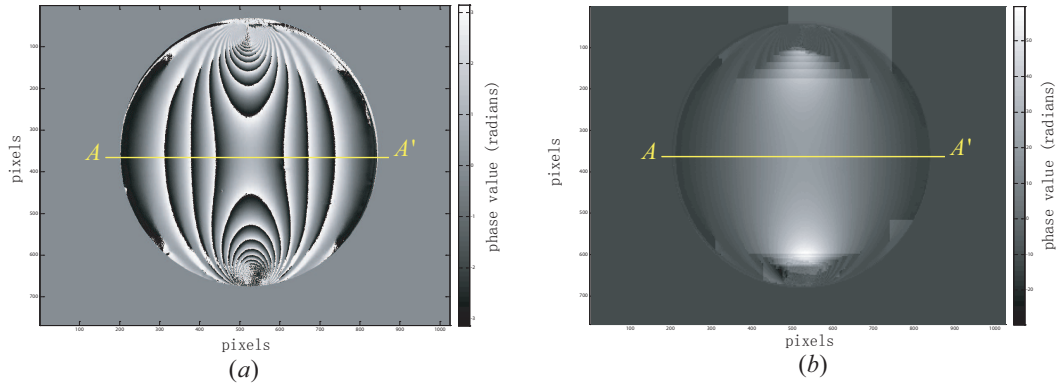

Figure 3.20 A middle crossline AA' on the wrapped and unwrapped phase map of the round disk.

Results are plotted in Fig.3.21. and Fig. 3.22. The periodically changing errors in the fringe order are evident.

Compare these results with the plot (a) and (b) in Fig. 3.21 and Fig.3.22. The phase stepping algorithms increases accuracy more than each single step for both the wrapped and unwrapped phase map, which are shown in Fig.3.23.

The accuracy in evaluating fringe order is substantially reduced when data is collected near the high density fringe concentration areas. The problem might be caused by the fact that the intensity data may not have been recorded accurately due to inherent difficulties associated with digitization in such areas of high fringe intensity. The choice of the hardware, particularly the camera and optical components used, has an influence on the accuracy of the results obtained. The quantitative analysis and calibration will be discussed in detail in chapter4.

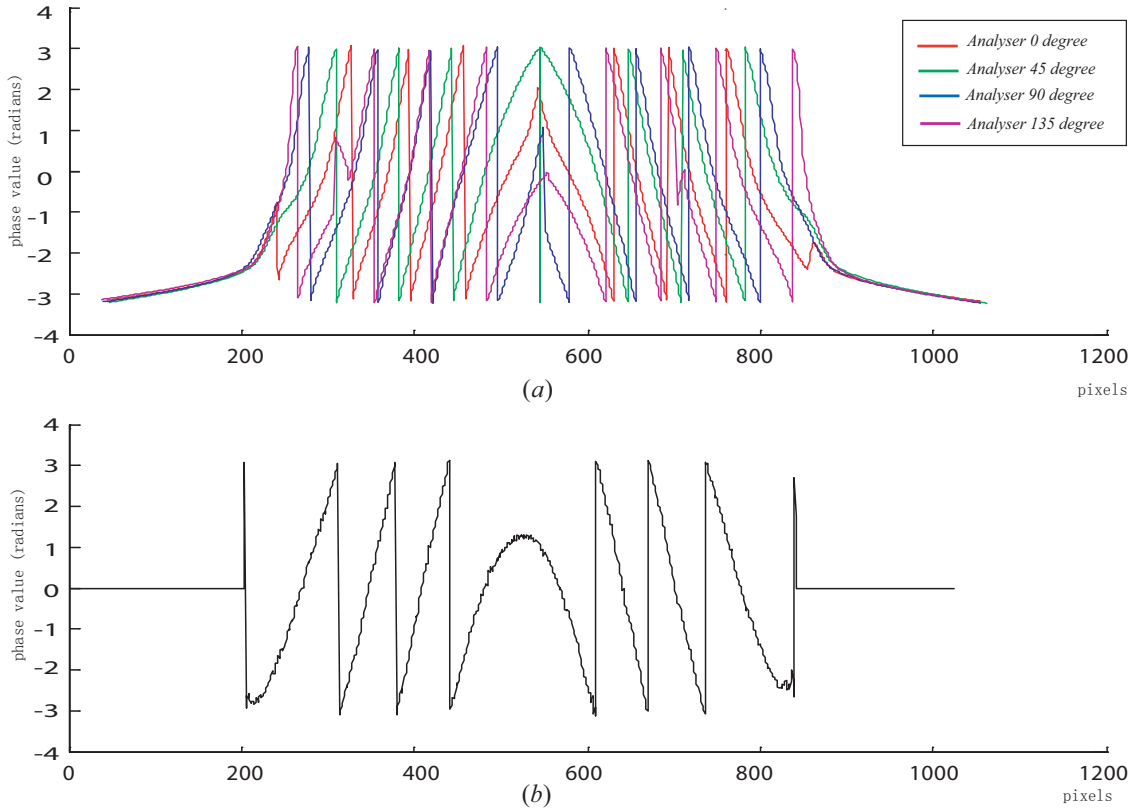

Figure 3.21 A corresponding plot along line AA' on the wrapped phase map of the round disk, (a) shows the four degrees condition (b) shows phase stepping wrapped map result.

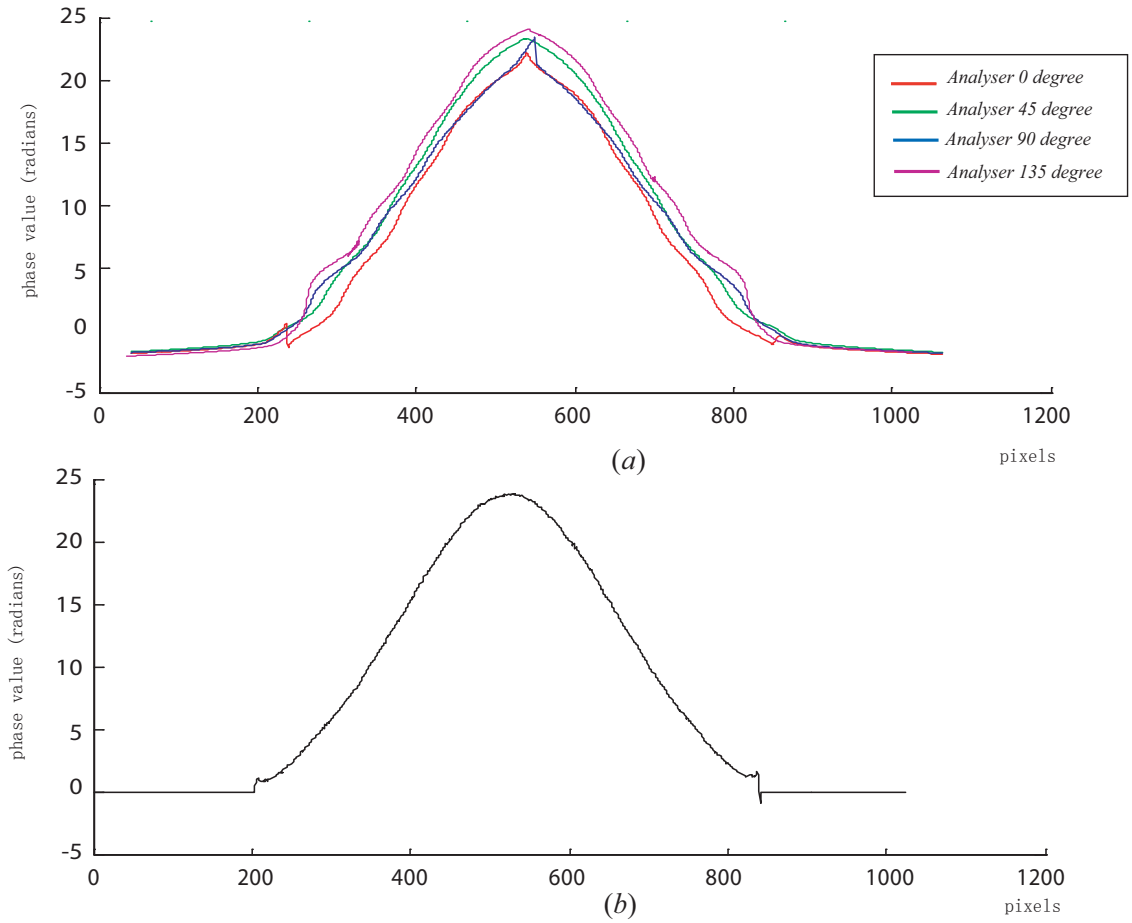

Figure 3.22 A corresponding plot along line AA' on the unwrapped phase map of the round disk, (a) shows the four degrees condition (b) shows phase stepping wrapped map result.

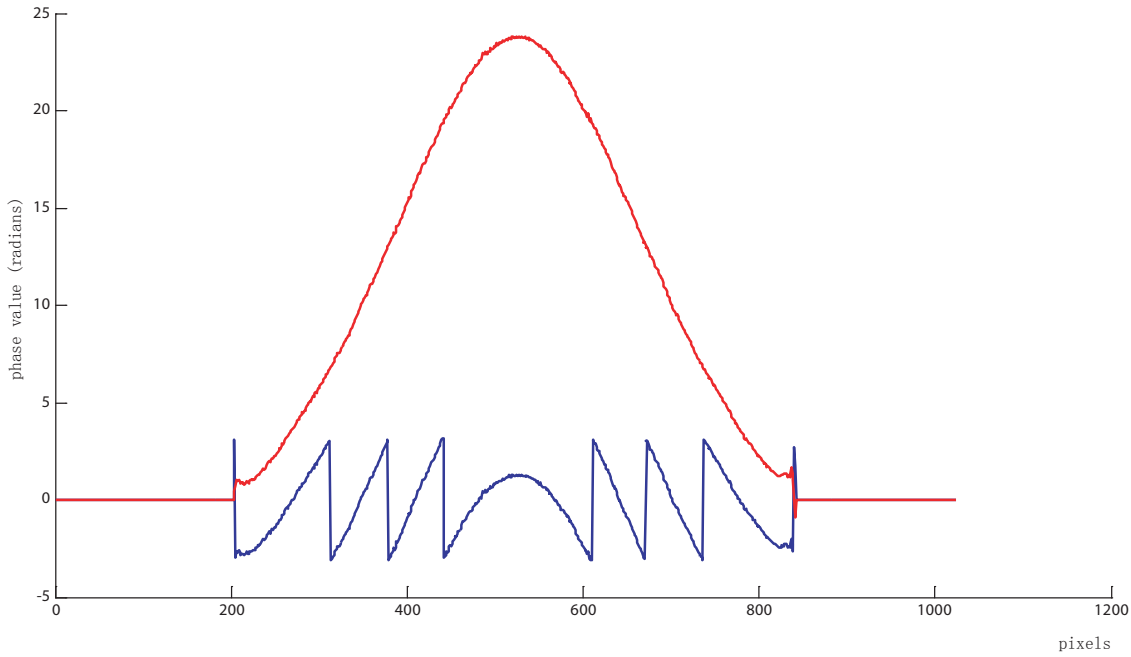

Figure 3.23 A corresponding plot along line AA' the wrapped and unwrapped on phase map of the round disk.

3.3.3 Develop Quantitative reflection Polariscope Technology in vivo Approaches

The application of the phase shifting measurement was made using a transmission system, but the clinical application needs a reflection system. So, in this research, a novel instrument is designed and developed for this purpose. A reflection system is designed as shown in Fig.3.24. The LED light source, polarized filter and first quarter-wave plate are placed on the same side of the camera. The most suitable angle for the two rails which carry the two groups of the polarized filter, and quarter-wave in the experiment was found to be 30 degree.

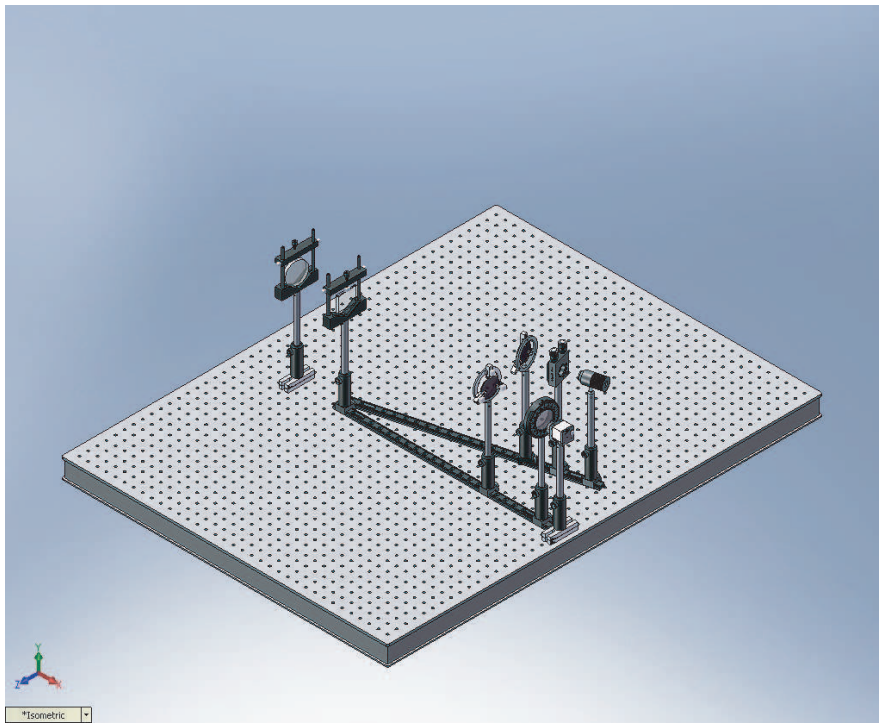

Figure 3.24 Reflection system diagram.

The image data, an example of which is shown in Fig.3.25 may be solved by the Fourier transform method.

The design of the reflection system has been improved structure which is illustrated in Fig.3.26.

The results analysis and discussion will be shown in Chapter6. The possibility has been proved by laser, because the good direction and coherent characteristic

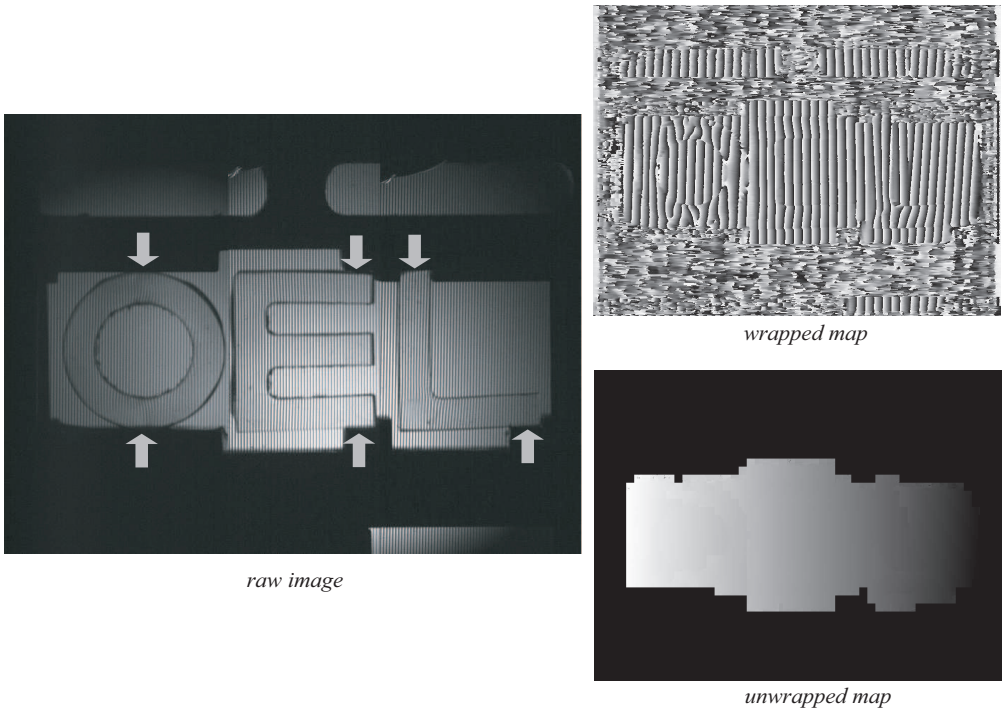

Figure 3.25 Birefringence material sample in the reflection system.

of laser, the fringe can be created by the wedge and projected on the screen. In application, the screen position will be replaced by cornea. Therefore, if the projected image could be obtained from the projector system by using laser, then, it could be considered to use LED as a replacement.

The implementation of laser for the system is designed and shown in Fig.3.26. In Fig.3.27 (a), it is the testing set up in experiment. The projected fringe is shown in Fig.3.27 (b). The bottom of the Fig is the design diagram plotted by software. The successful result shows that this design has the potential to be taken further in the design which is shown in Fig.3.26.

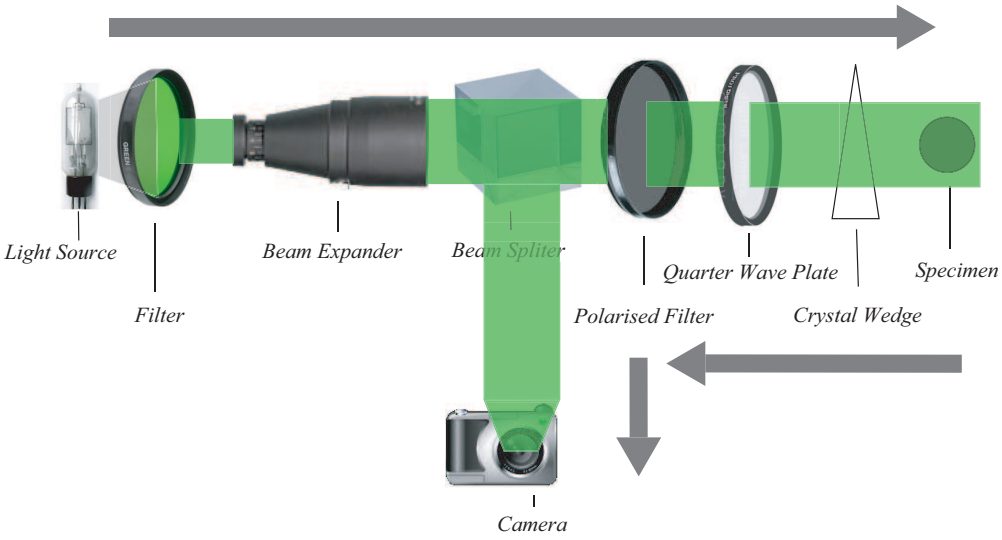

Figure 3.26 Reflection Polarisation Measurement System.

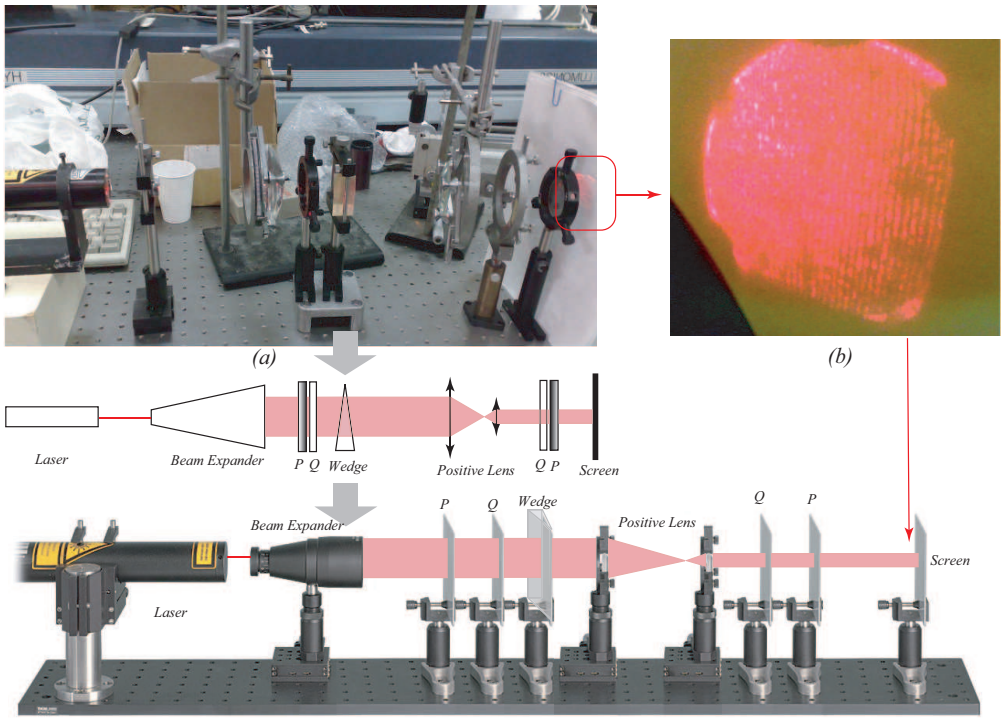

Figure 3.27 Fringe Projector System.

3.4 Camera Array Implemented for Phase Shifting Measurement with a Novel System

3.4.1 Introduction of the Camera Array

To make increasing imaging power available at decreasing cost, instrument size and power supply, a virtual camera which uses inexpensive imagers and processors has been designed and configured in various ways [41]. The pioneer, Stanford Computer Graphics Laboratory, has built an array of 100 $CMOS$-based cameras in 2004. There are many applications that could use a multi-camera system, which depend on the arrangement of the cameras. If the cameras are mounted closely and controlled together, to allow a virtual, synthetic aperture function, the camera array can increase performance in several ways, such as increased resolution, better depth of field and better dynamic range. It can be used to capture light-field data based on its function as a multiple center of projection camera. Lastly, a single camera with a large synthetic aperture function is created by cameras that are placed at an intermediate spacing apart. This allows them to view a distant object through an occluding foreground area[41].

There are three proposed applications for machining cornea measurements with this instrument. The simplest is to capture multiple phase images of the same phase event with a different ray path and numerically tomographically deconvolve the phase for a given depth. The second would be to combine the instrument with a sequential phase stepping system. Thus each set of images could first be unwrapped and the tomographically deconvolved. An alternative to a tomographic decovolution would be, to combine the unwrapped phase maps numerically and, the three dimensional phase structure extracts, using a synthetic depth of field approach.

Figure 3.28 The Set up of camera array.

Multi-camera Array

The camera array was set up using highly integrated, convenient and practical features. It minimizes the amount of custom hardware in the system. In order to accelerate the development cycle, a network camera has been adopted, it has an ultra high speed of data transmission and protocols interface making the use of the camera array easier.

- **Hardware Components**

The camera array system is composed of inexpensive off-the-shelf components. There are nine $CMOS$ cameras which use an $AXIS206$ chip board. They can work at a rate of up to $640 \times 480 \times 30$ fps. The cameras connect with HTTP servers, which respond to HTTP requests and send out motion JPEG sequences. The JPEG image quality is controllable. The cameras are connected to a central computer through 100Mbps Ethernet cables.

The server is controlled by the $3COM$ switch. Multiple cameras can be chained; thus, up to 26 cameras can be controlled simultaneously through a single serial connection to a computer in this system. Furthermore, if multiple controllers can be chained, then, there will unlimited camera clients supported in the system. In this proposed system, 9 controllers will be used to control 9 cameras.

Unlike any of the existing camera array systems in Stanford, our system uses only one computer. The JPEG image decompression and the camera lens distortion correction, which were usually performed with dedicated computers in previous systems, can all be conducted during the rendering process for a camera array at our scale.

- **Software architecture**

The system software runs as two processes; one for capturing and the other for image display. The capturing process is responsible for sending requests and receiving data from the cameras. The received images (in JPEG compressed format) are directly copied to some shared memory that both processes can access. The IP cameras cannot be easily synchronized. JAVA code especially used to control

the image capturing is edited. The code can control any of the cameras and any number of them working together; the capture time and frequency need to be input before capturing. The display is edited by HTML code, so that motion image stream or the live view can be shown in any of the tools for Internet Explorer.

- **System Architecture**

Fig.3.29 shows the architecture of the system. Each of the cameras is a separate internet device with three ports each with their own IP address. The cameras are connected through a one level tree, with one port connecting to a switch, and then connected to the host machine. Theoretically, the 100MB/s streaming bandwidth of switch port should accommodate non compressed video streams. Some implementation details (bus arbitration and our inability to get cycle-accurate control over the bus) will limit the data rate speed to the front-bus data transmission rate, although for the 9 cameras used in our application, there is no such worry. Our networked camera control application is run that allows the operation of the entire array to be driven from one PC[42].

Most systems would use the set trigger to synchronize all the cameras. Our system provides an arbitrary, constant temporal control for each camera. Because the timing signals for the image sensors are generated by the camera board, the clock frequency will be sent to the host machine from the terminal clients. Thus using one trigger signal, the starting point of the clock is set mandatorily by the trigger signal, and then all the camera time is triggered in a unified manner.

Our multiple camera array captures JPEG images at 30 frames per second (fps) from 9 cameras to one computer. The default $MPEG$ bit rate is 4Mb/s, the switch has 8.8 $Gbps$ switching capacity (maximum) and 6.6Mpps forwarding rate (maximum). The camera board has a 32-bit $RISC$ CPU Motion JPEG compression chip with 16 MB RAM, so before the data reaches the file size limit of the operating system, the data has already been captured and saved.

- **Camera calibration**

The camera calibration method was designed by $Jean-YvesBouguet$[43], and

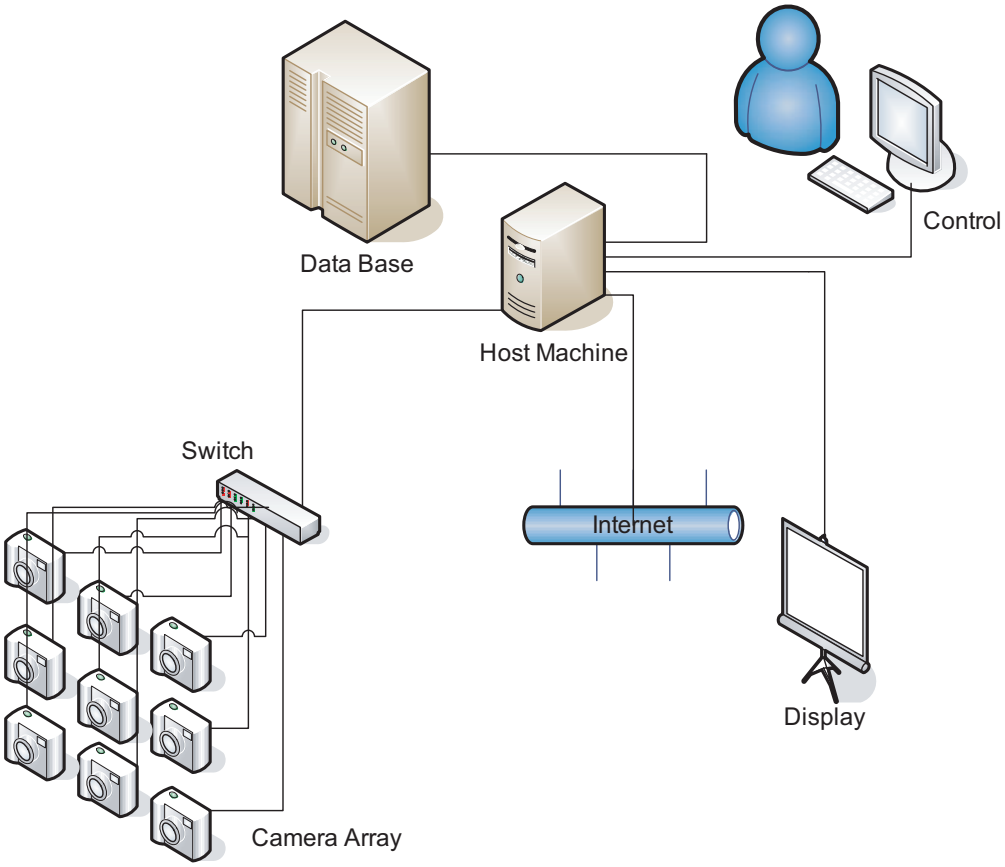

Figure 3.29 Camera array architecture.

this calibration toolbox is just used as a tool for measuring the accuracy of the multi-camera.

The camera calibration procedure consists of identifying the intrinsic camera parameters. A standard method is to acquire an image of a known 3D object and look for the set of parameters that best matches the computed projection of the structure with the observed projection of the image. The reference object is called the $calibration\ \ rig$, which is shown in Fig.3.30.

The complete set of images to be calibrated by the different cameras is also shown in thumbnail format.

Fig.3.31 shows the first four images with the detected corners (red crosses) and the re-projected grid corners (circles). The corners are extracted to an accuracy of about 0.1 pixel. Follow the same procedure for the 2nd, 3rd, ... , 9th images.

The re-projection error is also shown in the form of colour-coded crosses, which is

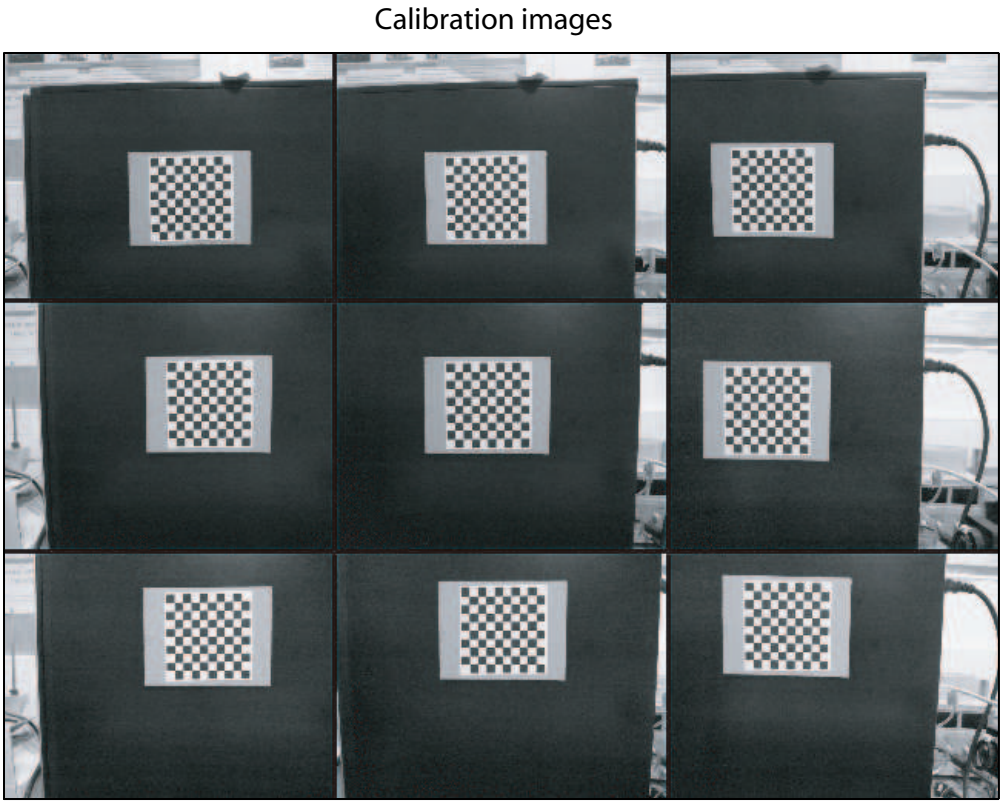

Figure 3.30 Camera array calibration - images are taken at different positions to capture $calibration \;\; rig$.

shown in Fig.3.32. After corner extraction, calibration is done in two steps: first initialization, and then nonlinear optimization. After comparison from the corner points of every camera's results, Fig.3.32 shows the error of the calibration work, from the scale of x and y axes, the error are controlled in about 0.5 pixels.

To calibrate the external parameters, we firstly extract the featured positions on the checkerboard by using two simple linear filters. Then the positions are refined to sub-pixel accuracy by finding the saddle points.

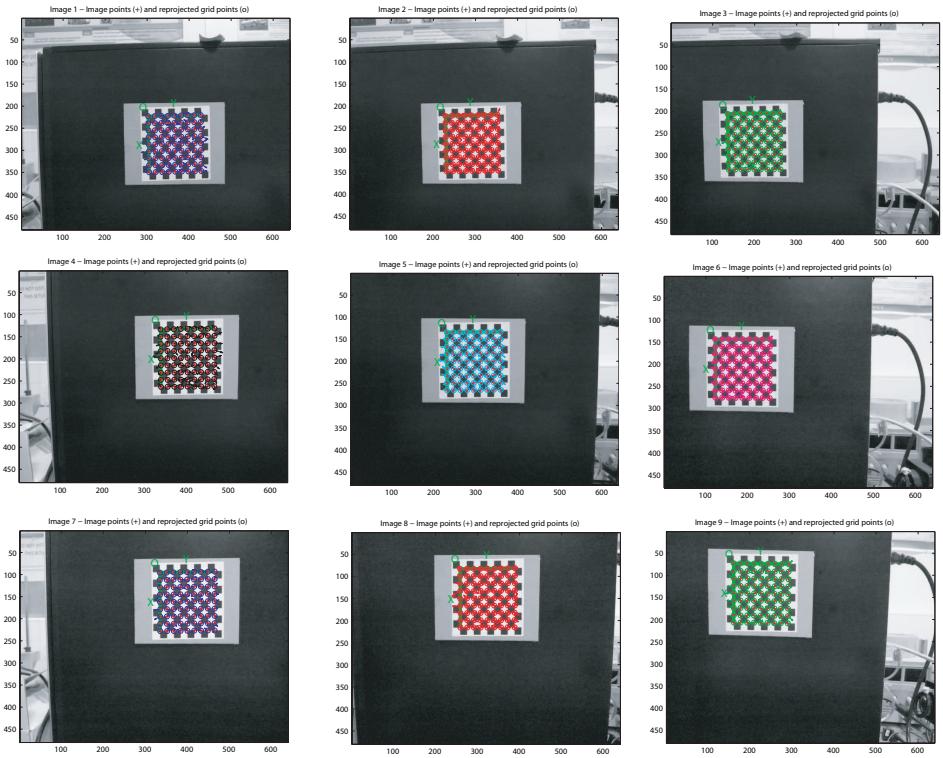

Figure 3.31 Camera array calibration - 9 camera images comparison.

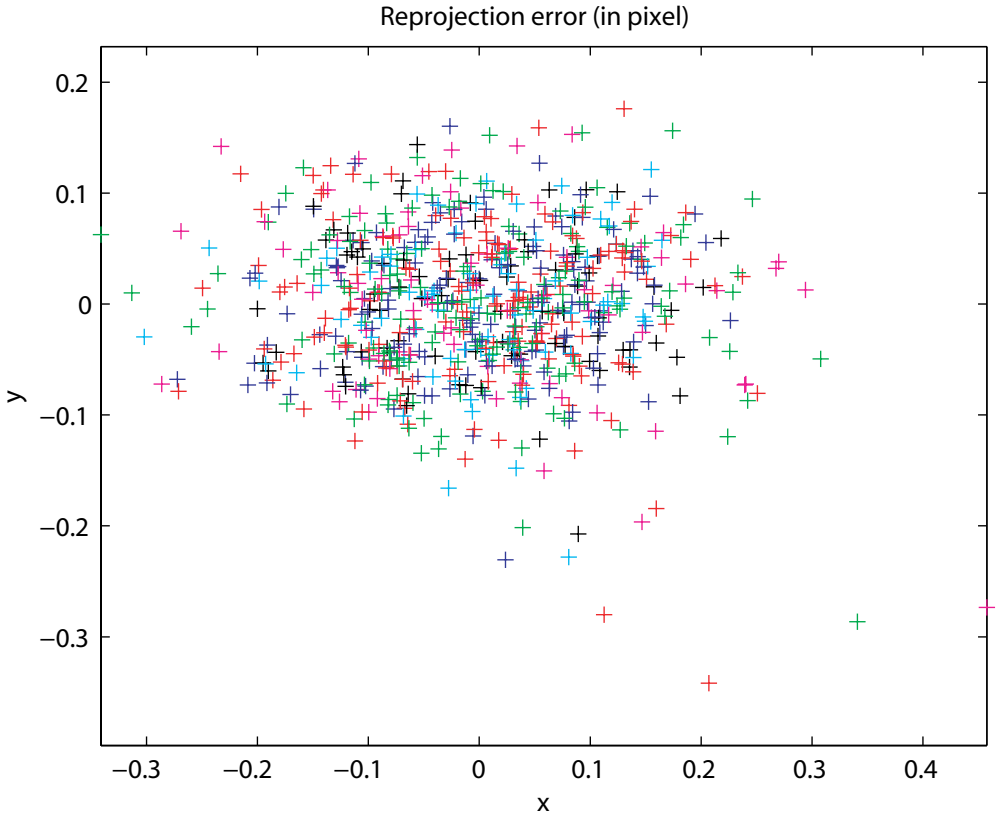

Figure 3.32 Camera array calibration - error.

The extrinsic parameters (relative positions of the grids with respect to the camera) are then shown in a form of a 3D plot Fig.3.33:

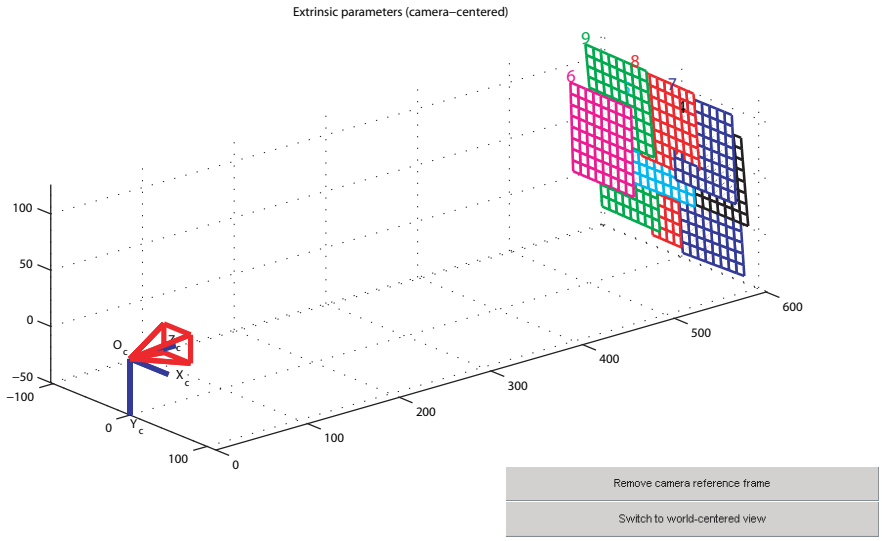

Figure 3.33 Virtual Camera aperture of 9-cameras and their views.

On this figure, the frame *(Oc,Xc,Yc,Zc)* is the camera reference frame. The red pyramid corresponds to the effective field of view of the camera defined by the image plane. To switch from a "camera-centered" view to a "world-centered" view, the figure is shown in Fig.3.34.

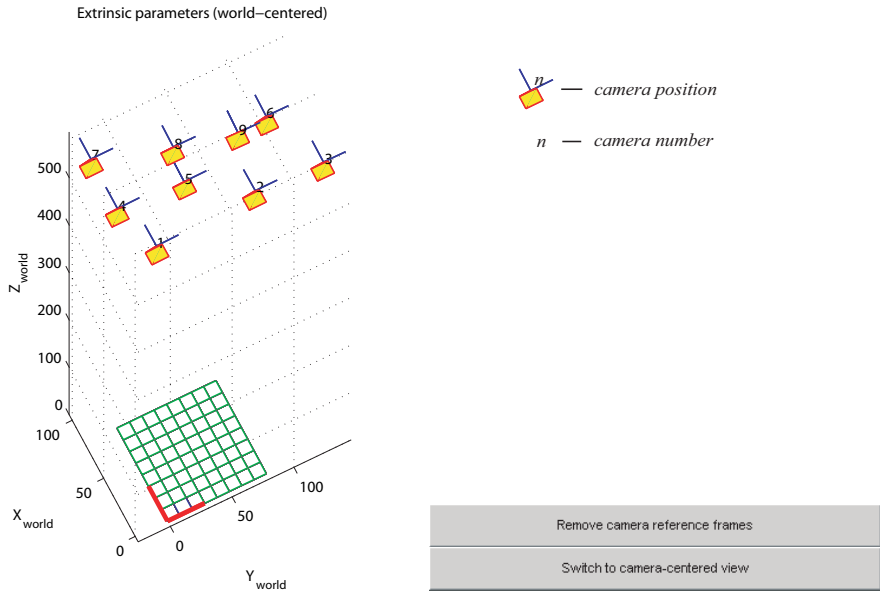

Figure 3.34 Camera Position Calibration in Experiment.

On this new figure, every camera position and orientation is represented by a

green pyramid. Looking back at the error plot, notice that the re-projection error is minimal. The reason for that is that we have not done a very careful job at extracting the corners on some little distorted images. Nevertheless, we can correct for that now by recomputing the image corners on all images automatically, and calibrate a position to make all cameras at the same plane as we designed.

- **Synthetic Aperture Focusing**

Synthetic aperture focusing is a technique using multi-images of a scene to simulate the defocus blur of the large aperture lens[44][45]. The images are captured from different positions, projected onto a desired focal surface, and their average is then computed. In the resulting image, the focal surface points are aligned and appear sharp, whereas points off this surface are blurred out due to parallax. The image are captured from different viewpoints, and projected onto a desired focal surface. After average computing, the objects lying off this surface are misaligned and hence blurred, points that lie on the focal surface are aligned and appear sharp. This can be see in the diagram from Fig.3.35. Synthetic aperture focusing includes projecting camera images onto a plane II_0 and computing their mean. Point Q on the plane II_0 is in focus; point P not on this plane is blurred due to parallax[41].

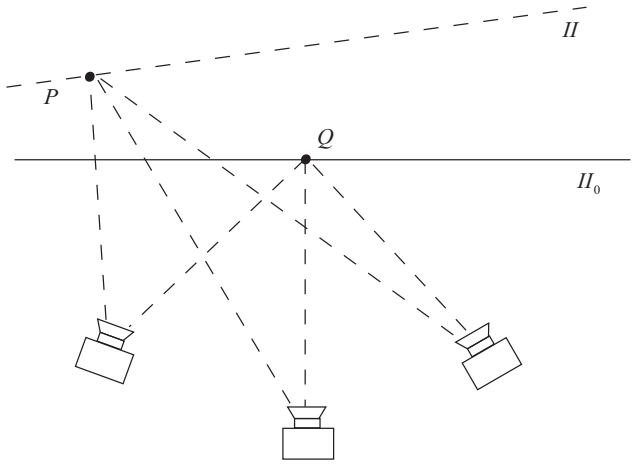

Figure 3.35 General configuration

Another case is considered when the cameras lie on a plane. Their images are on the parallel plane II_0, which is shown in Fig.3.36. All the cameras have the same

focus, and the focal planes show the range of depth of field that can be detected. To focus on any other plane parallel to the camera plane, the projected images just need to be shifted and then added.

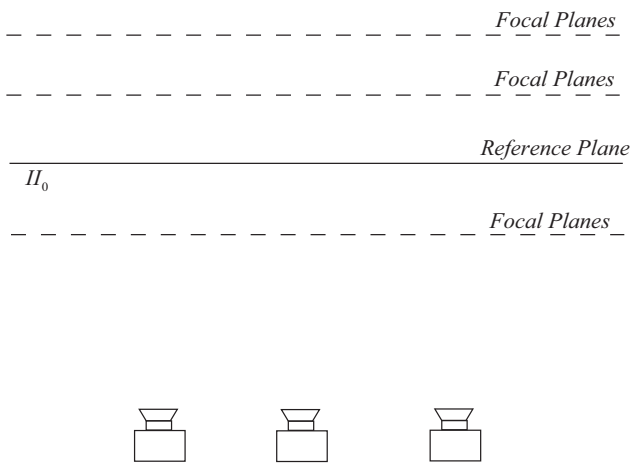

Figure 3.36 General configuration

This work builds on concepts in multi-view geometry, which are the notion of the plane and parallax. The different view onto the reference plane may be analysed used geometric calculation. To specify a new focal plane, the user firstly chooses a line l on the reference plane through which the focal plane passes. By picking a value for f, the user selects a particular focal plane through l. The synthetic aperture image with this focal plane can then be computed[46]:

$$I = \frac{1}{N+1} \sum_{i=0}^{N} K_i^{-1} \tag{3.11}$$

Varying f amounts to rotating the focal plane about axis l. At f equal zero, the focal plane overlaps with the reference plane. When the amount of f increases, the focal plane is approximately l away from the reference plane. So, we can compute a sequence of synthetically focused images with the focal plane rotating about l for a range of values of f.

- **Results**

The samples used are a black bolt, a silver bolt with nut, and a screw driver. The black bolt is the nearest to the cameras. The silver bolt with nut stands near the cameras' focal line, in another words, it is a reference object. The tiny screw driver is placed at the farthest place. The is shown in Fig.3.37.

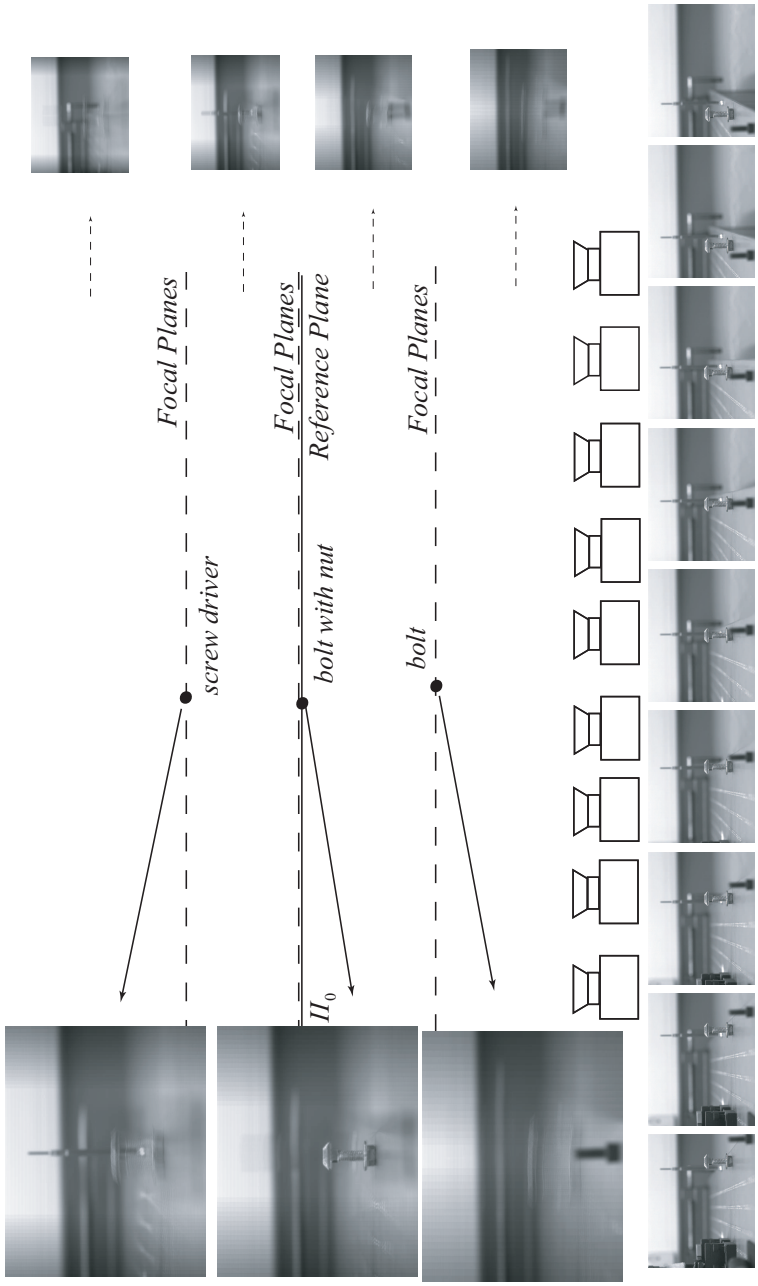

Figure 3.37 Diagram of experiment depth of field measurement

As can be seen, the system can change the focal plane without changing any position or focus of the cameras. Given the ability of synthetic aperture imaging

, it is suggested that this system would be useful for depth of field detection.

The main limitation of the system is due to the cameras' distance and the distance between the objects. The ability of the camera array can increase as the distance between them becomes as small as possible. In other words, if the camera density is higher, the depth of view can be detected more accurately.

3.4.2 Hardware Overview

With the development of multiple camera technology, comes the ability of image based rendering techniques to capture images of scenes from multiple viewpoints. While this novel method was implemented, camera hardware and polariscope system technology is also advancing. For semiconductor based techniques, the cost and power are constantly decreasing. The advent of $CMOS$ provides image sensors that are inexpensive and easy to use, because of their interface. Moreover, the processing power of a $CMOS$ sensor can be added to the sensor itself for future advanced work.

four-lens camera

In the work described by this thesis, we describe a four-lens array based on one image sensor, and a $CMOS$ image sensor array, called the "Full Angle Synchronised Phase-Shifting Polariscope Camera". The device is designed to record a synchronised phase shifting at different angle conditions with much visibility and control over the cameras. The four-lens system uses a high speed $CMOS$ camera based on the $RJ45$ interface with a $GPIO$ connector. The multi-camera array system is a modular embedded device based on the Ethernet $RJ45$ high speed $GigE$ bus, which is faster than the $IEEE1394b$ and $USB2.0$ techniques.

$CMOS$ image sensors normally have a worse noise performance than CCD sensor, but the former is suitable for this experiment for many reasons. $CMOS$ sensors do not require uncommon voltage supplies or clock signals, or extra circuitry, compared with CCD sensors. Furthermore, they are easy to use and control because $CMOS$ sensors contain some functions of digital processing and interfaces within. Furthermore, characteristics such as exposure times and auto-exposure algorithms, gamma correction, white balance, color gain, etc., can be easily configured in the processing of combined data from a multi-camera.

Camera Configuration

The four-lens instrument and the whole system diagram is shown in Fig. 3.38.

It is a standard circular polariscope, except for two groups of four quarter-wave plates and analysers, which are mounted with the lens in front of sensors in the camera.

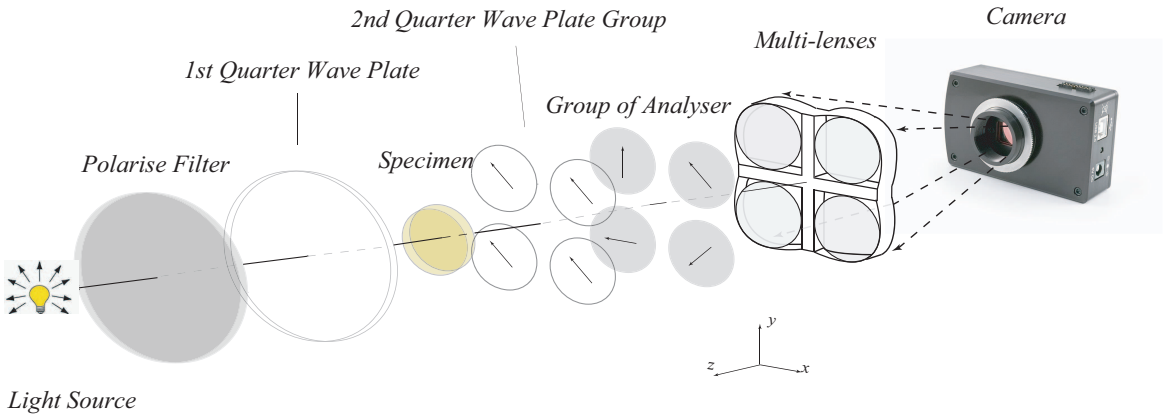

Figure 3.38 Schematic Diagram of the Synchronised Phase Shifting Polariscope System for Dynamic Real-Time Event.

The operation of the system is as follows. A collimated light beam passes through the polariser and quarter-wave plate, as we discussed in previous chapters and calculations, so that the circularly polarised light beam can be achieved. It transmits a birefringent specimen, then captured by the image sensor. When it arrives at the 4-lens camera, the optical energy of the beam is split into four paths along the beam axis in the same direction. The different configurable quarter-wave plates and analysers are inserted with each lens respectively to generate a phase shifting image. The phase shifting image is captured by a single $CMOS$ sensor. The instrument set up is shown in the Fig. 3.39.

Apart from its simplicity, this system has several advantages. Firstly, the instrument can be directly integrated with the configurations of the quarter-wave plates and analysers. The size and position of images can be adjusted easily, and the phase changes of each image can be adjusted separately. Another advantage of the design allows synchronised triggering for the image data, which is important for dynamic range analysis.

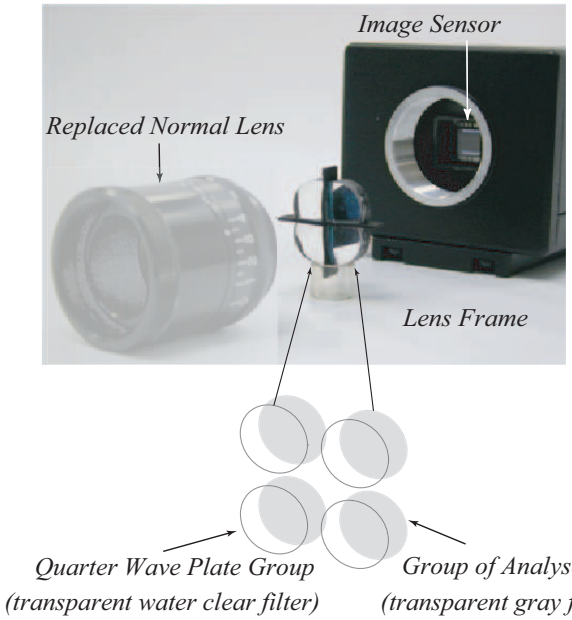

Group of Quarter Wave Plate and Analyser are Mounted in front of Image Sensor with Multi-lens

Figure 3.39 Synchronised Phase Shifting Polariscope System Camera.

Experiment

The demonstration of the proposed system is assessed using a ring model and "U" shape model, which is shown in Fig. 3.40. The forces are applied from the top and

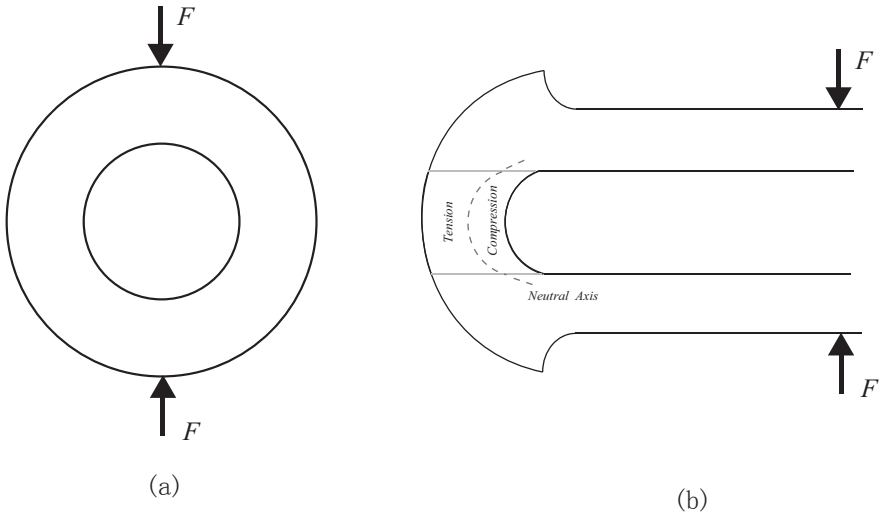

Figure 3.40 Schematic of specimens under vertical compression (a) Ring shape model (b) U shape model.

bottom at the same time, both on the ring shape model and on the "U" shape model. The ring model gives a simple demonstration which is very similar to that of the classical round disk. The "U" shape model shows that the stress distribution in

the area of the corner is subject to combined compression and bending and it serves as a good evaluation of this system since, for beam bending, the stresses on either side of the neutral axis have opposite signs. The configuration of the polariscope system is the same setting as in the previous four-step algorithm. The light source is monochromatic LED, of which the wavelength is 530nm. A $CMOS$ sensor camera which has 1024×1024 pixels is used for capturing the image. The four phase shifting images are captured as shown in Fig. 3.41.

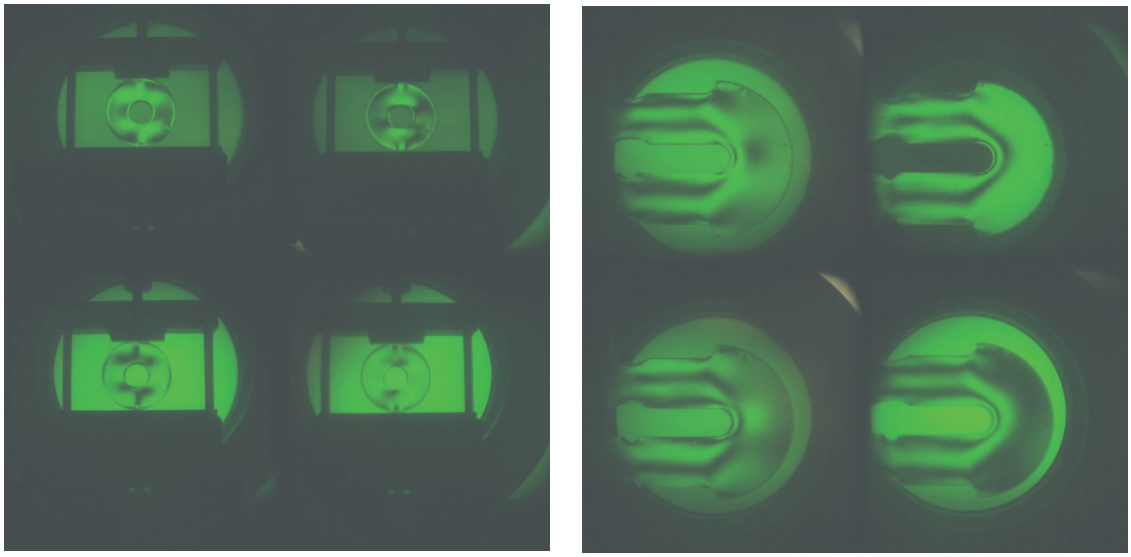

(a) (b)

Figure 3.41 Sample under vertical compression images (a) Ring shape model (b) "*U*" shape model.

With the calibration work, the whole (four-sum) images can be separated into four individual images of the same size, with no relative shifting between them. The calibaration images are shown below.

The four sub-images are cropped into four images separately, and the same pixels in each of the four separated sub-images represent the same point in the specimen. The reference is defined as the first position of the specimen at zero degrees. The complicated pattern distribution on the "*U*" shape sample causes the fringe on the surface to disturb the calibration work, which can be seen in Fig.3.43, and so the images are first calibrated using the sample without compression.

One image from the top and left-handside lens is set as a reference, other three

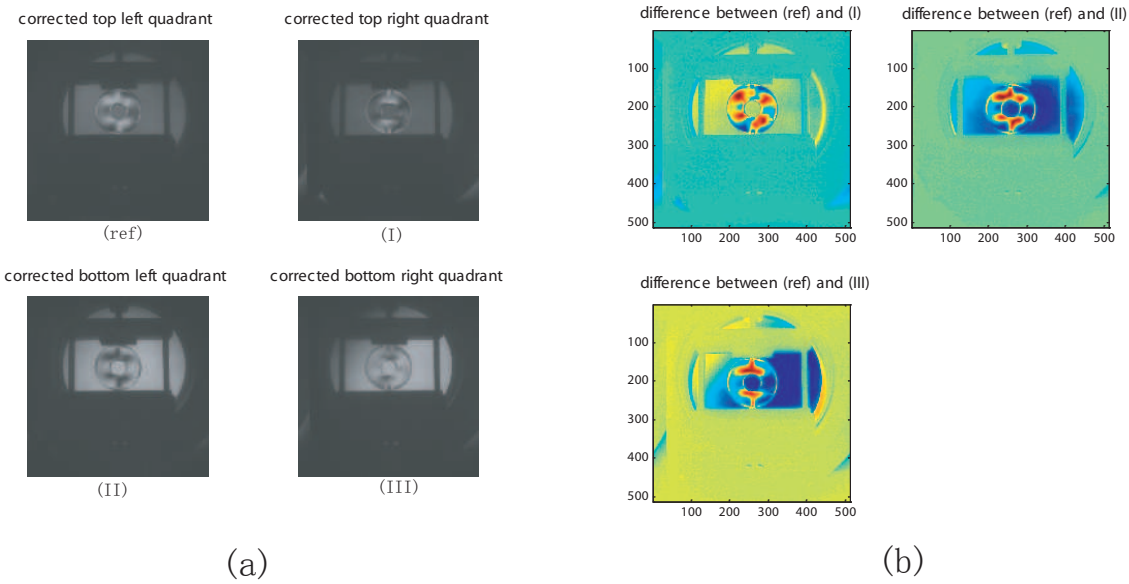

Figure 3.42 Ring shape sub-images (a) corrected image (b)difference between the first angle as reference.

images which captured from other three lens are compared with it respectively using edge detection techniques. This calibration determines the position of the camera and the sample, and to get a exactly fitting, as shown in Fig.3.44. Then the four images with the force load can be used for analysis. The ring shape sample is limited by the size and resolution of the camera; the fringe pattern has no more disturbance during calibration, therefore we can obtain the results as shown in Fig. 3.42.

The wrapped map and unwrapped map are shown in Fig. 3.45.

The contour map and surface map are shown in Fig.3.46 and 3.47.

The ambiguity in the isoclinic pattern and its effect on the isochromatic pattern can be seen in the figure. The discontinuities, which can be observed in the isoclinic map are a common problem with the phase shifting technique. These are caused by the non-deterministic isoclinic angle at points where the four light intensities are all equal to zero. It follows that discontinuities can generally be alleviated through interpolation if necessary. With the corrected isoclinic pattern, the isochromatic can be properly ordered as shown in Fig.3.48 which can be suitably unwrapped to give the fringe order distribution. Fig.3.49 and Fig.3.50 show the contour and surf map of the "U" shape specimen.

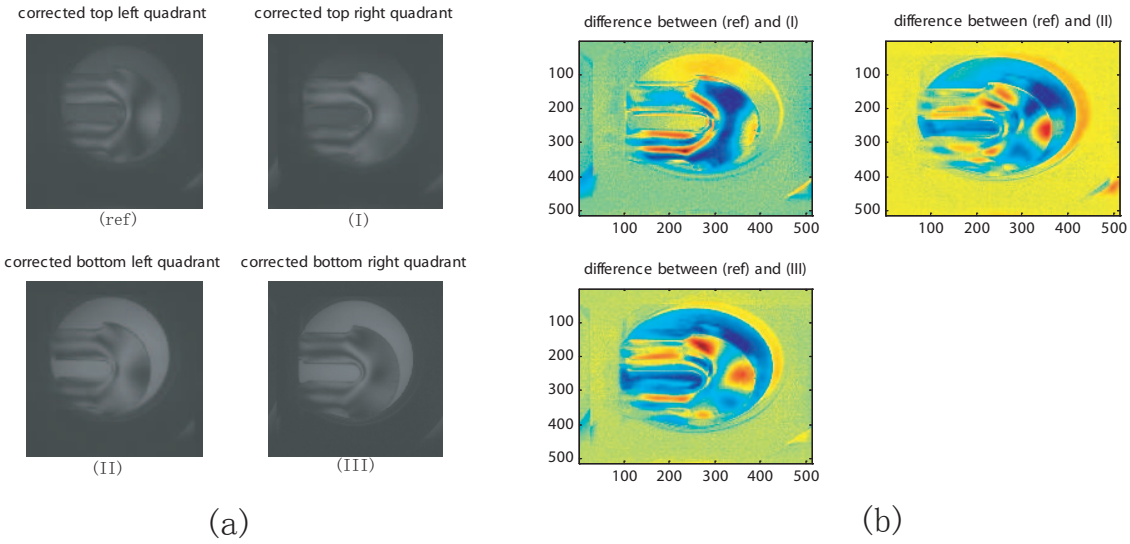

Figure 3.43 "U" shape sub-images (a) corrected image (b)difference between the first angle as reference.

The contour map and surface map are shown in Fig.3.46.

It can be seen from the results from the "U" shape specimen analysis, except for the noise and sample damaged part, that there is a phase jump occurring at the lines shown in Fig. 3.51. The fringe orders along a line AA' are also shown. The combined bending and compression effect is obvious from the different maximum fringe orders as is the shift of the neutral axis from the centroidal axis of the beam.

3.4.3 Discussion and Conclusion

A simple and efficient optical system for measuring birefringence has been proposed and demonstrated. Limited by the image sensor, the resolution is 1024 $\times$ 1024, and the $CMOS$ device has more noise than the CCD sensor, which will have influenced the the accuracy of the results. Based on the characteristics of the $CMOS$ sensor, the image data can be collected at high speed, and it is fit for high dynamic measurement in the photoelectric area of specimen.

With the aid of automatic calibration by computer, and multi-angle data collection, the processing speed is increased. Although the resolution of the image is not high, it will be increased with processing power. If the magnification can be selected to be good, the sensor can be used efficiently, then the accuracy can be also

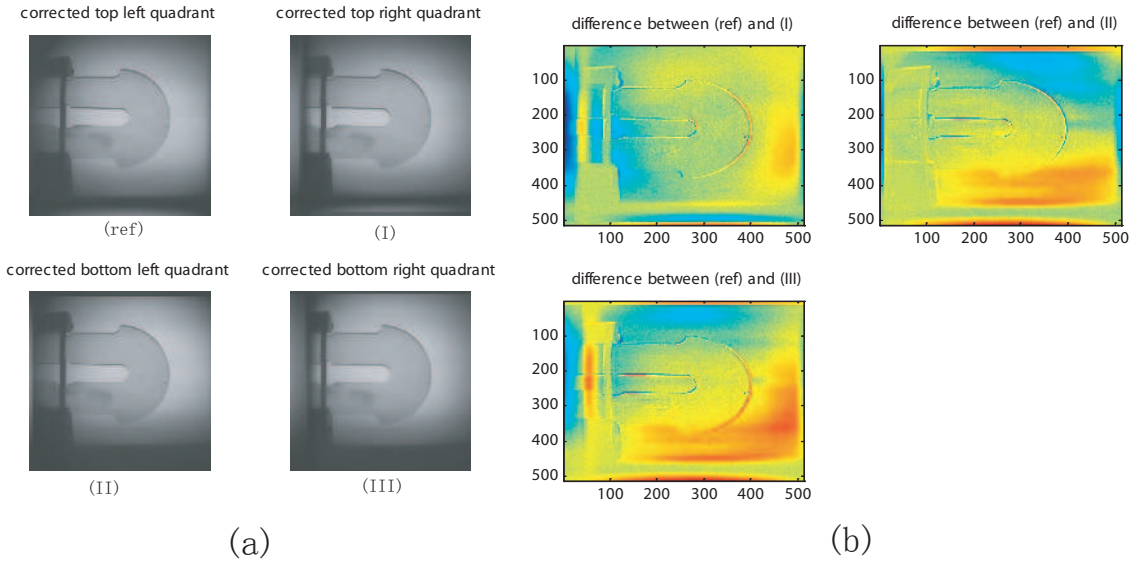

Figure 3.44 "U" shape sub-images without compression (a) corrected image (b)difference between the first angle as reference.

improved.

The accuracy of this system needs future investigation. However, it also depends on the linearity of the camera to light intensity, the distortion in shape and non-identical background intensities. In conclusion, the new design for automated analysis in real-time has been demonstrated and improved, and results obtained using phase shifting the algorithm. We concluded that the system has potential to be used in photoelasticity and interferometric techniques.

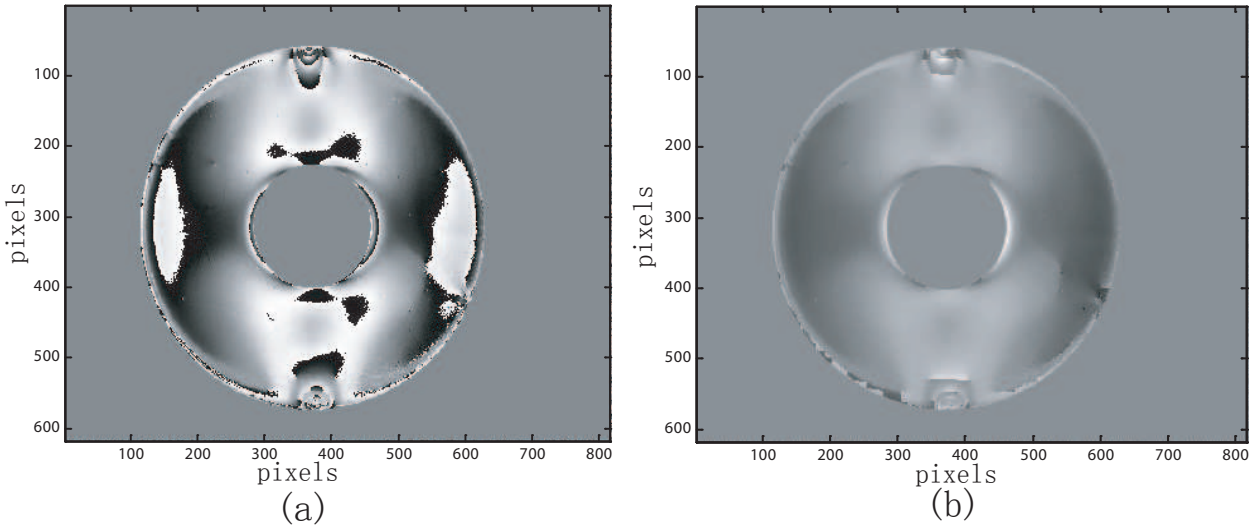

Figure 3.45 Ring shape corrected image(a) Wrapped Map (b)Unwrapped Map.

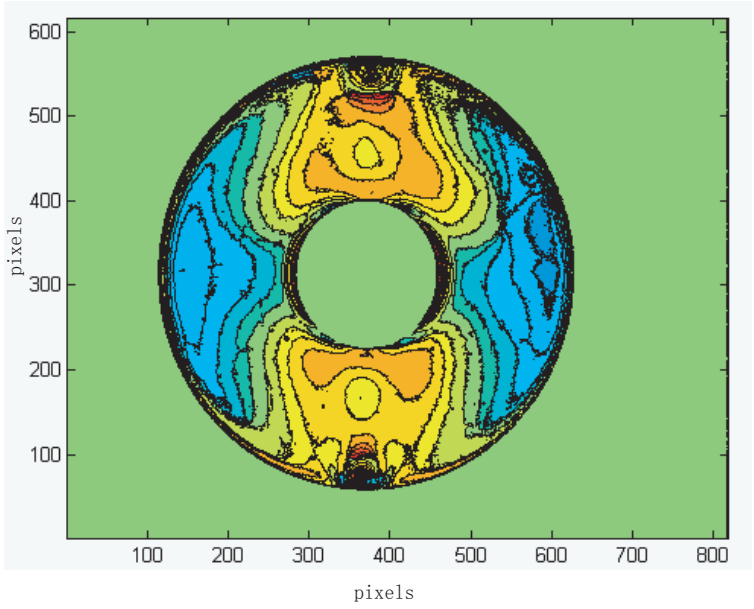

Figure 3.46 Ring shape corrected image contour map.

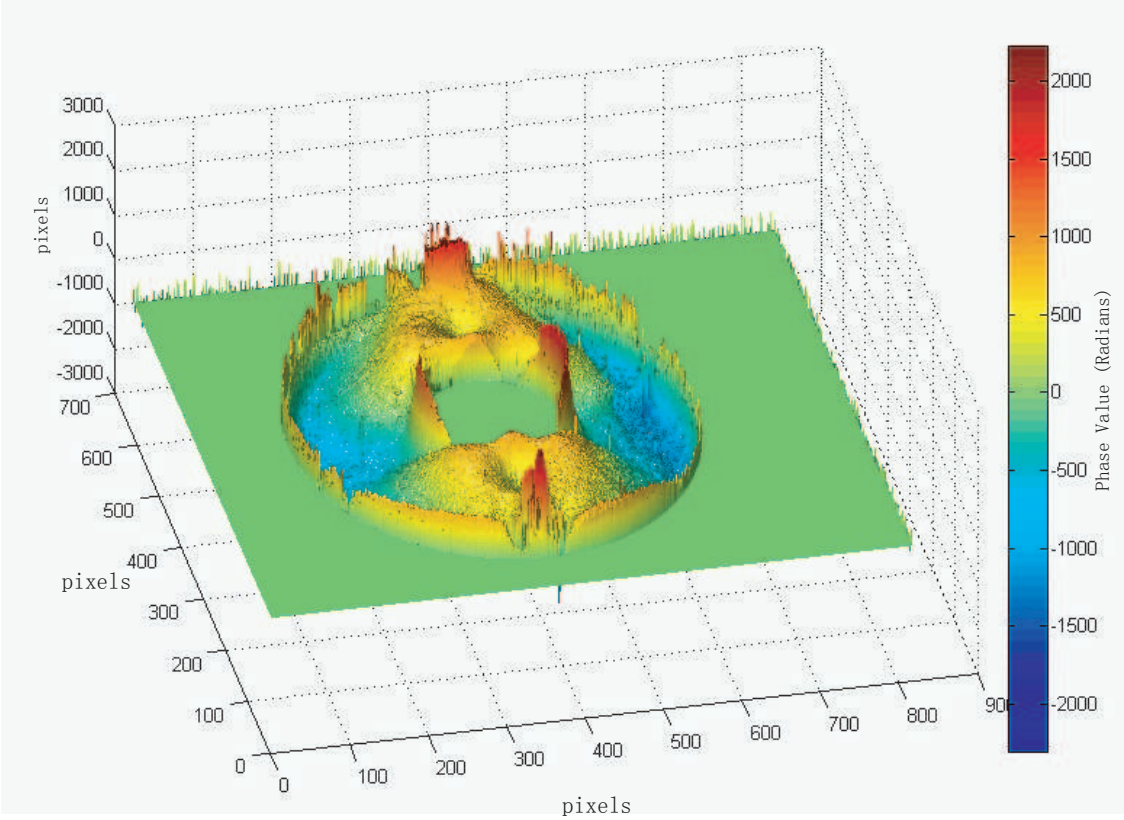

Figure 3.47 Ring shape corrected image surf map.

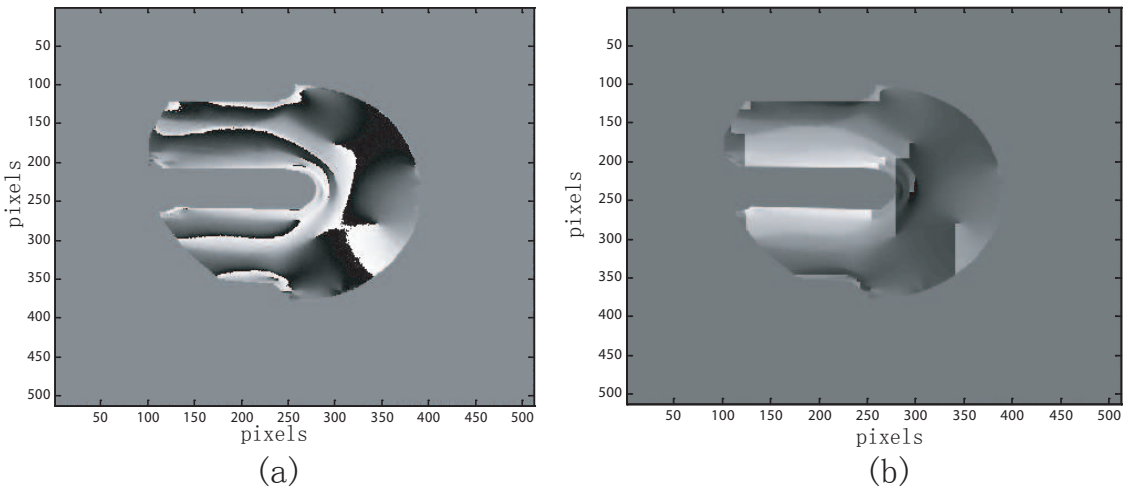

Figure 3.48 "U" shape corrected image(a) Wrapped Map (b)Unwrapped Map..

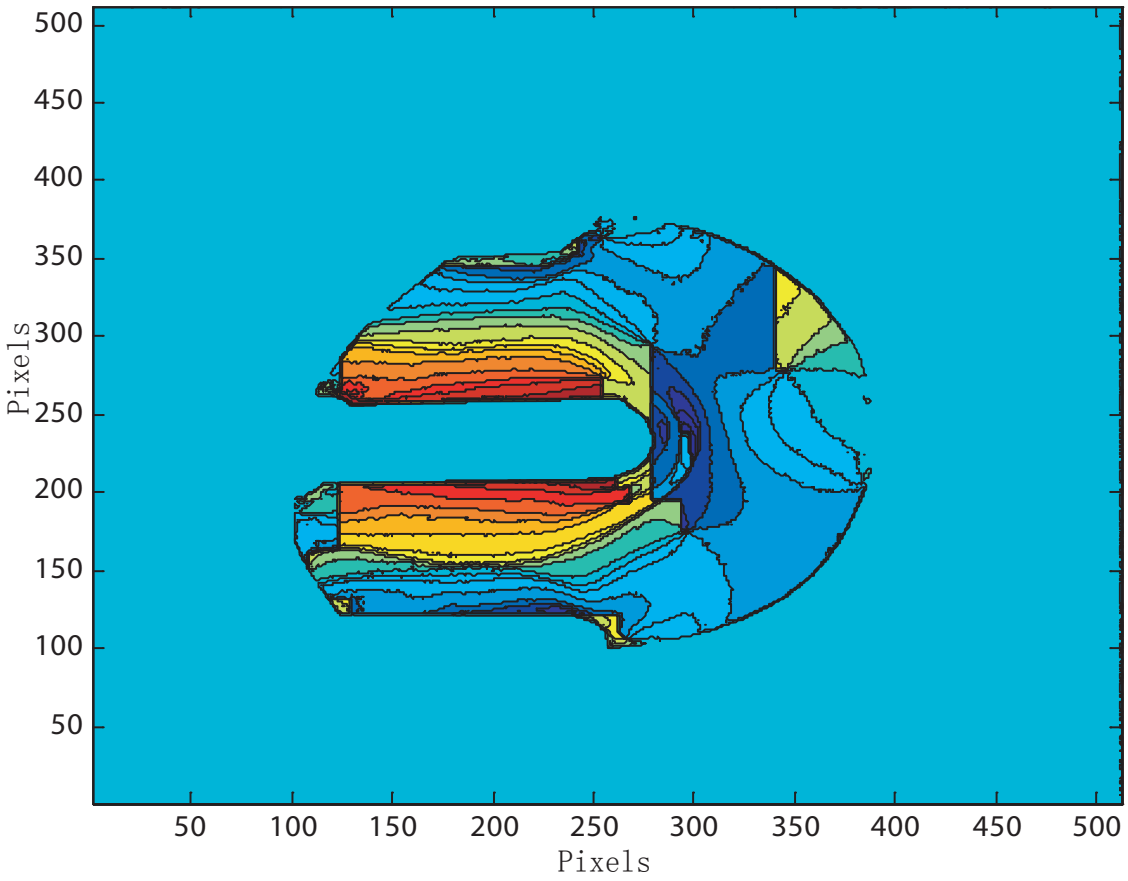

Figure 3.49 "U" shape corrected image contour map.

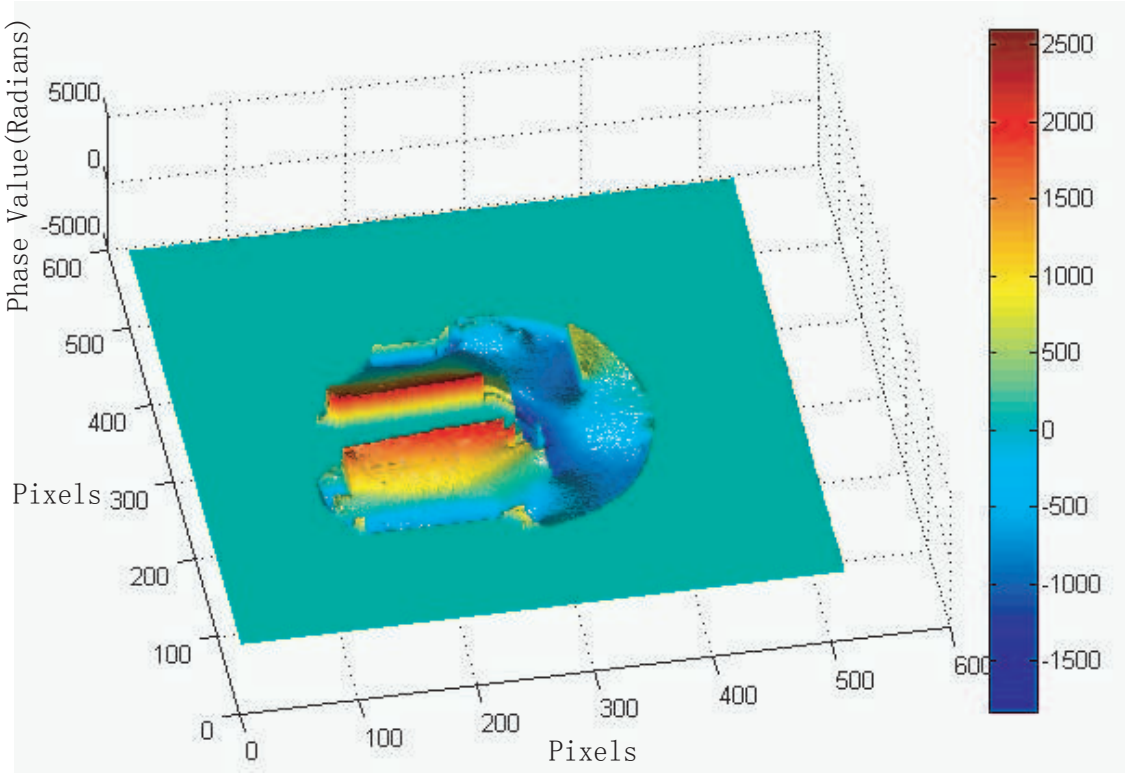

Figure 3.50 "U" shape corrected image surf map.

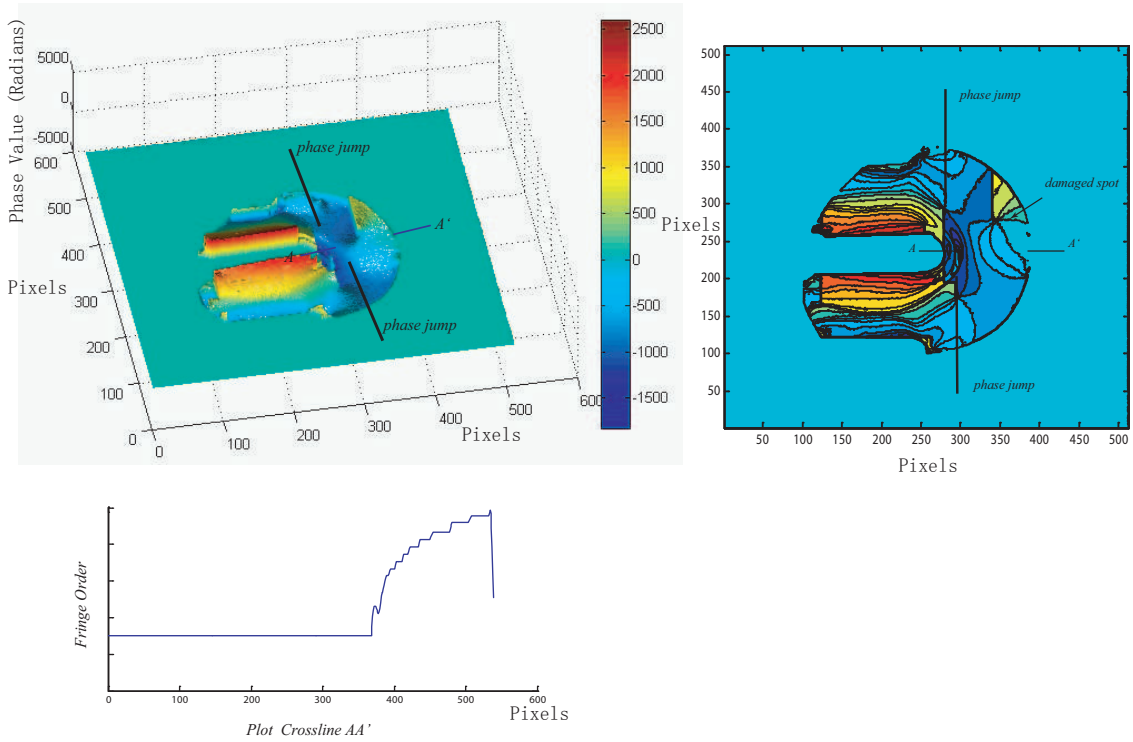

Figure 3.51 Unwrapped phase map and distribution along a cross line AA'.

Chapter 4

Optical Processing Approaches to Quantitative Birefringent Phase Measurement

In order to achieve better accuracy for birefringence measurement, phase sensitivity has been studied in this thesis. The investigation is based on a polarisation interferometric technique, where monochromatic light source is used in the experiments. Our improved design identified the accuracy of phase measurement in our experiment. The phase measurement results are improved in comparison to previous methodology based on quantitative analysis. In this chapter, phase sensitivity is evaluated. It is necessary to decide the precision of surface form measurement with phase unwrapping technique. Because this particular technique will be implemented into the measurement of complicated bio-fiber structure, which is an application of cornea birefringence measurement.

The accuracy of parameter evaluation by automated phase measurement techniques must be considered due to two aspects: theoretical formulation and experimental procedure. The sensitivity of phase shifting techniques to error in optical misalignment and quarter-wave plate mismatch will be discussed.

In the experiment, a approach to error analysis is presented. The investigation has shown how to associate the errors in the phase map with the misalignment. A

birefringent wedge is designed for generating fringes as a carrier in the polariscope. Retardation, introduced by a half-covered microscope slide with translucent cellulose tape inserted into the polariscope system, was calculated from the phase shifting using the phase matching technique. Through such experiments, the retardation calculation shows that the measurement accuracy of 0.02 radians has been achieved. The major contribution of this chapter is to determine the accuracy of phase changing for high-precision measurements of surface profile.

4.1 General Accuracy and Error Analysis in Experimental Physical Science

4.1.1 An Introduction to Error Analysis

There are no measurements that are free of error or uncertainty and this must be considered in the design of an instrument.

The word "error" does not have its usual meaning of "mistake", but here refers to the inevitable uncertainty which attends measurements. It is essential in the design of an experiment that the errors are understood and minimized as much as possible[47].

Normally, there are two main types of errors associated with experimental results, which are referred to as errors in $precision$ and $accuracy$. *The precision is usually related to the random error distribution associated with a particular experiment. The accuracy is related to the existence of systematic errors.* In laboratory experiments, the relative effects of the precision and accuracy on the final result normally depends on the particular experiment and the apparatus employed. Some experiments with large random errors need repeated measurements, in order to improve precision. The statement of uncertainty associated with a measurement should include factors that affect both the accuracy and precision of the measurement [48].

Errors can arise from three sources:

1) Careless errors

The errors due to mistakes in reading or careless setting. They can be eliminated by repetition of scales by one or more observers. Reading error refers to the uncertainties caused by the limitations of our measuring. It is difficult to reduce the inherent reading error in instruments, but it is possible to reduce it by repeating measurements of the same quantity and consequently averaging them.

2) Random errors

These lead to a spread or distribution of results on repetition of the particular measurement. They may arise from fluctuations in either the physical parameters due to the statistical nature of the particular phenomenon or the judgement of the observer. This type of error also affects the precision of the experiment[49][50][51].

3) Systematic errors

The error refers to built-in errors in the instrument either in design or calibration, which are present for every measurement of a given quantity with that instrument. Systematic errors affect the accuracy of the experiment which may be caused by a bias on the part of the experimenter, inaccurate calibration, or a faulty measuring instrument, etc.

4.1.2 Error Components in Experiments

In many methods of phase shifting technology, $Patterson$ and $Wang$'s algorithm is initial accepted and adopted by many researchers. A comparison and comprehensive study of error and accuracy analysis in phase shifting measurement reveals the intrinsic sensitivity of a particular algorithm to various sources of error.

In this section, experiments and data processing based on *Jones* calculus have been developed, where the accuracy is defined after calculation and error has been estimated for various phase shifting algorithms and experimental methods.

There are numerous sources of error that affect the accuracy of phase measurements in phase shifting algorithms. Error sources generally fall into three categories: 1) those associated with the data acquisition process, 2) those associated with defects in optical and mechanical design and fabrication, and 3) environmental effects [52].

Generic Simulation of Digital Polariscope Elements via Mathematic Analysis

As one of main functions we used in phase stepping method, the general form of Jones vector of any birefringent plate can be shown to be,

$$J_M = \begin{bmatrix} \cos\delta/2 - i\cos 2\theta \sin\delta/2 & -i\sin 2\theta \sin\delta/2 \\ -i\sin 2\theta \sin\delta/2 & \cos\delta/2 + i\cos 2\theta \sin\delta/2 \end{bmatrix} \tag{4.1}$$

where the angle θ is between the slow axis of the plate, and x axis, and δ is the relative retardation.

In the circular polariscope which is set up in the experiment, using *Jones* vector calculus, the components of the transmitted light vector perpendicular to and parallel to the analyser axis are:

$$\begin{bmatrix} U \\ V \end{bmatrix} = J_A J_{Q2} J_M J_{Q1} J_p a e^{iwt} \tag{4.2}$$

where the ae^{iwt} is the incident light. The components above are the vector in the order analyser, a quarter-wave plate, the model, a second quarter wave plate and a polariser respectively. The polariscope system can be expanded to be,

$$\begin{aligned} \begin{bmatrix} U \\ V \end{bmatrix} &= \tfrac{1}{2} \begin{bmatrix} \cos\beta & \sin\beta \\ -\sin\beta & \cos\beta \end{bmatrix} \begin{bmatrix} 1 - i\cos 2\phi & -i\sin 2\phi \\ -i\sin 2\phi & 1 + i\cos 2\phi \end{bmatrix} \\ &\times \begin{bmatrix} \cos\delta/2 - i\cos 2\theta \sin\delta/2 & -i\sin 2\theta \sin\delta/2 \\ -i\sin 2\theta \sin\delta/2 & \cos\delta/2 + i\cos 2\theta \sin\delta/2 \end{bmatrix} \\ &\times \begin{bmatrix} 1 + i\cos 2\varphi & i\sin 2\varphi \\ i\sin 2\varphi & 1 - i\cos 2\varphi \end{bmatrix} \begin{bmatrix} 0 \\ 1 \end{bmatrix} a e^{iwt} \end{aligned} \tag{4.3}$$

In equation 4.3, some new angles are introduced, which are β, ϕ and φ. In Fig. 4.1, which is a diagram of a circular polariscope, we can see that β, ϕ and φ are defined as the angles rotated of Analyser, Quarter-wave Plate 2 and Quarter-wave Plate 1 respectively.

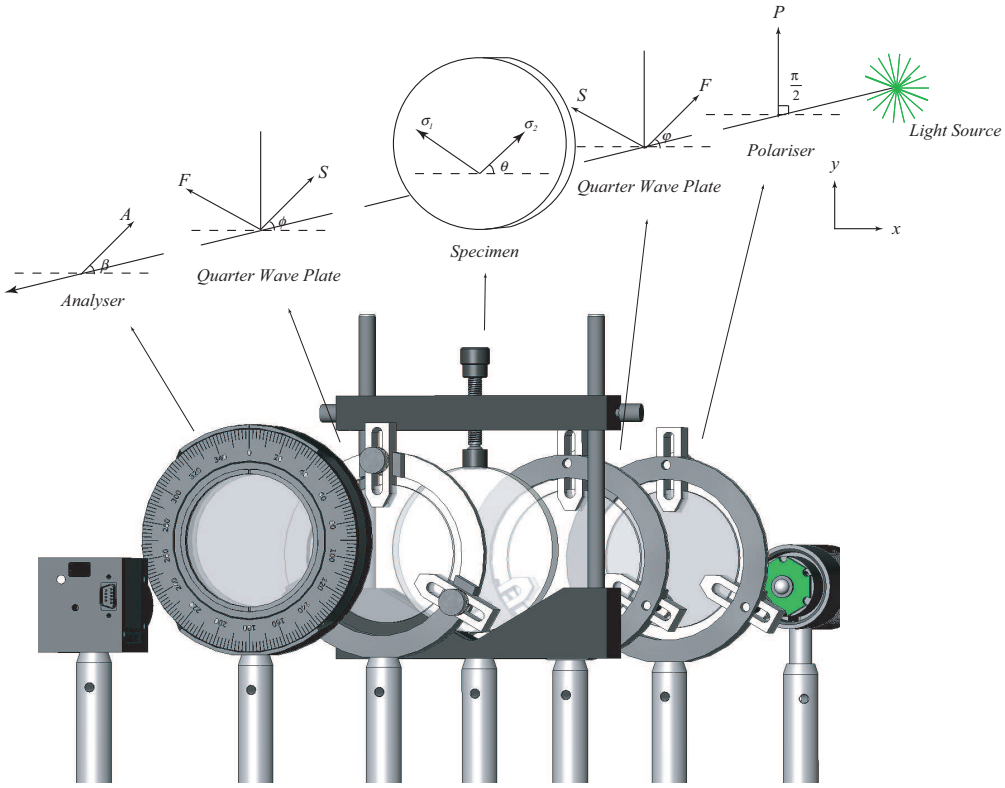

Figure 4.1 A Circular Polariscope.

Let δ equal $\pi/2$ in the configuration of the second quarter-wave plate and where θ is defined as the angle between the slow axis of the quarter-wave plate and the horizontal axis, it can be written as a *Jones* matrix as below,

$$\begin{bmatrix} 1 - i\cos 2\phi & -i\sin 2\phi \\ -i\sin 2\phi & 1 + i\cos 2\phi \end{bmatrix} \tag{4.4}$$

With the first quarter-wave plate, θ is the angle between the fast axis of the quarter-wave plate and the horizontal axis, this means that θ is replaced by $\theta + \pi/2$. The matrix of this quarter-wave plate can then be shown to be,

$$\begin{bmatrix} 1 + i\cos 2\varphi & i\sin 2\varphi \\ i\sin 2\varphi & 1 - i\cos 2\varphi \end{bmatrix} \tag{4.5}$$

Thus, we can get the dark field circular polariscope and the resulting pattern in the dark field fringes. The result can be calculated from the equations above and the normal result can be achieved, and $|U|^2$ with the light intensity total is the intensity we can gain from a point on the specimen.

$$I = I_0 + |U|^2 \tag{4.6}$$

where I_0 is the background intensity.

$$\begin{aligned} I = I_0 &+ \cos^2\beta \sin^2\tfrac{\delta}{2} \sin^2 2(\varphi - \theta) + \sin^2\beta \cos^2\tfrac{\delta}{2} \\ &+ \tfrac{1}{2}\sin 2\beta \sin\delta \sin 2(\varphi - \theta) + \sin^2\tfrac{\delta}{2} \cos^2 2(\theta - \varphi) \sin^2(\beta - 2\varphi) \end{aligned} \tag{4.7}$$

The following discussion will include the theoretical error calculation based on mathematical simulation. The system accuracy is discussed, and, each of the optical components will be simulated for the phase shifting algorithms. The results will be compared with the methods of $Asundi's$ four step method, $Patterson$ and $Wang's$ six-step method, and a simplified six-to-four steps algorithm. Not only the error of each optical components can be found, but also the whole system error can be simulated.

4.1.3 Numerical Simulation error analysis based on different algorithms

With the following error introduced in different kinds of algorithm, we will use mathematic way to calculate the error. This error comes from the wrong polarised and quarter-wave plate angle when we rotate them in experiments, because we cannot avoid rotating them a little bit more or less than the angle it should be. This error is one of the main factors which need to be considered.

$Asundi's$ algorithm Error Introduced

Table. 4.1 shows the orientation of optical elements for the phase shifting algorithm proposed by $Asundi$, where i_a is the amplitude of the light vector and i_b is the background light illumination.

$Number$	$AnalyserAngle\ \beta$	Intensity Equation
1	0	$i_1 = i_b + i_a \sin^2 \frac{\delta}{2}$
2	$\pi/4$	$i_2 = i_b + \frac{i_a}{2}(1 + \sin\delta)$
3	$\pi/2$	$i_3 = i_b + i_a \cos^2 \frac{\delta}{2}$
4	$3\pi/4$	$i_4 = i_b + \frac{i_a}{2}(1 - \sin\delta)$

Table 4.1 $Asundi's$ Algorithm .

As the table shows, when the value of β ranges from 0 to $3\pi/4$, we can simplify the four equations in Table. 4.1, and the fractional retardation δ is

$$\delta = \tan^{-1}\left(\frac{i_4 - i_2}{i_1 - i_3}\right) \tag{4.8}$$

The fractional retardation δ is obtained based as above on the ideal state. The optical component which we change in the experiment is only the analyser. Compared with the four special states above, the standard intensity of light transmitted can be shown to be:

$$i = i_b + i_a(\beta + \frac{\delta}{2}) \tag{4.9}$$

In experiment, β is the angle which the analyser has. So the error normally occurred when the analyser is rotated at each step of the phase changing, it cannot be avoided that the $\Delta\beta$ will be added to the value of β when it stops at $0, \pi/4, \pi/2$ and $3\pi/4$ angle of the four steps. Therefore, the analyser definitely has less or more than the correct value of angle it should be, even if it is just a very small deviation angle. That is the error which is brought from experiment. So, the equation of the intensity above becomes:

$$i' = i_b + i_a\left[(\beta + \Delta\beta) + \frac{\delta}{2}\right] \tag{4.10}$$

Table.4.2 shows the orientation of optical elements for the algorithm which introduces error,

Simplifying the four equations (shown in Table.4.2) in the same manner, allows

$Number$	$AnalyserAngle\ \beta$	Intensity Equation
1	0	$i'_1 = i_b + i_a \sin^2\left(\Delta\beta + \frac{\delta}{2}\right)$
2	$\pi/4$	$i'_2 = i_b + i_a \sin^2\left(\frac{\pi}{4} + \Delta\beta + \frac{\delta}{2}\right)$
3	$\pi/2$	$i'_3 = i_b + i_a \sin^2\left(\frac{\pi}{2} + \Delta\beta + \frac{\delta}{2}\right)$
4	$3\pi/4$	$i'_4 = i_b + i_a \sin^2\left(\frac{3\pi}{4} + \Delta\beta + \frac{\delta}{2}\right)$

Table 4.2 $Asundi's$ Algorithm with Error Introduced.

the fractional retardation δ' to be rewritten as,

$$\begin{aligned}\delta' &= \tan^{-1}\left[\tan(2\Delta\beta + \delta)\right] \\ &= \tan^{-1}\left(\frac{\tan 2\Delta\beta + \tan\delta}{1 - \tan 2\Delta\beta \tan\delta}\right) \\ &= \tan^{-1}\left(\frac{\tan 2\Delta\beta + \left(\frac{i_4 - i_2}{i_1 - i_3}\right)}{1 - \tan 2\Delta\beta\left(\frac{i_4 - i_2}{i_1 - i_3}\right)}\right)\end{aligned} \tag{4.11}$$

So, for the result of $\delta' = \delta + 2\Delta\beta$, in another word, the error $2\Delta\beta$ is introduced in the system by the rotated analyser.

From the results, we can see that $\delta' = 2\Delta\beta + \delta$, δ' has a linear relationship with δ. When $\Delta\beta$ is bigger than 3 degrees, the results will be periodic. So the accuracy can only reach 0.05 rad.

Patterson and Wang's algorithm Error Analysis

In this algorithm, apart from the fractional retardation δ and isoclinic angle θ, the parameter and background intensity i_a and i_b are unknown, therefore, at least four equations are needed to support solving for these variables. The analyser and second quarter-wave plate are both needed to be placed in six different settings. Still using *Jones* equation 4.3, the intensity of light transmitted for arbitrary position of the second quarter-wave plate and analyser is found to be,

$$i = i_b + \frac{i_a}{2} + \frac{i_a}{2}[\sin 2(\beta - \phi)\cos\delta - \sin 2(\theta - \phi)\cos 2(\beta - \phi)\sin\delta] \tag{4.12}$$

Table 4.3 shows the six configurations of the angle of optical components and the intensity equations which correspond to them, respectively. From these equations, the isoclinic angle and fractional retardation become,

$$\theta = \frac{1}{2}\tan^{-1}\left(\frac{i_5 - i_3}{i_4 - i_6}\right) \tag{4.13}$$

and

$$\delta = \tan^{-1}\left[\frac{i_5 - i_3}{(i_1 - i_2)\sin 2\theta}\right] = \tan^{-1}\left[\frac{i_4 - i_6}{(i_1 - i_2)\cos 2\theta}\right] \tag{4.14}$$

φ	ϕ	β	Intensity Equation
$3\pi/4$	0	$\pi/4$	$i_1 = i_b + \frac{i_a}{2}(1 + \cos\delta)$
$3\pi/4$	0	$3\pi/4$	$i_2 = i_b + \frac{i_a}{2}(1 - \cos\delta)$
$3\pi/4$	0	0	$i_3 = i_b + \frac{i_a}{2}(1 - \sin 2\theta \sin\delta)$
$3\pi/4$	$\pi/4$	$\pi/4$	$i_4 = i_b + \frac{i_a}{2}(1 + \cos 2\theta \sin\delta)$
$3\pi/4$	$\pi/2$	$\pi/2$	$i_5 = i_b + \frac{i_a}{2}(1 + \sin 2\theta \sin\delta)$
$3\pi/4$	$3\pi/4$	$3\pi/4$	$i_6 = i_b + \frac{i_a}{2}(1 - \cos 2\theta \sin\delta)$

Table 4.3 $Patternson$ and $Wang$'s Algorithm .

With the error of β and ϕ introduced, the intensity equation becomes,

$$\begin{aligned} i' = i_b + \tfrac{i_a}{2} + \tfrac{i_a}{2}[&\sin 2\left((\beta + \Delta\beta) - (\varphi + \Delta\varphi)\right)\cos\delta \\ &- \sin 2\left(\theta - (\varphi + \Delta\varphi)\right)\cos 2\left((\beta + \Delta\beta) - (\varphi + \Delta\varphi)\right)\sin\delta] \end{aligned} \tag{4.15}$$

Thus, Table. 4.3 can be rewritten to be,

φ	ϕ	β	Intensity Equation
$3\pi/4$	0	$\pi/4$	$i_{1'} = i_b + \frac{i_a}{2} + \frac{i_a}{2}[\sin\left(\frac{\pi}{2} + 2\Delta\beta - 2\Delta\varphi\right)\cos\delta - \sin\left(2\theta - 2\Delta\varphi\right)\cos\left(\frac{\pi}{2} + 2\Delta\beta - 2\Delta\varphi\right)\sin\delta]$
$3\pi/4$	0	$3\pi/4$	$i_{2'} = i_b + \frac{i_a}{2} + \frac{i_a}{2}[\sin\left(\frac{3\pi}{2} + 2\Delta\beta - 2\Delta\varphi\right)\cos\delta - \sin\left(2\theta - 2\Delta\varphi\right)\cos\left(\frac{3\pi}{2} + 2\Delta\beta - 2\Delta\varphi\right)\sin\delta]$
$3\pi/4$	0	0	$i_{3'} = i_b + \frac{i_a}{2} + \frac{i_a}{2}[\sin\left(2\Delta\beta - 2\Delta\varphi\right)\cos\delta - \sin\left(2\theta - 2\Delta\varphi\right)\cos\left(2\Delta\beta - 2\Delta\varphi\right)\sin\delta]$
$3\pi/4$	$\pi/4$	$\pi/4$	$i_{4'} = i_b + \frac{i_a}{2} + \frac{i_a}{2}[\sin\left(2\Delta\beta - 2\Delta\varphi\right)\cos\delta - \sin\left(2\theta - \frac{\pi}{2} - 2\Delta\varphi\right)\cos\left(2\Delta\beta - 2\Delta\varphi\right)\sin\delta]$
$3\pi/4$	$\pi/2$	$\pi/2$	$i_{5'} = i_b + \frac{i_a}{2} + \frac{i_a}{2}[\sin\left(2\Delta\beta - 2\Delta\varphi\right)\cos\delta - \sin\left(2\theta - \pi - 2\Delta\varphi\right)\cos\left(2\Delta\beta - 2\Delta\varphi\right)\sin\delta]$
$3\pi/4$	$3\pi/4$	$3\pi/4$	$i_{6'} = i_b + \frac{i_a}{2} + \frac{i_a}{2}[\sin\left(2\Delta\beta + \frac{3\pi}{4} - 2\Delta\varphi\right)\cos\delta - \sin\left(2\theta - \frac{3\pi}{2} - 2\Delta\varphi\right)\cos\left(2\Delta\beta + \frac{3\pi}{4} - 2\Delta\varphi\right)\sin\delta]$

Table 4.4 $Patternson$ and $Wang$'s Algorithm with Error Introduced.

The fractional retardation is shown as following,

$$\begin{aligned}
\delta' &= \tan^{-1}\left[\frac{i'_5-i'_3}{\left(i'_1-i'_2\right)\sin 2\theta}\right] \\
&= \tan^{-1}\left[\frac{2\sin 2(\theta-\Delta\phi)\sin\delta}{2\cos 2(\Delta\beta-\Delta\phi)\cos\delta\sin 2\theta}\right] \\
&= \tan^{-1}\left[\frac{2(\sin 2\theta\cos\Delta\phi-\cos 2\theta\sin 2\Delta\phi)\sin\delta}{2\cos 2(\Delta\beta-\Delta\phi)\cos\delta\sin 2\theta}\right] \\
&= \tan^{-1}\left\{\left[\frac{\cos 2\Delta\phi}{\cos 2(\Delta\beta-\Delta\phi)}-\frac{\cos 2\theta\sin 2\Delta\phi}{\cos 2(\Delta\beta-\Delta\phi)\sin 2\theta}\right]\frac{\sin\delta}{\cos\delta}\right\} \\
&= \tan^{-1}\left\{\left[\frac{\cos 2\Delta\phi}{\cos 2(\Delta\beta-\Delta\phi)}-\frac{\sin 2\Delta\phi}{\cos 2(\Delta\beta-\Delta\phi)}\frac{\cos 2\theta}{\sin 2\theta}\right]\frac{\sin\delta}{\cos\delta}\right\} \\
&= \tan^{-1}\left\{\left[\frac{\cos 2\Delta\phi}{\cos 2(\Delta\beta-\Delta\phi)}-\frac{\sin 2\Delta\phi}{\cos 2(\Delta\beta-\Delta\phi)}\frac{1}{\tan 2\theta}\right]\frac{\sin\delta}{\cos\delta}\right\} \\
&= \tan^{-1}\left\{\left[\frac{\cos 2\Delta\phi}{\cos 2(\Delta\beta-\Delta\phi)}-\frac{\sin 2\Delta\phi}{\cos 2(\Delta\beta-\Delta\phi)}\frac{i_4-i_6}{i_5-i_3}\right]\frac{\sin\delta}{\cos\delta}\right\} \\
&= \tan^{-1}\left\{\left[\frac{\cos 2\Delta\phi}{\cos 2(\Delta\beta-\Delta\phi)}-\frac{\sin 2\Delta\phi}{\cos 2(\Delta\beta-\Delta\phi)}\frac{i_4-i_6}{i_5-i_3}\right]\tan\delta\right\}
\end{aligned} \tag{4.16}$$

where the isoclinic angle is $\theta = \frac{i_5-i_3}{i_4-i_6}$. The result builds a relationship between $\Delta\beta$, $\Delta\phi$ and the intensity, The plot of the error distribution shows the difference of error occur at the range of 2^o, the accuracy is 0.03 radian.

The Six-to-Four Steps Algorithm with Error Analysis

The results from $Patterson and Wang's$ algorithm are based on the premise that the background light and maximum intensity of light are constant at a generic point during the phase stepping procedure. With the assumption, the six steps can be simplified to four steps, which is based on the ϕ equal with φ, because both of the values are equalled in the idealised state[38]. These two values could be config as the same value by rotating the plates and filters of the polariscope with the same angles. From Table.4.5,

ϕ	β	Intensity Equation
$\pi/4$	$\pi/2$	$i_1 = i_b + \frac{i_a}{2} + \frac{i_a}{2}\cos\delta$
$\pi/4$	0	$i_2 = i_b + \frac{i_a}{2} - \frac{i_a}{2}\cos\delta$
$\pi/2$	$3\pi/4$	$i_3 = i_b + \frac{i_a}{2} - \frac{i_a}{2}\sin\delta\sin 2\theta$
$\pi/4$	$\pi/4$	$i_4 = i_b + \frac{i_a}{2} + \frac{i_a}{2}\sin\delta\cos 2\theta$
$\pi/2$	$\pi/4$	$i_5 = i_b + \frac{i_a}{2} + \frac{i_a}{2}\sin\delta\sin 2\theta$
$3\pi/4$	$3\pi/4$	$i_6 = i_b + \frac{i_a}{2} - \frac{i_a}{2}\sin\delta\cos 2\theta$

Table 4.5 Four Steps Phase Shifting Algorithm.

θ and δ can be deduced to be,

$$\theta = \frac{1}{2}\tan^{-1}\left[\frac{i_5 - (i_1 + i_2)/2}{i_4 - (i_1 + i_2)/2}\right] = \frac{1}{2}\tan^{-1}\left[\frac{i_5 - (i_b + i_a^2/2)}{i_4 - (i_b + i_a^2/2)}\right] \tag{4.17}$$

$$\delta = \tan^{-1}\left[\frac{2(i_5 - i_4)}{(i_1 - i_2)(\cos 2\theta - \sin 2\theta)}\right] \tag{4.18}$$

It can be seen from the equation above that the phase angle δ depends on the proper determination of the isoclinic angle θ. Ambiguity in determination of the isoclinic angle will arise due to the $1/2$ period of phase angle in the determination of θ.

Then the error is introduced to the algorithm and the intensity equation is:

$$i = i_b + \frac{i_a}{2} + \frac{i_a}{2}[\sin 2(\beta - \phi)\cos\delta - \sin 2(\theta - \phi)\cos 2(\beta - \phi)\sin\delta] \tag{4.19}$$

With the error $\Delta\varphi$ and $\Delta\beta$ added, we can obtain,

$$\begin{aligned} i_1' = i_b + i_a^2[&\sin^2\Delta\beta\sin^2\tfrac{\delta}{2}\cos^2 2(\theta - \Delta\varphi) + \cos^2\Delta\beta\cos^2\tfrac{\delta}{2} \\ &+ \tfrac{1}{2}\cos 2\Delta\beta\sin\delta\cos 2(\Delta\varphi - \theta) + \sin^2\tfrac{\delta}{2}\sin^2 2(\theta - \Delta\varphi)\sin^2(\Delta\beta - 2\Delta\varphi)] \end{aligned} \tag{4.20}$$

Comparison with i_1 gives,

$$i_1 = i_b + \frac{i_a}{2} + \frac{i_a}{2}\cos\delta = i_b + i_a\left(\frac{\cos\delta + 1}{2}\right) = i_b + i_a\cos^2\frac{\delta}{2} \tag{4.21}$$

the i_1' can be simplified to

$$i_1' = i_b + i_a^2[\cos^2\Delta\beta\cos^2\frac{\delta}{2} + \lim error], \quad \text{where} \quad \lim error \to 0 \tag{4.22}$$

thus,

$$i_1' = i_b + i_a^2\cos^2\Delta\beta\cos^2\frac{\delta}{2} \tag{4.23}$$

With the same idea, we can achieve other intensity and error combined intensity equations,

$$i_2 = i_b + \frac{i_a^2}{2} + \frac{i_a^2}{2}(1 - \cos\delta) = i_b + i_a^2\sin^2\frac{\delta}{2} \tag{4.24}$$

where the error combined i_2' is,

$$i_2' = i_b + i_a^2 \sin^2 \frac{\delta}{2}[\cos^2 \Delta\beta \cos^2 2(\Delta\varphi - \theta) + \sin^2 2(\theta - \Delta\varphi) \cos^2(\Delta\beta - 2\Delta\varphi)] \tag{4.25}$$

The intensity i_4 is,

$$i_4 = i_b + \frac{i_a^2}{2}(1 + \sin\delta \cos 2\theta) \tag{4.26}$$

with error added,

$$i_4' = i_b + \frac{i_a^2}{2}\left(1 + (-\cos 2\beta) \sin\delta \cos 2(\theta - \Delta\varphi)\right) \tag{4.27}$$

The intensity i_5 is,

$$i_5 = i_b + \frac{i_a^2}{2}(1 + \sin\delta \sin 2\theta) \tag{4.28}$$

with error added,

$$i_5' = i_b + \frac{i_a^2}{2}\left(1 + \cos 2\beta \sin\delta \sin 2(\theta - \Delta\varphi)\right) \tag{4.29}$$

then, all values with error added will be in the δ equation, and they are calculated as below,

$$i_1' - i_2' = (i_1 - i_2)[\cos^2 \Delta\beta \cos^2 2(\Delta\varphi - \theta) + \sin^2 2(\theta - \Delta\varphi) \cos^2(\Delta\beta - 2\Delta\varphi)] \tag{4.30}$$

$$i_4' - i_5' = (i_4 - i_5) \cos 2\Delta\beta \sin 2\Delta\varphi \tag{4.31}$$

Thus, bringing the equation 4.18 into the new δ', we can obtain,

$$\begin{aligned}
\delta' &= \tan^{-1}\left[\frac{2(i_4' - i_5')}{(i_1' - i_2')(\cos 2\theta - \sin 2\theta)}\right] \\
&= \tan^{-1}\left[\frac{2(i_4 - i_5)}{(i_1 - i_2)(\cos 2\theta - \sin 2\theta)} \cdot \frac{\cos 2\Delta\beta \sin 2\Delta\varphi}{\cos^2 \Delta\beta \cos^2 2(\Delta\phi - \theta) + \sin^2 2(\theta - \Delta\phi) \cos^2(\Delta\beta - 2\Delta\phi)}\right] \\
&= \tan^{-1}\left[\tan\delta \cdot \frac{\cos 2\Delta\beta \sin 2\Delta\varphi}{\cos^2 \Delta\beta \cos^2 2(\Delta\phi - \theta) + \sin^2 2(\theta - \Delta\phi) \cos^2(\Delta\beta - 2\Delta\phi)}\right]
\end{aligned} \tag{4.32}$$

The accuracy is the same as the six-step, which is 0.03 rad.

Thus, with the comparison of the results between the methods above, we can see the error is estimated by theoretical calculation. The improvements of *Patterson and Wang's* six-step method could reach the minimum accuracy of 0.03 radian with easy operability.

4.1.4 Quarter-wave Plate Mismatch Error

Firstly, we discuss quarter wave plates. Optical misalignment in the modeling is very straightforward for the purpose of determining error. Quarter-wave plate mismatch is also one of the errors, which is considered about the light source problem. If the light source wavelength we actually used is λ, and assuming the reference wavelength is λ_{ref}, then the quarter wave plate will introduce retardation of $\pi/2 + \xi$, but not the standard $\pi/2$, and the ξ can be written as [53],

$$\xi = \frac{\pi}{2}\left(\frac{\lambda}{\lambda_{ref}} - 1\right) \tag{4.33}$$

Due to a mismatch error of ξ, the first quarter wave plate *Jones* matrix can be re-written as,

$$\frac{1}{\sqrt{2}}\begin{bmatrix} \left(\cos\frac{\xi}{2} - \sin\frac{\xi}{2}\right) & i\left(\cos\frac{\xi}{2} + \sin\frac{\xi}{2}\right) \\ i\left(\cos\frac{\xi}{2} + \sin\frac{\xi}{2}\right) & \left(\cos\frac{\xi}{2} - \sin\frac{\xi}{2}\right) \end{bmatrix} \tag{4.34}$$

Considering this aspect, $Ramesh$ and $Tamrakar$ [54]proposed a new algorithm to improve this problem.

In general, error due to misalignment are not easy to detect by just inspecting the images recorded for various optical arrangements. Moreover, except for considering quarter wave plates which were mentioned above, the general equation for the intensity of light emerging at a point on the specimen is given by equation4.7. The intensity equation can be simplified as below,

$$I = I_0 + a^2 \left[\sin^2 \frac{\delta}{2} \cos^2 \beta + \sin^2 \beta \cos^2 \frac{\delta}{2} + \frac{1}{2} \sin 2\beta \sin \delta \cos 2\theta \right] \tag{4.35}$$

which can be rewritten as,

$$\sin 2\beta \sin \delta \cos 2\theta + \cos 2\beta - 2\cos \delta + 1 - \frac{2(I - I_0)}{a^2} = 0 \tag{4.36}$$

As we discussed above, we can regard $f(x) = \sin 2\beta \sin \delta \cos 2\theta + \cos 2\beta - 2\cos \delta + 1 - \frac{2(I-I_0)}{a^2}$, and the value of a quantity x with an uncertainty Δx could be given by $\Delta f(x) = f(x + \Delta x) - f(x)$ then to $\Delta f(x) = \frac{df}{dx}\Delta x$. For multiple variables, $f(x, y)$, it can be shown to be,

$$\Delta f(x_1, x_2, x_3, \cdots) = \frac{\partial f}{\partial x}\Delta x + \frac{\partial f}{\partial x_2}\Delta x_2 + \frac{\partial f}{\partial x_3}\Delta x_3 + \cdots \tag{4.37}$$

Any difference between the real set up and the standard system can be determined by the change in values, which are β, δ and θ. Each component is listed below,

$$\frac{\partial f}{\partial \beta} = 2\cos 2\beta \sin \delta \cos 2\theta - 2\sin 2\beta \tag{4.38}$$

$$\frac{\partial f}{\partial \delta} = \cos \delta \sin 2\beta \cos 2\theta + 2\sin 2\delta \tag{4.39}$$

$$\frac{\partial f}{\partial \theta} = -2\sin 2\theta \sin \delta \sin 2\beta \tag{4.40}$$

4.2 Phase Stepping Approach to Phase Measurement

Phase Shifting is useful in many applications, such as photoelasticity. In equal steps as the above, the phase difference of interfering waves can be simply described and the phase at each point can be determined.

From the calculations and simulations above, we can find the intensity transmitted by the optical system by considering the products UU^*, where U^* denotes the complex conjugate of U, which is constructed of the components of the light vector besiding along the analyser axis. When the intensity of each element is expressed as *Jones* matrices, the intensity pattern over the model field can be computed.

Problems with fringe pattern, essentially similar to phase shifting, polarisation stepping and stress field load stepping could be solved by this method.

As mentioned in the sections above, in a normal circular polariscope, the two quarter wave plates are interlinked. It is evident that *Patterson and Wang's* algorithm can not be implemented in the normal system. This is because in this algorithm, a circular polariscope is used with the change in phase achieved by rotation of the output optical components of the polariscope. This means that the second quarter wave plate and analyser in the system can be rotated independently. Hence, here we will consider the normal conditions and make developmental changes towards what is ultimately desired.

4.2.1 Rotation Error Introduced

Whenever any algorithm is adapted, the optical component must be rotated for measuring, so the error and accuracy, which is included in the experimental configuration, also need to be considered.

The sections above discussed the error based on mathematical theory. This section will provide the results obtained from the experiments and determine the difference between the theoretical and experimental values.

Original State Analysis by Intensity Periodicity

In general, the dark field is the essential state needed in any algorithm, and in $Asundi's$ algorithm, it is the first state. In this algorithm, the optical component to be rotated is the analyser. Compared with other algorithms, only one polarised filter needs to be rotated at a time, thus this algorithm can effectively reduce the error.

In this test, there is no specimen placed into the system. The intensity of the light emitted from the system can be read by camera with only β changes. The out put intensity value can be recorded and shown to be an analog sine wave, which increases from zero to maximum value, then decreases to zero, and continues this

cycle. From this experiment, we can see that the light intensity changes from dark to bright, and then return to dark. This phenomenon corresponds to the analyser rotating through a full circle, thus it has period.

From Fig.4.2, we can see the sketch of this rotation, at angles 0, π and 2π with the analyser, and it shows a dark field such that the pixel value is 0 in in the field. When the analyser's angle is $\pi/2$ or $3\pi/2$, the pixel value in the bright field is the maximum at the value of 255, with normalization processing, and these values can be matched with the standard sine-wave form.

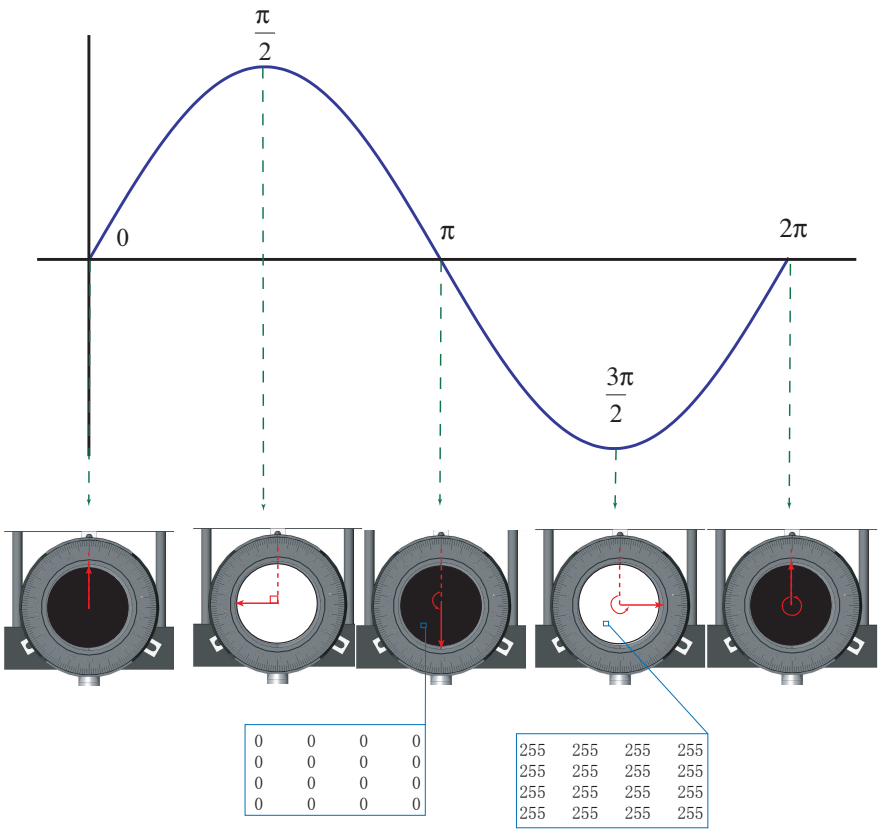

Figure 4.2 The rotation analyser bring dark field and bright field in periodic intensity changes in a circular polariscope.

In the experiment, data are collected at every 2 degrees of rotation of the analyser, from 0 to 2π, thus there are 180 frames collected. Fig.4.3 shows the experimental data which match the angle of the analyser.

The sum of pixels in each frame is recorded using $\sum I_0(x, y)$ from 0 degrees to 360 degrees using $\sum_{0}^{360} I_\theta(x, y)$. The average mean value $\overline{I_\theta}$ is defined by

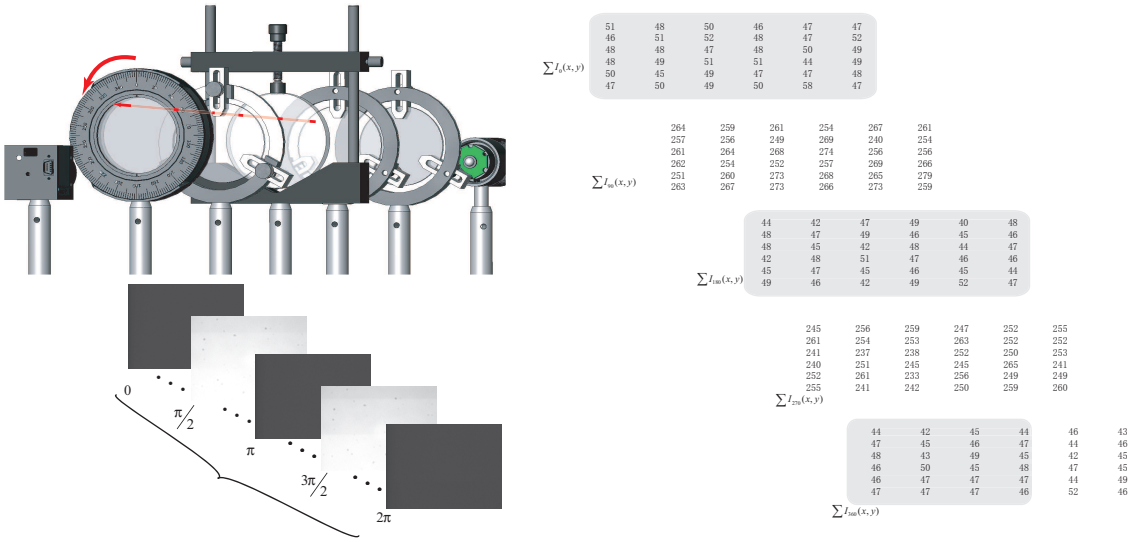

Figure 4.3 Experiment data of the rotation analyser bring dark field and bright field in periodic intensity changes in a circular polariscope.

$$\overline{I_\theta} = \frac{1}{n} \sum_{x=1,y=1}^{n} I_0(x,y) \tag{4.41}$$

where $I_0(x,y)$ is all of the pixels measured values and n is the pixel number of measurement. $\overline{I_\theta}$ will approach the standard intensity value which removes some error if there is some noise in each frame. With the increase of rotated angle β, the intensity changes can be shown in Fig.4.4.

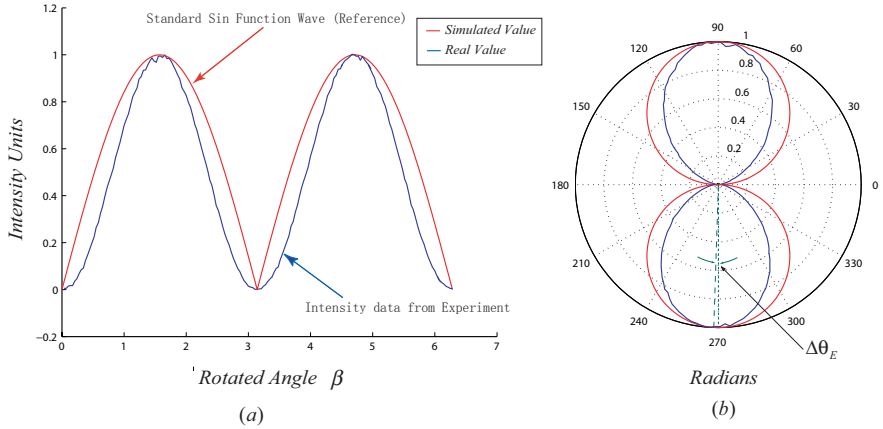

Figure 4.4 Comparison of standard and real experimental intensity changes (a) Linear plot (b)Polar angle in radians.

In Fig.4.4, the red line indicates the simulated value and the blue line indicates the experimental obtained measurement. In (a), the figure shows the result in a linear plot, and the curve of experimental data are very close to the curve of

theoretical sine wave form, the radians are used absolute value. It shows clearly the relationship between the rotated angle of the analyser and the changes in intensity. The polar coordinates of the angle in radians are plotted in (b), where the $\Delta\theta_E$ shows the error of the original state to the simulated version. The accuracy is about 0.02 radian.

4.2.2 Calibration by Carrier Fringes

Optical Component in Calibration

Another optical component is introduced for calibration of polariscope system. This can be defined as birefringent wedge, which will be mainly used in the Fourier Transform method for interferometry analysis in the next section. The wedge is designed for generating carrier fringes in a polariscope. A frozen stress wedge is used in this calibration, which is made using $Araldite\ CT-200\ Expoxy\ Resin.$ The resin is the most commonly used photoelasticity material in such applications. In the cast state, it exhibits good mechanical properties and strength, with little creep or time-edge effects. At freezing point, the amount of creep is negligible. The wedge is made in two stages:

1) The sample plate is loaded in an oven to create straight fringes in the plate. After several hours loading in the oven, the temperature is reduced, then the fringes are frozen in the sample plate.

2) A wedge is cut from a frozen stress plate, and the fringe spacing is determined by the angle of the wedge, and by the material characteristic.

The ultimate tensile strength of *CT-200* epoxy at the stress freezing temperature is $2.07\ NM.m^{-2}$ $(Newton/Meter^{-2})$, the material fringe value f' is $0.28KN.m^{-1}.fr^{-1}$ [55]. and the fringe order which is possible to freeze into the material is given ac-

cording to the equation below:

$$\delta = \frac{nf'}{h} \tag{4.42}$$

where δ is the principal stress difference, n is the fringe order, and h is the thickness of material. The maximum fringe order that can be achieved is $n_{\max} = 44.25$. A sketch of the wedge is shown in Fig.4.5.

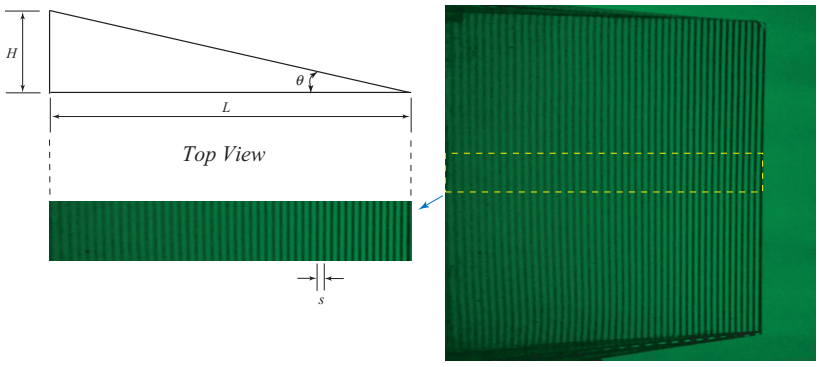

Figure 4.5 Schematic Diagram of a Frozen Stress Wedge.

The length of wedge L can be obtained from a height H of $12mm$ (millimetre) plate of epoxy material and the wedge will taper down to 0 size of thickness at one end. The fringe spacing s is 1.2 mm(millimetre) , thus the angle of the wedge θ is

$$\theta = \tan^{-1}\left(\frac{12}{n \cdot 1.2}\right) = 13^o \tag{4.43}$$

Here it is important to clarify that the calculation is based on a nominal value at an ultimate tensile strength of $300\ lbf.in^{-2}$ $(Pounds\ per\ square\ inch)$. Considering the ratio between the specimen and the density of the fringe, which is created by the wedge, high density fringes can be obtained by improving contrast in the experiment. Furthermore, the high frequency fringe will bring higher precision for results analysis than the results of low frequency fringe. To achieve this performance, the use of two wedges of the same size is recommended, and the two wedges are placed together back-to-back. The θ of the wedge shows in Fig.4.5 become doubled, which is 26^o.

Experiment Configuration

The phase retardation is caused by moving the wedge to simulate the fringe shifting. The configuration of the system can be shown in Fig.4.6.

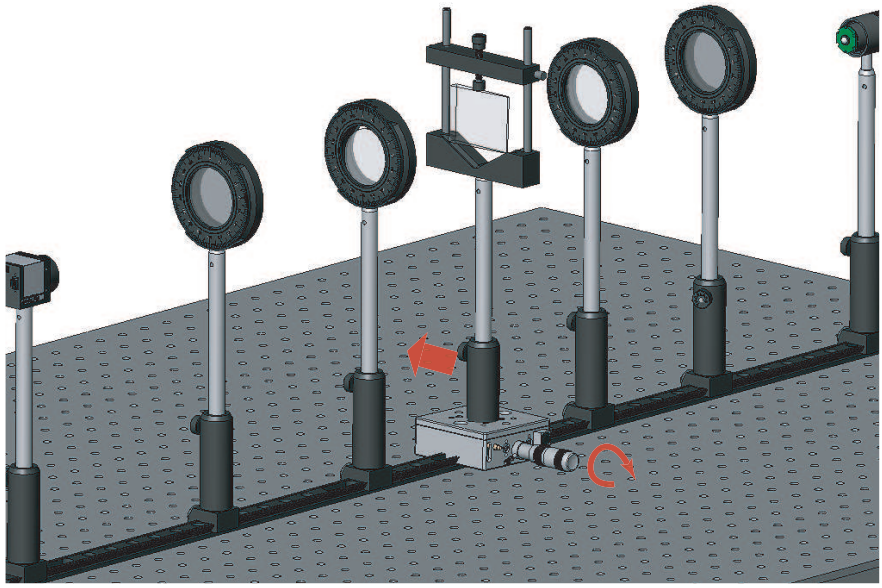

Figure 4.6 Diagram of set up.

The wedge is placed on a nano-positioning stage, and the moving direction is cross the light beam axis with no displacement in the vertical direction. The data are collected at the movement of each $\pi/2$ phase retardation; to guarantee that the movement is accurate, a 10 μm increment is used for each shifting, and then $0, \pi/2, \pi$ and $3\pi/2$ angles are selected from the data.

With our measurement, the period of the fringes is 72 pixels, and each 10 μm moving will bring 3 μm of shift. Thus, the images can be chosen when the fringe at the replacing 0, 60, 120 and 180 μm place. The phase shifting of the fringe moves $0, \pi/2, \pi$ and $3\pi/2$ correspondingly. The results are shown in Fig.4.7.

The movement uses a nano-positioning stage to calibrate the scale in nanometers. Therefore, the phase shifting changes with the constant value in the experiment as we designed. In our case, we designed $\pi/2$ phase shifting for each movement of the wedge. The results are shown in Fig.4.8,

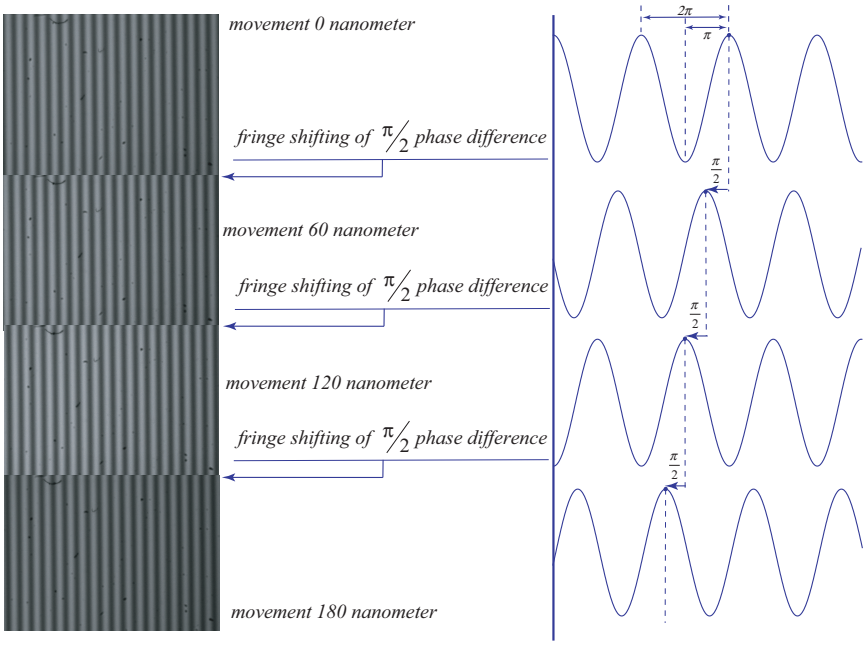

Figure 4.7 Phase difference and Fringe Shifting by Wedge Movement.

As a bench mark, these results will be compared with the phase measurement obtained by the phase stepping method to calibrate the polariscope system step. To avoid introducing further uncertainty error, $Asundi's$ algorithm is tested with only the analyser being rotated. This test had been performed with the test above in one experiment. The configuration did not change and it will reduce some error, such as differences of intensity, camera position and etc. By rotating the analyser, the four images with the same phase changes are shown in Fig.4.9.

The experimental results are shown below in Fig.4.8and Fig.4.10, which can be compared with the wedge movement results.

Fig.4.11 shows the comparison of gradient of the wrapped and unwrapped maps by the wedge rotation method and phase stepping method.

From the wrapped map result shown on the left hand-side, the difference in shifting between the red line and blue line, which represents calibration phase shifting and phase stepping in the experiment respectively, are quite small. Measuring from the pixel axis, the shifting difference Δp is 2 pixels, and as we know the periodic P is 72 pixels. Thus uncertainty error (accuracy) can be defined to be $\Delta p/P = 0.027 \approx 0.03$. From the unwrapped result shown on the right hand-side,

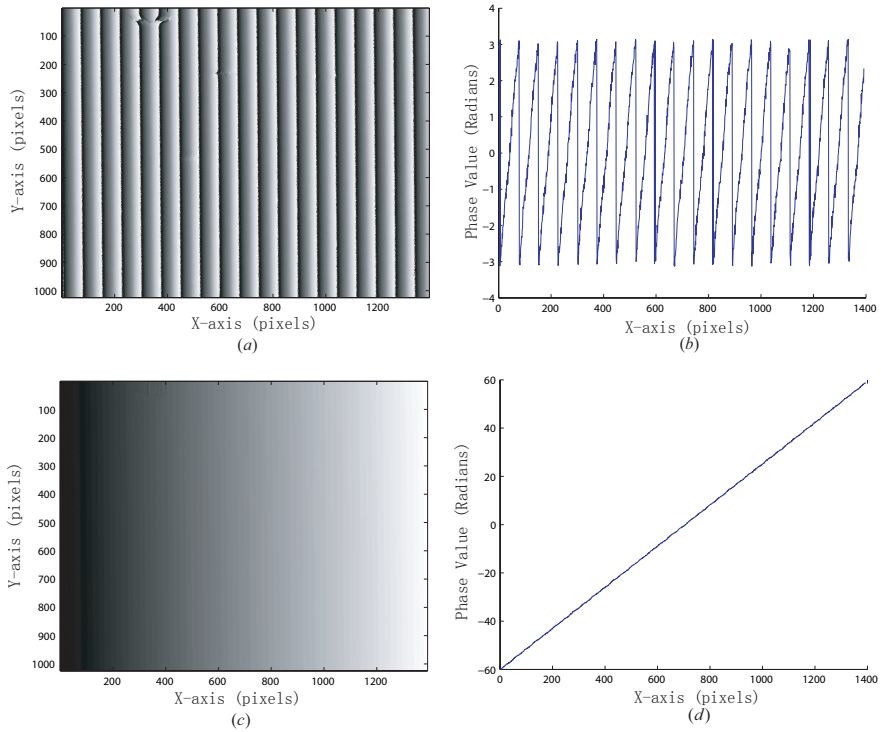

Figure 4.8 Phase Wrapped Map and Unwrapped Map with their gradient by Wedge Movement Calibration (a) wrapped map (b)gradient of wrapped map (c)Unwrapped map (d)gradient of unwrapped map.

the gradient is a good fit to the two lines.

We can see there is little difference between results shown in Fig.4.12 (a) and (b), although they all have some error occurs at the bottom of the wedge. . From (c), there is basically no difference between (a) and (b), except that some noise error in a special place, and the top view (d) shows that only the bottom of map is different, and other place are the same value. The error might be due to some noise or impurity at the edge of the interface. Thus, the system accuracy is sufficiently high for future experiments.

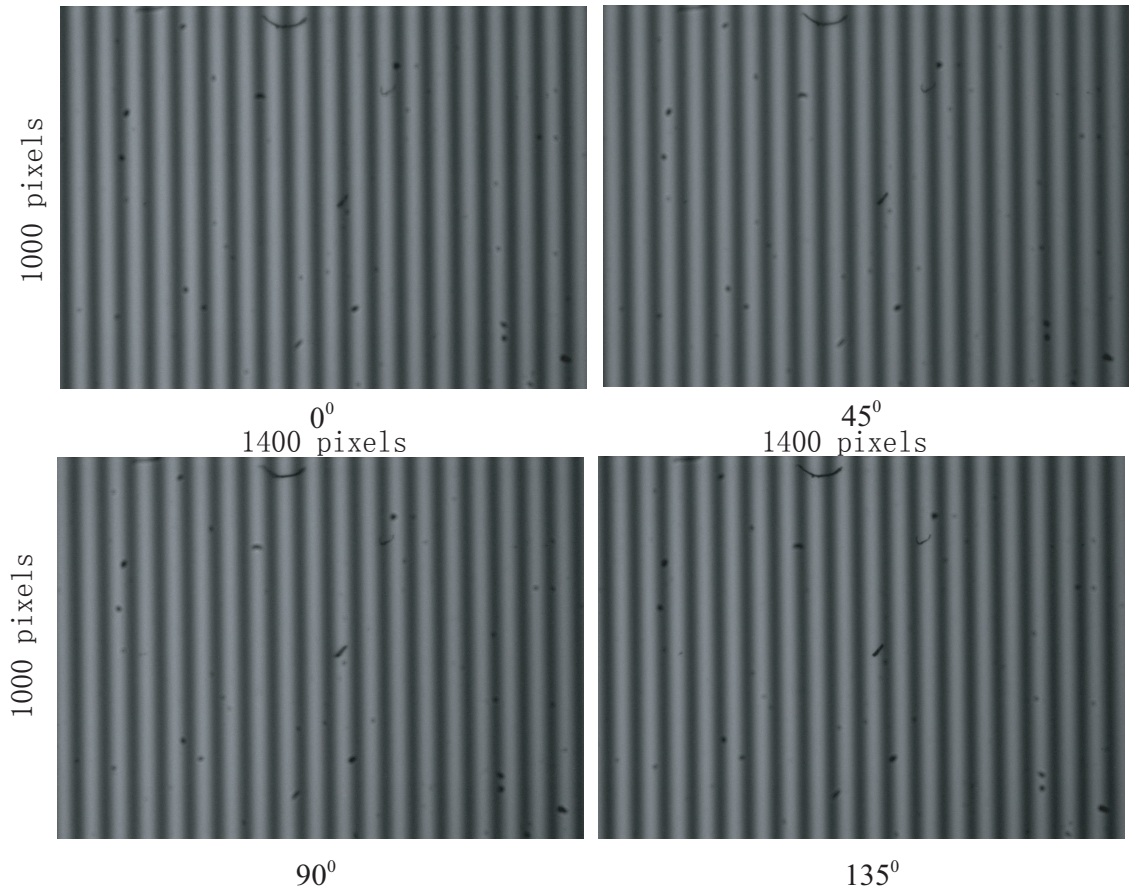

Figure 4.9 Phase difference and Fringe Shifting by Wedge Rotation.

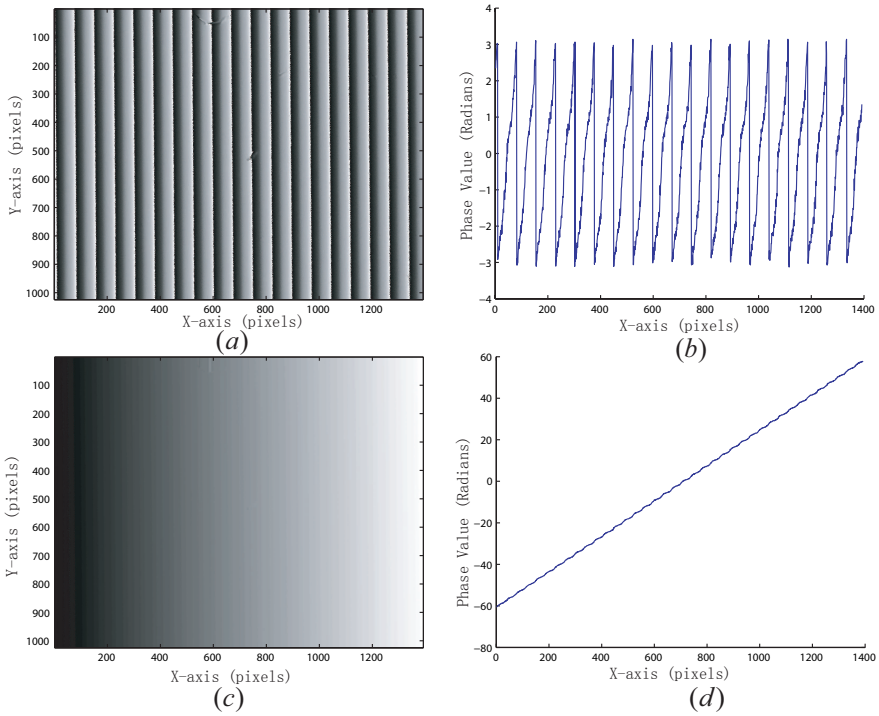

Figure 4.10 Phase Wrapped Map and Unwrapped Map with their gradient by phase stepping method (a) wrapped map (b)gradient of wrapped map (c)Unwrapped map (d)gradient of unwrapped map.

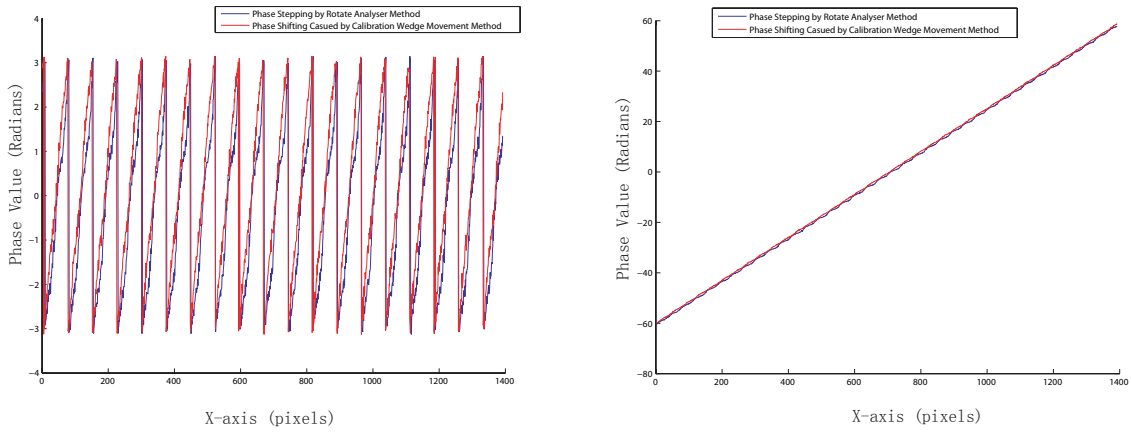

Figure 4.11 Comparison of gradient by Wedge Rotation method and phase stepping method.

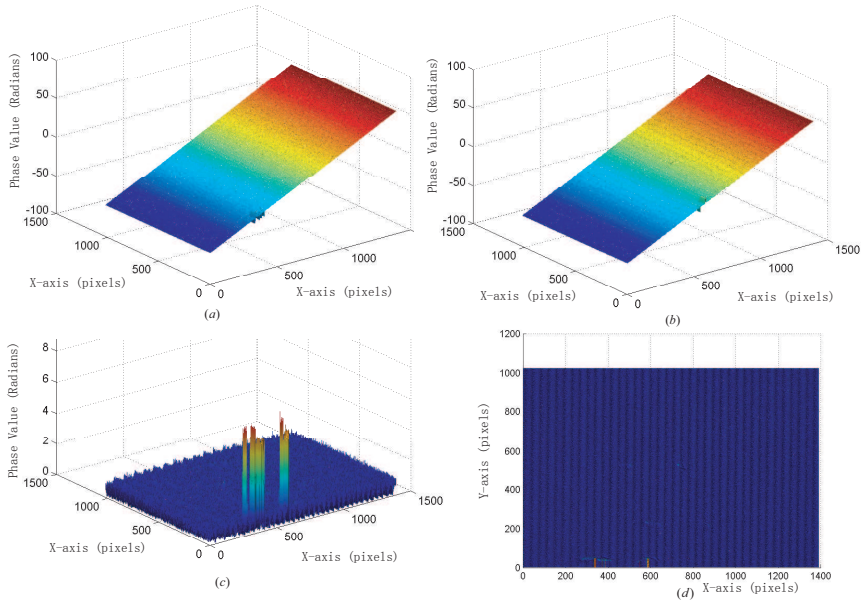

Figure 4.12 Phase unwrapped map and unwrapped map difference (a)wedge calibration phase unwrapped map (b)analyser rotation phase unwrapped map (c) the difference between the two maps (d)top view of (c).

Accuracy Between 4-step and 6-step Phase-Stepping Measurement

Traditionally, both isoclinic and isochromatic fringe patterns can be measured by the different algorithms that we indicated in above sections. They may bring more errors or be very time consuming. *Patterson and Wang* and *Asundi's* algorithms were used in this comparative study. Theory and calculation have been deduced as in the previous sections.

To verify the theory, a quartz wedge was introduced as a ruler because its phase map and direction distribution was calibrated and marked. A polariscope with four separated elements is set up, which means each of them can be rotated independently. A *CCD* camera was fitted with a monochromatic filter whose filtering characteristics were centered at 530 nm. The phase shifting measurement with its polariscope setting as described in *Asundi*, *Patterson and Wang's* and their six to four step algorithms have been discussed previously.

Quartz is birefringent and so perpendicular components of linearly polarized light travel at different speeds through the material, emerging with a phase difference that depends on the thickness of the material and the wavelength of the light. In general, the light emerges elliptically polarized.

The quartz wedge is cut so that it varies in thickness from about 0.01 mm to about 0.08 mm and covers several orders of retardation colours. The quartz optical axis oriented parallel or perpendicular to the edge of the birefringent crystal cut quartz crystal block design. Orthogonal polarizations between the fast and slow waves traverse the wedge surface along the optical path difference, and are a continuously variable function of the thickness of the wedge-shaped bevel.

Michael Levy produced a color chart which plots the thickness of an isotropic specimen, its birefringence and its retardation in nanometers. Once two of these variables is known, the third can be easily determined.

The resulting wrapped phase and direction maps are shown in Fig.4.13 for three approaches and show good quality agreements [38].

The three results were quantitatively compared along the horizontal central lines

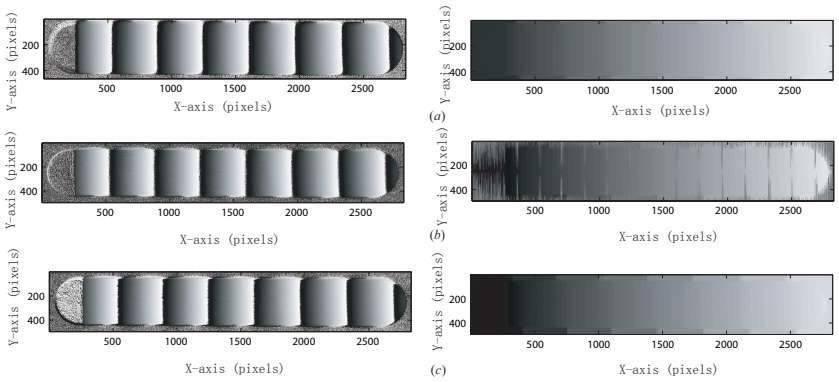

Figure 4.13 Wrapped phase map (left hand-side) and unwrapped phase map (right hand-side) of the calibration wedge (a)by $Asundi's$ algorithm (b)by $Patterson$ and $Wang's$ algorithm (four steps)(c)by $Patterson$ and $Wang's$ algorithm (six steps).

as show in Fig.4.14.

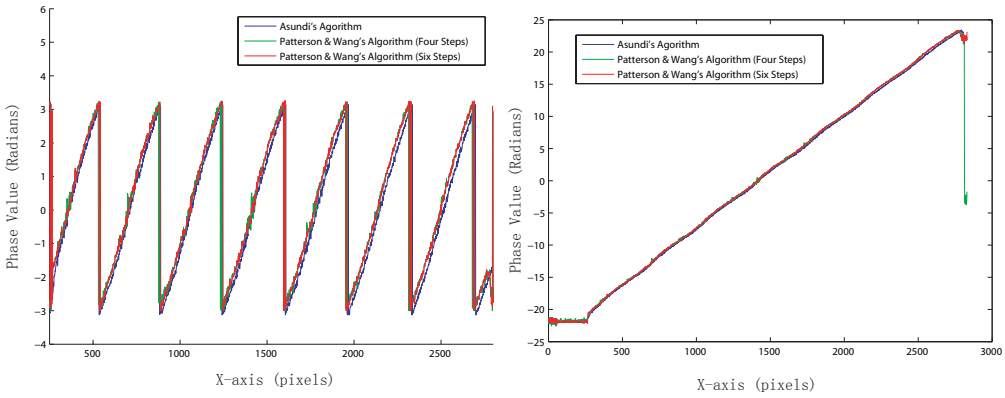

Figure 4.14 Comparison between $Asundi's$ algorithm and $Patterson$ and $Wang's$ (four and six steps) algorithm (a)Phase distribution along horizontal diameter on wrapped maps(b)Phase distribution along horizontal diameter on unwrapped maps.

The blue line is the value of $Asundi's$ algorithm, and the green and red lines are $Patterson$ and $Wang's$ algorithm with four and six steps, respectively. From these values was obvious that all three results are nearly a perfect match. Except that the green line value shows noise at some places, all three methods are acceptable, considering the time consumed and the computational complexity, the prioritization order can be defined to be: $blue > green > red$.

The three dimensional data comparison with the unwrapped maps was performed and is shown in Fig.4.15 as below,

It is clear that there is a noise appearance in the phase map result of *Patterson and Wang's* four-step algorithm. The *Patterson and Wang's* six-step algorithm

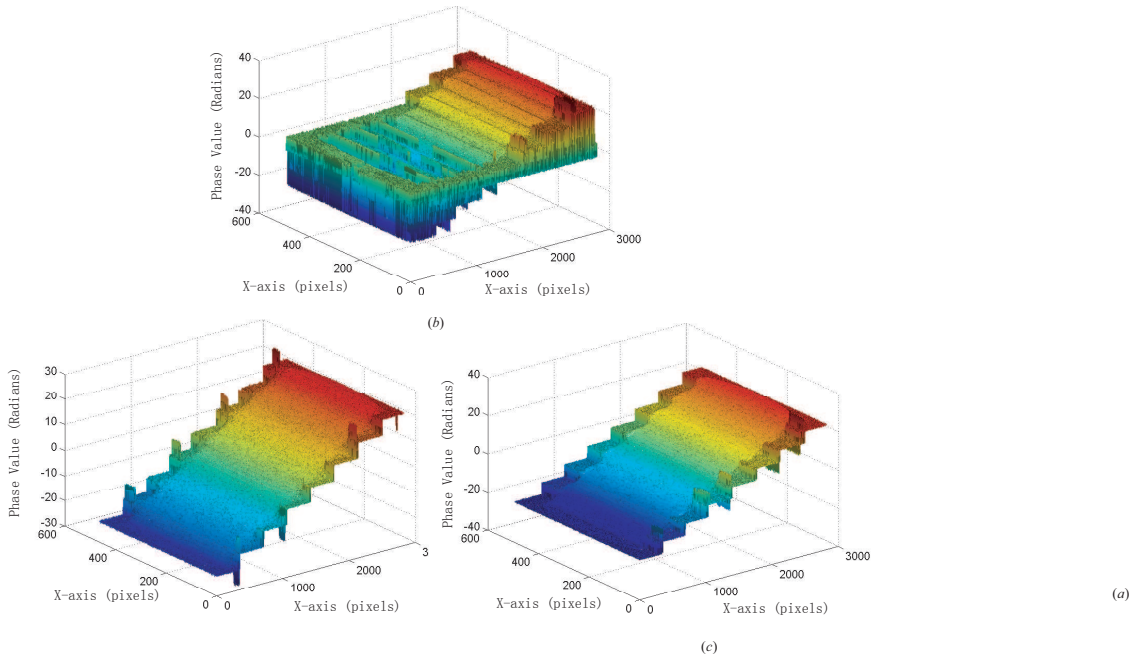

Figure 4.15 Comparison between $Asundi's$ algorithm and $Patterson$ and $Wang's$ (four and six steps) algorithm (a)Phase distribution by $Asundi's$ algorithm (b)Phase distribution $Patterson$ and $Wang's$ four steps algorithm (c)Phase distribution $Patterson$ and $Wang's$ six steps algorithm.

and *Asundi's* algorithm results are acceptable. Considering the time consumption of code running and computational complexity, the prioritization order can be re-defined as: $blue \approx red > green$.

It further follows that the comparison is refined to be between *Asundi's* algorithm and *Patterson and Wang's* six-step algorithm. The Fig.4.16 shows the difference between these two methods,

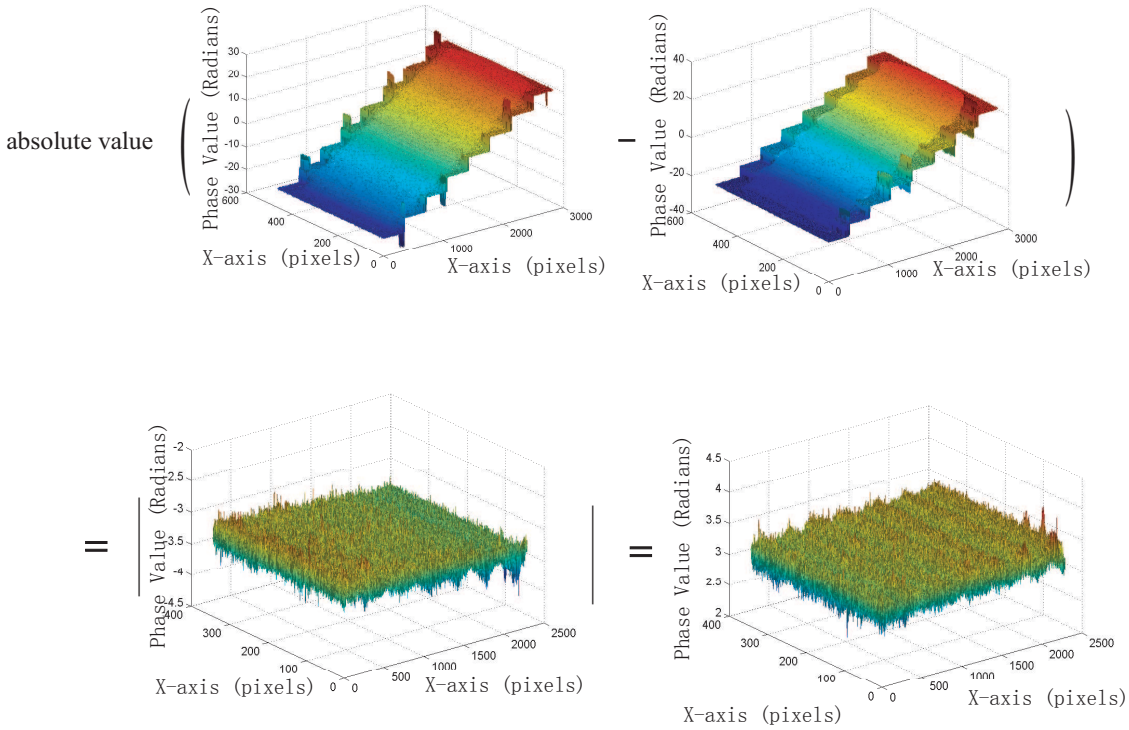

Figure 4.16 Comparison between $Asundi's$ algorithm and $Patterson$ and $Wang's$ six steps algorithm.

From the details of value difference and the parameter of the quartz wedge, the six steps method wins with a slight advantage in the results with less noise and more accuracy in measurement. The experiments and data analysis we have done proves that both four-step and six-step phase stepping methods could be used in the application. In order to simplify operations in experiments, we used the four-step phase stepping method. Moreover, not every polariscope supports polarised filter and quarter-wave plate can be rotated independently, then the *Asundi's* four-phase step method is only the only method to be recommended. Meanwhile, we need consider the computer calculation of algorithm less time consuming with less phase steps changing.

However, the isoclinic angle is undefined by the six-step algorithm when $\delta = 0, \pi, 2\pi, ...$, which means $I_3 = I_4 = I_5 = I_6$. The values of both isoclinic and the isochromatic are unreliable from calculation [38]. Moreover, since θ is in the range $(-\pi/4, \pi/4)$ in which the inverse arctangent function is used, at points where the true value of θ exceed the range, ambiguity and error results need to be compensated.

Conclusion

In this section, different phase stepping algorithms were discussed and compared. We conclude either four or six steps methods are appropriate for use. Although, accuracy is the most important factor, cost and time must be considered as well. Thus, each algorithm has its advantages, and the error occurs in the acceptable range for each. The significance of this experiment and calculation is not only to calibrate our working platform system, which will ensure that the data we obtained in future applications is correct, but also provides some alternative phase-shifting technique to carry out phase measurement taking account of quality and intergraded error analysis. The accuracy analysis includes theoretic mathematic computation and experiment data analysis. Both aspects are combined in a refined data analysis method, which can be widely used in laboratories.

4.3 Fourier Transform Approach to Phase Measurement

4.3.1 Summary and Review

This section describes the phase-encoded intensity distribution obtained with the digital Fourier transform method. This is used not only to present a method for phase measurement, but also to analyse the accuracy. Interferometric fringe information is added to form a phase map, which could be calculated by the Fast Fourier Transform (FFT) algorithm. The results will be processed in to a continuous full fringe field using phase unwrapping. The technique needs only one set of image data, is quite efficient, and is easy to perform, when compared with the phase stepping method. Its purpose is to be implemented as the reflection system in cornea measurement.

This part of the thesis will present a theoretical analysis of the carrier fringe technique. It is based on creating a high density linear phase carrier and works well for complex fringe processing. This technology has developed rapidly in the last three decades [56] [57]. In phase measurement of fringe fields, carrier fringe technology has also been developed. *Reynolds* [58] reports holographic fringe linearisation interferometry for defect measurement. *Plotkowski* (1985)[59]proposed to improved fringe carrier techniques for unambiguous determination of holographically recorded displacement. *Mattys* (1988)[60] used carrier fringe technique for automatic analysis of surface displacement. $Long$ described cylindrical fringe carrier techniques in interferometry. *Peter Bryanston-Cross* (1993)[55] presented the holographic measurement of deformation using the carrier fringe and FFT techniques. This FFT method provides an efficient manner of analysing fringes.

The carrier fringe method operates on a single fringe pattern produced using monochromatic illumination. After a set of forward and inverse Fourier transform function calculations, the method yields the retardation phase map.

It combines the Fourier transform method and the phase shifting method [55] [61]. The Fourier transform method is more advantageous for using only one image to perform analysis, which is suitable for time-dependent field measurement

and analysis.

In the processing of the FFT method, the phase distribution is wrapped into the range $-\pi$ to π, which has discontinuities with a 2π phase jump for variations more than 2π. Phase unwrapping full field phase, which produce a continues phase distribution can be related to detect parameter encoded with the intensity distribution.

4.3.2 General Theory for Fourier Transform Fringe Analysis

The normal interferograms of a fringe pattern is analysed by the Fourier transform method. The phase function must be a slowly varying function compared to the variation introduced by the carrier frequency. The irradiance distribution in a general interferogram can be written as

$$g(x,y) = g_0(x,y)[1 + v(x,y)\cos\phi(x,y)] + n(x,y) \tag{4.44}$$

where $g(x,y)$ is the measured intensity distribution, and $g_0(x,y)$ and $v(x,y)$ are background illumination and fringe contrast, respectively. $n(x,y)$ is the noise distribution introduced. $\phi(x,y)$ is the phase of the object wavefront.

For example, a sample of phase values of carriers is shown in Fig.4.17.

For the purpose of Fourier fringe analysis, after adding the linear carrier fringes to the fringe field, the input fringe pattern can be written as,

$$g(x,y) = g_0(x,y)[1 + v(x,y)\cos(\phi(x,y) + \phi_0(x,y))] + n(x,y) \tag{4.45}$$

where $\phi_0(x,y)$ is the phase value due to the carrier fringes, which is shown as $\phi_0(x,y) = 2\pi f_0 x$, where f_0 is the spatial carrier frequency. The spatial carrier frequency is modulated by the object phase $\phi(x,y)$, so that the interference fringes become closely spaced and nearly linear.

The input fringe pattern is then written as,

$$g(x,y) = g_0(x,y) + c(x,y)e^{2\pi j f_0 x} + c^*(x,y)e^{-2\pi j f_0 x} \tag{4.46}$$

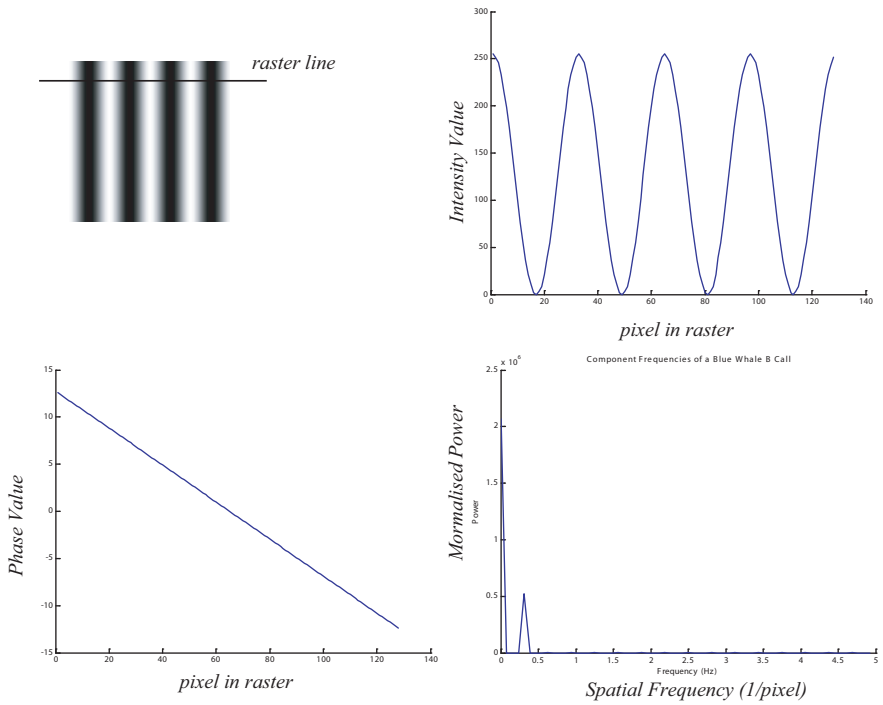

Figure 4.17 Fringe sample, linear phase value of the carrier, intensity distribution of the linear carrier fringes and Spectrum of the linear carrier fringes.

where $c(x,y) = (1/2)v(x,y)e^{j\phi(x,y)}$ and $*$ denotes a complex conjugate. By applying the inverse Fourier transform, we can obtain the phase map. The phase distribution can be calculated by,

$$\phi(x,y) = \tan^{-1}\frac{\mathrm{Im}[c(x,y)]}{\mathrm{Re}[c(x,y)]} \tag{4.47}$$

where $\mathrm{Im}[c(x,y)]$ and $\mathrm{Re}[c(x,y)]$ denote the imaginary and real parts of $c(x,y)$ respectively.

The phase value between the adjacent pixels must be less than π; because of the discontinuous form of the arctangent function, the phase distribution should be wrapped into the range of 0 to 2π. If the sampling rate of the interference pattern is f, the condition for phase difference is,

$$\max|grad\Delta(\phi+\phi_0)| < \pi f \tag{4.48}$$

where ϕ_0 is the carrier fringe phase value, which equals $2\pi f_0 x$.

From the equation above, the conditions for limitation of the allowable gradients of the object phase using the spatial carrier frequency can be given by,

$$\Delta\phi_{\max} < \pi - \pi f_0/f \tag{4.49}$$

and

$$\Delta\phi_{\min} < -2\pi f_0/f \tag{4.50}$$

They show the maximum and minimum gradients of the phase, which depend on the ratio of the spatial carrier frequency and the sampling rate. The difference between the maximum and minimum gradient is always π. The unwrapped phase map could be obtained by using the phase unwrapping procedure. If the carrier frequency is over a certain limit, the unwrapped phase map can not be recovered from the Fourier transform; similarly, if the carrier frequency is under a certain limit, the wrapped phase map will have a large error.

The major advantage of this technique is that only one image needs to be analysed for phase information. The carrier fringe technique not only gives the advantages of automatic fringe analysis, but also removes the sign ambiguity of the displacement.

4.3.3 Fringe-Carrier with Polariscope

The fringes are generated by a carrier inserting a crystalline quartz wedge or a temporary birefringent frozen wedge. The set up is shown in Fig.4.18:

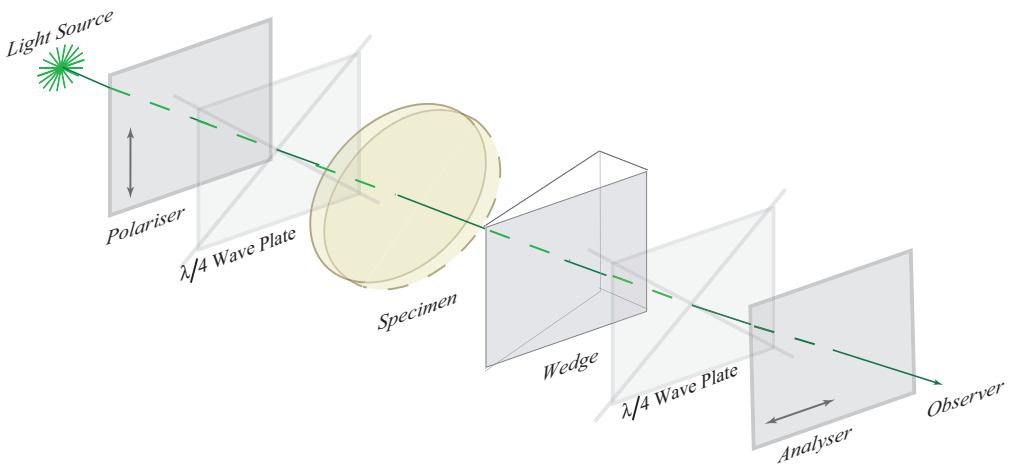

Figure 4.18 Experimental set up using polariscope with birefringent wedge.

The configuration is quite similar to that described previously, in which a light beam comes out from a light source and passes through a linear polariser, whose optical axis is horizontal. After that, it passes through a quarter-wave plate, whose fast axis is at an angle of -45^o to the x-axis of the wedge. Then, the specimen is in position with retardation δ. In the next step the light will pass the wedge. Later, the light passes through a quarter wave plate again whose fast axis is at an angle of 45^0 to the x axis.

Regarding the situation as being a standard condition, and using $Jones$ calculus for each component, we have:

the vertical polariser:

$$P_{90} = \begin{bmatrix} 0 \\ 1 \end{bmatrix} \tag{4.51}$$

and two quarter-wave retardation plates:

$$Q_{45} = \frac{i+1}{2} \begin{bmatrix} 1 & i \\ i & 1 \end{bmatrix} \tag{4.52}$$

and

$$Q_{-45} = \frac{i+1}{2} \begin{bmatrix} 1 & -i \\ -i & 1 \end{bmatrix} \tag{4.53}$$

The $Jones$ matrix of the birefringent plate M with retardation δ whose fast axis is at an angle of θ to the x-axis is:

$$M = \begin{bmatrix} e^{i\delta}\cos^2\theta + \sin^2\theta & (e^{i\delta}-1)\sin\theta\cos\theta \\ (e^{i\delta}-1)\sin\theta\cos\theta & e^{i\delta}\sin^2\theta + \cos^2\theta \end{bmatrix} \tag{4.54}$$

The carrier wedge C with retardation δ whose fast axis is along the $x - axis$ is shown

$$C = \begin{bmatrix} e^{i\delta} & 0 \\ 0 & 1 \end{bmatrix} \tag{4.55}$$

The analyser, whose optical axis is horizontal, is

$$P_0 = \begin{bmatrix} 1 & 0 \\ 0 & 0 \end{bmatrix} \tag{4.56}$$

So, the light beam that emerges from the analyser is:

$$a = P_0 Q_{-45} C M Q_{45} P_{90} \tag{4.57}$$

Thus,

$$\begin{aligned} a = & \begin{bmatrix} 1 & 0 \\ 0 & 0 \end{bmatrix} \tfrac{i+1}{2} \begin{bmatrix} 1 & -i \\ -i & 1 \end{bmatrix} \begin{bmatrix} e^{i\delta} & 0 \\ 0 & 1 \end{bmatrix} \\ & \times \begin{bmatrix} e^{i\delta}\cos^2\theta + \sin^2\theta & (e^{i\delta}-1)\sin\theta\cos\theta \\ (e^{i\delta}-1)\sin\theta\cos\theta & e^{i\delta}\sin^2\theta + \cos^2\theta \end{bmatrix} \\ & \times \tfrac{i+1}{2} \begin{bmatrix} 1 & i \\ i & 1 \end{bmatrix} \begin{bmatrix} 0 \\ 1 \end{bmatrix} \end{aligned} \tag{4.58}$$

The intensity of the fringe pattern in the observing plane is given by,

$$I = \sin^2\left(\frac{\delta - \delta_1}{2}\right)\sin^2\theta + \sin^2\left(\frac{\delta + \delta_1}{2}\right)\cos^2\theta \tag{4.59}$$

when θ =0, the fast axis of the model disk is along the x axis, and the equation above can be re-written as,

$$I = \sin^2\left(\frac{\delta + \delta_1}{2}\right) = 1 - \cos(\delta + \delta_1) \tag{4.60}$$

The phase of the stress fringes is modulated by the phase of the carriers, and the complicated phase of stress fringe field can be demodulated using FFT fringe analysis.

Wedge Design

This crystalline quartz wedge designed to generate high frequency. The characteristic of crystalline substances is optically anisotropic, and so the light will be resolved into two rays traveling with different velocities in wedge. The sketch of

the wedge is the same as Fig.4.5. Assuming a section which is parallel to the wedge edge H and perpendicular to the boundary plane L, and which is in the middle part of wedge, its thickness is d, and the relevant phase difference which is introduced in this section is δ, and therefore we have:

$$\delta = \frac{2\pi}{\lambda} d(n_e - n_o) \tag{4.61}$$

and

$$\tan\theta = \frac{f\lambda}{n_e - n_o} \tag{4.62}$$

where f is the carrier frequency (line/millimeter). For crystalline quartz, $n_e =$ 1.5534, and $n_o = 1.5443$. The frequency $f = 3.3$ lines/millimeter, the wavelength $\lambda = 530$ nanometer, and the wedge angle θ is,

$$\theta = \tan^{-1}\frac{f\lambda}{n_e - n_o} = 0.1899 \tag{4.63}$$

thus,

$$\theta = 10.8795^o = 10^o 53' \tag{4.64}$$

The wedge will be put between the two quarter-wave plate in the dark field in the polariscope system. The monochromatic light beam passes through the plane polarised filter to become a linear beam, and then becomes a circular polarised light beam after passing through the quarter wave plate. Then the circularly polarised light is split into two rays along the principal axes of the birefringent wedge. The doubly-refracting wedge will produce an angular phase difference as the two beams travel through the wedge. The phase difference introduced by the wedge, and hence the amount of interference produced, is determined by the angle of the wedge and the refractive index of the material. The second quarter-wave plate restores the polarised light or rotates it through ninety degrees, depending on whether it is positioned parallel or perpendicularly to the first quarter-wave plate. The emerging ordinary and extraordinary rays are combined to produce the interference fringe pattern; the analyser can block or pass the outgoing light according to the desired background.

As example picture of a fringe pattern which is produced by such a wedge is shown in Fig.4.19.

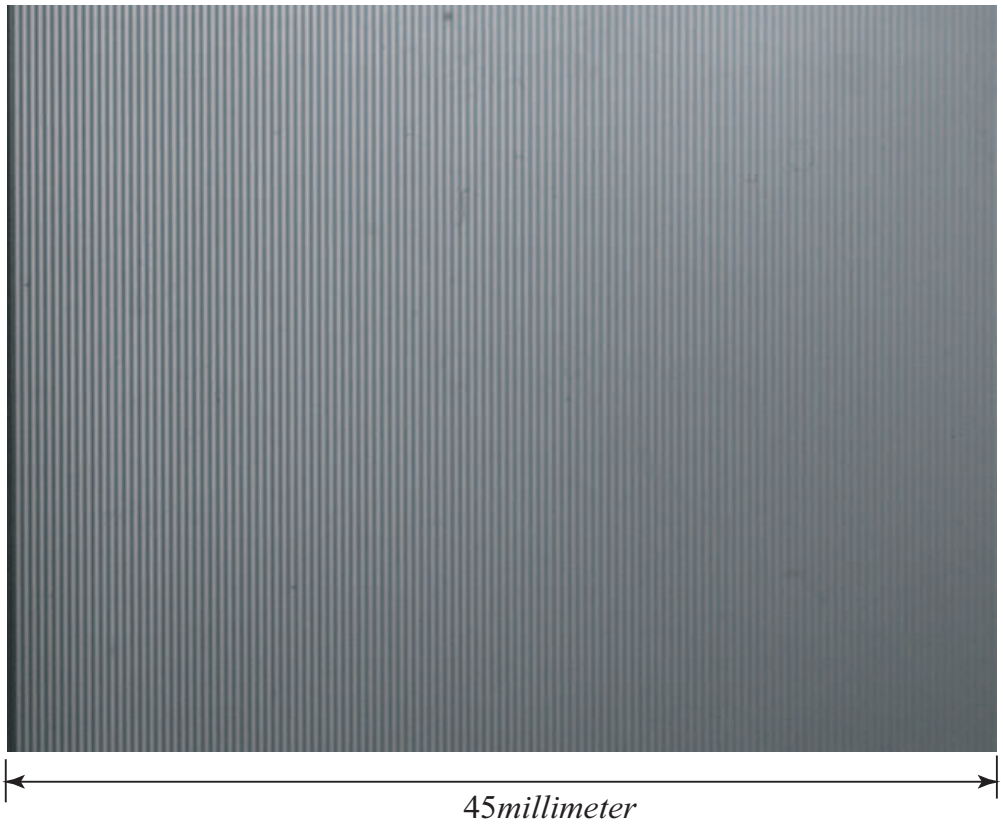

Figure 4.19 Carrier fringe pattern produced by crystalline quartz wedge in polariscope system.

4.3.4 Experiment Data and Discussion

By using the same specimen which is the quartz wedge, FFT method could be compared with the phase stepping method. With monochromatic light, the data is recorded with a CCD camera in a dark field in a polariscope. The resolution is with 1024×768 pixels in the whole field. The raw image is shown in Fig.4.20 and Fig.4.21.

The intensity data of the central raster for the quartz wedge and with the fringe carrier are shown in Fig.4.22. (a) and (b), respectively.

The phase information difference can be gained from using of the FFT. Fig.4.23(a) shows the wrapped phase map of the quartz wedge. Despite the edge-effect and

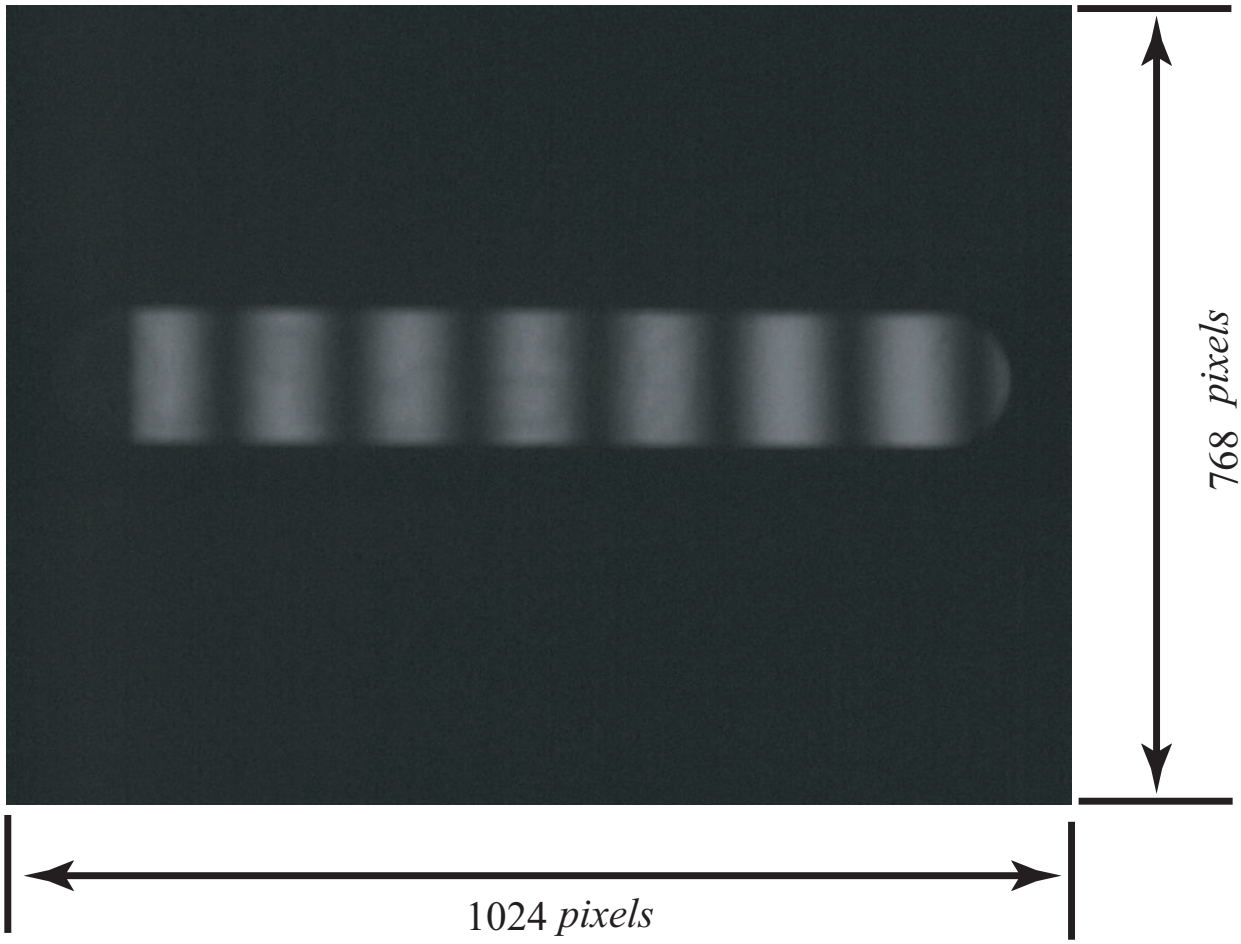

Figure 4.20 Quartz wedge raw image.

the scratched surface of the specimen, the result phase map is smooth as long as phase modulation by the carrier is high.

When the discontinuities occur (because phase modulation by the carrier is small), the unwrapped map will not show a continuous smooth phase map. The 3-D phase distribution of the specimen and the contour map is shown in Fig.4.24.

Compared with the previous wedge which is made with $CT-200$ Epoxy Resin, it contains a low-density fringe. The low carrier frequency causes poor modulation. The image data in Fig.4.25 is recorded and processed as a specimen which is a small round disk with force on top and bottom. It combined with low frequency wedge and high density fringe wedge respectively. The results are compared in Fig.4.25.

In Fig.4.25, (d) is the intensity raw data of the loaded disk with high frequency

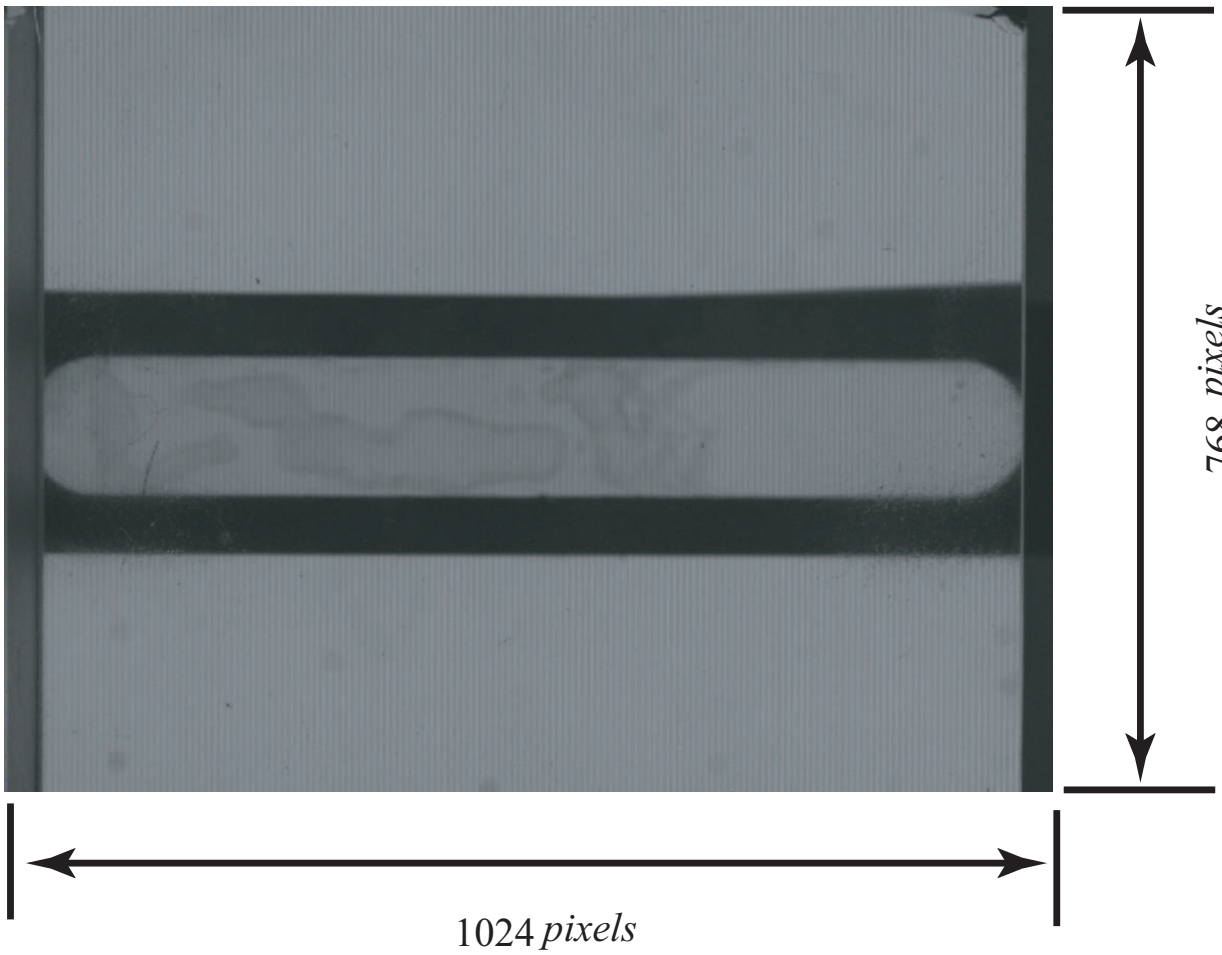

Figure 4.21 Quartz wedge with carrier fringes.

fringe carrier. (e) shows the wrapped phase map of it. Despite the time edge effect and the scratched surface of the circular disk, the resultant phase profile is smooth as long as the phase modulation by the carrier is high. However, discontinuities may occur when the phase modulation by the carrier is small, as shown in top and bottom of the area in (f). For comparison, (a) is the raw data of the loaded circular disk with the frozen wedge which has a low carrier frequency. The carrier frequency is not high enough to separate the side lobe from the centre lob in power spectrum. This will bring large errors in the phase map which we can see (b) and (c) in Fig.4.25. So, a high-frequency fringe carrier will provide more information and more accuracy than use of a low-frequency fringe carrier.

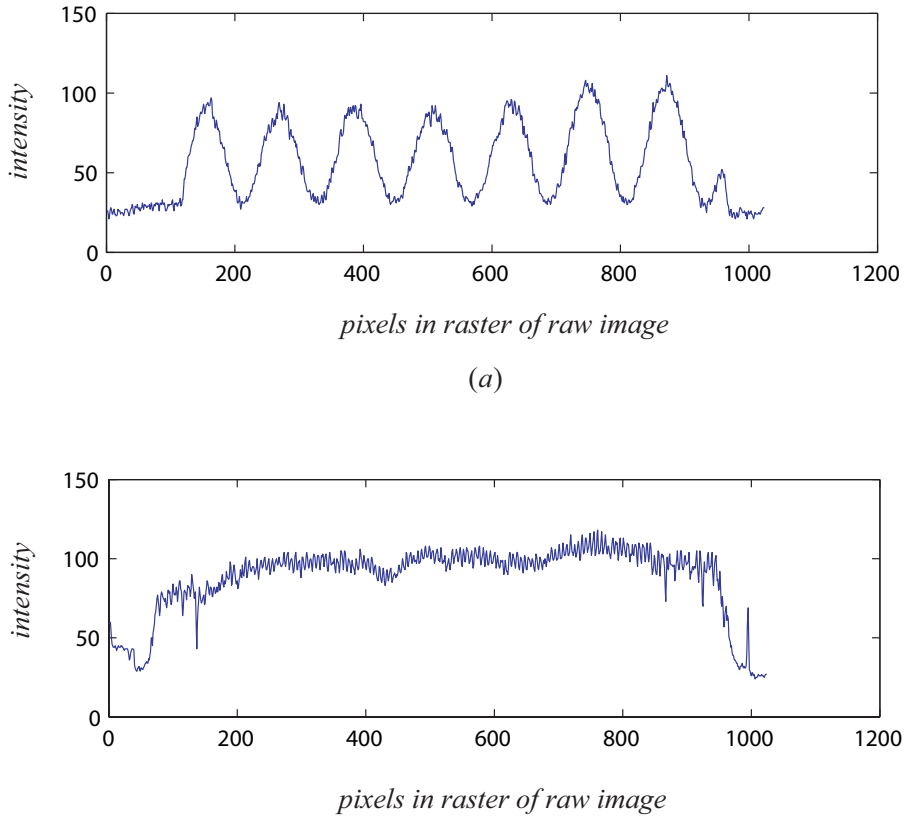

Figure 4.22 Digitised intensity data of central raster with the condition of Fig.4.20 (b)Digital intensity data of central raster with a fringe carrier which likes the condition of Fig.4.21.

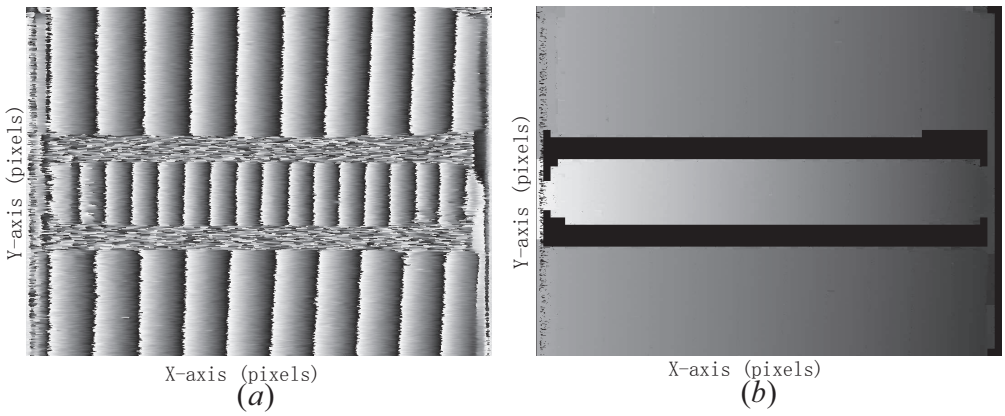

Figure 4.23 (a)wrapped phase map of quartz wedge (b)unwrapped phase map of quartz wedge.

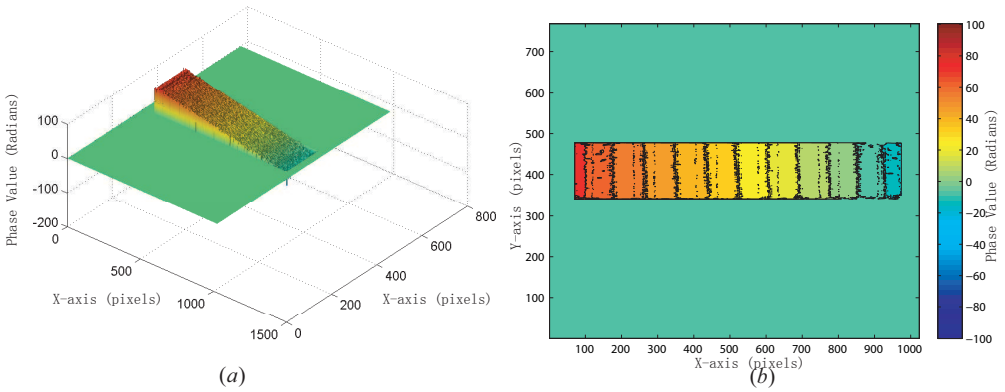

Figure 4.24 (a)3D perspective plot of phase difference for the wedge (b)contour map of quartz wedge.

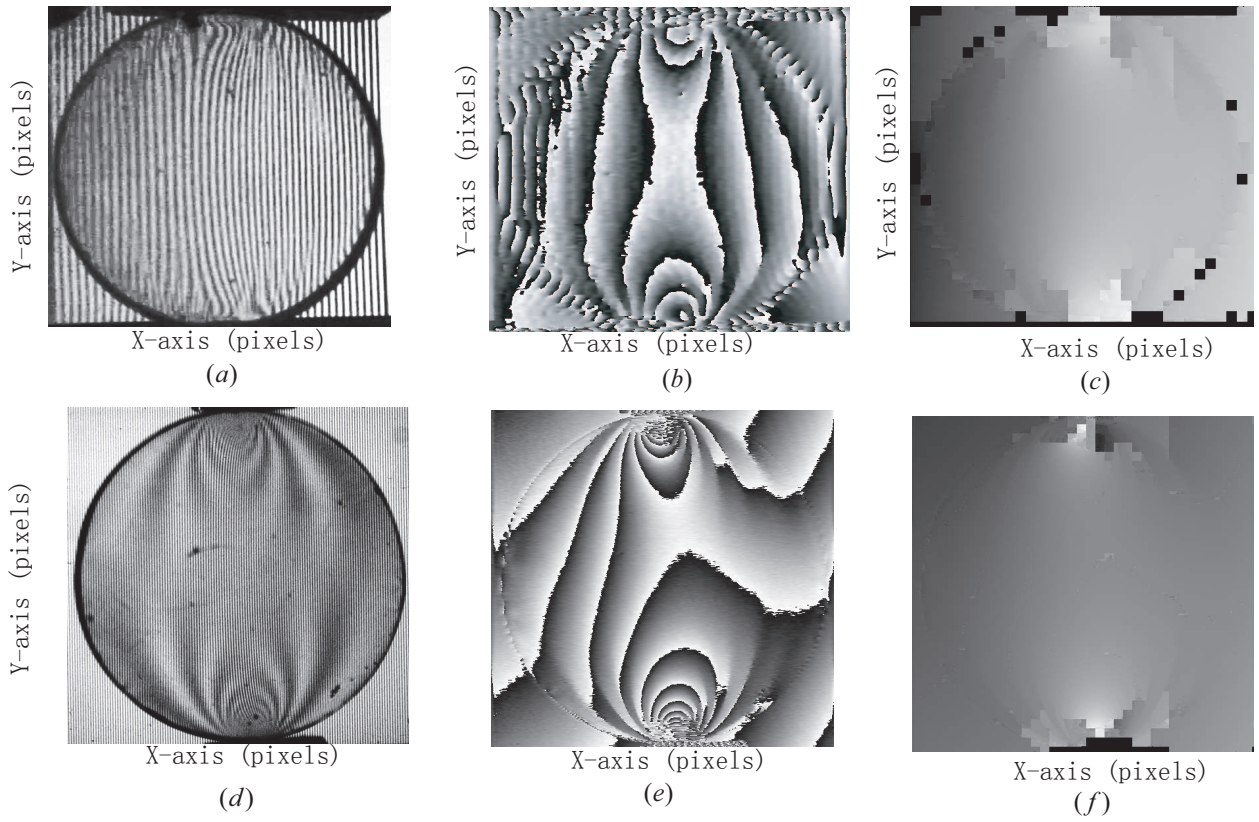

Figure 4.25 (a)raw image of low density fringe with disk; (b)wrapped map of (a); (c) unwrapped map of (a); (d) raw image of high density fringe with disk; (e)wrapped map of (d); (f) unwrapped map of (d).

Comparing the phase stepping method and the Fourier transform method, a ring model is used for measuring. Fig.4.26 shows the wrapped and unwrapped phase map of the ring shape specimen obtained with the phase stepping method. Fig.4.27 shows the contour map of the phase.

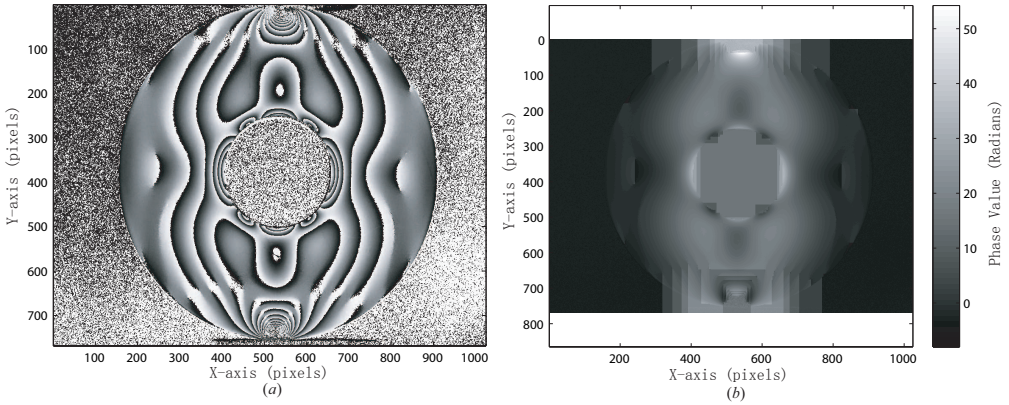

Figure 4.26 Ring shape model phase map solved by phase stepping method(a) wrapped phase map (b) unwrapped phase map.

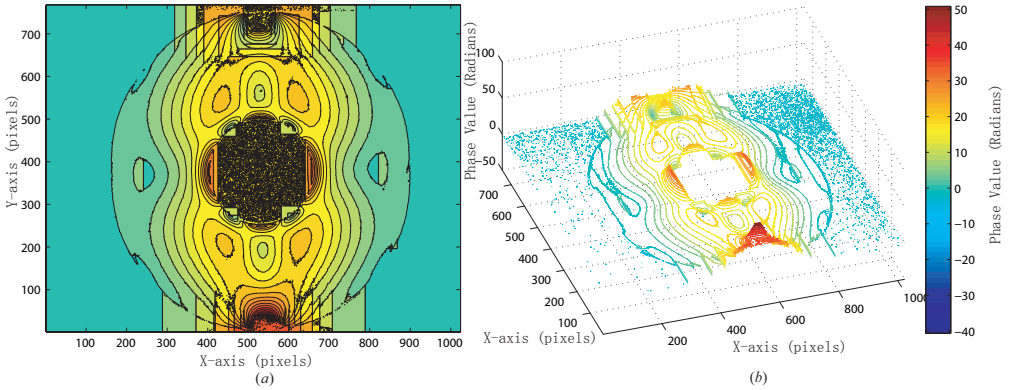

Figure 4.27 Ring shape model contour map (a) normal contour map (b) 3-D contour map.

The FFT method gave the results shown in Fig.4.29.

The phase stepping method shows better results than the FFT method, although the experiment is time consuming.

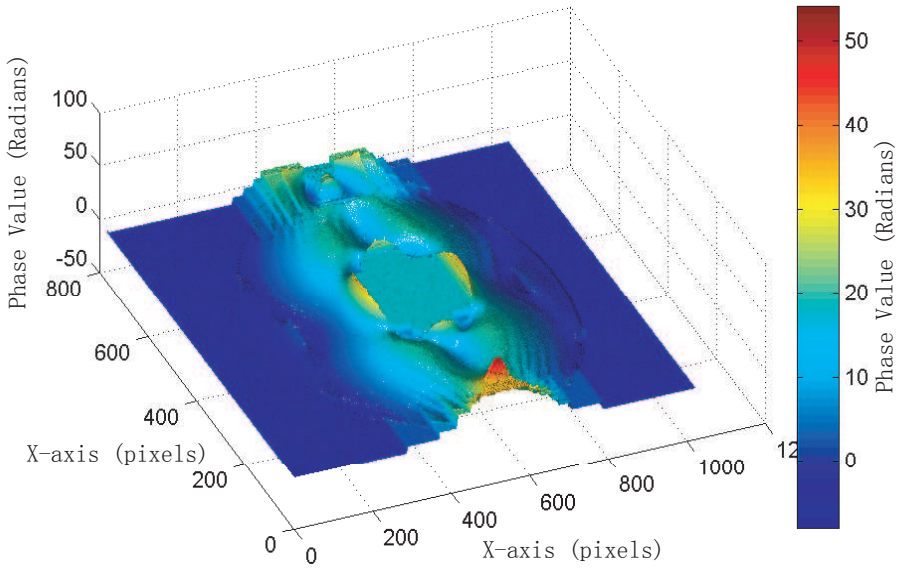

Figure 4.28 3-D plot of the unwrapped phase of the Ring shape model reconstructed from *FFT*.

4.3.5 Accuracy measurement by Novel rotation

High resolution solutions

The phase map and unwrapped map for high resolution data are solved using $Fran$ (*Automatic Fringe Analysis, Written by T. R. Judge, Optical Engineering Laboratory, 1996*) software which performs the FFT automatically. New generations of computers and camera equipment have resulted in software that performs rapid automatic processing and noise removal, but the analysis of the high-resolution image data remains problematical. To achieve more accuracy and to deal with undesired signals, the 2-D FFT algorithm is used in the $Matlab$ programming. Here the high resolution of 3272×2469 image data are used. The raw image is shown in Fig.4.32and Fig.4.33.

The intensity data of the central raster for the quartz wedge and the fringe carrier are shown in Fig.4.34. (a) and (b), respectively.

Fig.4.35 shows the phase wrapped map and the unwrapped map of the wedge.

Information beyond the edge is redundant, and so only the wedge body is shown. This can avoid unnecessary processing.

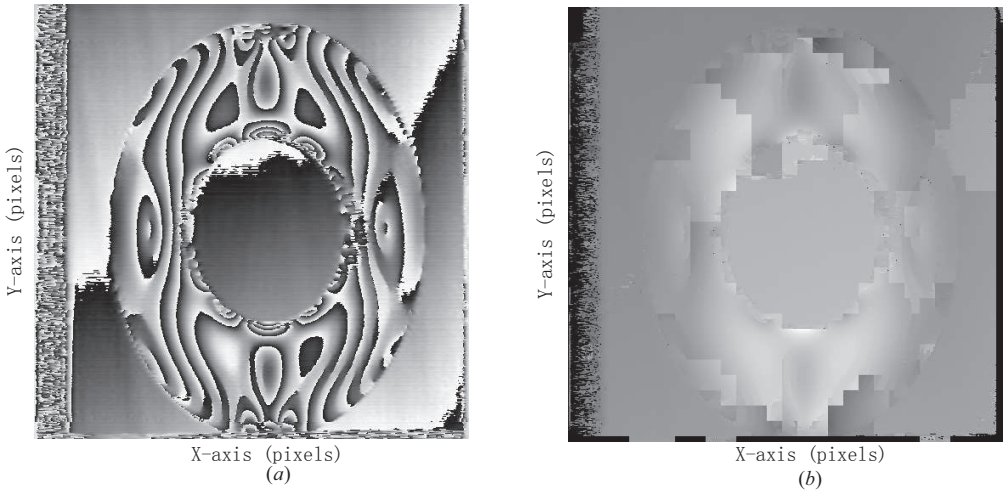

Figure 4.29 Ring shape model phase map solved by FFT method (a)wrapped phase map (b)unwrapped phase map.

The ring model will be discussed in the following section, which will be compared with the phase stepping method.

4.4 Rotation Method for Phase Sensitivity and Accuracy

In this section, the successful quantitative analysis is performed for phase sensitivity, and surface profile of birefringent object is measured. The measurement of phase sensitivity is based on the polarization interferometric approach. By using monochromatic Light-Emitting Diode (LED), a novel polarization interferometric method, incorporating the birefringence technique and wave-plate, is developed. . In experiments, a birefringent wedge is designed for generating fringes as a carrier in the polariscope. Retardation is introduced by a microscope slide with a adhesive tape which covers half the area of the slide in the polariscope system. The retardation was calculated from the phase shift using the phase matching technique. Through such experiments, the calculation of retardation shows that the measurement error is less than 0.02 radians. The major contribution of this section is to determine the accuracy of phase measurement by phase-shifting interferometry for high-precision measurements of the surface profile.

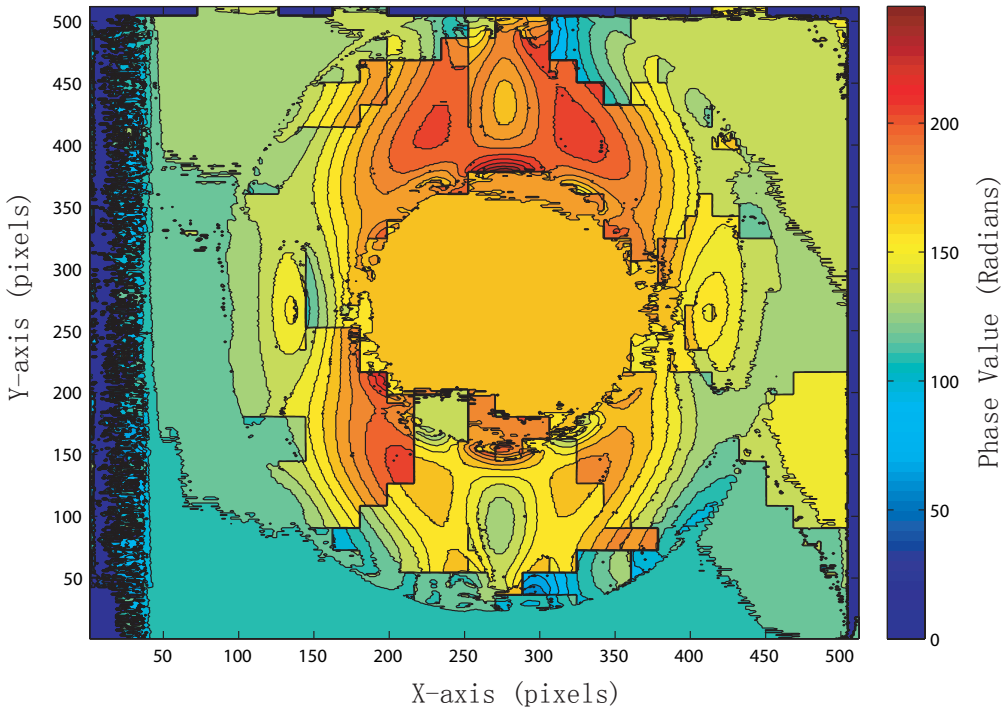

Figure 4.30 Ring shape model contour map.

4.4.1 Introduction

Optical interferometry technology is widely used for precision measurements. A variety of techniques have been proposed to overcome the difficulties arising from the necessity of obtaining maximum fringe division. Different methods and algorithms, such as those based on phase stepping [62] and the Fourier Transform [23] [63], were applied to improve the accuracy of performance. However, a priori knowledge is still required for achieving an accurate measurement system [64].

In our experiments, a birefringent wedge is designed, which generates fringes in polariscope. The position and contrast of the fringes are determined by the polarization of the incident light source. This can be understood with the aid of the 2×2 coherent matrices [65], which represent the correlation between the two orthogonal vibrations. The trace of the matrix is equal to the total intensity of the light. The fringe pattern indicates the phase difference of light traveling in divergent optical paths. As the two light beams in the polariscope can always be treated together, a phase shift in one light beam is introduced as a corresponding phase shifting in the other light beam. The phase shifting method has been applied

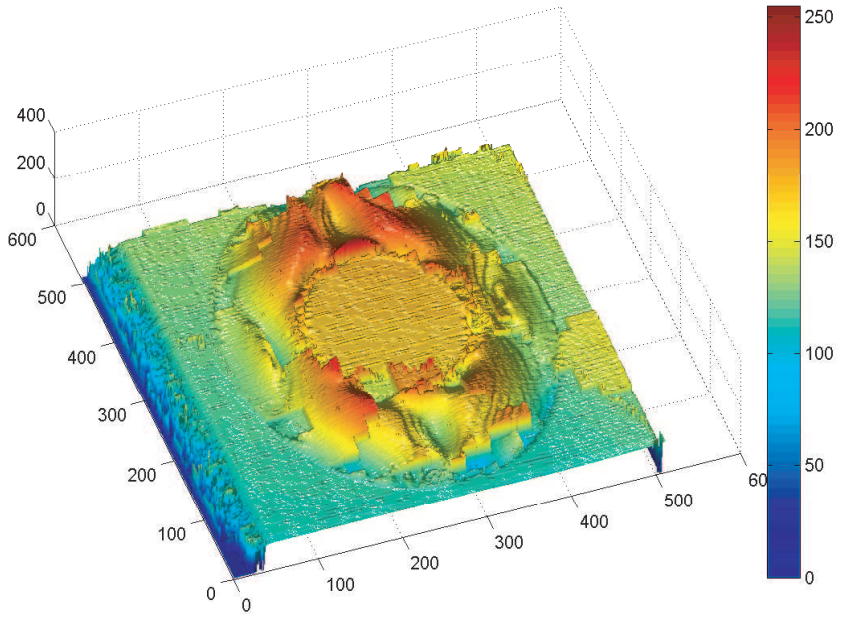

Figure 4.31 Ring shape model 3-D perspective plot of phase distribution on the specimen (FFT).

to many classical interferometric cases , in which the phase difference is changed by altering the optical path length of either one of the two beams. Traditionally, this phase change is achieved by rotating the optical elements in the polariscope, such as the polarising filter and the wave-plate.

In this section, we develop a new approach which uses the fringe carrier and a rotating birefringent medium to perform the measurement of phase shifting [66]. From the measurements of fringe shift, the phase difference, introduced by the wave-plate, can be calculated. A detailed study on the transmitted light intensity reveals the association between the birefringent medium rotation and the phase change.

A high contrast of fringe patterns on the wedge can be obtained, providing that the angle between the optics the axis of the wave-plate and axis of the polarised filter is 45^o. Moreover, the vertical axis of the microscope slide with adhesive tape directly introduces a phase difference of 180^o at its standard position, because of the optical birefringence of the adhesive tape. A measurement is taken at this position to determine the phase retardation, once the microscope slide rotates.

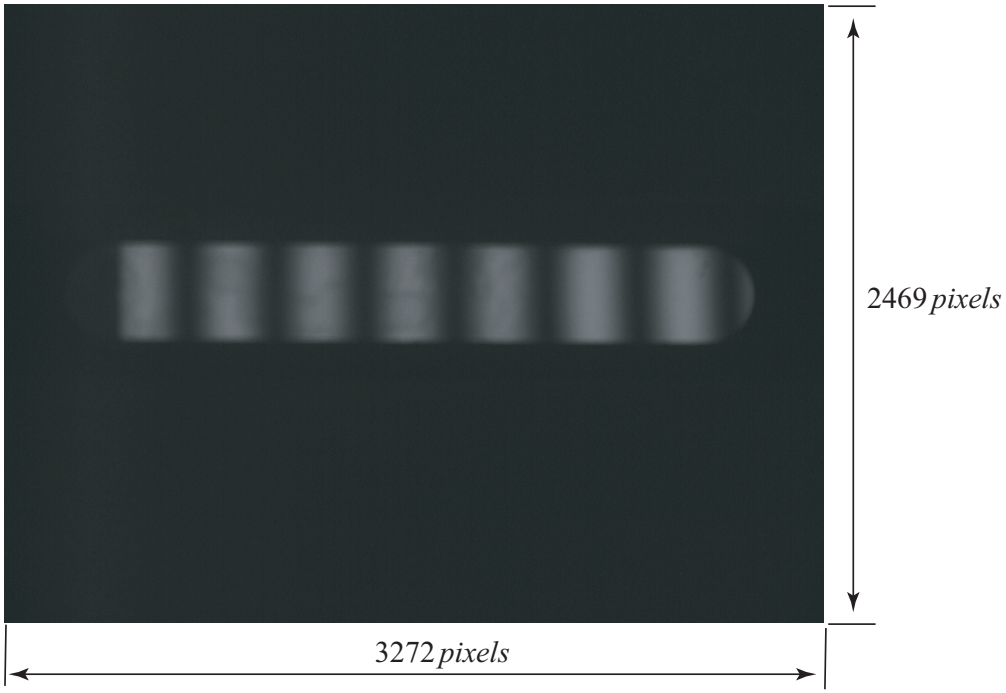

Figure 4.32 Quartz wedge raw image.

The fringe shifts at the different angles of the slide orientation are measured, so as to more accurately determine the retardation.

4.4.2 Technique and Principle

The experiments include four measurements:

- Measurement of the fringe pattern with the crystal wedge in the polariscope system
- Measurement of the fringe pattern with the half-covered wedge
- Measurement of the fringe pattern by rotating the half-covered wedge
- A calibration measurement of the system through the method of optical lever

The measurement of phase retardancy has been introduced previously. The wave-plate was kept with its optic axis at 45^o angle to the input polarized light. A CCD camera was arranged to record the fringe data, and was analysed to measure the fringe shift with accuracy of a fraction of a pixel. A piece of adhesive tape was used as a part of the specimen for covering half of the surface of the microscope

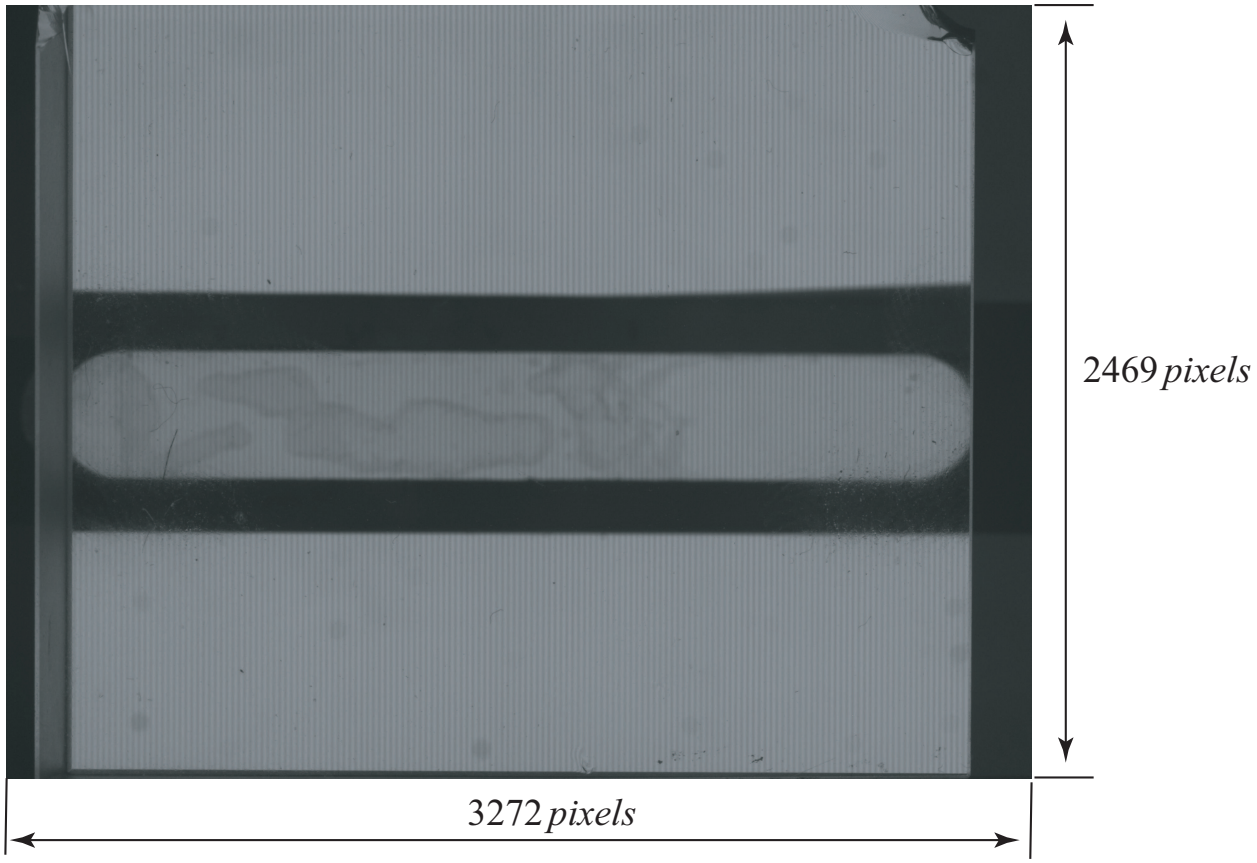

Figure 4.33 Quartz wedge with carrier fringes.

slide, which cause a phase change due to birefringent overlays.

The experimental set up is given in Fig.4.37, which is aligned in such a way so that the fringe patterns are aligned with the row in CCD. Instead of using traditional methods of polariscopic use [67], the polarising filter and wave-plate were mounted on the holder, fixed at certain angles.

On the measurement platform, the microscope slide was mounted on a rotating goniometer to enable the measurement of fringe shifting for different orientations of angle on the measurement platform. The minimum angle of roatation by the scale of goniometer is 1^o. To determine the fringe shifting, the reference position was marked as 0^o. Different frames data are collected and analysed, at 60^o increments of the angle.

As a result, there will be a fringe shift with magnitude dependent on respect to the reference fringe. The fringe shift is different for different positions of the slide

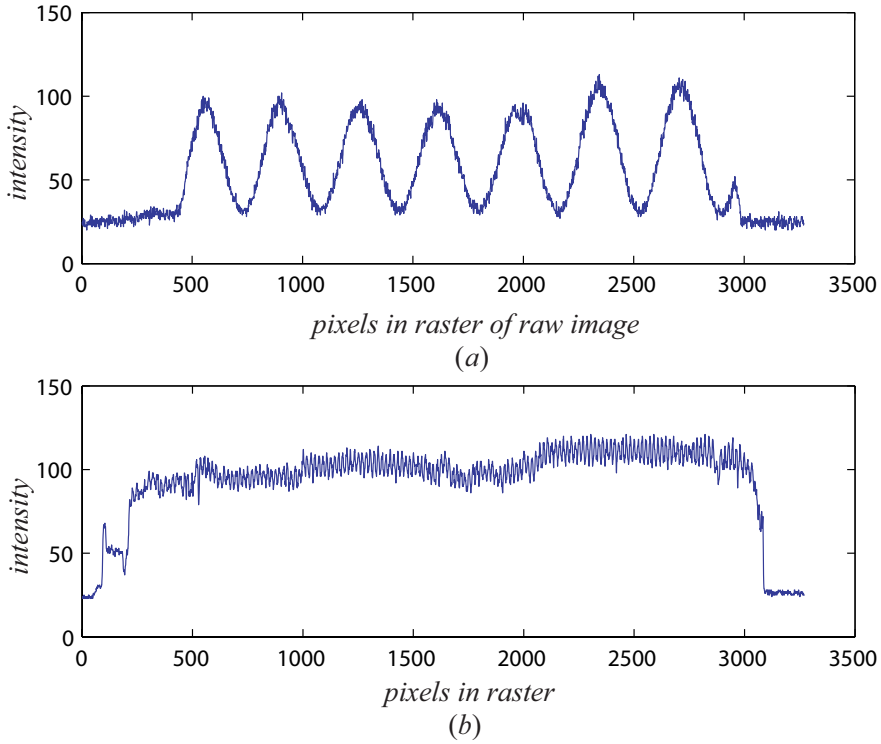

Figure 4.34 Digital intensity data of central raster in a quartz wedge (b)Digital intensity data of central raster in a quartz wedge with fringe carrier.

optic axis. An analytical relation for the fringe shift can be calculated by tracing the position of the fringe via the minimum or maximum angle varieties.

A different operation between the intensity weight on x and y axis $I_o x$ and $I_o y$ results in the following equation

$$I = I_{oy} - I_{ox} = \frac{a^2}{2} \cos \alpha \tag{4.65}$$

This can also be expressed as:

$$I(x, y) = C(x, y, k) + C^*(x, y, k) \tag{4.66}$$

where x and y are the parameters corresponding to spatial coordinates, and k is the parameter corresponding to object load [68]. Thus,

$$C(x, y, k) = \frac{a^2}{4} \left[\cos \alpha \, (x, y, k) + j \sin \alpha \, (x, y, k)\right] \tag{4.67}$$

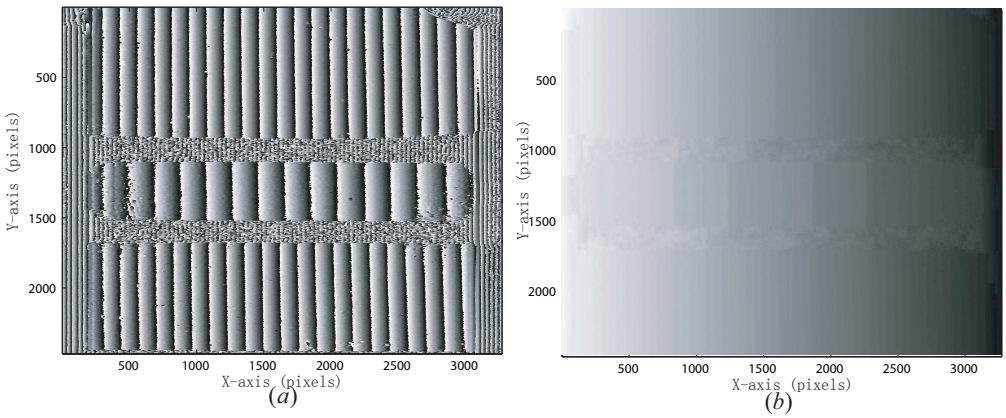

Figure 4.35 (a)Wrapped phase map of quartz wedge (b)Unwrapped phase map of quartz wedge.

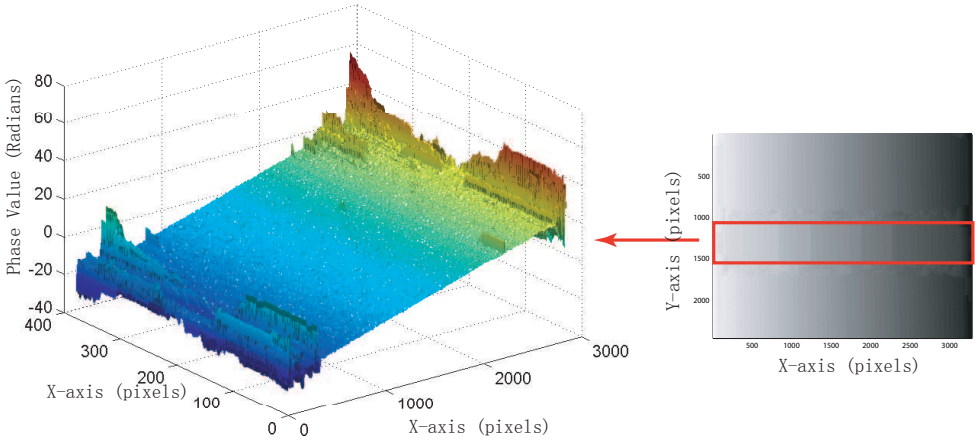

Figure 4.36 3D perspective plot of phase difference for the wedge.

It is possible to use the real and imaginary components of C to compute α using

$$\alpha(x, y, k) = \tan^{-1}\left(\frac{\mathrm{Im}\left[C\left(x, y, k\right)\right]}{\mathrm{Re}\left[C\left(x, y, k\right)\right]}\right) \tag{4.68}$$

where Re denotes the real portion and Im denotes the imaginary portion of C. Based on this procedure, it is possible to derive the phase at any load-related spatial point on the model.

4.4.3 Experimental Demonstration

Phase derivation measurement by using a fringe carrier and accuracy calculation of phase shift

Fringe carrier

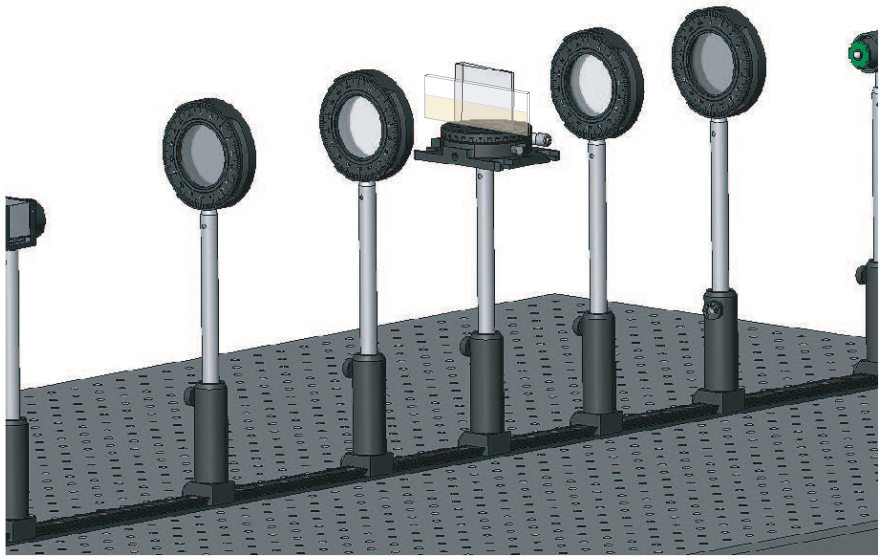

Figure 4.37 Experimental set up.

Based on the previous discussion and equation 4.66, in order to create an extra retardation of $\pi/2$, the wedge must move to another location where the wedge thickness d' such that,

$$\frac{\pi}{2} = \frac{2\pi}{\lambda}\left(d - d'\right)\left(n_e - n_o\right) \tag{4.69}$$

Then, by taking into consideration that θ is the wedge angle, the amount of distance of wedge travel x' in the x direction is,

$$x' = \frac{d - d'}{\tan\theta} = \frac{\lambda}{4\tan\theta\left(n_e - n_o\right)} \tag{4.70}$$

From the simulation used in the calculation of the accuracy in the phase matching technique, it shows an accuracy of 0.01 radian [69].

The accuracy the real experimental cases including noise is investigated by measuring the variation of the fringe width for different wavelengths. Since the source used is monochromatic, the wavelength can be easily changed. Fringes are taken with and without the wave-plate for different wavelengths while keeping the optic axis of the wave-plate fixed. The fringe widths and fringe shifts for different wavelengths are calculated by comparing the frames with and without the wave-plate. The calculated data points using the phase matching algorithm are shown in the

equation below [70],

$$FringeWidth(FW) = \frac{\lambda}{4\left(n_e - n_o\right)\tan\theta} \times pixelsize \tag{4.71}$$

The fringe width is given in term of the number of pixels, as the generated fringe width is fitted with data obtained from using the phase matching algorithm.

Phase Spatial Measurement

The wedge is half covered by a piece of adhesive tape. The image is shown in Fig.4.38.

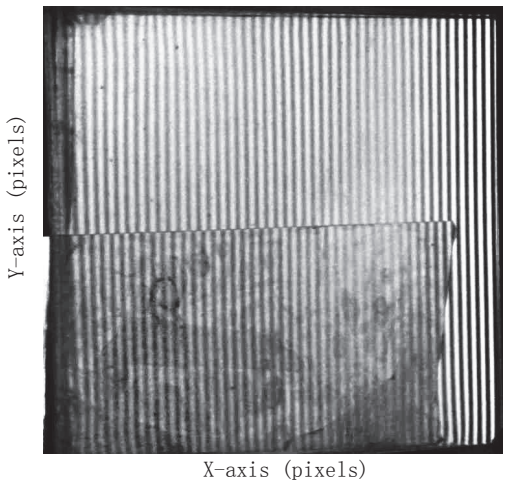

Figure 4.38 Wedge is covered half bottom areas with birefringent overlap.

The wrapped and unwrapped phase map are shown in Fig.4.39.

The overlay caused a virtual displacement ΔL of the wedge. This displacement can be calculated using the equation,

$$\Delta L = nt/(n-1) \tag{4.72}$$

where *n* and *t* are the refractive index and the thickness of the cover layer, respectively [71][72].

The refractive index of adhesive tape gives ΔL. If the cover slip is put in place, the period of the imaged fringes is increased by a factor $1 + \Delta L/L$, and the gradient

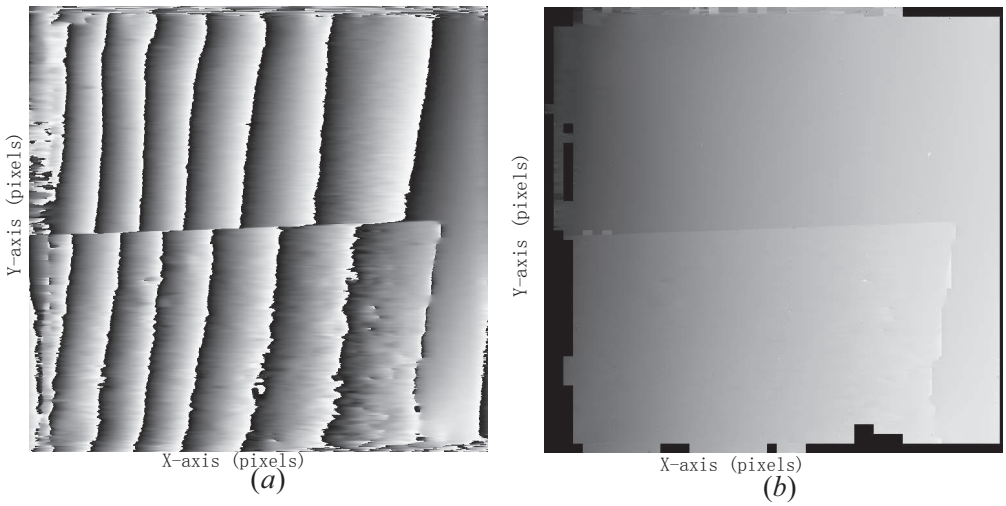

Figure 4.39 (a) Wedge covered half bottom areas with birefringent overlap(a) wrapped phase map (b) unwrapped phase map.

of the phase decreases by a factor $1/(1+\Delta L/L)$. The fringe period was set to 16 pixel periods, corresponding to a phase gradient of 0.39 radians/pixel. Between the surface of the adhesive tape and the wedge, the precision of phase shifting was found to be 1.575 radians.

Regarding the fringe pattern on wedge as the reference, and fringe pattern on adhesive tape come with shift fringe. Then the fringes are moved vertically in the pattern, and the mismatch function can be shown to be [73].

$$m(d) = \frac{1}{L \times W} \int \int_r [I_0(x,y) - I_n(x \pm d, y)]^2 dxdy, \quad \text{for} \quad n = 0, 1, 2, 3, ... \tag{4.73}$$

where d is the fringe shift distance, and r is the region of reference image patch, and L and W are the length and width of the area of the region r, respectively.

The standard deviation [74] can be calculated as below:

$$\sigma = \sqrt{\frac{\sum_{n=1}^{N} (m_n - \bar{m}_n)^2}{N-1}}, \quad \text{for} \quad n = 0, 1, 2, 3, ... \tag{4.74}$$

where for each value m_n, we calculate its deviation $(m_n - \bar{m}_n)$ from the mean, and where N is the number of non-zero weight elements.

That is the measurement of the N samples.$\bar{m}_n = m_n - noise$.

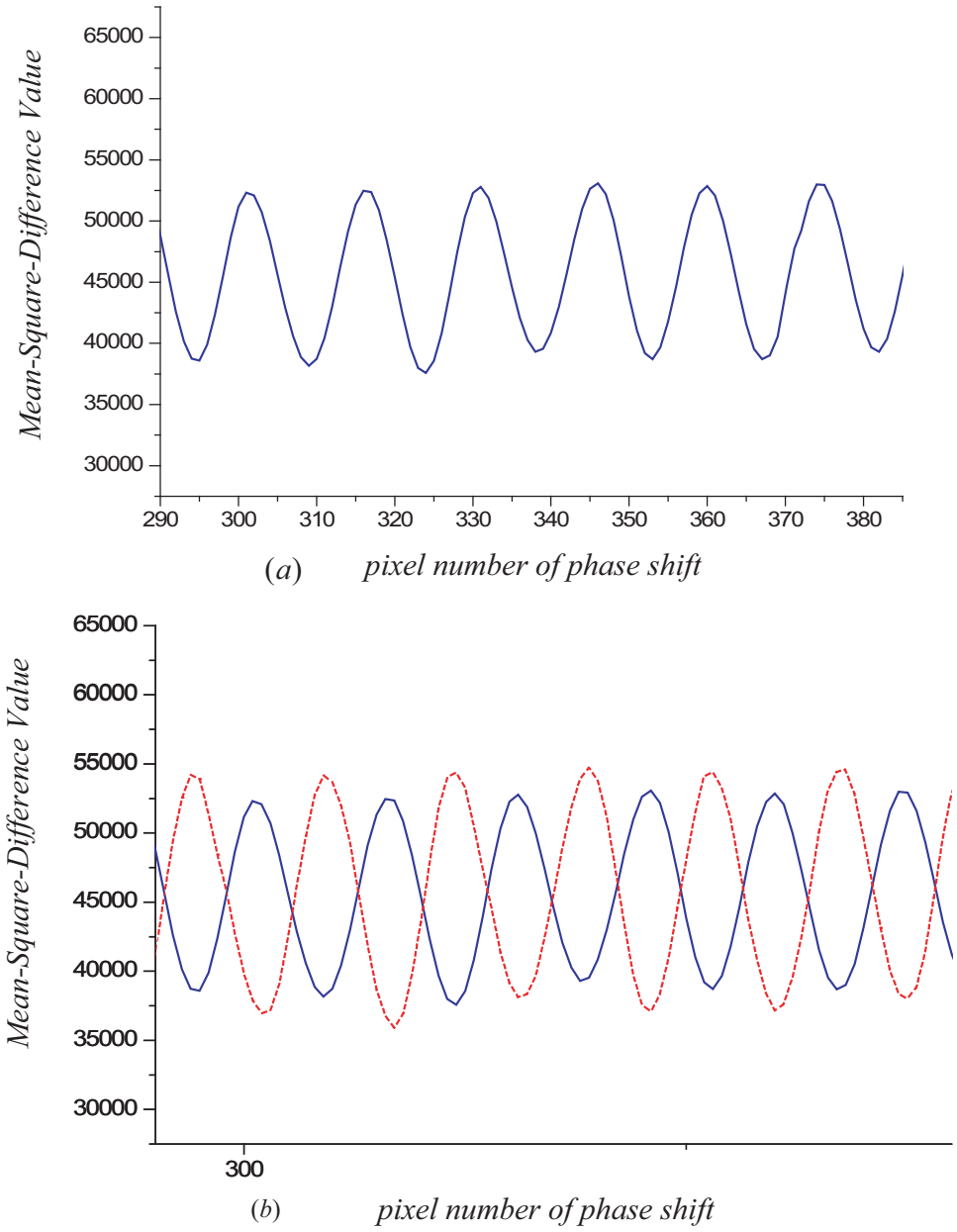

Figure 4.40 (a)phase curve from fringe pattern (b)phase curves of the two surface fringe pattern with phase shift of π.

The shift of the fringe could be counted in pixel values; the period of the fringe $2\pi/f$ (f is the spatial carrier frequency) would then correspond to a discrete number of pixels.

The values of the adhesive tape pattern indicated in the unwrapped pattern were measured to examine phase changing, and the phase offset were then calculated.

The offset and the calculation of inclination were defined as the reference (shown by the blue line in the Fig.4.40, compared with the red one line the surface of the adhesive tape.

In order to calculate the displacement, the sequential phase shifted images before and after deformation are recorded. The difference of the phases between images before and after deformation is analyzed. From the phase difference, the displacement is calculated using the following equation:

$$u = \frac{\lambda}{4\pi}\Delta\varphi \tag{4.75}$$

where u is the displacement, λ is the wavelength of the light source and $\Delta\phi$ is the phase difference between before and after deformation [75].

In this experiment, a green filter is used with the light source, the wavelength λ is 545.5 nm, and phase difference is π, and thus $u = 0.136\mu m$(micrometer). The cell size of the sensor is $2.7\mu m/pixel$. The thickness of the adhesive tape is $40\mu m$.

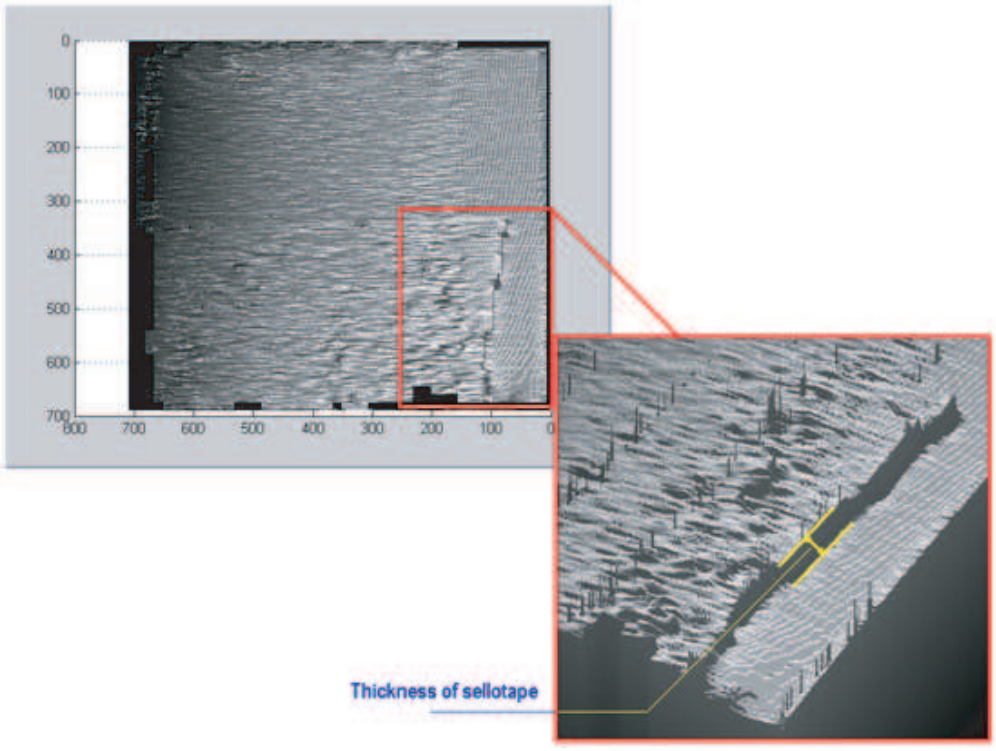

Figure 4.41 Spatial map details.

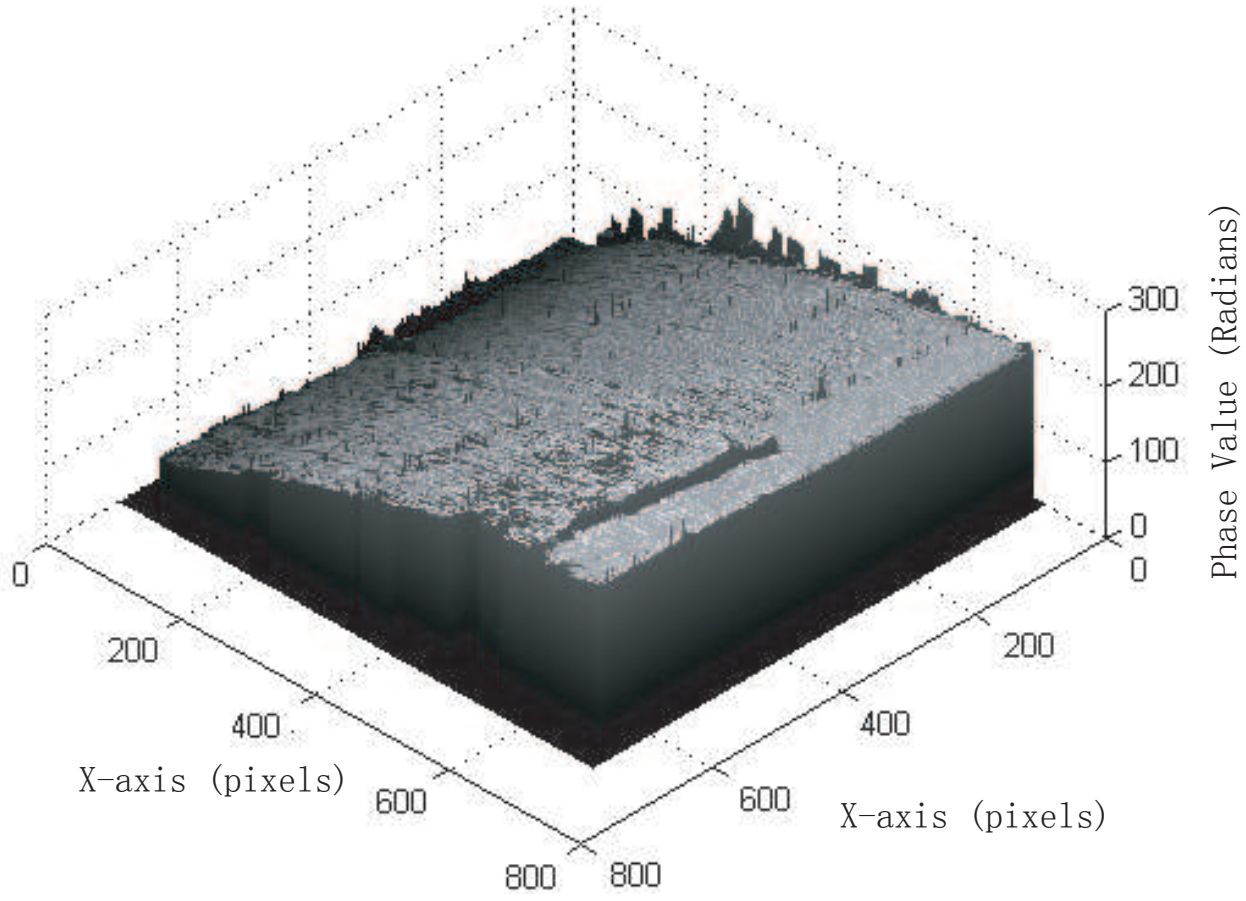

Figure 4.42 Three dimensional reconstruction spatial map.

From the results above, the surface of the background and covered layer can be detected. This thin layer is simulated as the cornea. The information on the surface of this layer is obviously based on the 3D spatial map. But it puts forward another question, the information of the layer and wedge are added together at the bottom half part of the specimen.

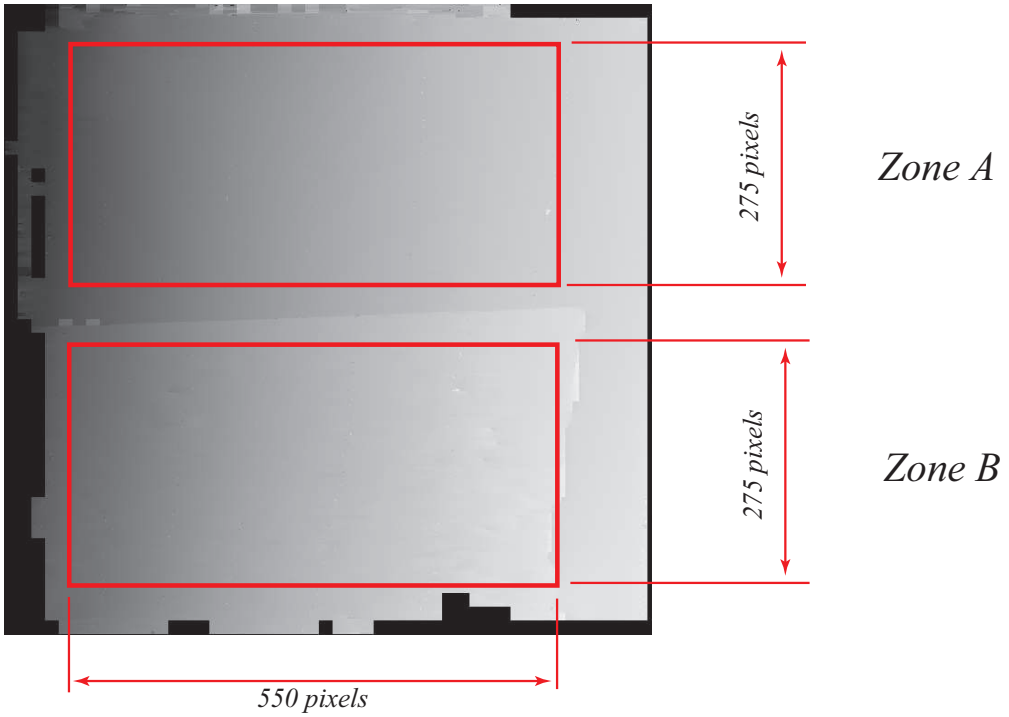

Figure 4.43 Compare background and layer zone on the phase unwrapped map.

In Fig.4.43, *Zone A* and *Zone B* are the same size, which is $550\ pixels \times 275\ pixels$. *Zone B* is the area which the layer covered, and *Zone A* is only the wedge area (the background information). The information from *Zone B* is important to us, if the background shows a perfect state. So, the *Zone A* and *Zone B* are filtered. Then the noise from the background is removed, and only the layer's information is left after processing. Fig.4.44 shows the filtered *Zone B* area.

The three dimensional surface profile is shown in Fig.4.45. The obvious noise information with red colour high peak points which are regular distributed on the surface are caused by Fourier algorithm. It shows the period of the Fourier distribution. Except for this information, around the points (200,50) there are noise information. It also occurs at the edge of layer around the points (500,y).

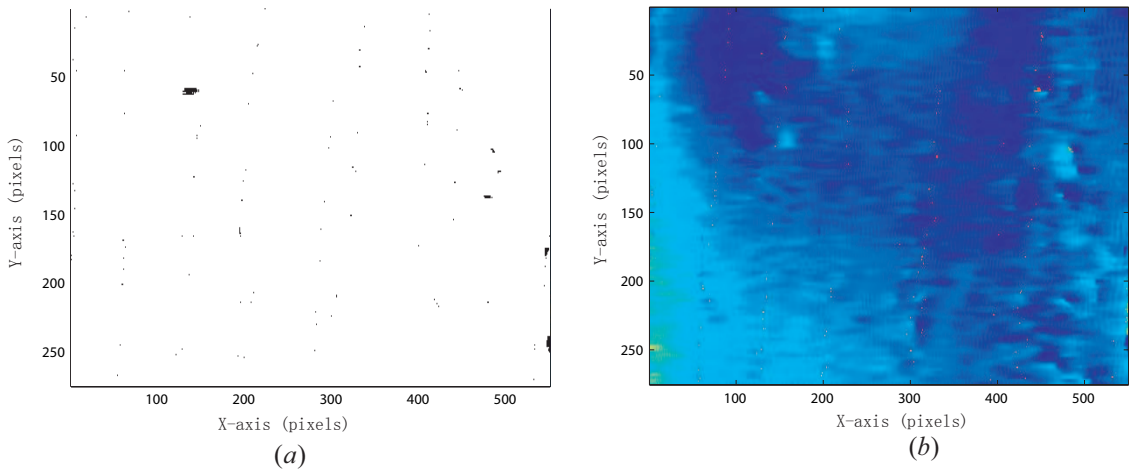

Figure 4.44 Zone B with removing background noise (a)Noise is in Zone B; (b) phase information of the layer without background information.

Some of them are caused by the dirty points on the surface of the layer, and some of the noise on the edge are caused by scratched structure of the layer surface.

Except for the noise, the layer surface shows the fiber structure of the layer surface, the profile shows the stretched characteristic of the layer fiber. For the complicated and thin layer structure under the pressure, the specimen is suggested by surgeon for simulating cornea. The surface profile and birefringent information are measured successfully. The possibility of the methodology for cornea measurement is proved by this experiment.

Phase Spatial Measurement

It has been found that conventional techniques have the common feature of using only a small part of the fringe pattern to determine the phase difference, and their accuracies are affected by non-ideal fringe patterns with background noise present.

In this chapter, fringe pattern matching is a region-based image matching, which is used to determine the phase difference between two interferogram images. A reference image patch, in one interferogram, and a search or shifted image patch in the other with the same size as the reference image patch are selected for matching. The phase curves with the phase difference between the two interferogram are produced by shifting the image patches with respect to each other pixel by pixel.

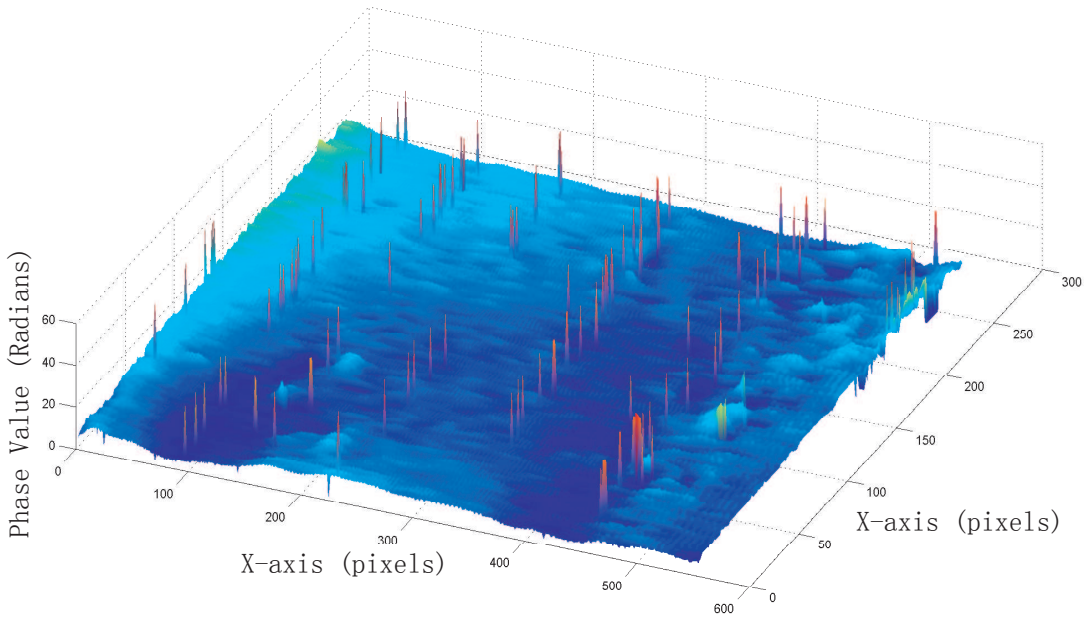

Figure 4.45 3-D plot of the layout reconstructed from the phase information.

Furthermore, the mean-square-difference values for each shift were calculated. The phase difference can be determined from the matching point where the mean-square-difference value is at a minimum.

In order to describe the fringe shift with the angular rotation, the phase, $\phi(x, y)$, is extracted from the fringe pattern image using the procedures described below. The difference in phase is taken as the error of phase extraction.

As shown in Fig.4.46 (a) and (b), the degree of surface error can be determined by comparing the distance $b(B)$ and $a(A)$. The wavelength of the light source is 545.5 nm in this experiment. The flatness error is given by $Aberration = B/A\ Fringes$ or $B/A * \lambda/2$ for double pass [76].

Next, the analysis was carried out with fringe patterns captured at $0^o, 1^o, 2^o, 5^o\ and\ 10^o$ about the wedge when rotated. The least-mean-square method was used to achieve the linear fit and deviation with the same scanning line at the $900th$ pixel, for which the results can be found as shown below.

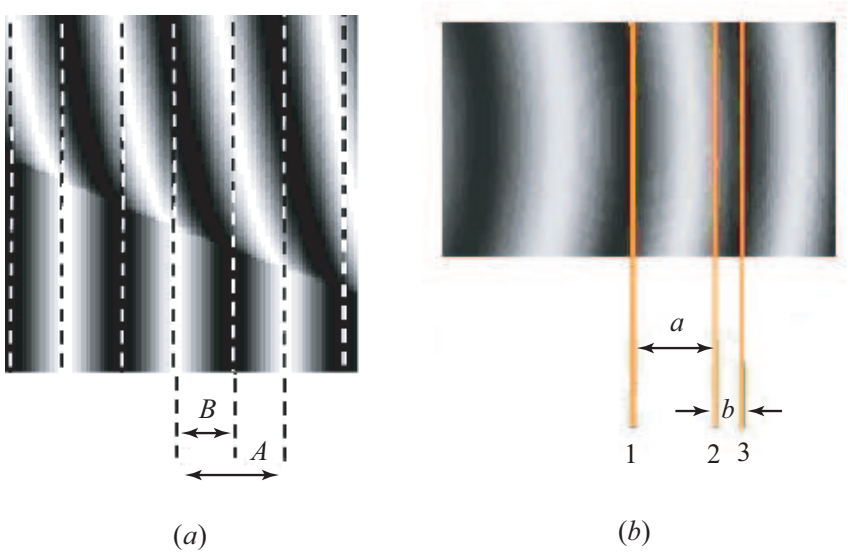

Figure 4.46 Interferometric fringes, (a) and (b)show different phase shifting situations.

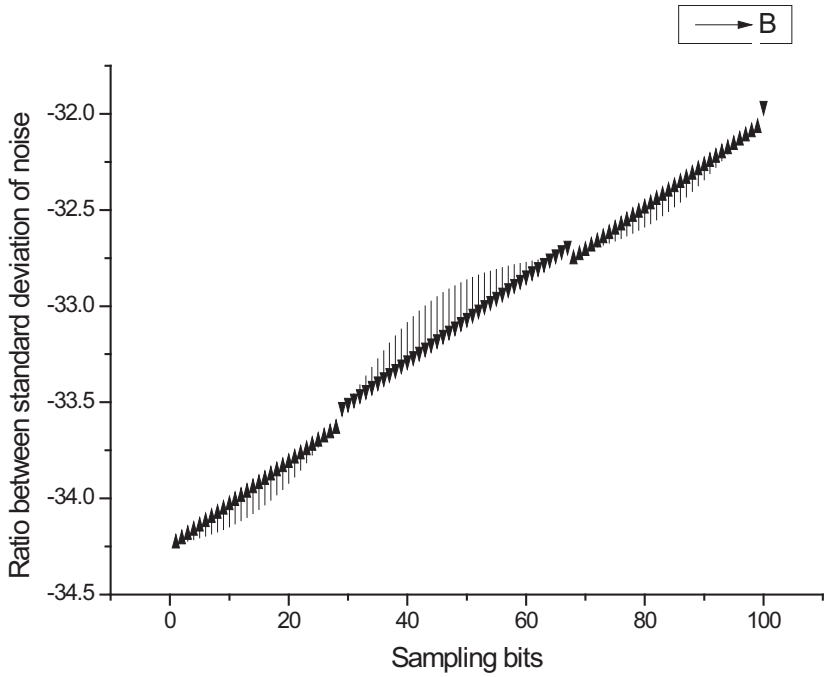

Figure 4.47 At the range of 1-100 pixel of original image, the deviation of the gradient.

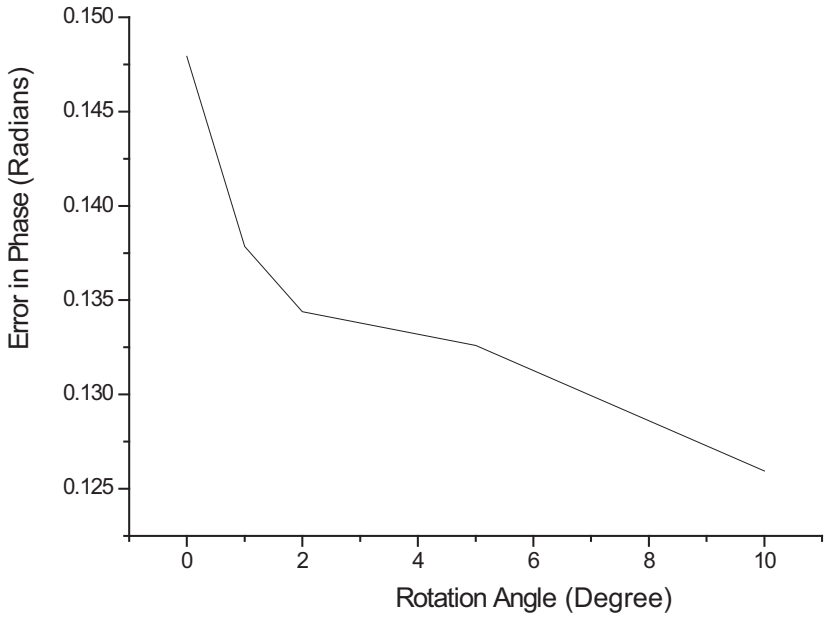

Figure 4.48 The deviation changes at the range of rotation angle.

The small arrows in Fig.4.47 indicate the positions of wedge imperfections, which evidently cause errors for the evaluated phases. Fig.4.48 shows that as the rotation angle increases, the deviation reduces slightly. However, it is clearly shown that the acute transition occurs at 2^o in Fig.4.48. As it is relative to a small shifting, the phase changes to a great extent and the wedge may be been to be sensitive. Furthermore, as the angle increase, the phase error decreases slowly. This is the same as the calculation carried out with the sensitivity of the phase change 2^o, and the accuracy level is 0.01 radian.

The phase difference is determined by fringe pattern matching, which was examined when we described the interferometer system for the introduction of phase shifts.

The calculation of fringe shift is done by using matching algorithm to minimize the function, while varying angles and fringe shift magnitude over the range [77],

$$\delta^2(\theta_1, \Delta) = \sum_{i=1}^{n} \left(x_i - x_i^{theory} \right)^2 \tag{4.76}$$

where x_i is the calculated fringe-shifts from the phase matching algorithm and x_i^{theory} is the theoretical fringe shift.

$$\begin{aligned} x_i^{theory} &= \frac{\lambda}{4\pi(n_e - n_o)\tan\theta} \times (\delta^n_{\min} - \delta^0_{\min}) \\ &= \frac{\lambda}{4\pi(n_e - n_o)\tan\theta} \times \tan^{-1}\left[\frac{\tan\delta^n_{\min} - \tan\delta^0_{\min}}{1 + \tan\delta^n_{\min}\tan\delta^0_{\min}} \right] \end{aligned} \tag{4.77}$$

3D Phase Map Reconstruction at Different angles

As the set up is shown in Fig.4.49, the experiment designed from the microscope slide and adhesive tape rotate from -60^o to 60^o in this transmission polariscope system. The processed images are at $-60, -30, 0, 30\ and\ 60^o$. Fig.4.50 shows that each pattern has three parts, where the top part is the pure fringe from the wedge. There is a piece of glass in front of the fringe pattern from the observed field. The fringe could be seen through the adhesive tape and the microscope slide from bottom part of the apparatus.

The fringe shifting in the Fig.4.50 are due to the refractive index bending that comes from the light path. The light rays are bent when they travel from a medium of one optical density into another, for example from air to glass. Light travels

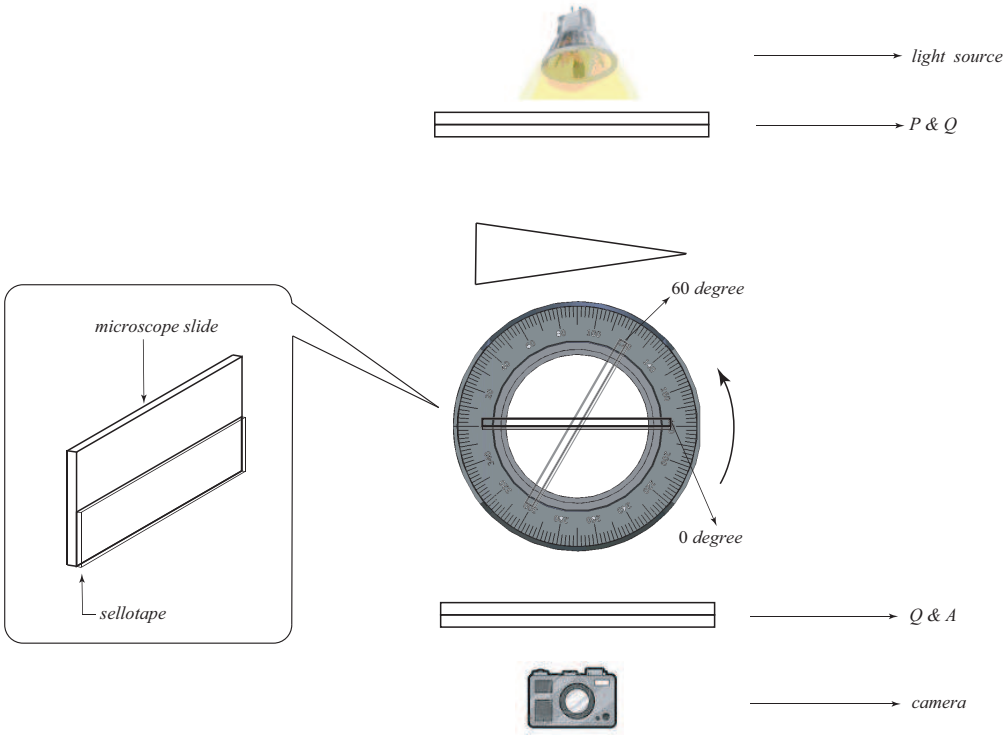

Figure 4.49 Structure of the experimental configuration.

at $3 \times 10^8\ m/s$ (metre/second) in air, whereas in glass its speed is $2 \times 10^8 m/s$ (metre/second) .

In addition, the fringe itself has shifted phase during the rotation. The glass can not add any phase information to the shift. Therefore the small changes can be ignored , as it comes with the refraction movement of fringes. [78][55].

In comparison, it is clearly shown that there is no phase information at the edge of the microscope slide and the background. The changes appear at the surface, and the profile with the fringe shift is due to the glass refraction.

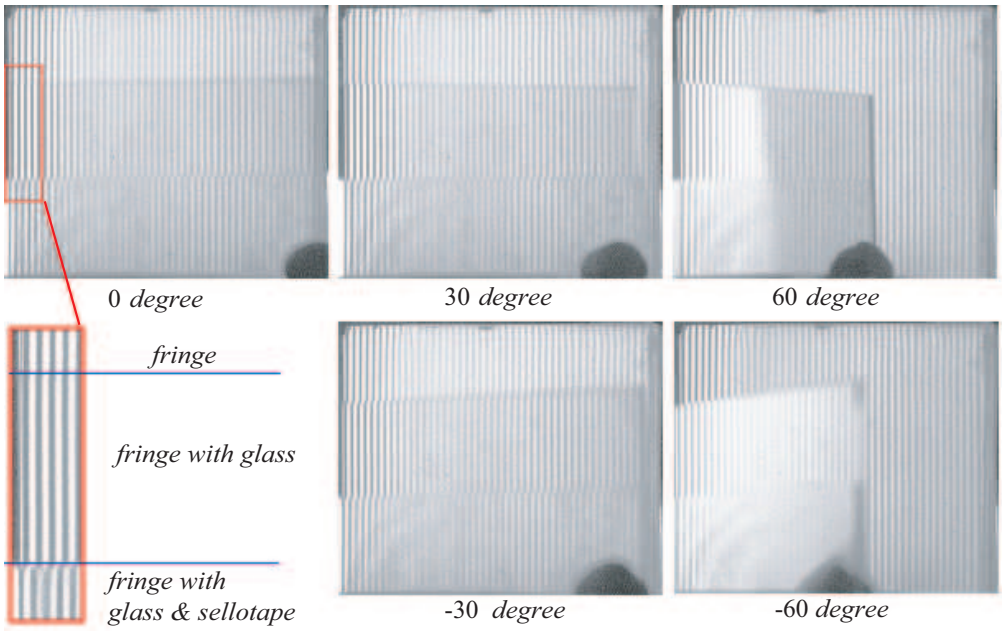

Figure 4.50 Original data achieved from experiment.

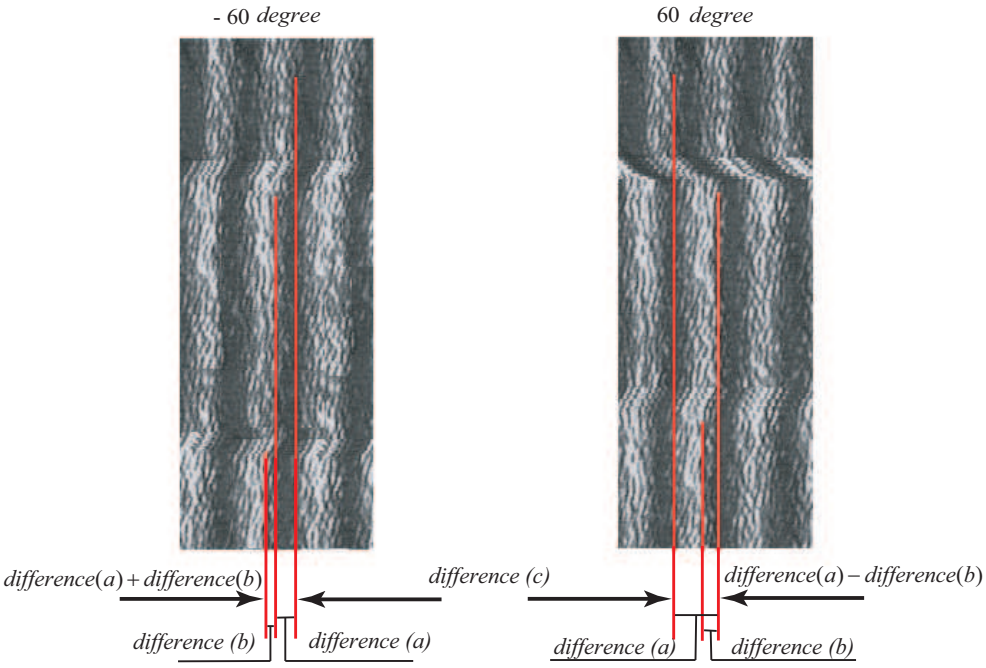

Figure 4.51 Fringe shift ruled shift and refractive bending with -60 and 60 degree images.

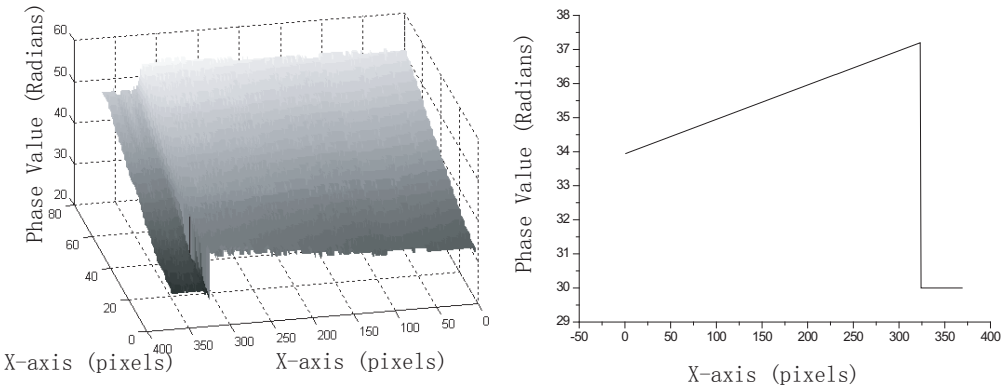

Figure 4.52 0 degree 3D map reconstructed and side elevation

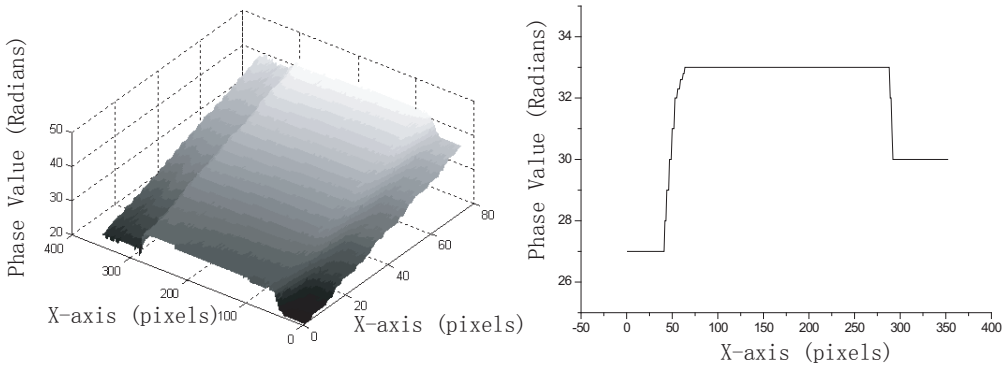

Figure 4.53 60 degree 3D map reconstructed and side elevation

4.4.4 Conclusion

For phase sensitivity measurements, there are many other ways to measure retardance. These include techniques that involve electro-optic modulation, a rotating sample, a rotating retarder, and a rotating polarizer. Each technique has its own advantages and disadvantages such as simplicity, speed of measurement, precision and accuracy. Our goal is a highly accurate measurement technique whose uncertainties can be controlled for standardised.

The chapter proposed a technique to calculate the retardance of any birefringent material using birefringent crystal quartz and polariscope system with a CCD camera. A theoretical analysis of the principle and the uncertainty of this method were given. This technique does not require any prior knowledge about the axis of the wave plate. It is a low-cost measurement since the expensive revolving polariscope is replaced with the a cheap LED, used as a light source. Moreover, for the steady system design and set up, the error can be reduced and restrained.

For 2D image processing, the grey level resolution, or which means the dynamic range, presents the actual range of grey-scale levels being used. Compare the results of the 8-bit image and 16-bit image, a limit dynamic range will impact on the quantitative results. An 8 bit image uses numbers from 0 to 255 (2^8) to represent the colour (grey-scale, intensity level) of each pixel, while a 16 bit image file has 65536 (2^{16}) possible grey-scale values for each pixel. So, a grey-scale image of 16 bit will has more 256 times shades of gray than a 8 bit image. In our case, the fringe shifting will decide the phase changes, so the fringe contrast which adjusted by the intensity value will impact on the accuracy. As a rule, 16 bit image which could show more levels of grey represented in an image, then it could obtain better the ability to differentiate low abundance spots from background and the greater the quantitative accuracy[79]. The details of accuracy analysis comparison between these two images will depend on the case. Because of the limitation of our device (we only have 8 bit camera), we cannot give the exactly value of accuracy of phase shifting by these two dynamic range images.

The phase matching technique for fringe shift calculation does not need to consider the presence of noise. Although this method requires an expensive computation of the retardance, the fringe shift method is used in this experiment set up to get an accuracy of 0.058 radians, which is more accurate than other methods and their results [80]. Consequently, we conclude that our system is useful due to its improved accuracy and ease of operation, and the accuracy it reaches could afford the measurement of cornea structures and optical birefringence.

Stability of the light source is important both in frequency as well as in amplitude. Random intensity fluctuations of the source can be mitigated by resorting to time averaging. The error due to detector non-linearity, source instability, digital to analog conversion, and error due to digitisation can all be modeled as error in measuring intensities[53]. Furthermore, during phase shifting processing, error could possibly arise because of angular misalignment of the optical elements and imperfections in the optical elements. Angular misalignment includes two possible conditions. One is at the time of manufacturing, relating to the optical elements of the polariscope, and the other is at the time of aligning the optical elements for a specific position. The first condition will lead to manufacturing error and the second causes a random error. One of the imperfections in the elements is inhomogeneity of the optical elements, which is normal in all components we used in our experiment. The other is specific to the quarter-wave plate. It may lead to errors if the light source wavelength does not quite match its special value. Thus, manufactured component error, misalignment of the set up in experiments, and mismatch of quarter-wave plates are all possibilities which need to be considered for occurrence of the errors.

Chapter 5

Description of the Human Eye

5.1 Function of the Human Eye

The eye is not a perfect sphere, but an integrated two-piece unit. The smaller, less curved component is called the cornea, which is linked to the larger component called the sclera. Both cornea and sclera are connected by a ring called the limbus [81]. The iris and its black center, the pupil, are visible, while the cornea is transparent.

The dimensions of the components differ among adults by only one or two millimeters. For a normal eye, when the eye muscles are relaxed, the vertical height of eye, generally less than the width of eye, is about 24 mm among adults, and about 16-17 mm at birth [82].

The eye is covered by three coatings, with three transparent structures. The outside layer is composed of the cornea and sclera. The middle layer consists of the choroid, ciliary body, and iris. The inner is the retina.

Within these coatings are the vitreous body, the aqueous humor, and the flexible lens. The aqueous humor is a type of water clear liquid that is contained in two areas: the anterior chamber between the cornea and the iris and exposed area of the lens; and the posterior chamber, behind the iris and the rest. The lens is connected to the ciliary body by the suspensory ligament ("Zonule of Zinn"), which is structured by fine transparent fibers. The vitreous body is a clear jelly

that is much larger than the aqueous humor, and is bordered by the sclera, zonule, and lens. They are connected via the pupil.

The Schematic diagram of the human eye is shown in Fig.5.1[83].

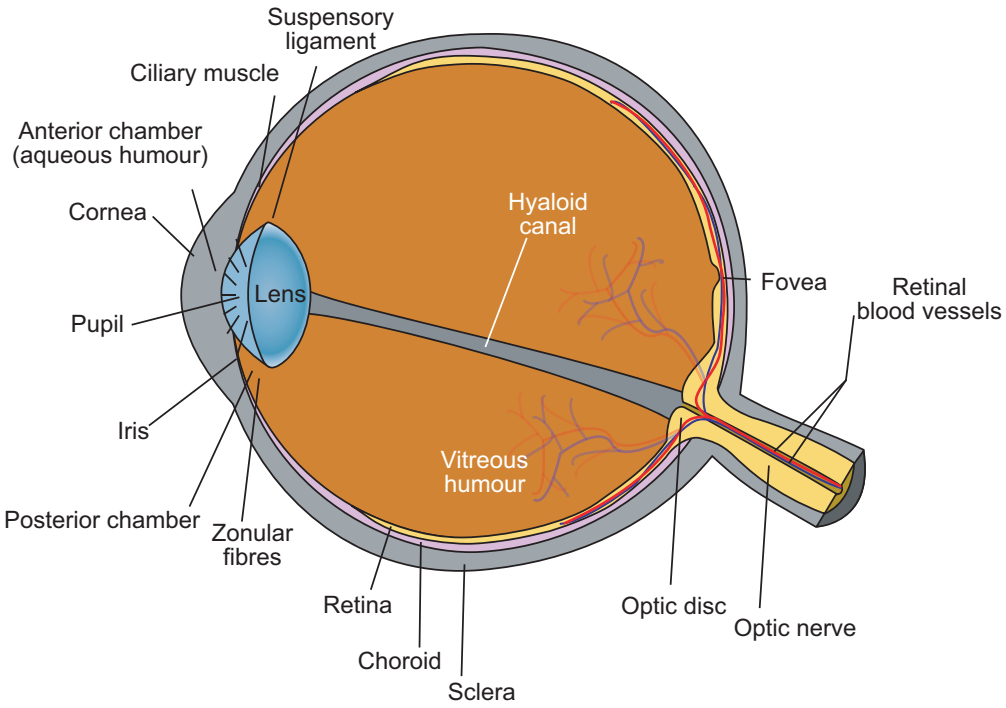

Figure 5.1 Anatomy of the Eye.

5.1.1 The Structure of Cornea

The cornea is the transparent, dome-shaped window covering the front of the eye. It is a powerful refracting surface, providing two-thirds of the eye's focusing power. Like the crystal on a watch, it provides a clear lens through which to see.

Because there are no blood vessels in the cornea, it is normally clear and has a shiny surface. The cornea is extremely sensitive - there are more nerve endings in the cornea than anywhere else in the body.

Standard Shape

The standard shape of the cornea has parameters that are estimated using statistical data. The central zone of 1-3 mm is closely fitted by a spherical surface. At the paracentral zone, there is a 3-4 mm ring, with an outer diameter of 7-8 mm,

which is an area of progressive flattening. The peripheral zone has the greatest flattening and asphericity, and has an outer diameter of 11 mm. The limbus is an edge part of cornea, which steepens before joining the sclera. The outer diameter of sclera averages 12 mm[84].

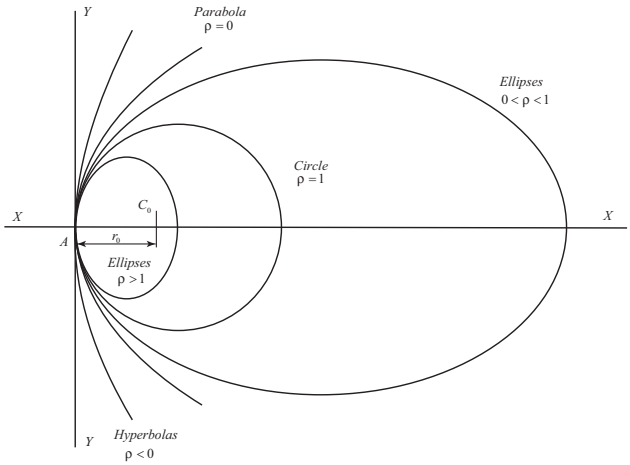

Figure 5.2 Conic section.

Because of its peripheral flattening, an ellipsoid has been suggested as a schematic representation of the front surface of the cornea.

The conic section is[84]:

$$Y^2 = 2r_0X - \rho X^2 \tag{5.1}$$

The equation 5.1 presents by the Fig.5.2. The shape of the curvature changes according to ρ in the equation. When $\rho = 1$, the curve is a circle; if $\rho = 0$, the curve is a parabola; if $\rho < 0$, the curve is a hyperbola; and when $0 < \rho < 1$, the curve is a ellipse. For a typical cornea, ρ is between 0.6 and 0.8[85].

On the top of the cornea, there are two kinds of top points defined, one is $corneal\ apex$ and the other is $corneal\ vertex$. The corneal apex is the point of maximum curvature or height, while the corneal vertex is the point located at the intersection of the patient's line of sight (visual axis) and the corneal surface. It is represented by the corneal light reflex when the cornea is illuminated coaxially.

Although the cornea is transparent, it is a highly organized group of cells and

proteins. Unlike most tissues in the body, the cornea contains no blood vessels to nourish or protect it against infection. Instead, the cornea receives its nourishment from the tears and aqueous humor that fill the chamber behind it. The cornea must remain transparent to refract light properly, and the presence of even the tiniest blood vessels can interfere with this process. To see well, all layers of the cornea must be free of any cloudy or opaque areas.

Elements in the corneal shape

The cornea is exposed to the environment on its outer surface, and is epithelial in nature [86]. The outermost part of the cornea is a stratified squamous layer, the corneal epithelium. This layer is not normally keratinized, and it varies in thickness between different species. The corneal epithelium is continuous at its margins with the conjunctiva of the eyelids and the eyeball[87].

The inner surface of the cornea, demarcating the limit of the eye's anterior chamber has a very thin, single layer of corneal endothelium. This is a row of cuboidal cells. Between it and the substantia propria is found Descemet's membrane, the basal lamina of the endothelial cells.

The adult cornea is approximately 0.5mm thick (0.0196 inches). In comparison, a skin freckle is 1mm wide, and a strand of hair is typically about 0.1mm thick.

The human cornea has five layers: epithelium, Bowmans membrane, stroma, Descemets membrane, and the endothelium. The corneas of dogs, cats, and other carnivores have only four layers. The structure is shown in Fig.5.3[88][89].

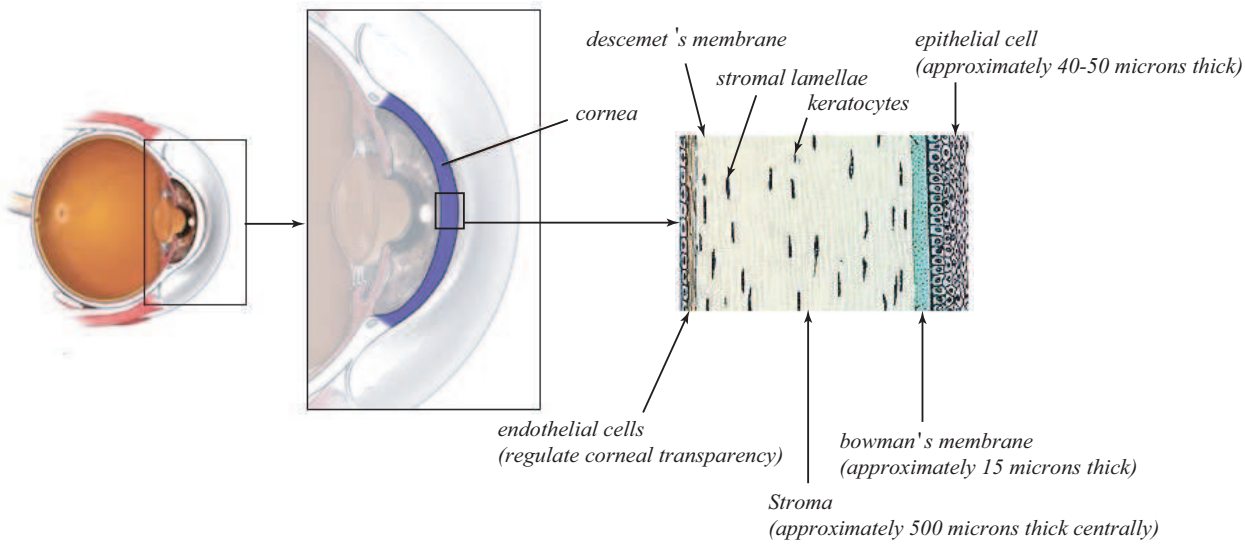

Figure 5.3 Normal Structure and Function of the Eye.

The eye is similar to a camera in which lenses focus the picture on a light sensitive film. In the human eye, the transparent cornea and lens focus light on the retina, which changes it into electrical signals, which are then transmitted to the brain by

the optic nerve to be perceived as images.

The corneal tissue is arranged in five basic layers, each having an important function. These five layers are[90]:

- Epithelium: this layer covers the surface of the cornea, it is a outermost region, comprising about 10 percent of the tissue's thickness, which is about 5-6 cell layers thick and filled with tiny nerve endings, making the cornea very sensitive to pain. This layer blocks the passage of dust and germs, and provides a smooth surface that absorbs oxygen and cell nutrients from tears, and then distributes these nutrients to the rest of the cornea. The base membrane is the part where the epithelial cells anchor and organize.

- Bowman's Membrane : this layer lies beneath the epithelium and is very difficult to penetrate. It is a transparent sheet of tissue composed of strongly layered protein fibers called collagen. Once injured, Bowman's layer can form a scar as it heals. The scar becomes an opaque area, causing the cornea to lose its clarity and luster.

- Stroma: a layer accounting for 90% of the cornea's thickness, consisting primarily of water (78 percent) and collagen (16 percent), and does not contain any blood vessels. Composed of tiny collagen fibrils that run parallel to each other, this precision formation gives the cornea its clarity, strength, elasticity, and form. Collagen's unique shape, arrangement, and spacing are essential in producing the cornea's light-conducting transparency.

- Descemet's Membrane: lying beneath the stroma, it is a thin but strong sheet of tissue that serves as a protective barrier against infection and injuries. It is composed of collagen fibers and is made by the endothelial cells that lie below it. Descemet's membrane is regenerated readily after injury.

- Endothelium: the extremely thin, innermost layer of the cornea. Endothelial cells are essential in keeping the cornea transparent. Once endothelium cells are destroyed by disease or trauma, they cannot be recovered. Too much damage to endothelial cells can lead to corneal edema, and blindness ensues, with corneal transplantation the only available therapy.

The shape of the cornea is related to the curvature, thus determining Refractive power. A keratometer can be used to measure the radius of curvature of a small portion of the central cornea, assuming it to be spherical. Radius is calculated using geometric optics, considering the cornea as a spherical reflecting surface.

Calculations are based on the geometry of a spherical reflecting surface: the cornea is described as a prolate (flattening) ellipsoid (true apical radius steeper). Quantitative data are based on only four points within the central 3 millimeters of the cornea.

5.1.2 Numerical Simulation of the Human Optical System Based on in Vivo Corneal Data

Data can be obtained from medical practice. The distribution of corneal thickness and the coordinates of at least 3 points can be obtained using non-linear equations which can be called the curvilinear equation of cornea surface[91].

In angular coordinates and polar coordinates, these equations can be written,

$$\begin{aligned}(\rho, \theta_0) &= (6.9 + 0.5, \theta) \\ (\rho, \theta_1) &= (6.9 + 0.7, \theta) \\ (\rho, \theta_2) &= (6.9 + 0.8, \theta)\end{aligned} \tag{5.2}$$

assuming that,

$$y = a\theta^2 + b\theta + c \tag{5.3}$$

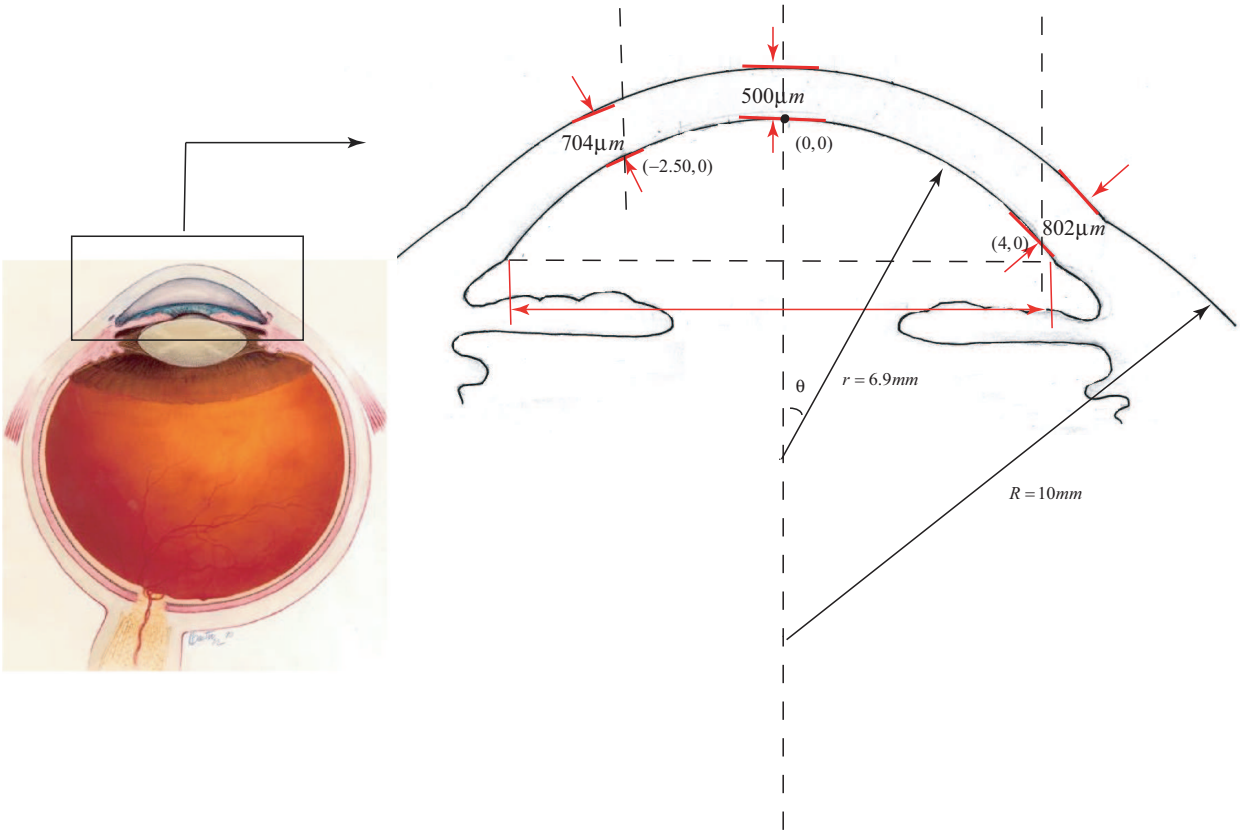

Figure 5.4 Corneal profile and 3-point coordinates[1].

and bring the three points coordinates values which are shown in Fig.5.4, the equation is shown as,

$$\begin{cases} 0 = a \times 0 + b \times 0 + c \\ 0.2 = a \times \left(\frac{\theta}{2}\right)^2 + b \times \frac{\theta}{2} + c \\ 0.3 = a \times \theta^2 + b \times \theta + c \end{cases} \tag{5.4}$$

Angular coordinate equations can be solved

$$\begin{bmatrix} a \\ b \\ c \end{bmatrix} = \begin{bmatrix} -0.5329 \\ 0.8162 \\ 0 \end{bmatrix} \tag{5.5}$$

so, the cornea curve equation is,

$$\rho = \rho_0 + \rho' = 7.4 + (-0.5329\theta^2 + 0.8162\theta) \tag{5.6}$$

This cornea curve equation is the raster line of the diameter of the cornea, by

using a piece of software called $SolidWorks$, the cornea 3D structure can be reconstructed as a drawing, Fig.5.5 shows the 3D cornea reconstructed model. The model will be used to show the stress loading in simulation in a future chapter.

Figure 5.5 cornea 3D simulation by SolidWorks.

5.2 Polarised Light Studies of Cornea

5.2.1 The Need for the Measurement of Birefringence in the Human Eye

The unique characteristics of the cornea and the peculiar circumstances of its transparency have stimulated study in recent years. Although the method using polarised light was studied in recent years, there have not been any adequate quantitative investigations. The quantitative measurements of the photoelastic properties of the cornea were studied in experiments in this project.

If the biological tissues can be examined in a polarised microscope, the accuracy can be decided in the measurement, although there are many difficulties in the applications of quantitative polarisation techniques to the tissues. For measuring such a special specimen, modifications of the usual techniques of measuring retardation are necessary.

Since 1950, much research into the cornea has occurred, though research methods and experimental equipment have developed significantly since then. With the help of advances in computational resources, optics data can be studied by digital image processing using by numerical simulation.

Polarised light is a useful tool for investigating of the structure of cornea. It changes its polarisation state giving information about its optical and mechanical properties when it passes through the cornea. The cornea is made up of several layers, however the birefringence is due to the stroma, which is the main structure of the cornea, at around 90% thickness of the whole[92]. The layers of collagenous fibers which are named *lamellae* make up the stroma. In this structure, each lamella is aligned parallel with fibers, but makes large angles with adjacent lamellae. According to the theory from Born and Wolf in 1980[93], there are two different sources of corneal birefringence:

- the intrinsic birefringence due to each individual fiber; and,

- the form birefringence that has its origin in the stack formed by the lamellae.

The physical nature of corneal birefringence was recognized early ($Bour(1991)$)[92]. Most previous work has focused on corneal birefringence, and the polarimetric method has been little used. However, some authors have used Muller-matrix polarimetry to determine the polarisation properties of the eye[94][95][96][97]. The $Mueller$ matrix of a system is a 4×4 matrix M with elements $M_{ij}(i,j=0,1,2,3)$ which includes information about all its polarisation properties[98].

The purpose of the present work is to study more completely the resolved polarisation properties of the cornea using the birefringence method. Based on previous work, we used Jones matrices instead of Mueller matrices in numerical set up to make experiment and analysis easier and more accurate. These are implemented into phase stepping and the Fourier transform algorithms.

5.2.2 Vitro Cornea Specimen Introduction

The cornea used in the specimen are cut and removed from animals, such as pigs, foxes, and cats. Each steps of the operation to strip the cornea are shown in Fig.5.6. Using a sharp cutting tool, a cut is made a around the middle of the globe. The cut is deep enough to enter the vitreous cavity. Once we remove the vitreous layer and everything forward of it, we will have access to the posterior structures, including the retina and the beginning of the optic nerve. When everything thaws, the cornea and then the iris can be removed using tweezers.

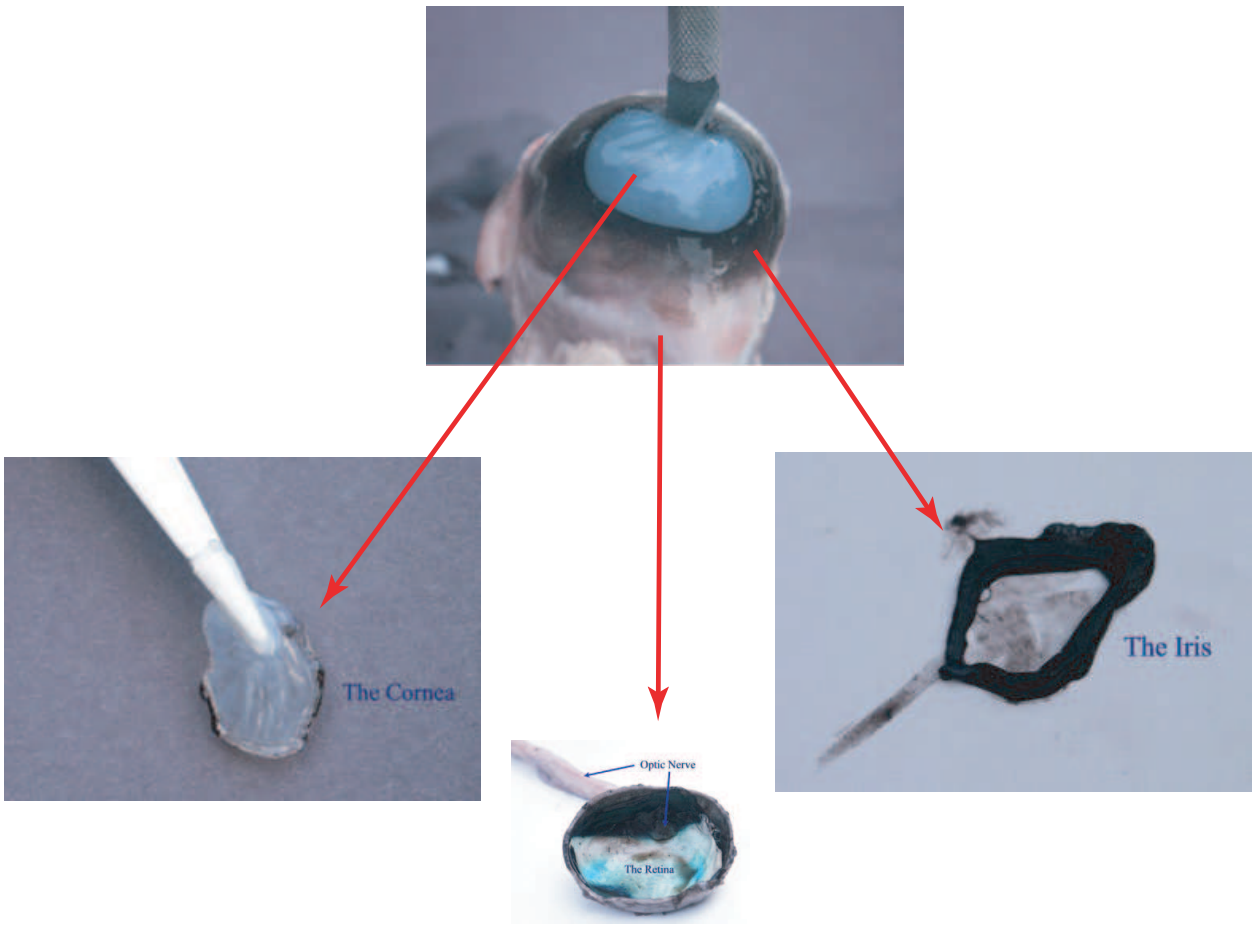

Figure 5.6 Dissection of an eyeball[2].

Examination of the cornea of a pig was performed using green LED light source, and a monochromatic camera through a circular polariser. For the smooth surface with few scratching, we use porcine cornea, but not other animals. Under low magnification and using a reflection system, we can obtain the image which is shown in Fig.5.7, this is the image of porcine cornea which was put in the reflection polariscope system.

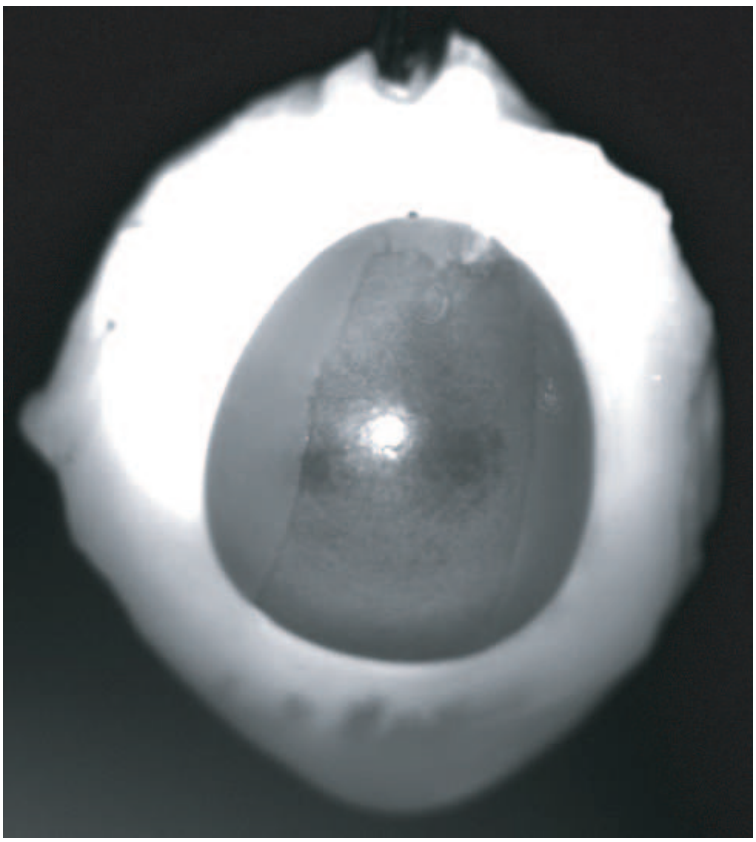

Figure 5.7 Porcine cornea in a reflection polariscope system.

Thus, our system could work with reflection system and be implemented into measurement in vivo. Nevertheless, in our experiment, for the high contrast and proving the possibility of the methodology, we still use transmission system, and the specimen image, with a porcine cornea put into polariscope system, is shown in Fig.5.8,

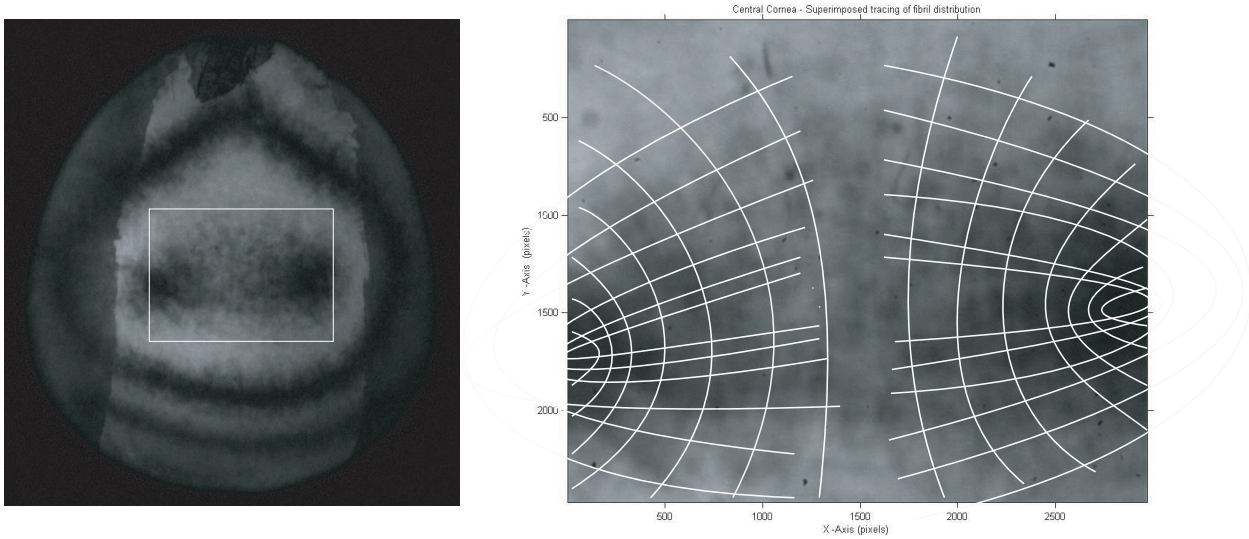

Figure 5.8 pig's cornea in through polariscope system.

5.2.3 Comparative Birefringence of Cornea

In order to interpret the measured optical retardation properly in terms of collagen fibril orientation, nearly 75% of the values are obtained dues to the form birefringence, the special rod-shaped collagen fibres being embedded, it makes the refractive index different from the fibres. Only 25% can be assigned to preferential fibril orientation[99][100]. Moreover, the birefringence originates from intrinsic optical anisotropy of the fibres that have a non-random distribution. This is a preferential orientation. Then, maps of birefringence isochores in the cornea of a number of species were compared.[101]. The lowest birefringent areas were at the center or slightly off center and the birefringence increases as one moves toward the periphery.

As expected, there are a variety of birefringent images among individuals of each species. They are the cornea of foxes, cats and pigs, shown in Fig.5.9(a),(b), and (c), respectively. On the left-hand side is the raw data, and right-hand side is the wrapped phase map. It is proposed that the distribution of the low birefringent areas in the cornea of the different species has a definite relationship to the optimal field of vision needed [101].

The general tendency found from the data in many corneas is that the periphery usually has a higher birefringence than the center areas, however this may arise

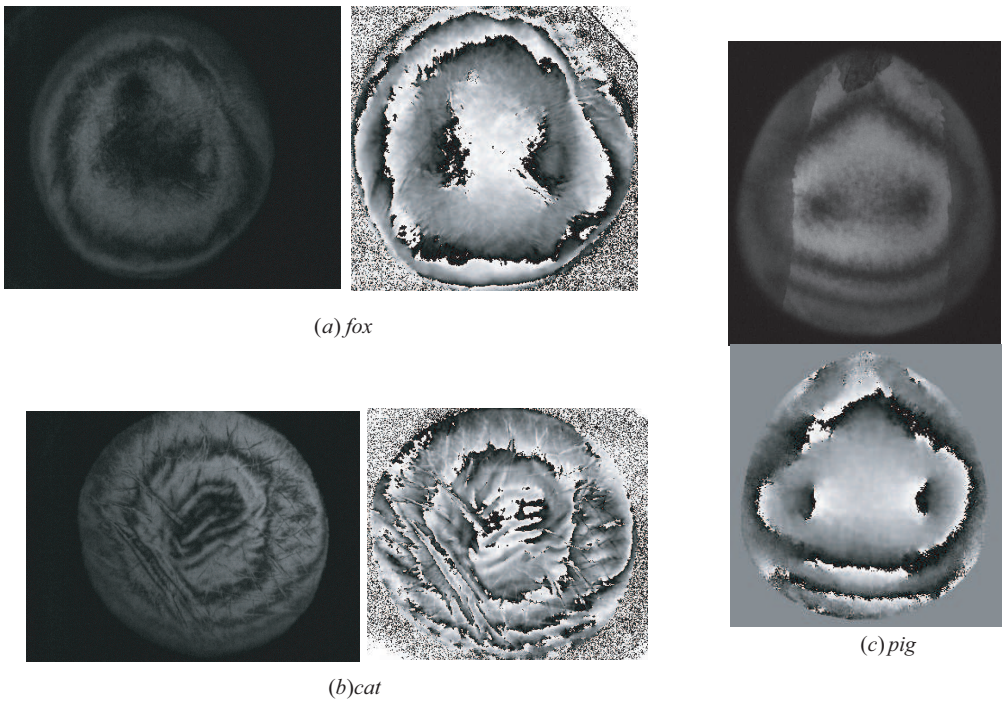

Figure 5.9 Variation in the distribution of birefringent between raw data and wrapped phase map of three cornea (a)fox (b)cat (c)pig .

from stress. On the other hand, it is interesting to note that the area of low birefringence in the cornea of different species is found in the center, or along the visual path.

As a result, the area of high birefringence on the periphery stress-induced orientation of the collagen fibre provided the needed mechanical properties. On the other hand, the low birefringence area is at the position which different animals use most frequently on the visual path[102].

Clearly, the cornea sample study can not warrant generalization over all species. However, the cornea in animals of different species have different distributions of birefringent areas, each adapted to the needs of the animal. The lowest birefringent area lies in the visual path to provide the least polarisation of the incoming light, and the high birefringence area lies on the periphery adjacent to the sclera to provide the suitable collagen orientation to yield to instant stresses.

The next chapter will give a quantitative measurement of the birefringence distribution of the cornea, using the phase stepping method, and the Fast Fourier transform method.

Chapter 6

Quantitative Measurement for Cornea Birefringence

6.1 Simulation

In this section, computer simulation of cornea model is studied. Computer simulation consists of three aspects. The first refers to a computer program that simulates model for analysis. The second refers to the use of special software to create three-dimensional graphics with display objects in three-dimensions. Finally, computer simulation can refer to the practice, known as emulation, whereby a specific function of the system is duplicated for the purposes of experimental investigation.

Computer simulation is widely used in the sciences and social sciences as an extension of mathematical modeling, which creates a sampling of representative outcomes of events in simulations.

3D models are formed in different ways. They are comprised of basic geometric shapes, such as circles, squares, triangles, and other 2D surfaces. Most 3D models take the approach, where, on one hand, objects are shown as a solid object and are defined by its volume. On the other hand, models also show the boundary or shell of the object.

The general procedure for constructing a simulation is characterised by the follow-

ing steps:

Step One: Problem formulation

Step Two: Construction of the model

Step Three: Model validation

Step Four: Using the model, evaluate various available alternatives

Step Five: Implementation and maintenance of the solution

The above steps are not carried out just once. Rather, during the course of an cornea simulation exercise, they are iterated. For the purpose of cornea measurement, the three dimensional model is made based on the numerical simulation. By using $SolidWorks$ software, not only the 3D shape could be drawn, but also stress can be added through a plug-in function $COSMOS$.

The isolated cornea is valuable, and fragile, thus before an experimental evaluation a physical model was created. The cornea is also a highly complex three dimensional phase structure which is very difficult to model. An intermediate stage was conceived which resembled many of the birefringent features without such complexity. This simplified physical testing and the fringe analysis approaches at a realistic size, shape and also with a similar interferometric fringe distribution. It also allowed a direct mathematical comparison to be made with a highly simplified cornea model. Two models that are designed for the experiment.

Firstly, an equal-proportion model is designed, based on a design from $SolidWorks$, and the model can be generated by $3D\ Prototyping$ technology. This technology is a form of additive manufacturing technology where a three dimensional object is created by successive layers of material. A 3D printer is generally faster, more affordable and easier to use than other additive technologies, and it can read $SolidWorks$ files directly to create the model efficiently.

Secondly, in order to simplify the experiment to verify feasibility, a simplified test procedure is designed. Not considering the curvature, the model can be approximated by a birefringent disk. The model is then easier to manufacture. If phase

measurement works with this model, then the cornea model can be studied further.

6.1.1 Solidworks Simulation

Based on the two designs above, SolidWorks simulates the stress acting on the models. Firstly, the round disk is designed with 12 mm (millimetre) diameter, and thickness is 1 mm (millimetre). There are two pinholes with 1 mm (millimetre) diameter on the disk, symmetry distributed around the centre point with 4 mm (millimetre) between both of them. The backward force is given from the pinholes hypothetically. This should be followed by the axially symmetrically stress distribution on the disk.

The simulation results are shown in Fig.6.1 and 6.2.

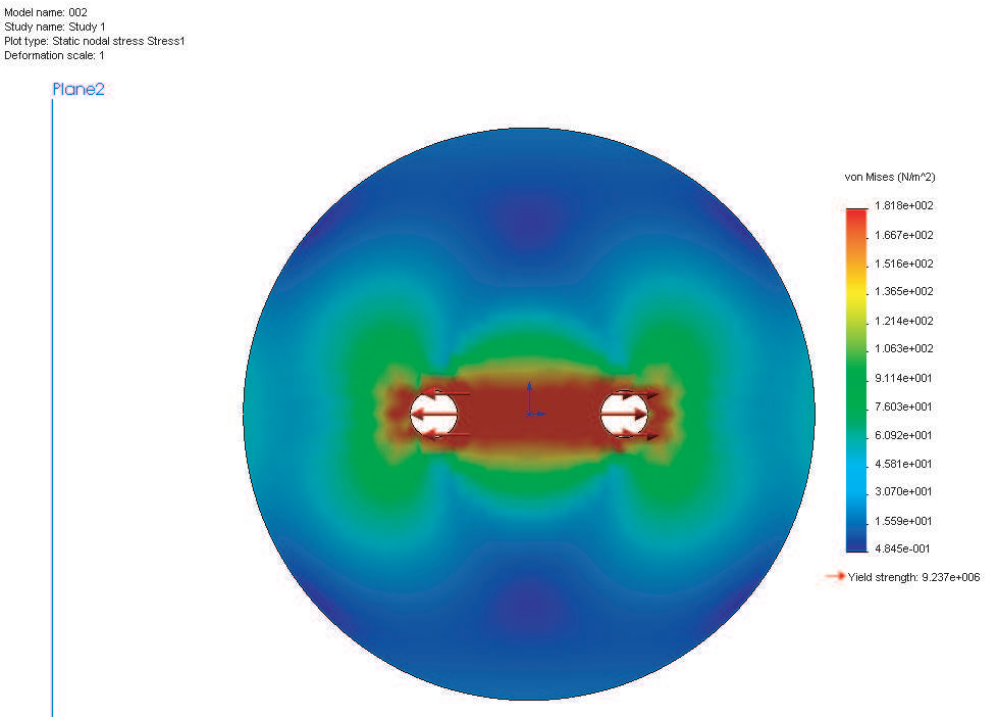

Figure 6.1 SolidWorks simulation of Disk model with stress distribution by backward force.

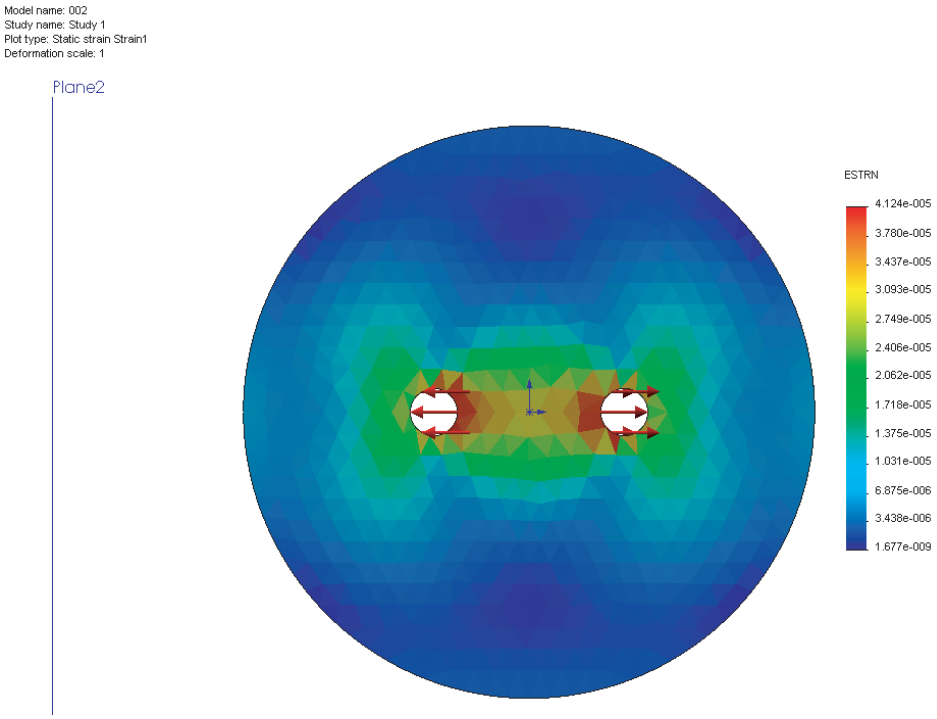

Figure 6.2 SolidWorks simulation of Disk model with strain distribution by backward force.

Similarly, the same design is used in the cornea model, the results obtained are in Fig.6.3 and 6.4.

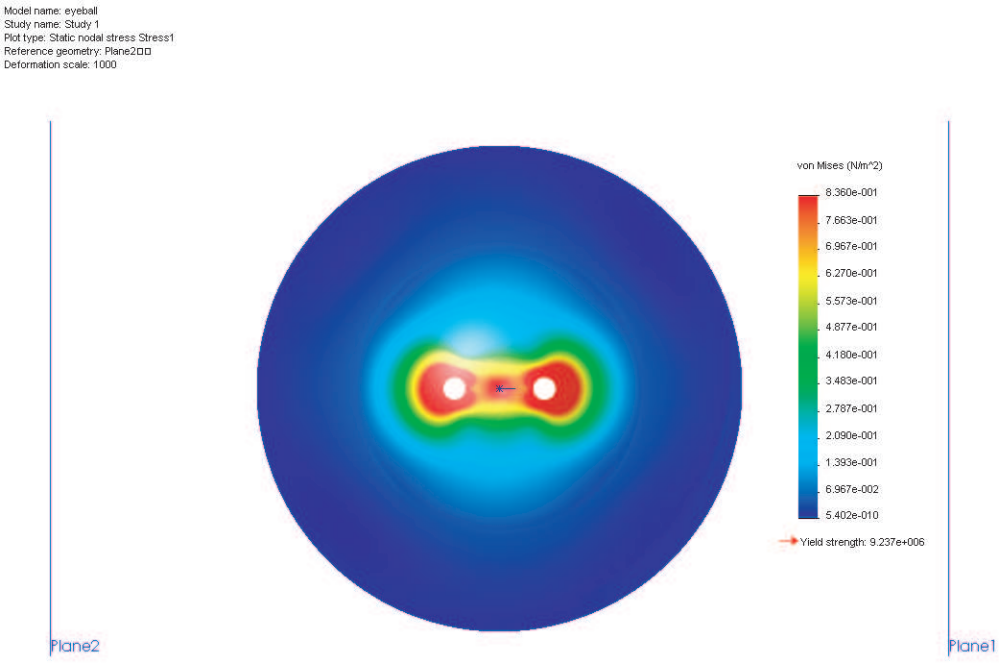

Figure 6.3 SolidWorks simulation of cornea model with stress distribution by backward force.

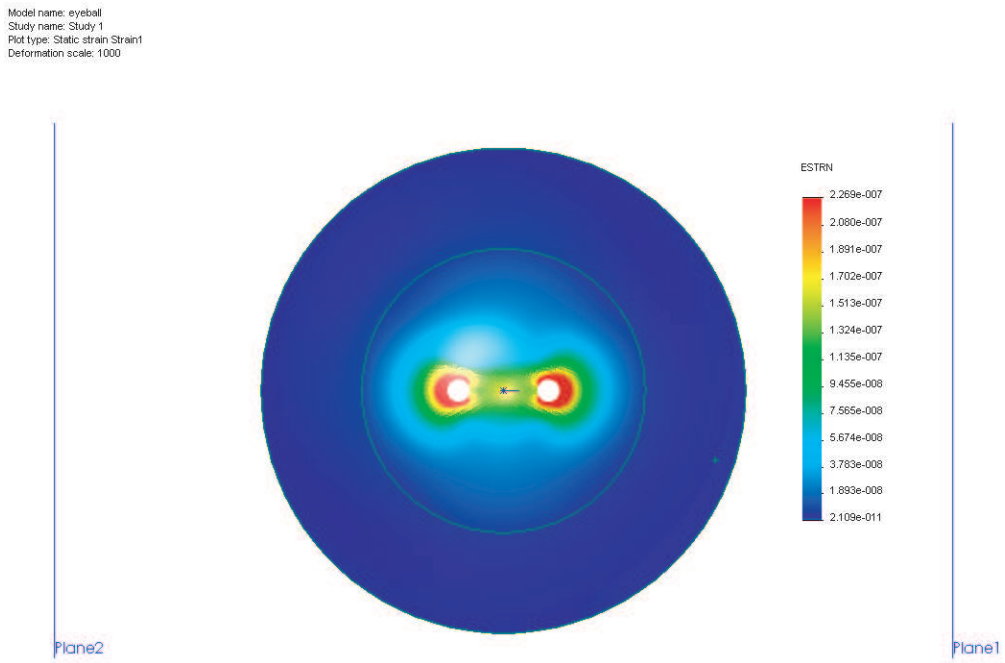

Figure 6.4 SolidWorks simulation of cornea model with stress distribution by backward force.

Calibration by software simulation

Based on the computing simulation work, the parameters of the material can be calculated. Comparing software simulation data with the experimental data of physical model can prove the validity. If the fringe patterns are the same or have the same ratio as the experimental data, then the simulation is successful, and the cornea model simulation can be trusted.

From Fig.6.5, we can set the value of the fringe constant f_σ, and it can be determined by stress difference $\sigma_1 - \sigma_2$ in a model that is made of the same material as the specimen of interest. From the Equation6.1, the strongly birefringent materials will have low values of f_σ, since the stress required to produce a given corresponding value of *N* will be small.

$$f_\sigma = h\frac{\sigma_1 - \sigma_2}{N} \tag{6.1}$$

A common calibration specimen is the circular disk of diameter D and thickness h loaded in diametral compression[103][104].

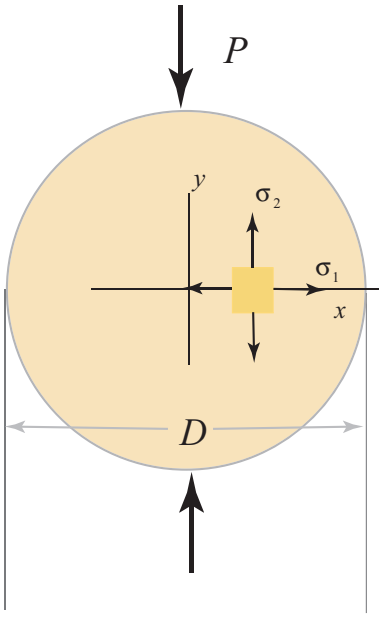

Figure 6.5 Disk in compression.

The horizontal and vertical normal stresses along the *x* axis are principal stresses because the shear stress τ_{xy} vanishes due to symmetry about the *x* axis.

Along the horizontal diameter, the maximum difference $\sigma_1 - \sigma_2$ occurs at the center. At this point,

$$\sigma_1 - \sigma_2 = \frac{8P}{\pi h D} \tag{6.2}$$

Combine equation 6.1and 6.2together,

then,

$$f_\sigma = \frac{8P}{\pi D N} \tag{6.3}$$

where D is the diameter, P is the force loaded and N is the fringe value. The thickness of *h* is not used in the equation, because the relative retardation is proportional to *h*, but for a given force *P*, the stresses are inversely proportional to *h*. f_σ then is independent of *h*.

Fig.6.6 shows the real specimen loaded at the top and bottom in polariscope.

Figure 6.6 Dark-field isochromatic in a diametrally loaded circular disk.

The image data are shown in Fig.6.7. There is a raster line in the middle position cross image data (a) and (b) in Fig.6.7, (a) in Fig6.7 is the computer simulation result of the stress by the software $SolidWorks$, and (b) in Fig.6.7 is the result of physical specimen in experiment. (c) is the intensity distribution of the raster line. The blue line is the result from (a) and red line is the result from (b). Because of the different greyscale between the simulation data and experimental data, the intensity value are different, so in the (c), the blue line is a little bit higher than red line. Although there is some difference at the intensity value, it is not the basis for estimation. The fringe distribution are quite similar between these results. So, combined with calculation, the confirmatory experiment can prove the validity of the system.

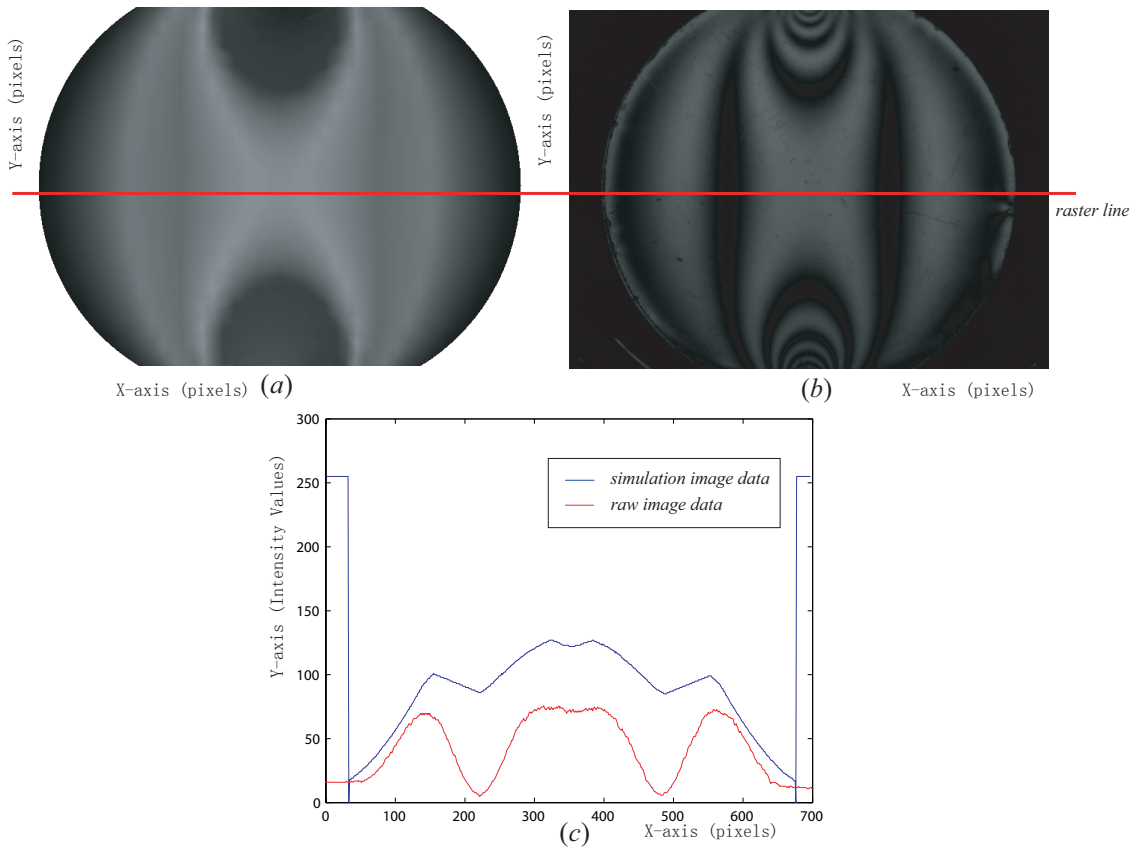

Figure 6.7 Comparison between simulated and experimental results.

Similarly, another specimen is also tested and compared by the same way. The small disk has two pinholes, a backward force has been implemented at opposite directions. This physical model has been made for cornea simulation, the test

results are shown in Fig.6.8.

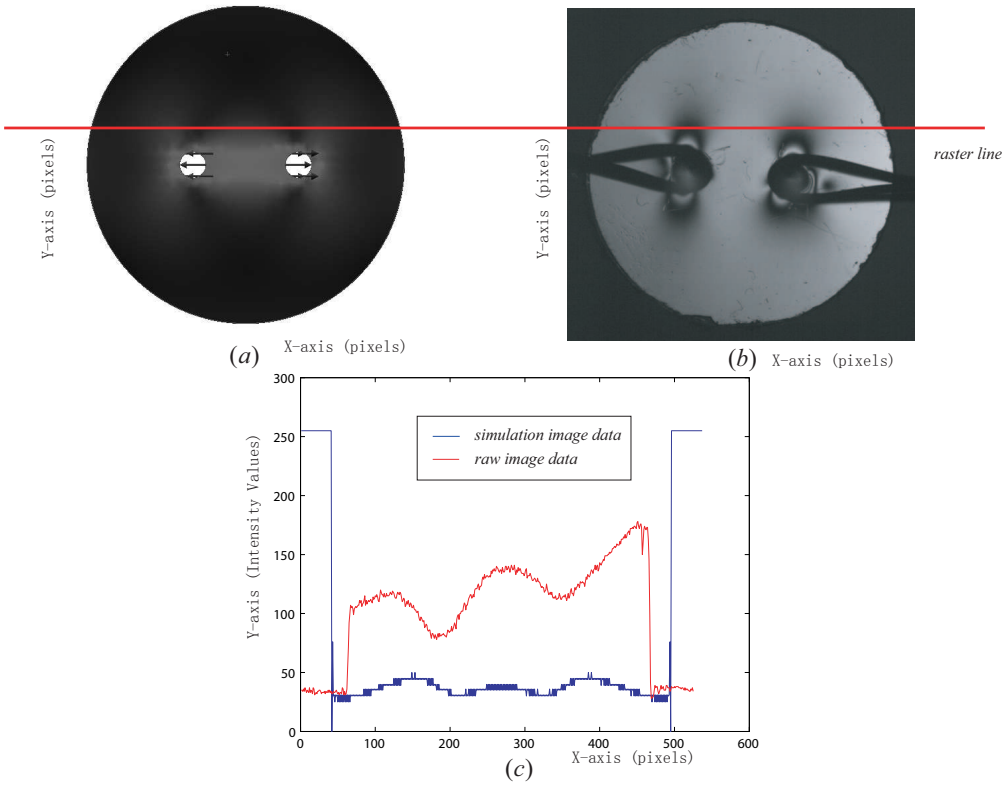

Figure 6.8 Comparison between simulated and experimental results with semi-cornea model.

6.1.2 Simulated Experiment

Summary

A carrier fringe technology for birefringence and phase shifting analysis is described and verified experimentally, where the processing is similar to that in photoelasticity stress analysis. A quartz wedge generates linear carrier fringes. The fringes are superimposed, and are formed by the stress acting on the specimen at the overlapped region. A charge coupled device (CCD) camera is used for capturing the resultant data of fringe patterns. The Fast Fourier transform method is then used to process the complete fringe image over the whole surface of the model. The experiment also uses the phase unwrapping technique to create a continuous map of the unwrapped map field. Finally, the whole field of phase shifting measurement has been calculated and plotted from a single image, which shows the method's potential for use as a reflection analysis system. This is suitable for application to non-stationary objects and complex situations.

Specimen Design

The specimen used for simulating a cornea is of polymethylmethacrylate material. This material is not only a kind of birefringent material, but also a transparent material. A sketch of the specimen disk is shown in Fig.6.9

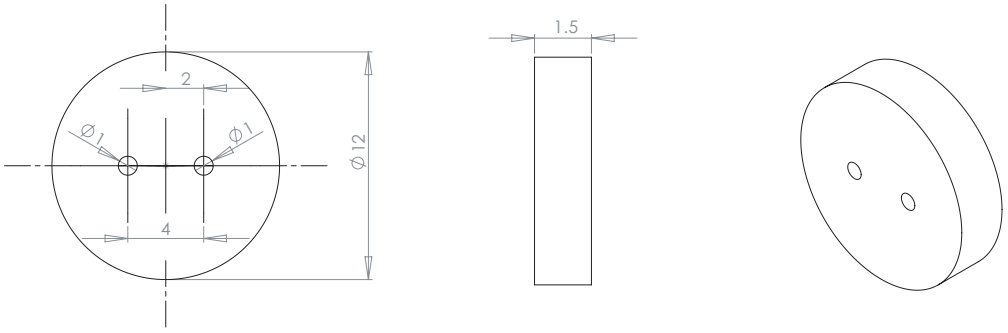

Figure 6.9 Sketch of specimen disk.

The parameter can be read from the design diagram in Fig.6.9, there are two pinholes designed to be axisymmetric to the center point. Another design required

for the component is the frame which holds the specimen. A sketch is shown in Fig.6.10,

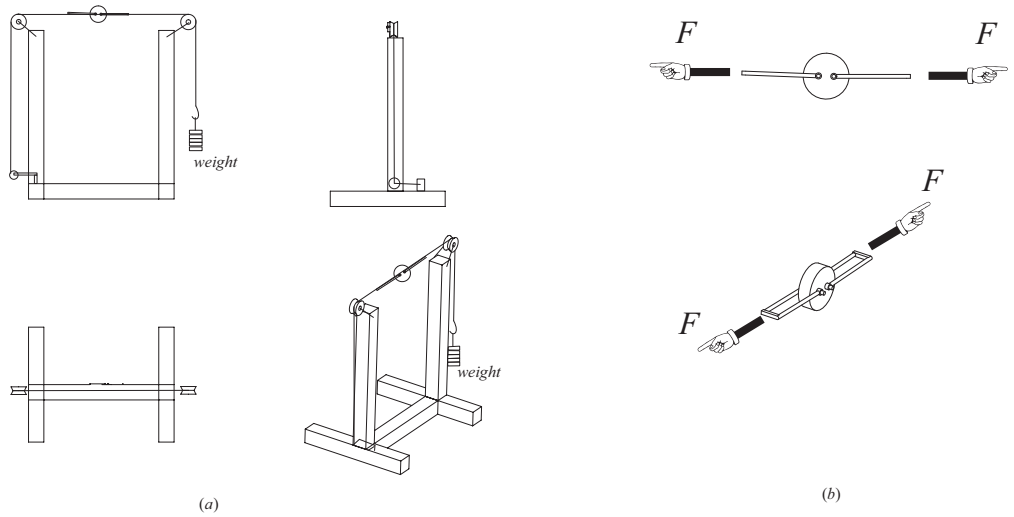

Figure 6.10 Sketch of frame to hold the specimen disk (a) frame (b) specimen disk.

In Fig.6.10, (a) Framework; Two pulleys are attached at both sides. A rope is applied so as to hold weight on one side and is firmly attached on the other. The sample is located in the mid-point of the rope. (b) Two sticks upon which is generated force F via small U-shape components are used as stress points, allowing the generation of force F in the opposite direction.

Experimental Set-up

This section shows an experiment for the whole field of phase measurement based on photoelastic carrier fringe and polariscope using the FFT technique. The continuous phase map will be produced by the phase unwrapping procedure.

A schematic diagram of the experiment is as follows: the system includes two polarisers and two quarter-wave plates, the composition of polariscope, in addition to the light source and diffuser. A CCD camera is used to collect data where the image resolution is 3272×2469 pixels, where each pixel size is $2.7\mu m$, and where the image has a greyscale resolution of 8 bits giving 256 grey levels.

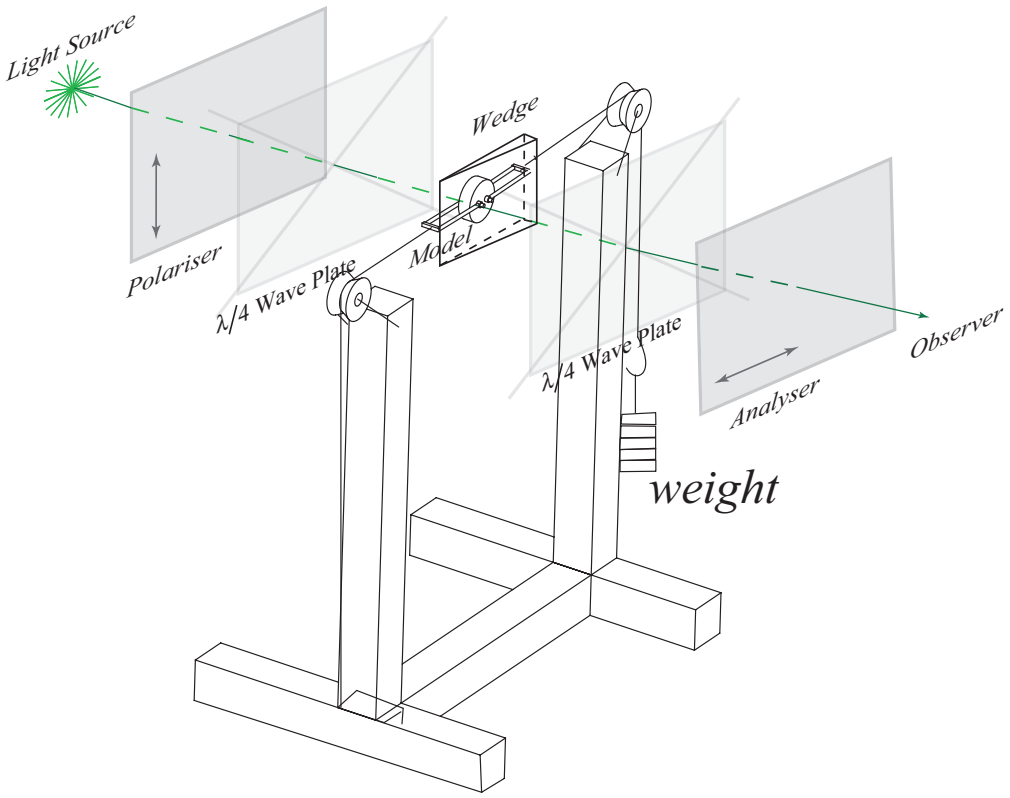

Figure 6.11 Experiment Set-up diagram.

6.1.3 Fourier Transform and Results

In fringe pattern analysis, the Fourier transform method is an efficient evaluation for interferometry. A spatial carrier frequency is introduced by tilting the wavefront. The reconstructed image has a spatial fringe pattern which is phase modulated by

the tilt.

Polymethylmethacrylate is a transparent thermoplastic, it is slightly softer than glass, thus if a small force is applied, the phase shifting will be small. Therefore, for this experiment, another specimen which is a half circular disk 40mm diameter and which is made by $CT-200$ $EpoxyResin$ under a diametrical load will be tested. The experimental data are shown in Fig.6.12 and Fig.6.13.

With a fluorescent light source, the dark field fringe pattern is obtained. This is shown in Fig.6.12.

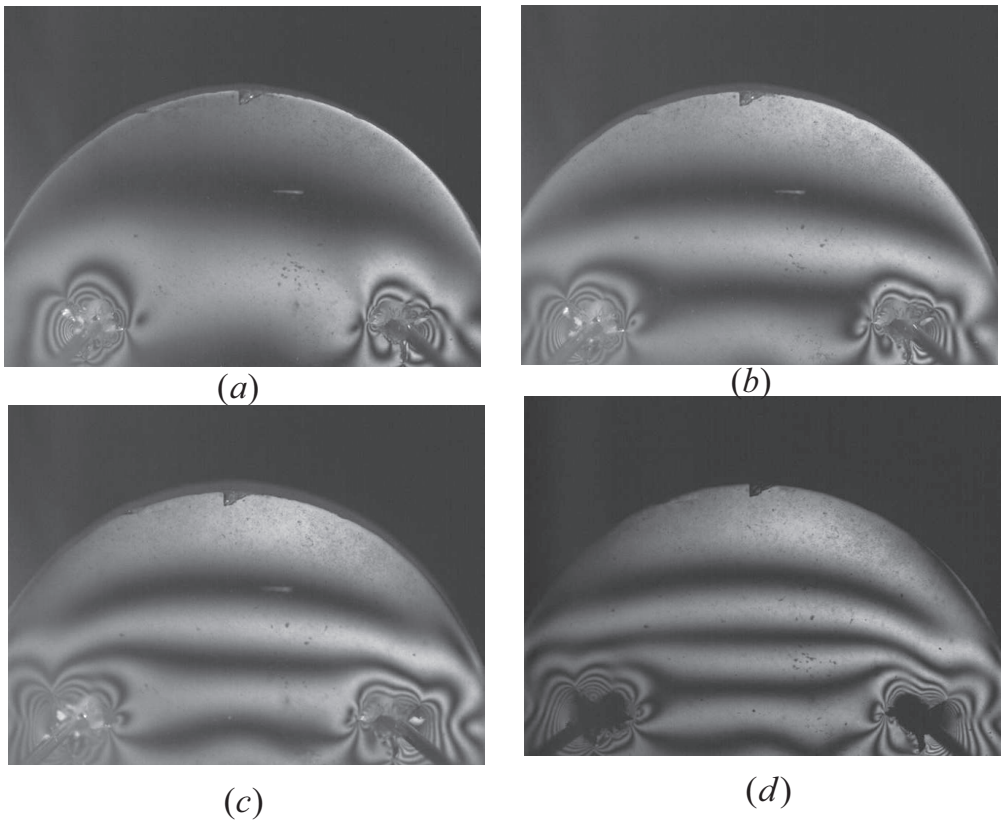

Figure 6.12 Isochromatic fringe pattern of a half circular disk under diametrical force outwards (a) weight is 200g (b) weight is 400g (c) weight is 600g (d)weight is 800g .

To analyse the fringe using the FFT method, the fringe-carrier system is introduced into the polariscope, which is performed by putting a birefringent wedge in front of the specimen for analysis. In this case, even if the phase changes smaller than 2π, it still can be detected and measured.

In the case here, the fringe pattern and stress pattern are overlapped. For com-

parison, a frozen wedge which contains a low frequency fringe pattern is used in the polariscope system as well, and the result is also shown with the high density fringe result. Because of the low frequency, the phase changes of the disk can not be modulated well, especially at the sites of the two pin-holes. The result is shown in Fig.6.13,

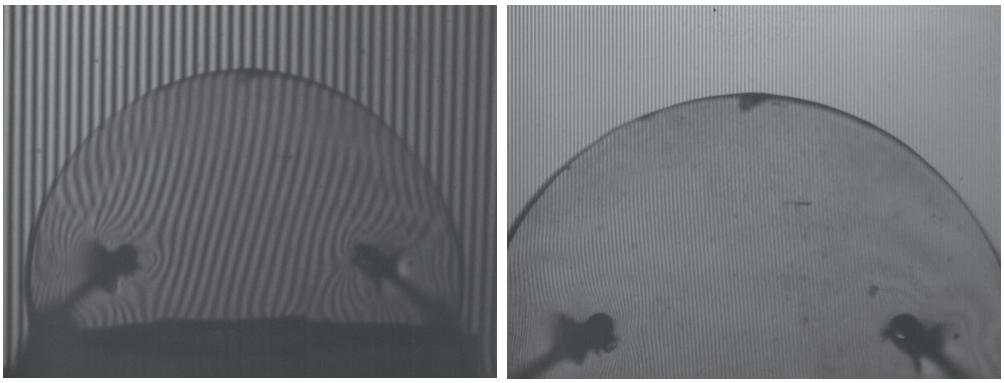

(a) (b)

Figure 6.13 Isochromatic fringe pattern of a half circular disk under diametral force outwards with fringe modulation(a) specimen is with low density fringe (b) specimen is with high density fringe.

Fig.6.14 shows the wrapped and unwrapped phase map of the samples with low density and high density fringe, respectively. As can be seen, for results (a) and (c) in Fig.6.14, the low density fringe results are not smooth as long as the phase modulation by the carrier is low. Also, errors occur in the determination of the direction of the circle. The continuous phase distribution has the opposite orientation in the unwrapped map relative to the high density fringe results. If the carrier frequency is not high enough to separate the sidelobe from the center lobe in the power spectral frequency analysis, a large error will be introduced. (b) and (d) in Fig.6.14 show results which are obtained from high frequency conditions.

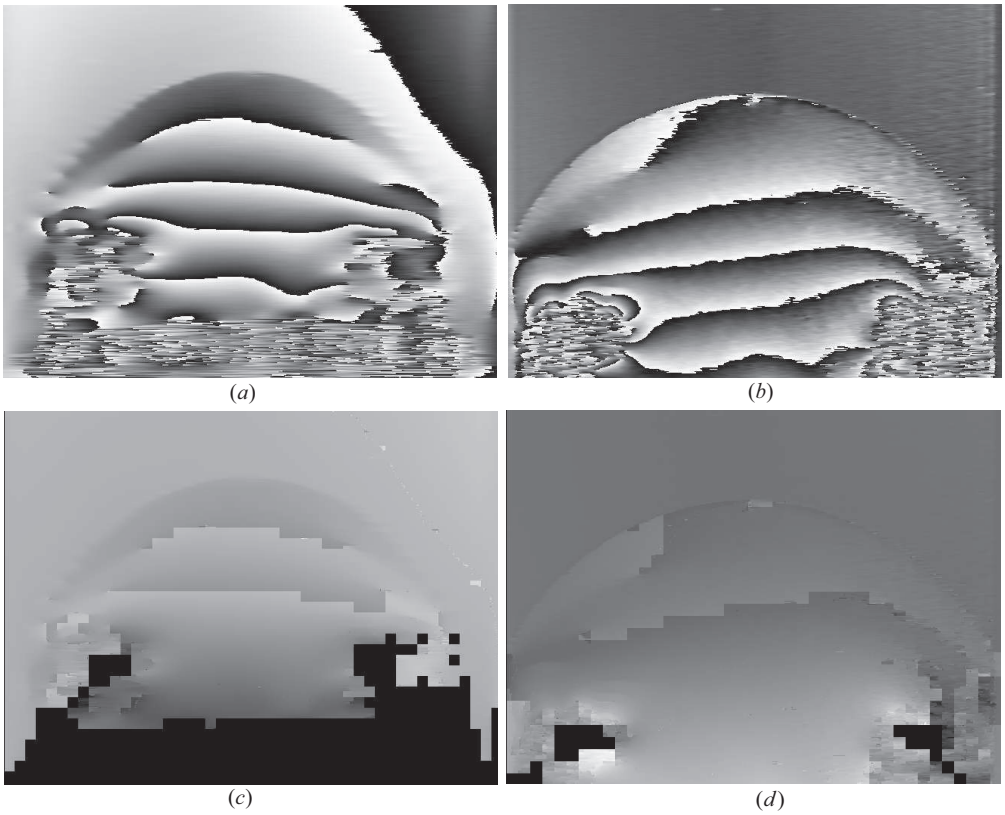

Figure 6.14 Wrapped map and unwrapped map of specimen with low and high density fringe respectively (a) wrapped map with low density fringe (b) wrapped map with high density fringe (c) unwrapped map with low density fringe (d) unwrapped map with high density fringe.

For the high frequency modulation example, the raw image and sample with fringes are shown in Fig.6.15, followed by the wrapped and unwrapped phase maps. Moreover, the 3D perspective plot of phase difference is shown in Fig.6.16. In Fig.6.16, the two maps shows the different angle of the reconstruction.

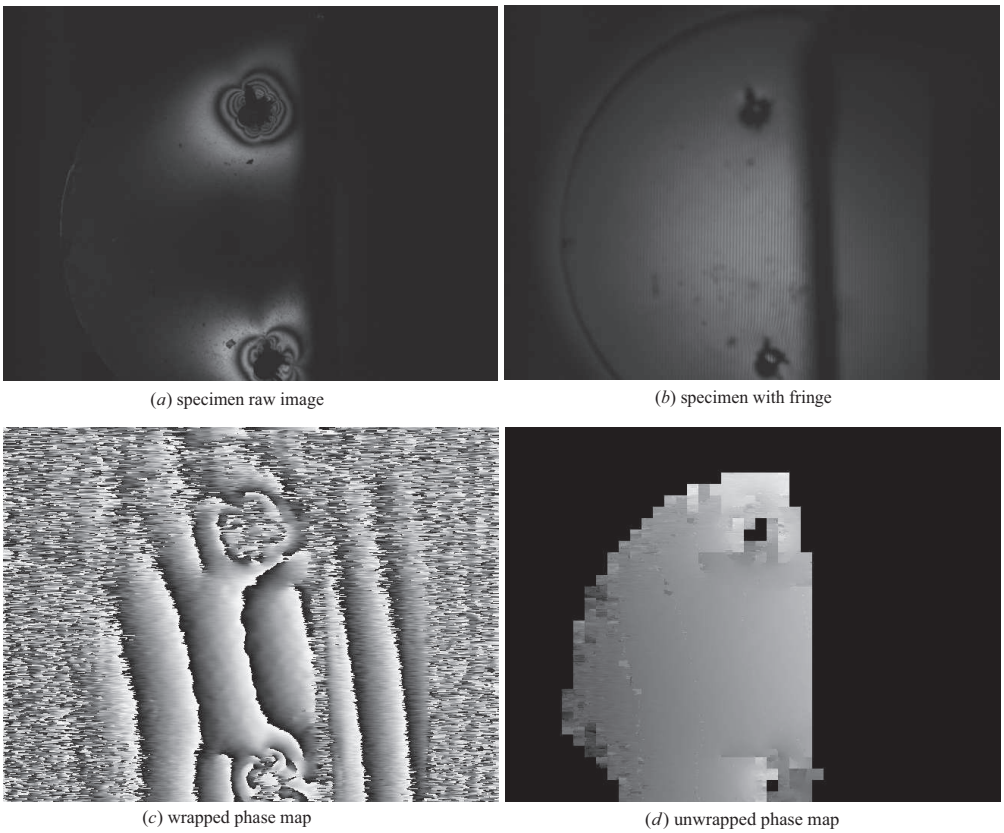

(*a*) specimen raw image (*b*) specimen with fringe

(*c*) wrapped phase map (*d*) unwrapped phase map

Figure 6.15 Specimen without loading example (a) original situation (b) specimen with fringe (c) wrapped phase map (d) unwrapped phase map .

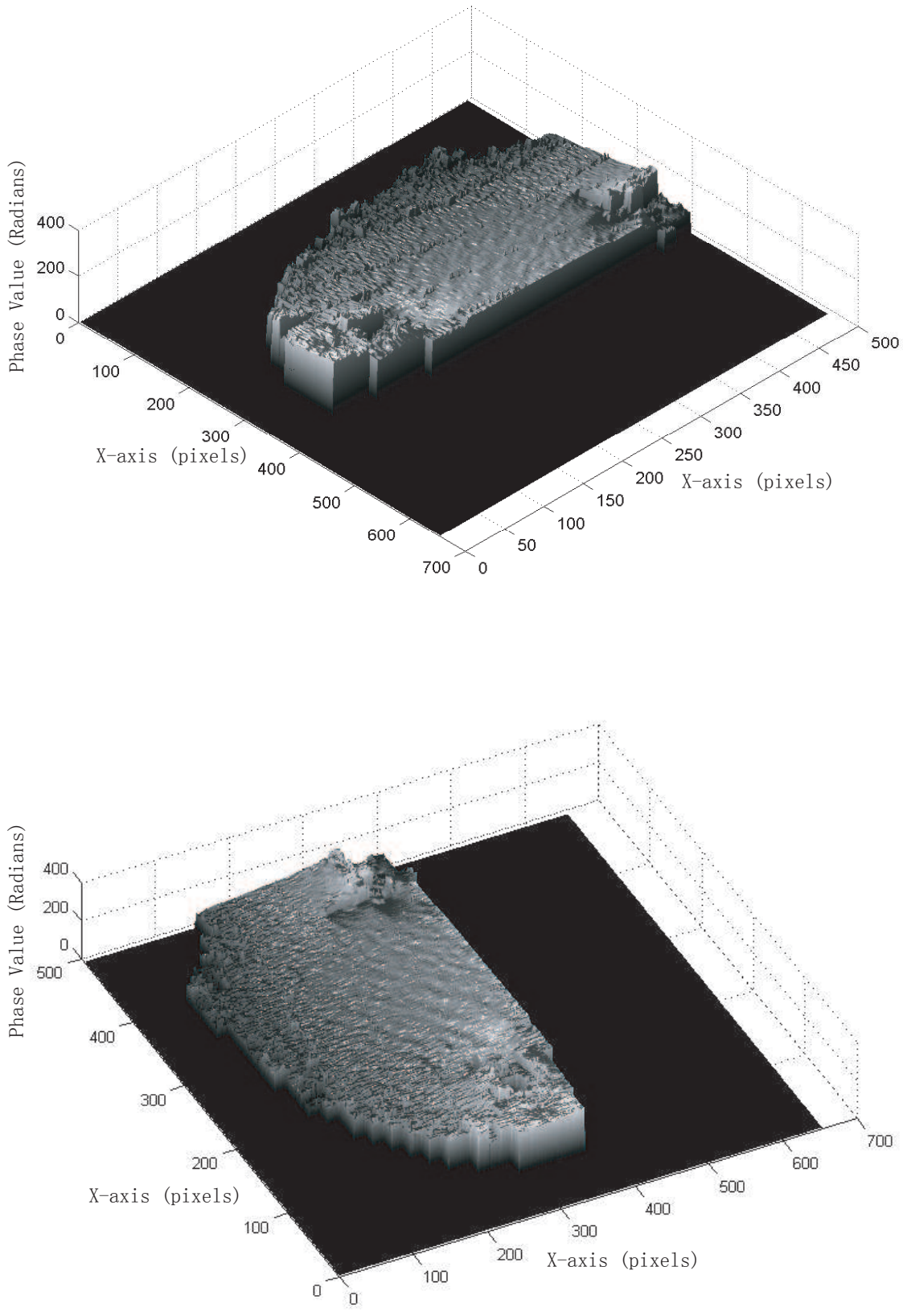

Figure 6.16 3D prespective plot of phase difference distribution.

Moreover, discontinuities may occur when the phase modulation is small, such as the sites near and around the two pin holes. Using the high density fringe wedge, we can see from Fig.6.17 captured the specimen which was not under any pressure. It shows the original orientation of specimen.

Figure 6.17 Specimen without stress loaded (a) without wedge (b) with wedge (c) wrapped phase map.

The phase change can be seen clearly if the stress is introduced in different stages. Fig.6.18 shows the specimen loaded with 200g, 400g, 600g and 800g weights, and shows the wrapped phase maps for each.

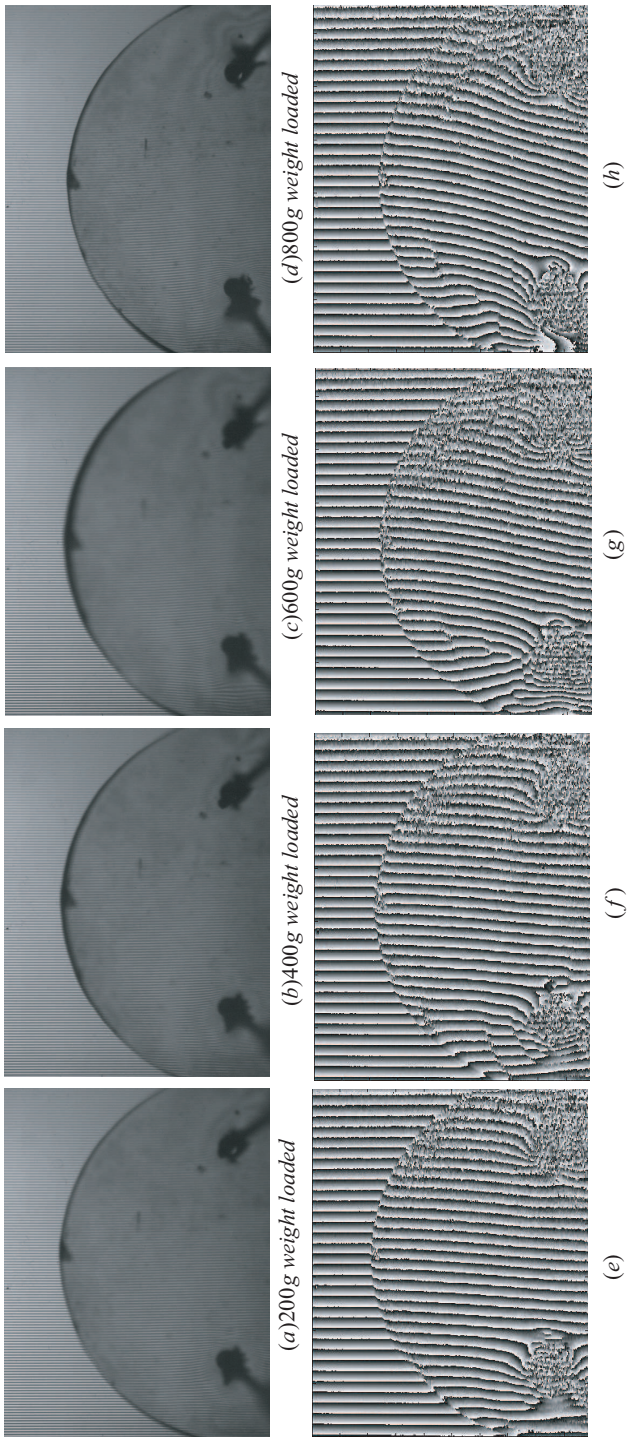

Figure 6.18 Specimen with different stress loaded (a) with 200g weight loaded (b) with 400g weight loaded (c) with 600g weight loaded (d) with 800g weight loaded (e) (a) wrapped phase map (f) (b) wrapped phase map (g) (c) wrapped phase map (h)(d) wrapped phase map.

To analyse phase shifting, we need to put the original data which were obtained from the specimen without any stress loading and the stress loaded specimen together for comparison.

For the specimen without loading stress, the phase wrapped map is shown in Fig.6.19, in which the raster line of pixels 150 and 1110 are shown in blue and red, respectively, and where the green line is shown for the 1800 pixel line position.

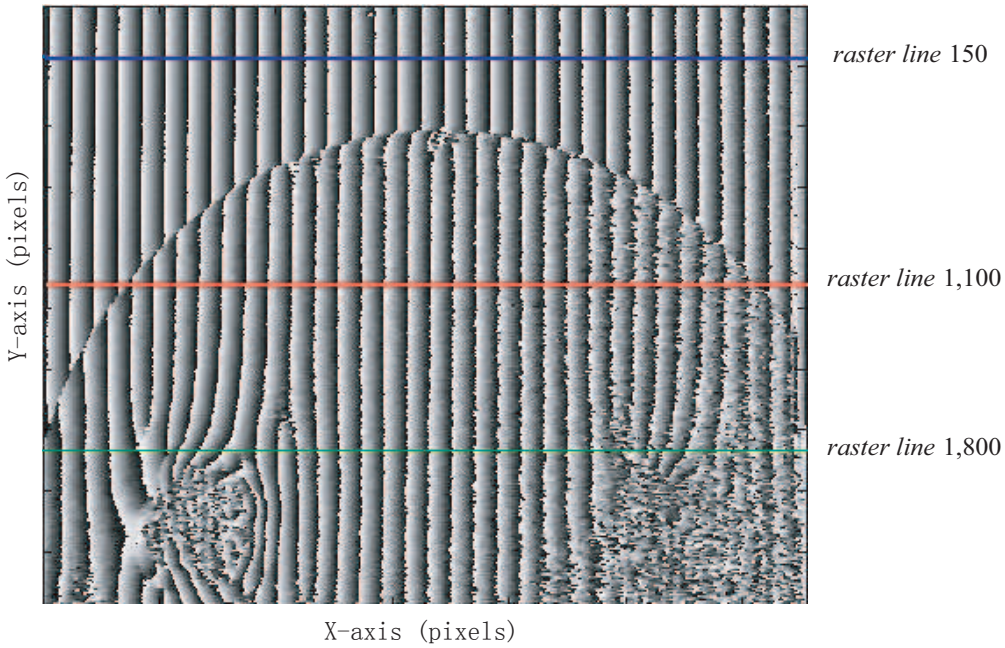

Figure 6.19 Specimen without stress loaded wrapped phase map.

In Fig.6.20, we can see the phase wrapped data of the rasters described as the intensity value, obtained using $Matlab$. The color matches the raster lines color in Fig.6.19.

In Fig.6.21, some details of Fig.6.20 could be studied.In the starting range from 0 to 50th pixels, the red and blue data should be at the same position. We can see some noise occurred in this range about 10 pixels at background. At the range of 140th to 170th pixels, the displacement is around 55 pixels.

If we compare these with the green raster line at 1800 pixels, the fringe displacement between the red line and green line is also no more than 10 pixels. So, compared with the background fringe which the fringes are around 150 raster line, we could not identify any tilt of the fringe if there is no phase shifting.

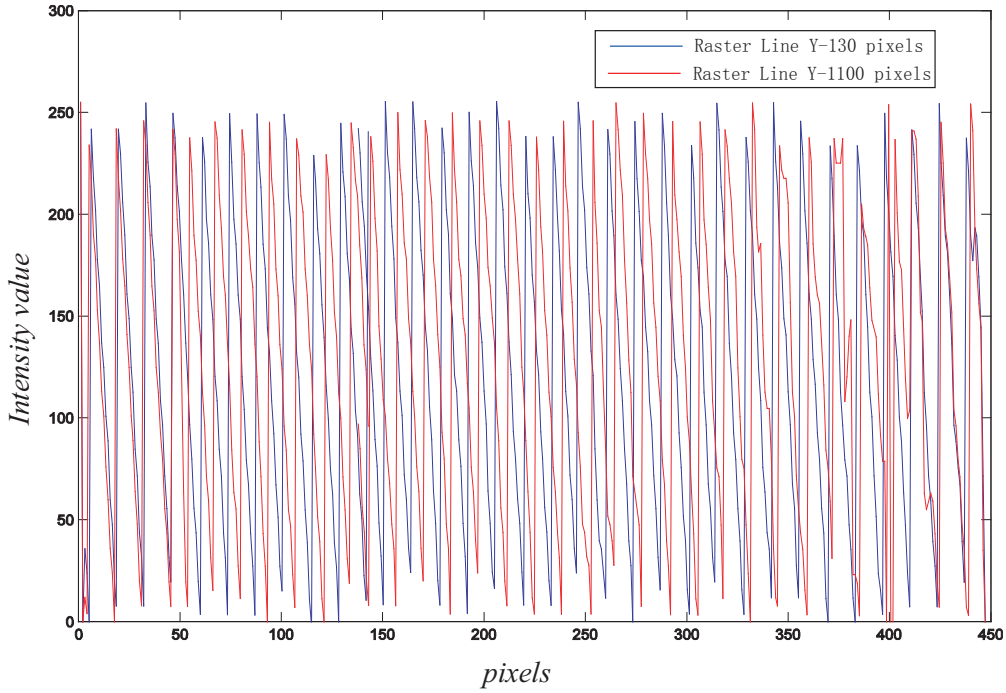

Figure 6.20 Comparison of phase between the raster line at Y axis 150 and 1100 .

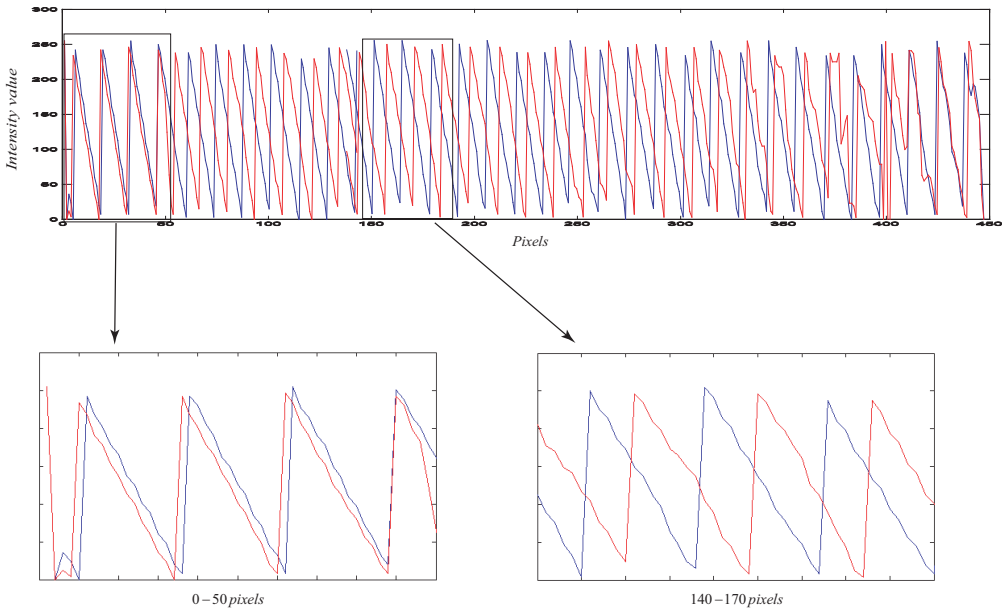

Figure 6.21 Digitized intensity data of phase wrapped map of rasters in sample.

With the stress loaded, the 200g weight loading result is compared with the 800g weight loading result in Fig.6.22. The yellow line shows the phase shifting change and the magenta line shows both the bending curve of the fringe and phase shifting by the stress at the bottom of the sample.

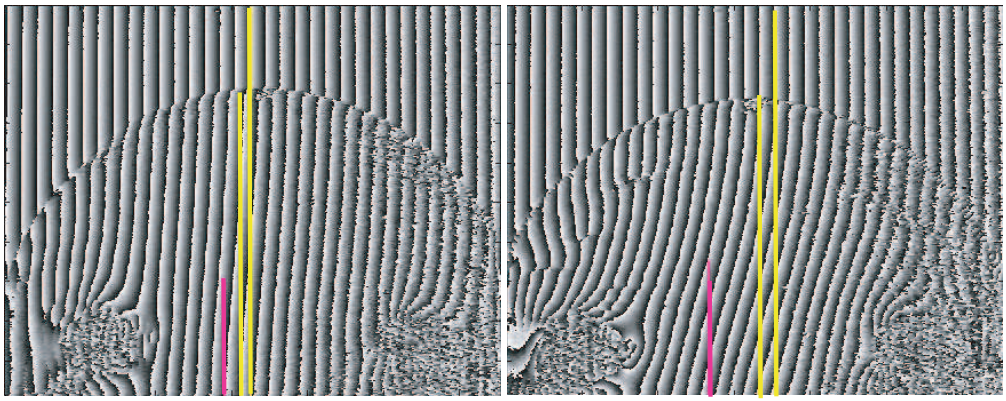

(a)200g weight loaded phase wrapped map (b)800g weight loaded phase wrapped map

Figure 6.22 Compared fringe displacement between 200g weight loaded and 800g weight loaded with phase wrapped map.

To compare the fringe displacement and phase shifting, we can a draw curve from the pixel value from the phase wrapped map. The $X-axis$ is the pixel value at the vertical direction from top to bottom. The $Y-axis$ shows the fringe curvature change on the area of the bottom of sample. So if phase shifting occurred, the blue line (fringe displacement) will changes significantlly compared with the reference red line. It is shown by the results shown in Fig.6.23, that the 800g weight loading result results in larger phase shifting than the 200g loading case.

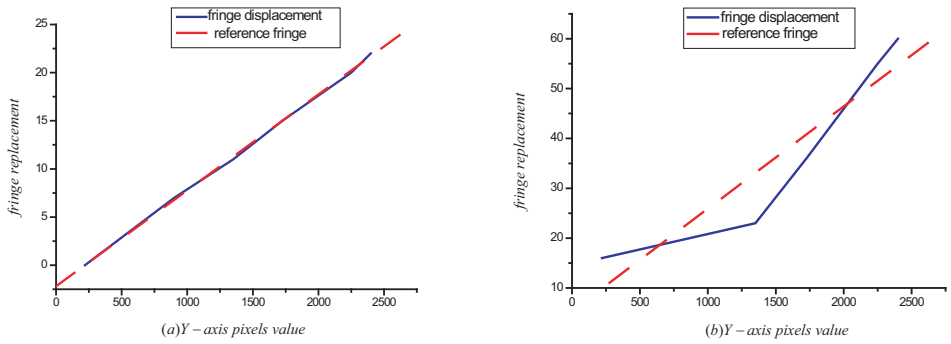

Figure 6.23 Compared phase shifting between 200g weight loaded and 800g weight loaded by curvature changes.

In another experiment, the polymethylmethacrylate disk specimen is tested with the same method. The set up structure is as was shown in Fig.6.11. Although this kind of material sample is hard to deform, the thickness is around 1.5mm, and so the fringe shift could be observed using the polariscope.With the weight increased from 0g to 1500g, the correspondent images are shown in Fig.6.24,

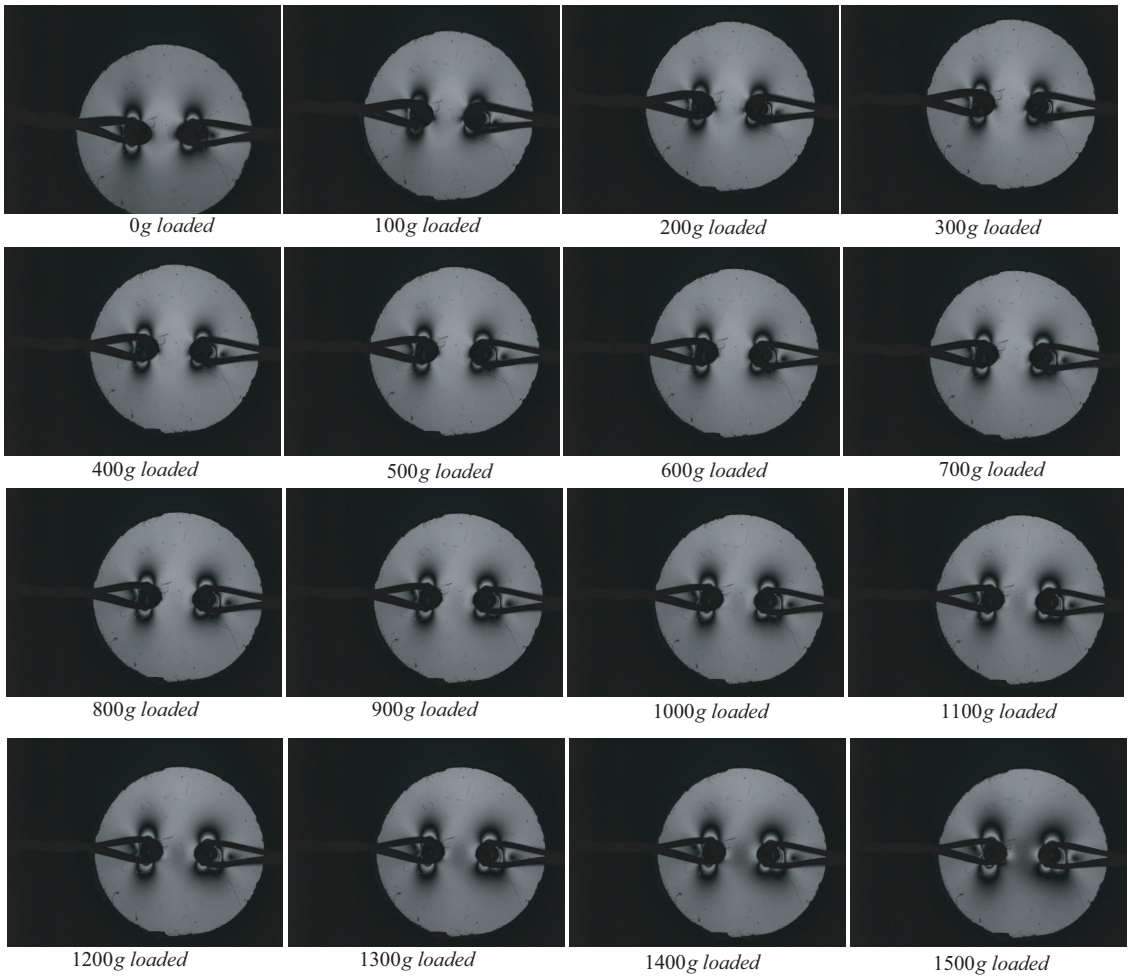

Figure 6.24 Stress distribution on Disk specimen with the load increasing from 0 gram to 1500 gram.

When the crystal quartz wedge is put in front of the specimen, the fringe shifting can be detected. The 300g and 1500g weight loaded results are compared below as an example. The raw data are shown in Fig.6.25.

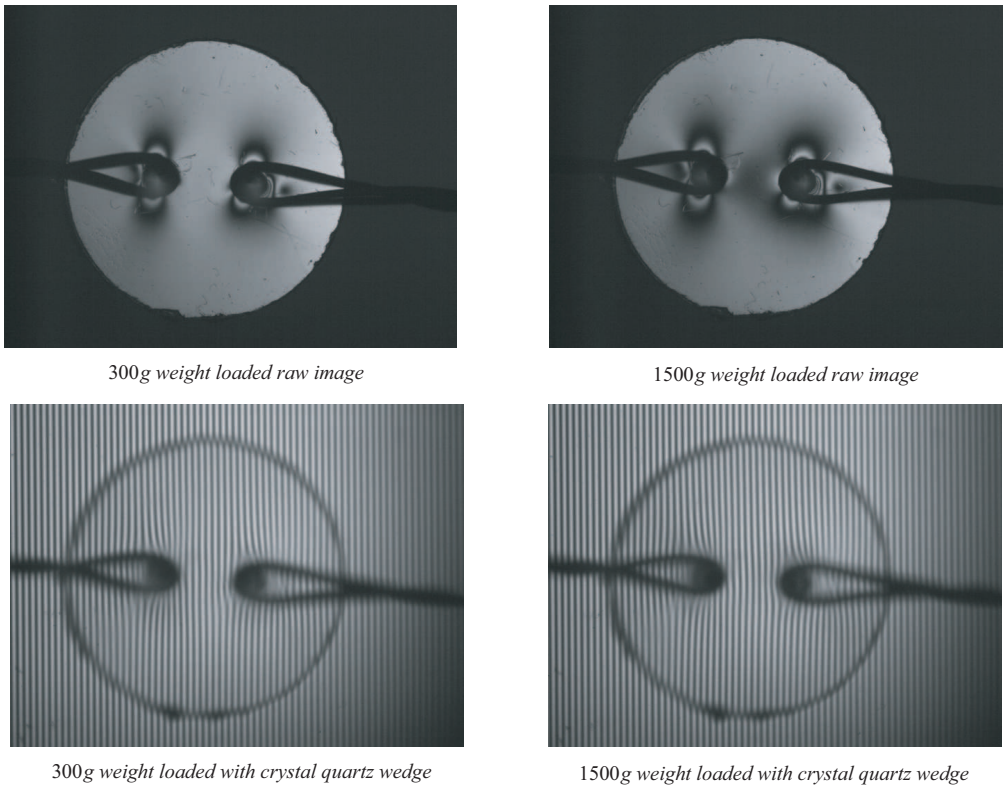

Figure 6.25 300 gram and 1500 gram raw image and with fringe.

By using Fourier transform method, the phase wrapped map and unwrapped map are shown in Fig.6.26 separately,

Using the wrapped map of these two results to do differential analysis, we can estimate the phase shifting in the experiment to know if the phase change occurred. And phase changes distribution can also be seen in Fig.6.27.

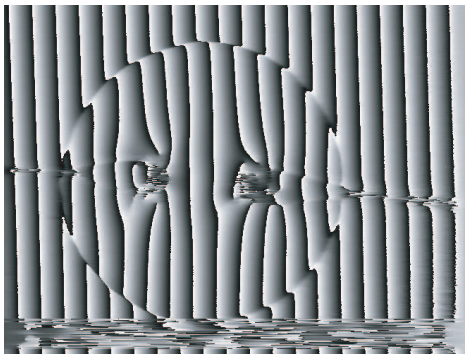

300g *weight loaded wrapped map*

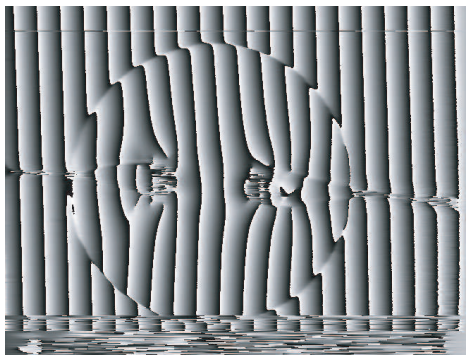

1500g *weight loaded wrapped map*

300g *weight loaded unwrapped map*

1500g *weight loaded unwrapped map*

Figure 6.26 300 gram and 1500 gram wrapped and unwrapped phase maps.

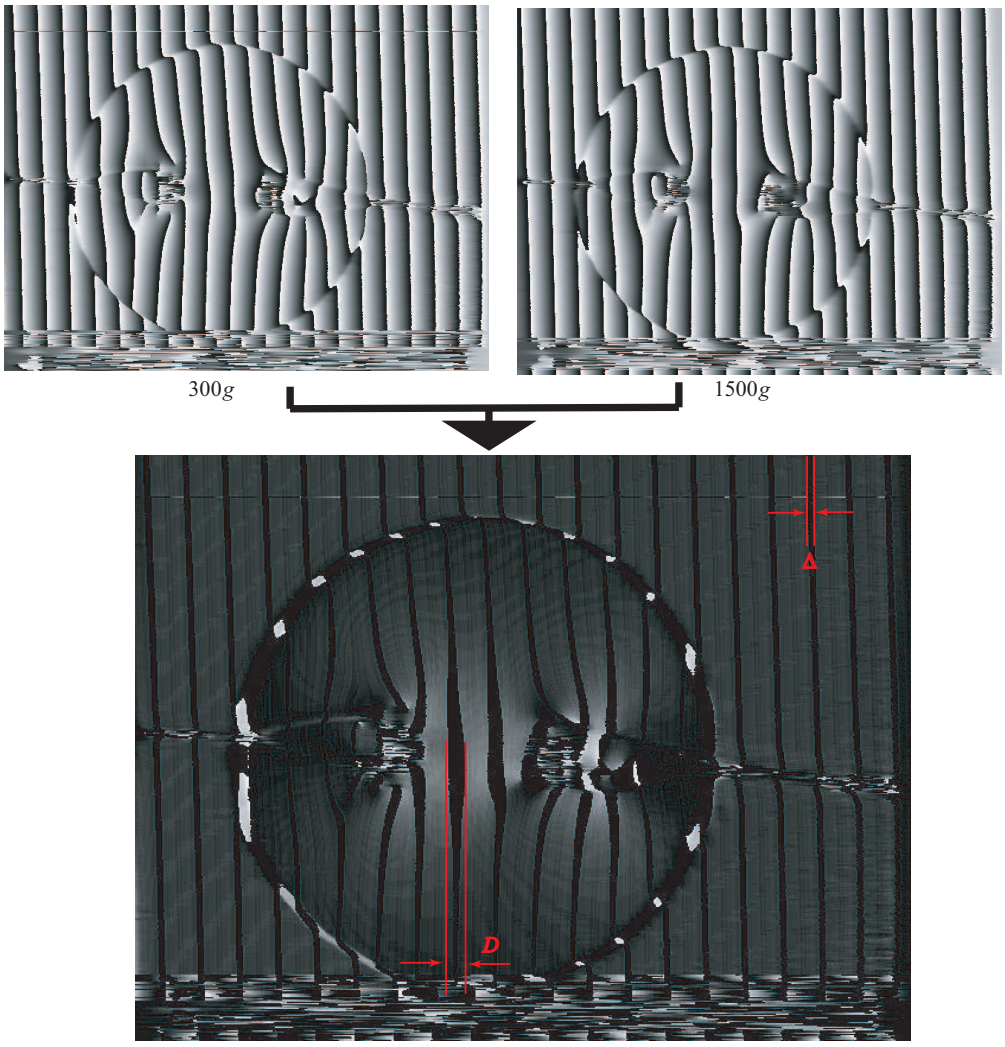

Figure 6.27 300 gram and 1500 gram wrapped map comparison.

Fig.6.27 shows the difference of phase changing between 300g weight loaded and 1500g weight loaded results. Δ is the background phase error difference, D means how much the phase changes. In the center part, D is much bigger than the Δ value, so the value of phase changing is $D - \Delta$. In order to better compare the results of phase change, a raster line is shown in Fig6.28. and Fig.6.29. From Fig.6.28 and Fig.6.29, the raster line and the gradient of the phase map can be compared.

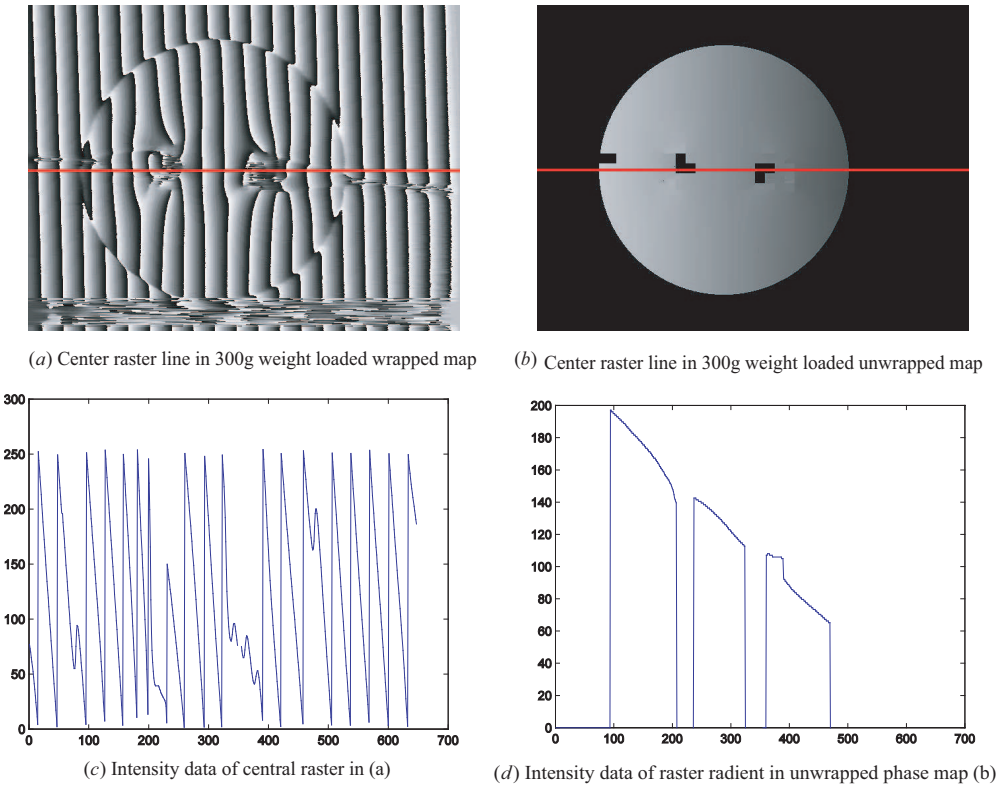

(*a*) Center raster line in 300g weight loaded wrapped map

(*b*) Center raster line in 300g weight loaded unwrapped map

(*c*) Intensity data of central raster in (a)

(*d*) Intensity data of raster radient in unwrapped phase map (b)

Figure 6.28 300 gram weight loaded condition.

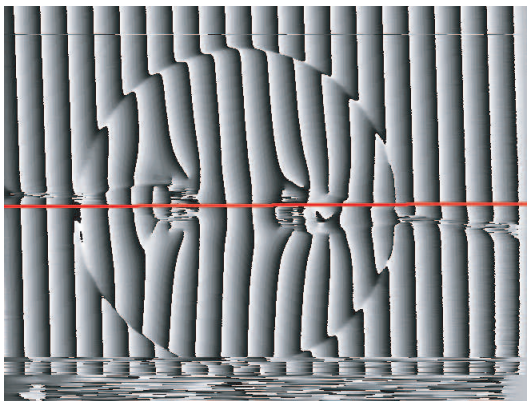

(*a*) Center raster line in 300g weight loaded wrapped map

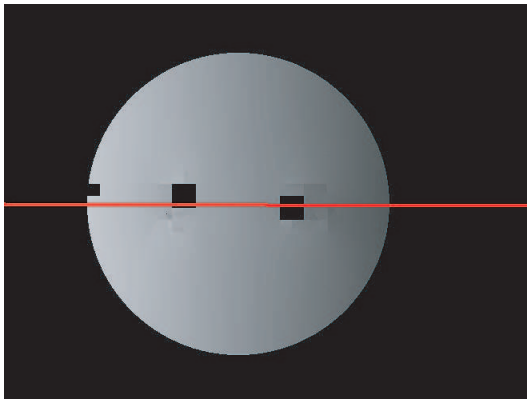

(*b*) Center raster line in 1500g weight loaded unwrapped map

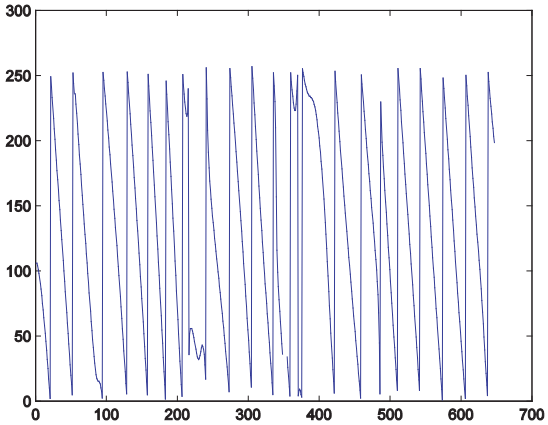

(*c*) Intensity data of central raster in (a)

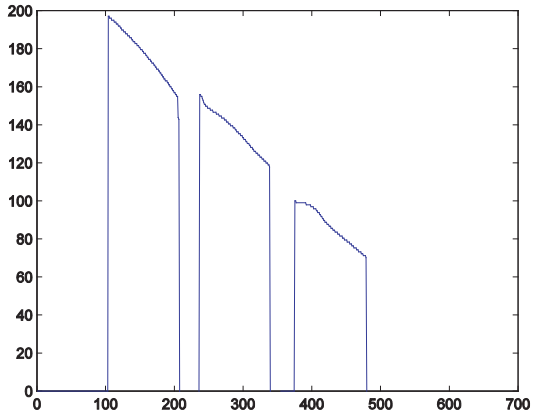

(*d*) Intensity data of raster radient in unwrapped phase map (b)

Figure 6.29 1500 gram weight loaded condition.

All in all, when the different value of forces are added, the phase changes could be observed clearly from the results. Here, the 300 gram weight loaded and 1500 gram weight loaded results are listed in Fig.6.30. The raster line with red colour cross the (a),(b),(c)and (d) at the middle position of each image. (a) is the raw image of the disk with the force loaded; (b) is the situation of the fringe added with (a); (c) and (d) are the results of the wrapped and unwrapped map comes from (b) by using *FFT* phase technique processing. These image data are examples of 300 gram weight loaded, the same processing results of 1500 gram weight loaded are used to compare with them, not shown in the Fig.6.30. In Fig.6.30, (e),(f),(g) and (h) are the comparison of raster line information between 300 gram and 1500 gram weight which are loaded respectively.

The position of the pinholes are the area around 1100 and 1700 pixel points. From (e), the phase changed information can be obtained clearly from the middle part, which is around 1500 pixel at the X-axis. it is nearly a half fringe period changes, but it is not obviously to see from (f). From (g)and (h), it is obviously to see the big phase changes at the area between the two pinholes and small area around the pinholes. In (g), the phase shifting is changed about half period from 1100 to 1700 pixels of X-axis. From phase unwrapped map, the red line shifts much between two pinholes and some phase changes around right pinhole happened at the 1900 pixel of X-axis.

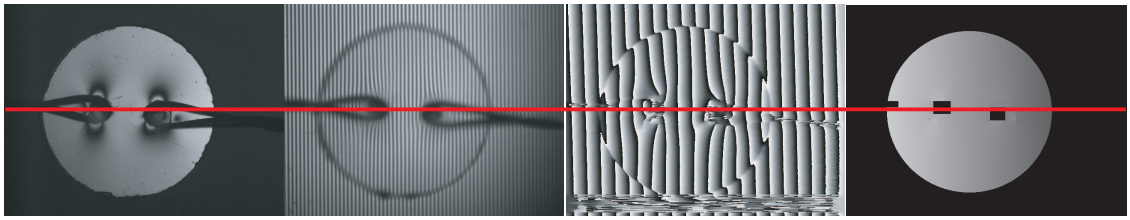

(a) Disk speicmen with weight loaded (b) (a) with fringe added (c) Phase wrapped map (d) Phase unwrapped map

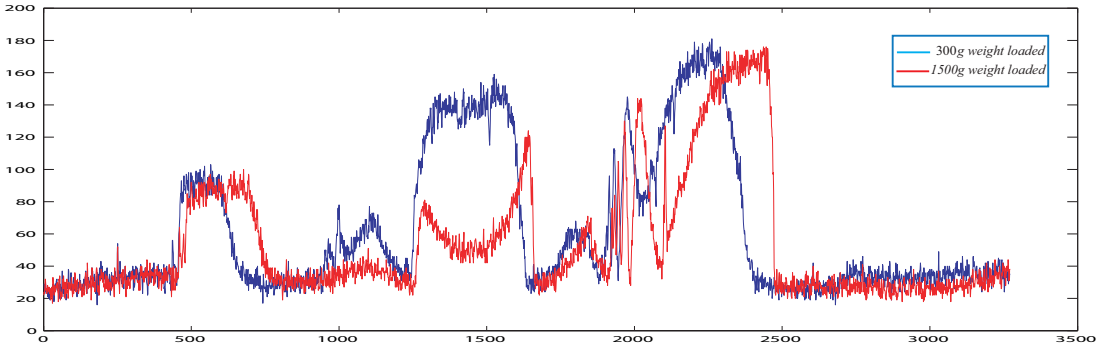

(e) Raster line information from (a)

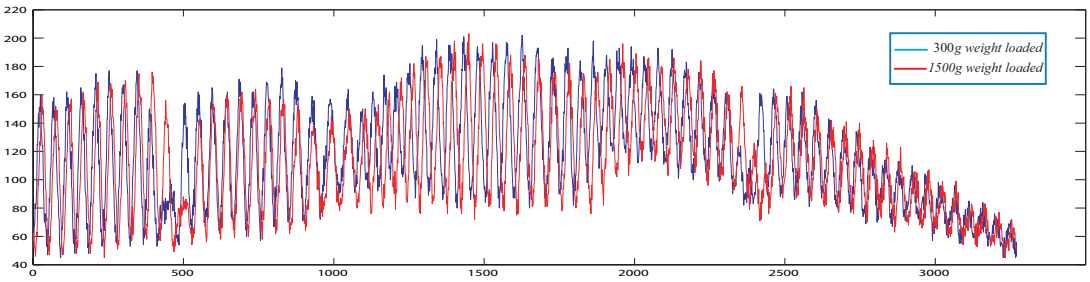

(f) Raster line information from (b)

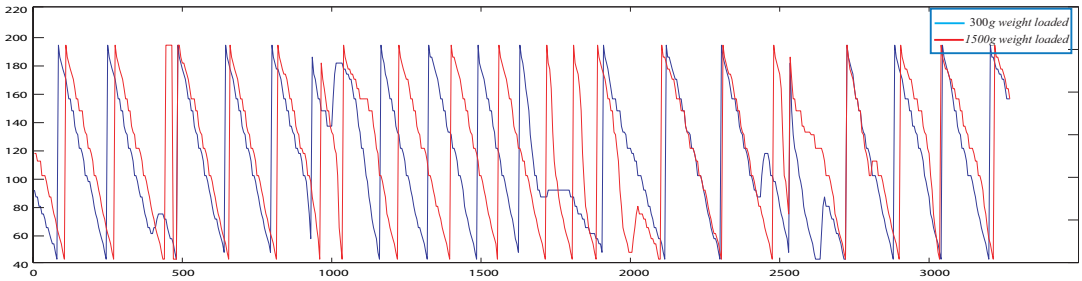

(g) Raster line information from (c)

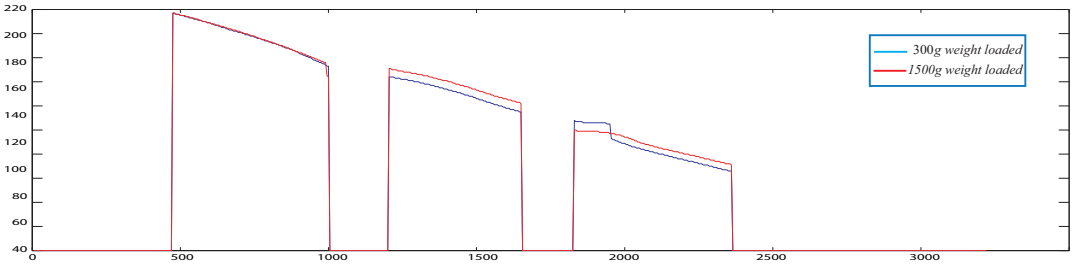

(h) Raster line information from (d)

Figure 6.30 Phase shifting comparison between 300 gram and 1500 gram weight loaded by raster line.

After removing the gradient of the background, Fig.6.31 shows the 2D stress distribution on the disk when a weight of 300g weight is loaded. Fig.6.32 shows a 3-D plot of the distribution of the stress difference for the sample. This shows that the stress difference is large near the loading point, and because of the free boundary of the disk, the value of the stress difference is zero around the edge of the disk. Fig.6.33 shows a contour map of a disk under the force of a 300g-weight.

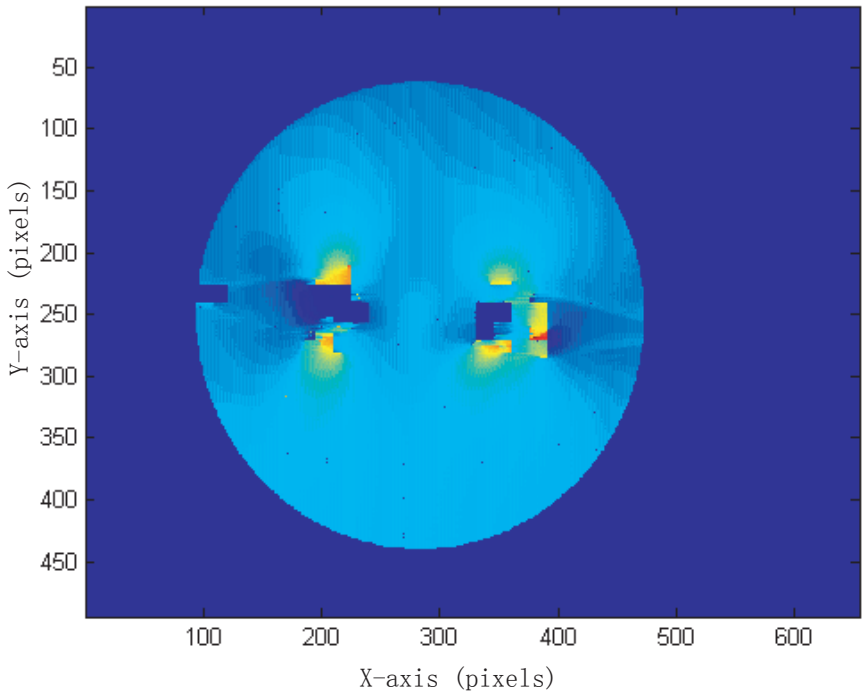

Figure 6.31 300 gram weight loaded phase distribution.

For the sample loaded with 1500g weight, Fig.6.34 shows the 2D stress distribution on the disk loaded with 1500g-weight. Fig.6.35 shows a 3-D plot of the distribution of the stress difference for the sample. Fig.6.36 is a contour map of a disk under a force of 1500g-weight.

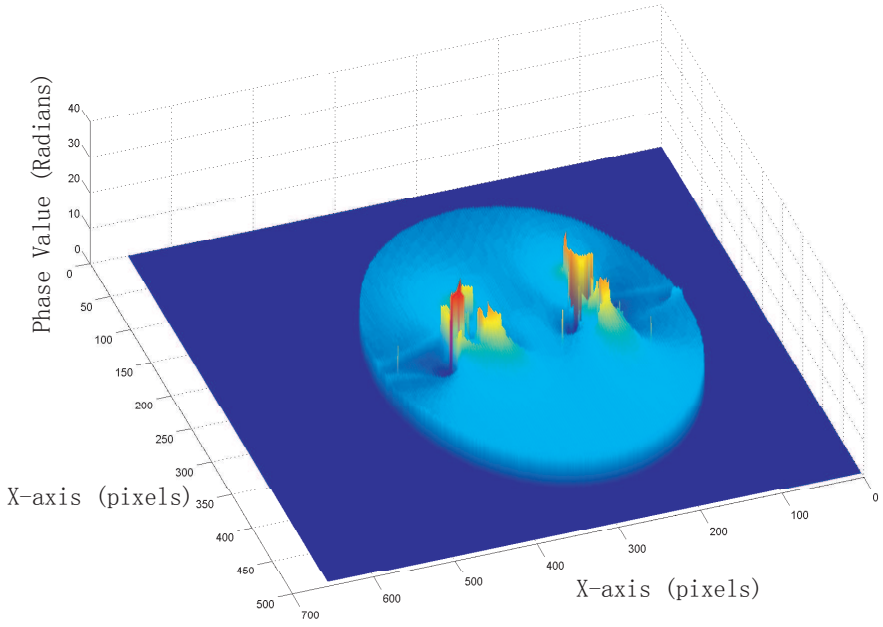

Figure 6.32 300 gram weight loaded 3D perspective plot of principal phase difference for the disk.

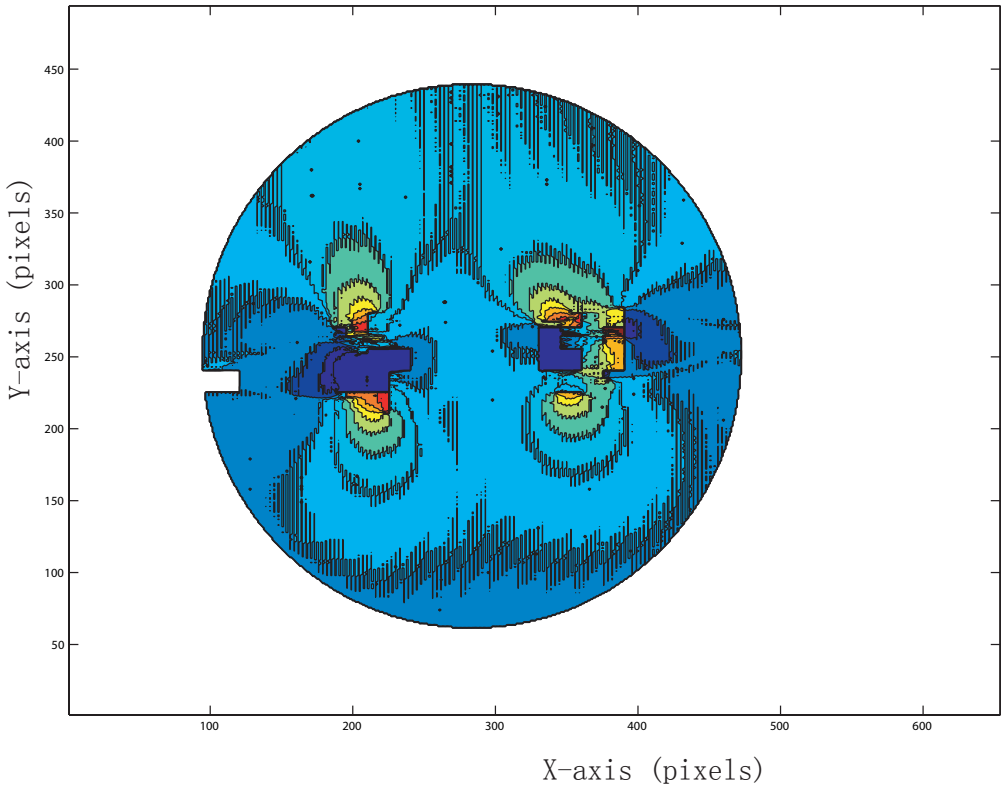

Figure 6.33 Contour map of the disk.

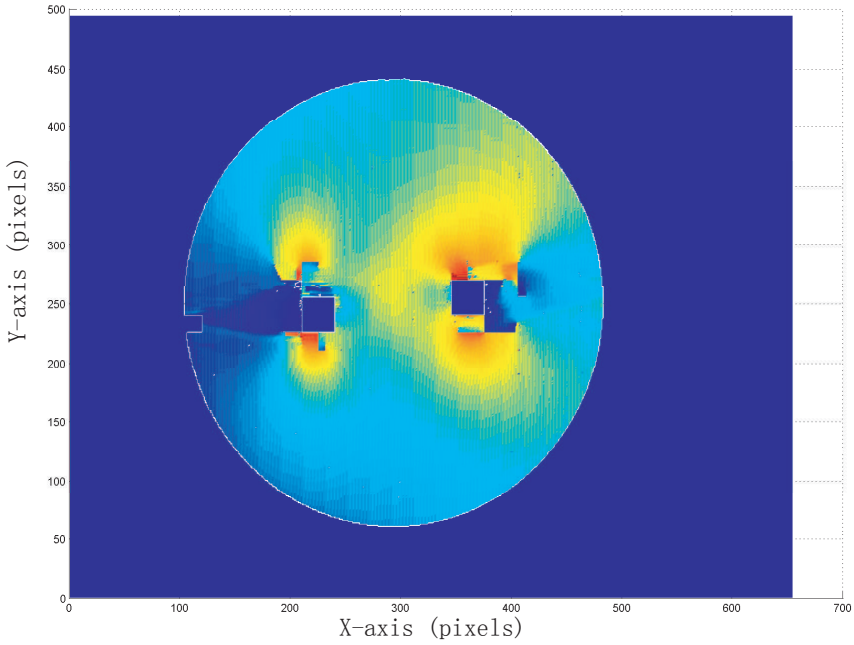

Figure 6.34 1500 gram weight loaded phase distribution.

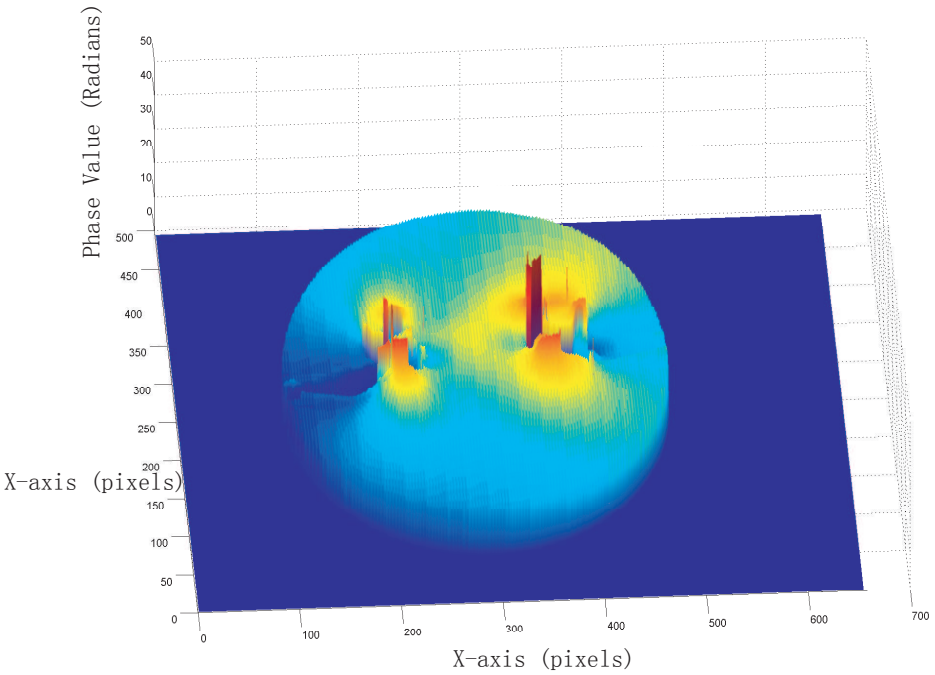

Figure 6.35 1500 gram weight loaded 3D perspective plot of principal phase difference for the disk.

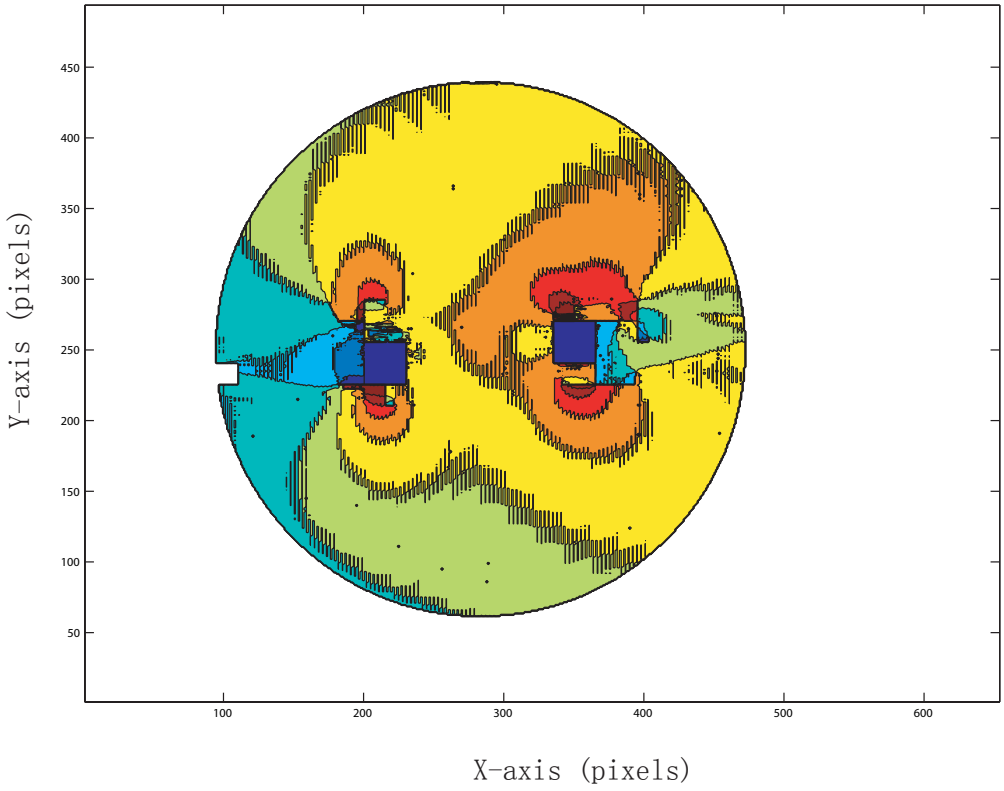

Figure 6.36 Contour map of the disk.

In this section, the novel feature of the research to explore a simulation method for a cornea, which is to generate a linear carrier fringe to phase measurement has been described. The main focus of this work is to apply carrier fringe and Fourier transforms techniques to phase measurements during simulation. The successful simulation of the cornea phase measurement will demonstrate the methodology, and will provide a new method which may be compared with phase stepping measurement. In the following section, the accuracy and advantages of the two methods will be examined and compared. Moreover, in clinical medicine applications, simple and quick measurement processing has a more practical application.

The fringe carrier has been applied to the phase shifting measurement, although the fringe could easily be generated by the birefringent wedge in the polariscope system. The fringe is modulated by the linear carriers. A theoretical analysis of the carrier fringe technique is carried out by using $Jone's$ matrix method. Interactive software for the analysis phase is provided while new $Matlab$ code has been developed for its use, which can also work for high resolution image data, during low frequency conditions. The fringes may also be modulated and analysed.

Unlike the phase stepping technique, only one frame is needed to form the fringe information using the FFT method. But it has been found that the high stress concentration area can not be solved completely using the high density frequency wedge. Although it could be demonstrated by increasing the density of the wedge fringes, this is difficult to accomplish through material processing.

6.2 Cornea Measurement - Transmission Polariscope System

6.2.1 Study of Isolated Cornea with Polarised light

In this section, a real cornea will be examined with polarised light. The study of a cornea which was placed between a polariser and crossed analyser with a dark cross-shaped figure with peripheral concentric coloured bands was produced

in 1861, and the earliest example was reported by Brewster in 1815 with a cornea that was anisotropic[105].

The application of quantitative polarization techniques on biological tissues has many difficulties; however measurements can be carried out with accuracy of 0.05 radian if the tissues can be suitably examined in a polarizing microscope. In this case, the polariscope system is implemented, and based on this system; phase stepping and Fourier transform techniques may be implemented. Comparisons of both techniques for measuring phase retardation are therefore analysed, which may be of some interest to those concerned with the measurement of biological tissues elsewhere.

A study of corneal stromal lamellar organization by using polarization biomicroscopy has been undertaken[96]. The $Mueller$ matrices and circular polariscope system has been used for describing and testing using a physical model, and investigating the lamellar structure of human corneas.

In this research, phase retardation has been analysed demonstrating that it is possible to show the phase distribution and accuracy deduced from the measurements of the birefringence of the individual corneal fibres. This research differs from previous work in that here $Jones$ matrices are applied using the Fourier transform method, while at the same time; the results obtained are compared with those using the phase shifting method.

6.2.2 Phase Stepping Method

Description of System

Fig.6.37 shows the diagram of the system which is drawn by $SolidWorks$.

The system consists of a normal polariscope structure which includes a light source, a diffuser, a polariser plus quarter wave plate, a specimen,a quarter wave plate plus an analyser and a camera. A CCD camera is used to capture the image where the resolution may reached approximately 10 megapixels. Every pixel has a resolution of 8 bits, which is a 256 grey level. Through adopting another monochromatic

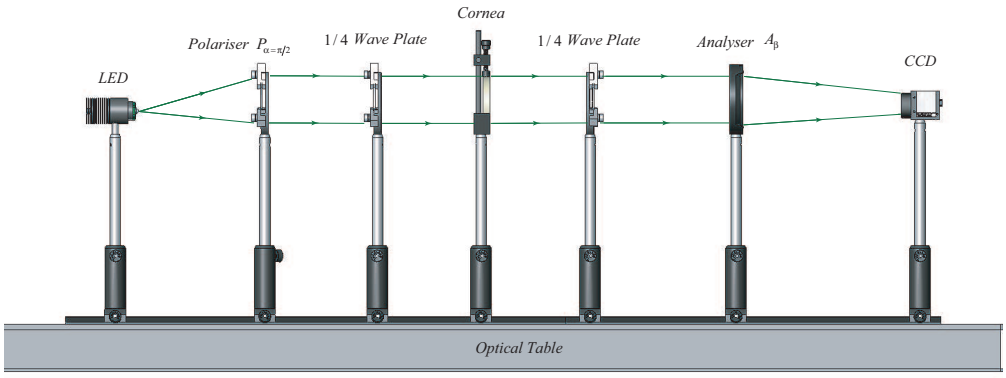

Figure 6.37 Diagram of the cornea phase measurement system.

CCD camera, the pixel resolution could be 16 bits which is a 65536 grey level.

The monochromatic LED is used in the experiment. Laser is the traditional light source used in the such measurements, but this will lead to many speckles and noise. The LED light source could provide image with high contrast and little noise whilst using low power and cost. A reduction in the power supply makes the system more simple and portable. But if *LED* implementation provides the low coherent light source, this increases the difficulty of implementation during the FFT method experiment. The crystal quartz wedge can not show fringes in the broad bandwidth wavelength light, and so a filter which limits the bandwidth of the light must be added to the light source. This will lead to a better performance being obtained during its application.

The polariser, analyser, and quarter wave plates are set up on the rail to ensure that they are on the same optical axis. Although the components of the installation is highly integrated, each component is installed on a separated base. The reason for separate installation is that it is easier to adjust each component when measuring the phase stepping. Later in this research it will be shown how this novel approach will streamline the design.

Results and Discussion

The pig's, fox's and cat's cornea samples are used in the experiment. The pig's cornea is the main specimen for study. Considering the anisotropy axis and the distribution of the birefringence, the porcine cornea was tested using two angles for comparison. The raw image the positions as shown in Fig.6.38:

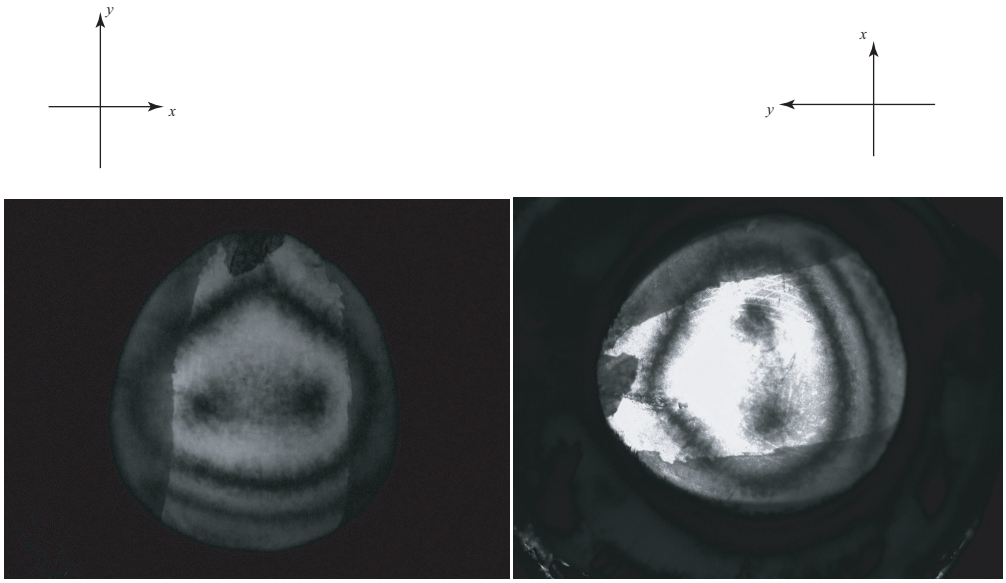

Figure 6.38 Pig's Cornea and cornea specimen at different angles.

By using the phase stepping method, the image data are shown in Fig.6.39 and 6.40. The images indicate the cornea situation when the phase changes once each time by $\pi/2$ based on mathematical calculation. The analyser is set at 0, 45, 90 and 135 degrees respectively.

The other angle's data are:

The phase changes by half of π from image (a) to (b), from (b) to (c) and from (c) to (d) in Fig.6.39 and Fig.6.40.

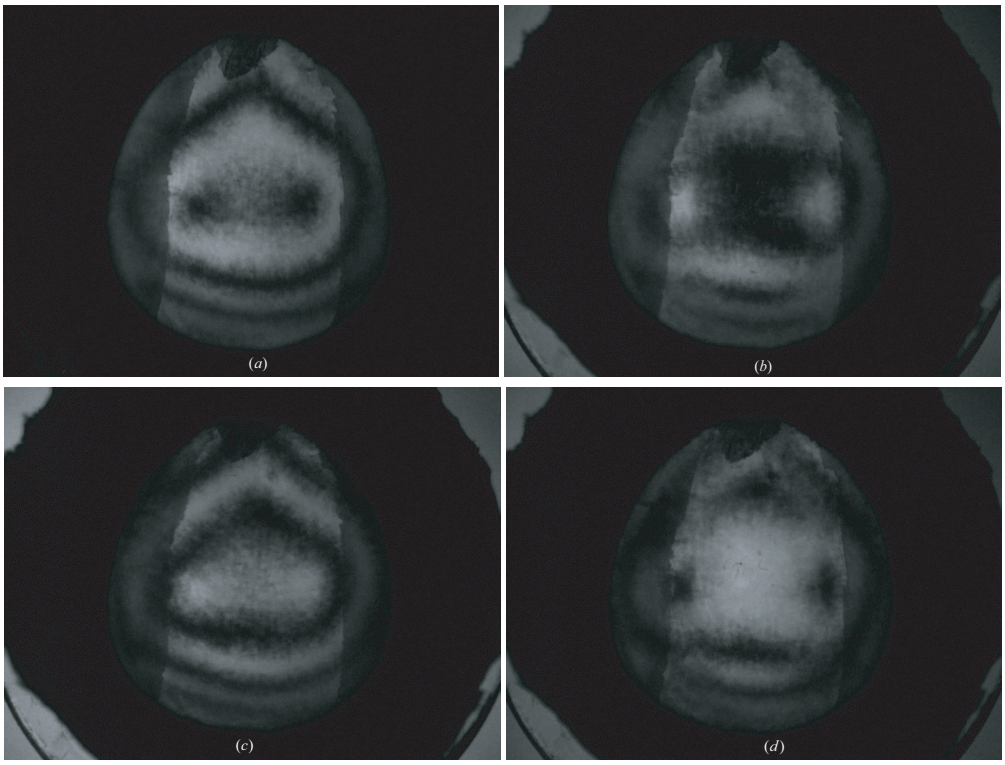

Figure 6.39 Pig's Cornea phase stepping (a)analyser 0 degree (b) analyser 45 degree (c) analyser 90 degree (d) analyser 135 degree.

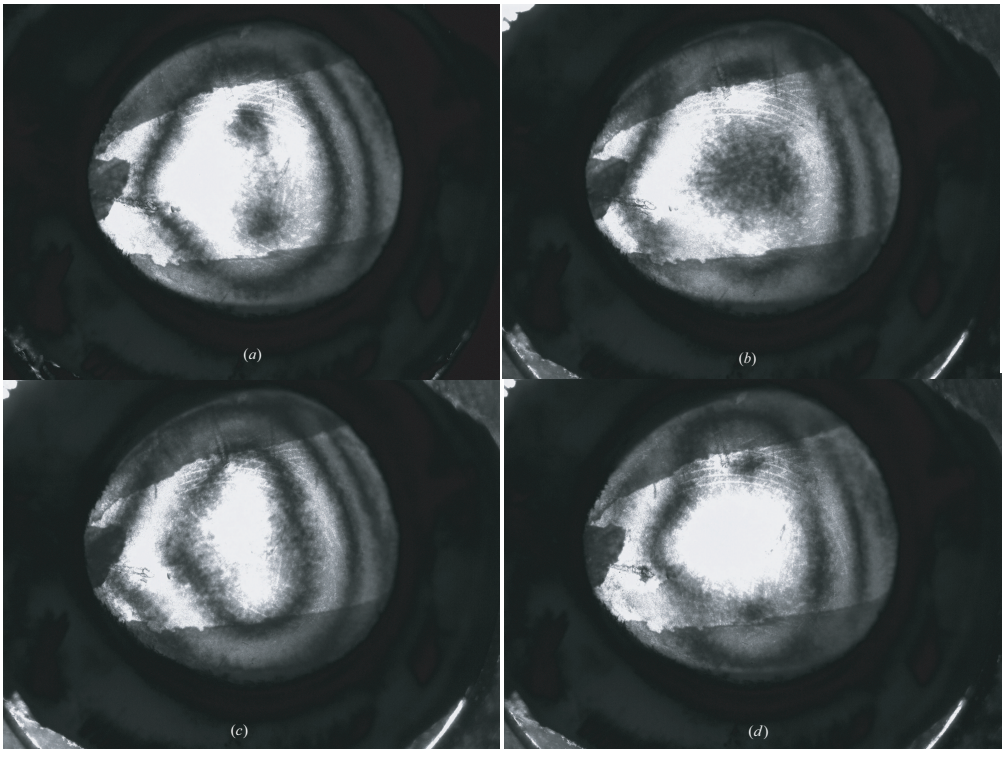

Figure 6.40 Pig's Cornea phase stepping (a)analyser 0 degree (b) analyser 45 degree (c) analyser 90 degree (d) analyser 135 degree.

Fig.6.41 shows the wrapped phase map of the cornea, (a) and b are the different angles for each of them.

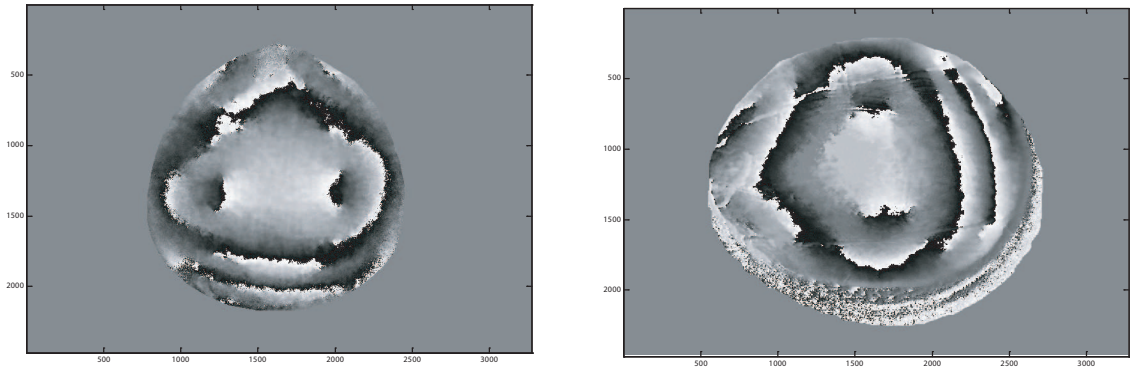

Figure 6.41 Pig's Cornea wrapped phase map (a)cornea position 1 (b) cornea position 2.

Fig.6.42 shows unwrapped phase map of the cornea, (a) and b are the different angles for each of them.

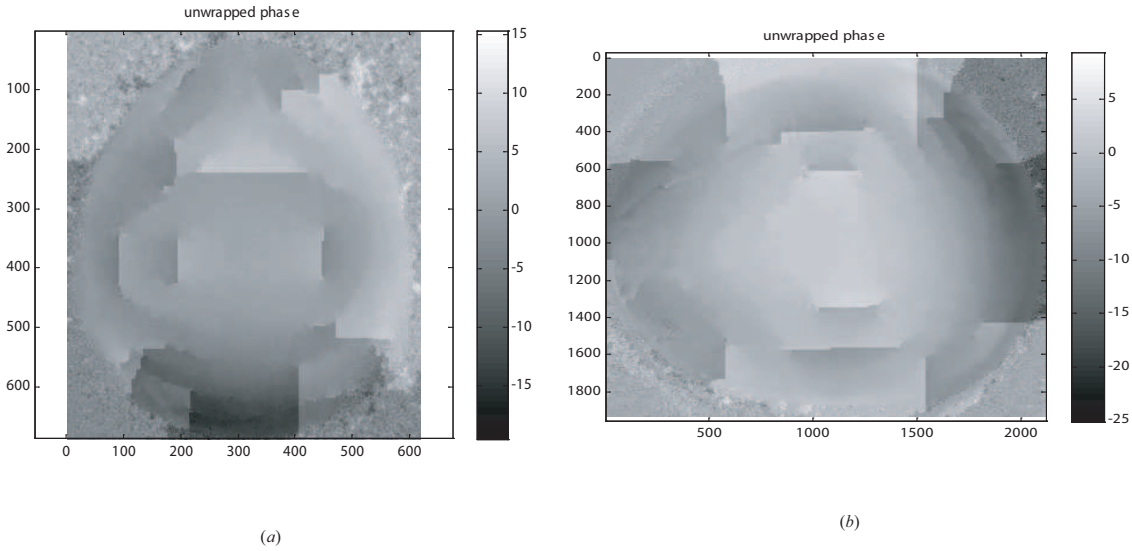

Figure 6.42 Pig's Cornea wrapped phase map (a)cornea position 1 (b) cornea position 2.

Fig.6.43 and 6.44 show a 3-D plot of the phase difference distribution of the cornea.

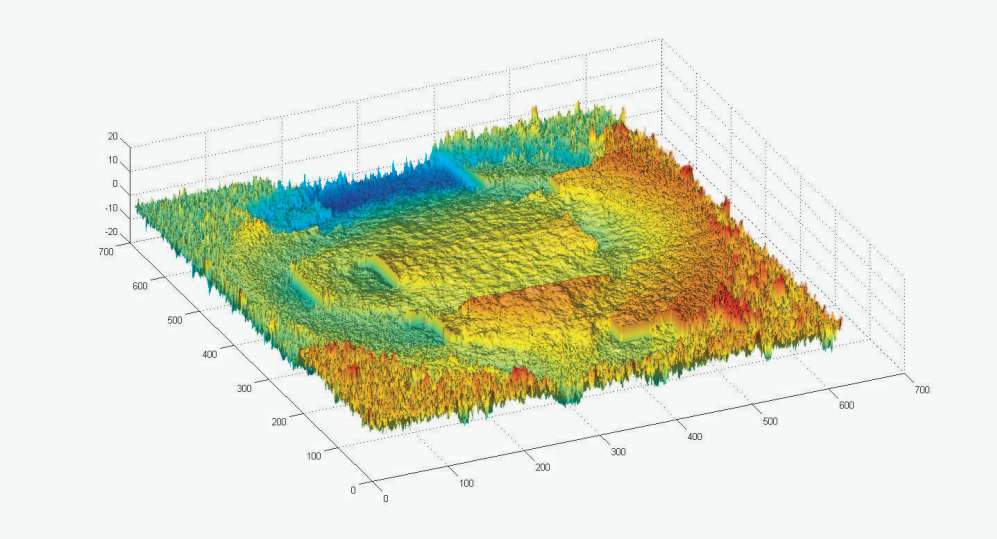

Figure 6.43 Porcine Cornea position1 3-D perspective plot of phase difference.

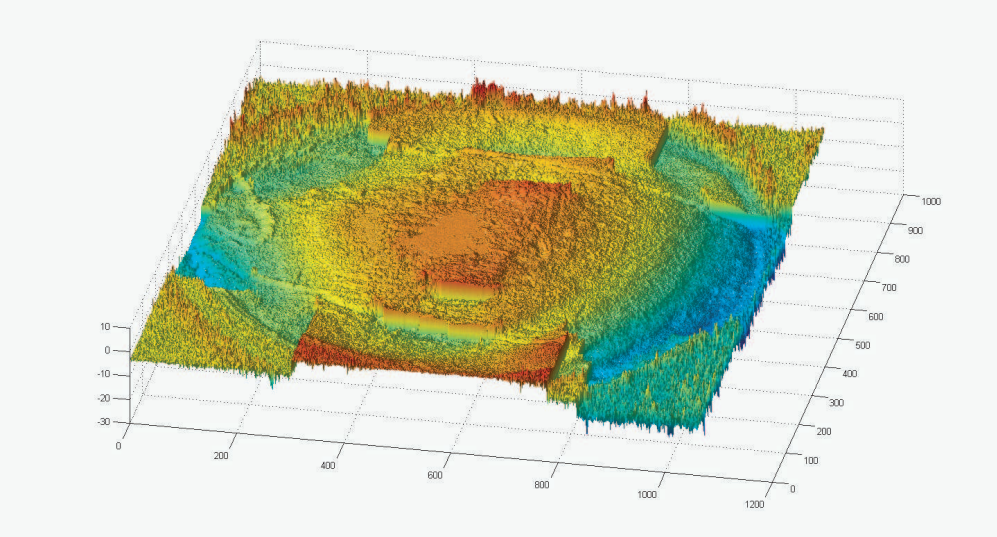

Figure 6.44 Porcine Cornea position2 3-D perspective plot of phase difference.

From the phase map in Fig.6.45 and 6.46, the phase distribution on the cornea can be found. There is a boundary on both sides of the corneal edges, the phase reverses at these areas. The reverse phase also occurs in the area of the collagen. The details of the collagen phase distribution will be examined in the following section using the microscope $K2$ lens.

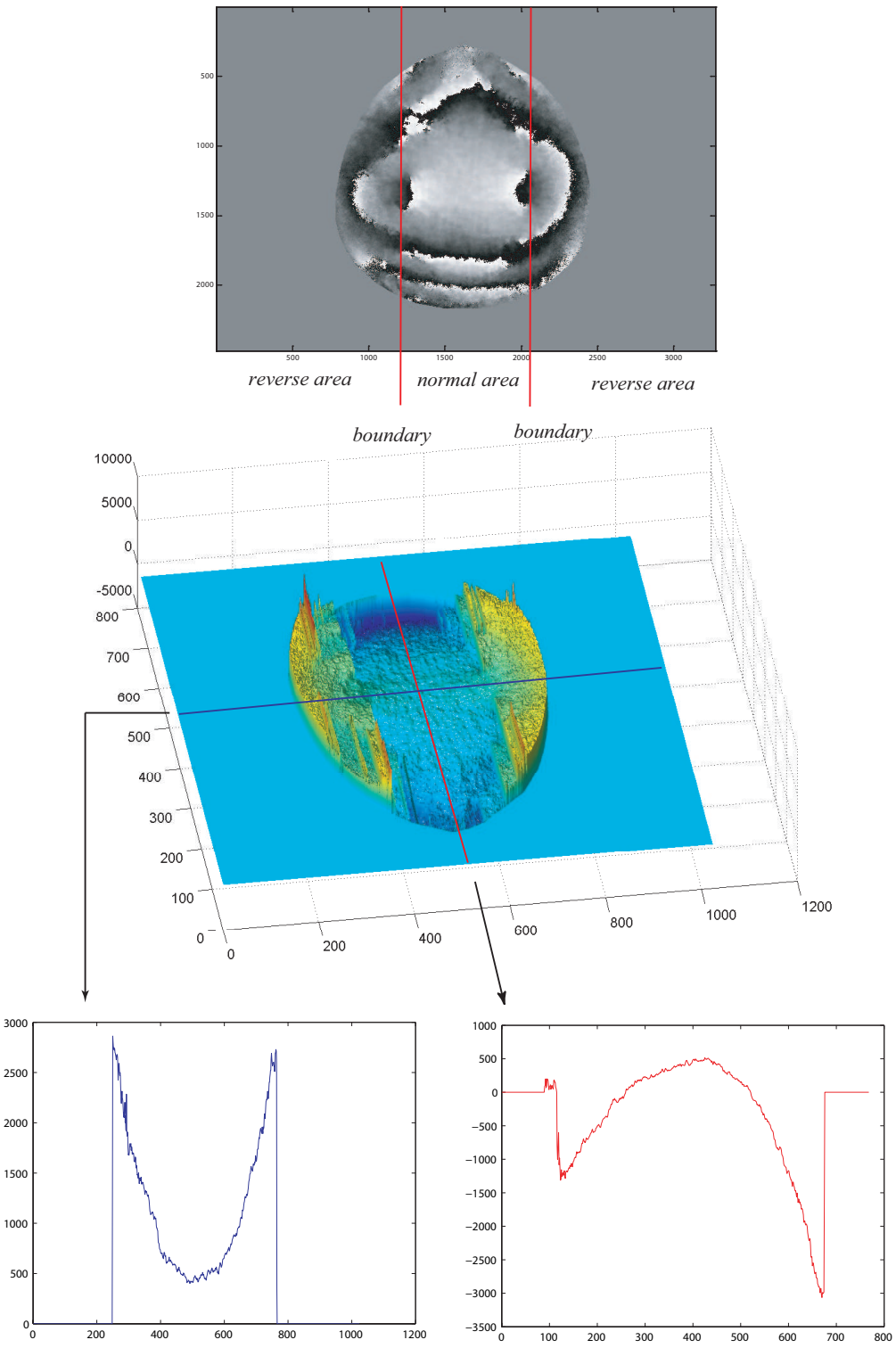

Figure 6.45 Porcine Cornea phase map analysis-position1.

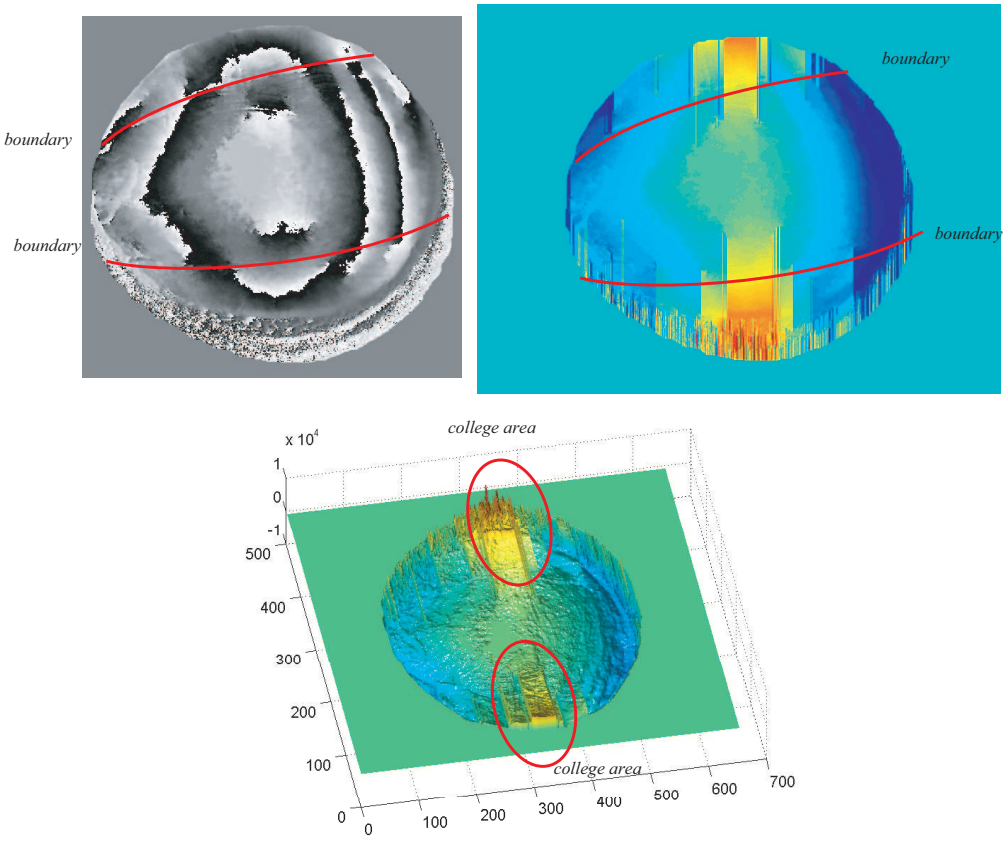

Figure 6.46 Porcine Cornea phase map analysis-position2.

6.2.3 Fourier Transfer Method

In this methodology, the birefringent crystal quartz wedge will be placed in front of the specimen. The wedge can generate fringes with phase information, which will be added to the specimen. The measurements are encoded within a fringe pattern, where the fringes represent lines of constant phase. This technology provides a successful method of measuring the fields of the refractive index and displacement. The height will show the surface profile, the displacement, or the optical path difference through a phase object.

Results and Discusstion

In order to achieve good performance, the polariscope is set to the dark field situation which gives good contrasting quality image. The container has been proved that it does not provide unwanted birefringent information in the system. So, it does not affect the results of cornea. The cornea raw image with crystal quartz wedge is shown in Fig.6.47:

Firstly, the automatic software Fran is used to process the image. Due to software limitations, the image data has reduced resolution for Fran. Because Fran was made about twenty years ago, with the increasing of the image resolution, it cannot load and analysis big size image data. Fig.6.48 shows the wrapped phase map and unwrapped phase map in (a) and (b) respectively.

Fig.6.49 shows the 3D perspective plot of the phase difference map.

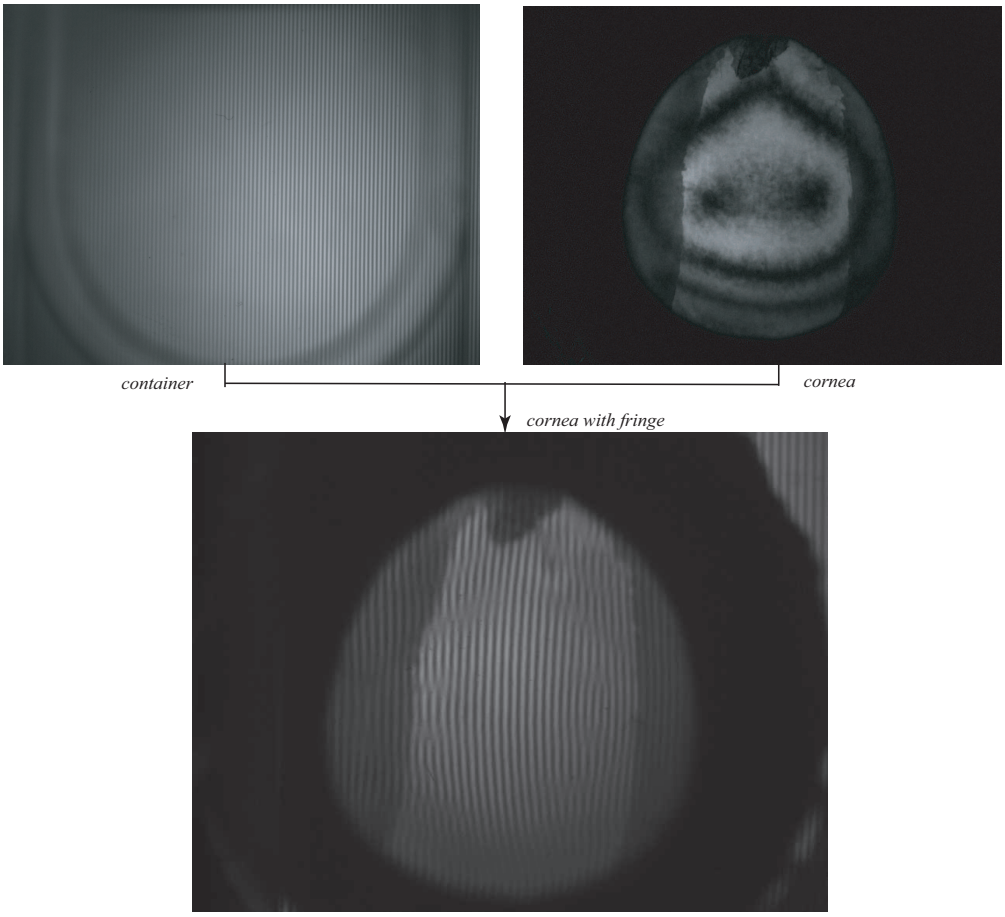

Figure 6.47 Cornea with fringes.

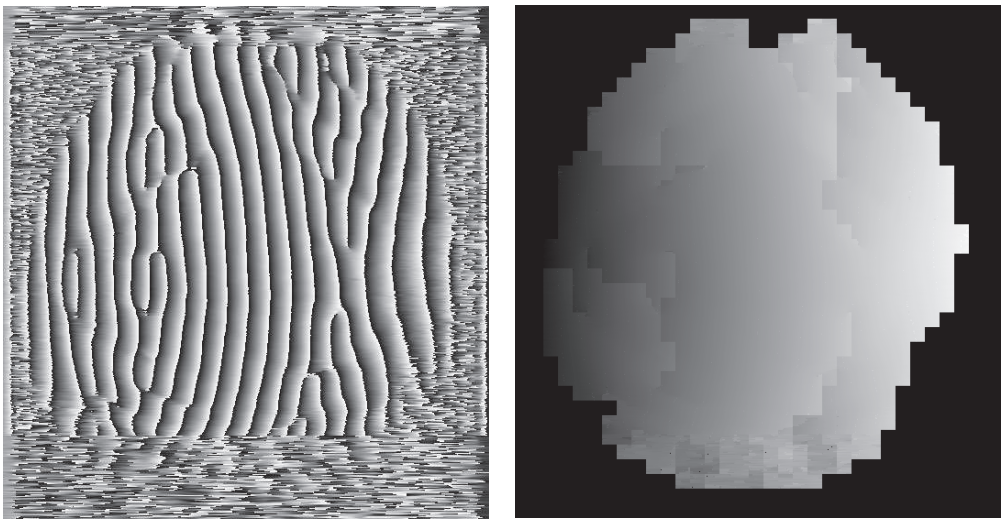

(*a*) Wrapped phase map of Cornea by Fran

(*b*) Unwrapped phase map of Cornea by Fran

Figure 6.48 Cornea with fringes.

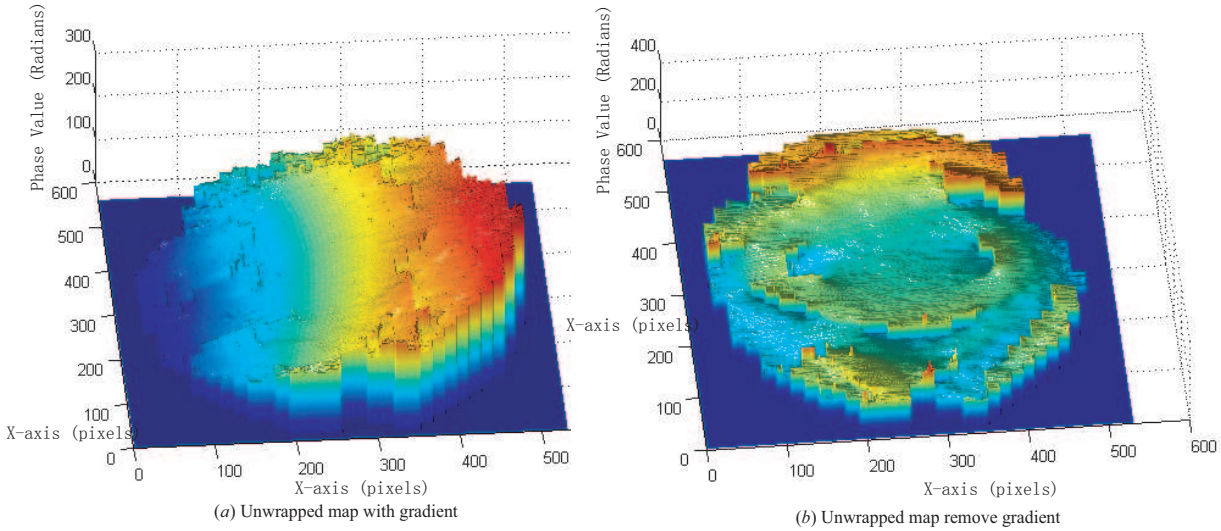

(*a*) Unwrapped map with gradient

(*b*) Unwrapped map remove gradient

Figure 6.49 3D perspective plot of the phase difference map.

With another set of professional photoelastic equipment, which named $GFP1000$, measurements, the phase map are shown in Fig.6.50. Unfortunately, this machine can only process low resolution image data. But the results are smoother and better than those provided by $Fran$.

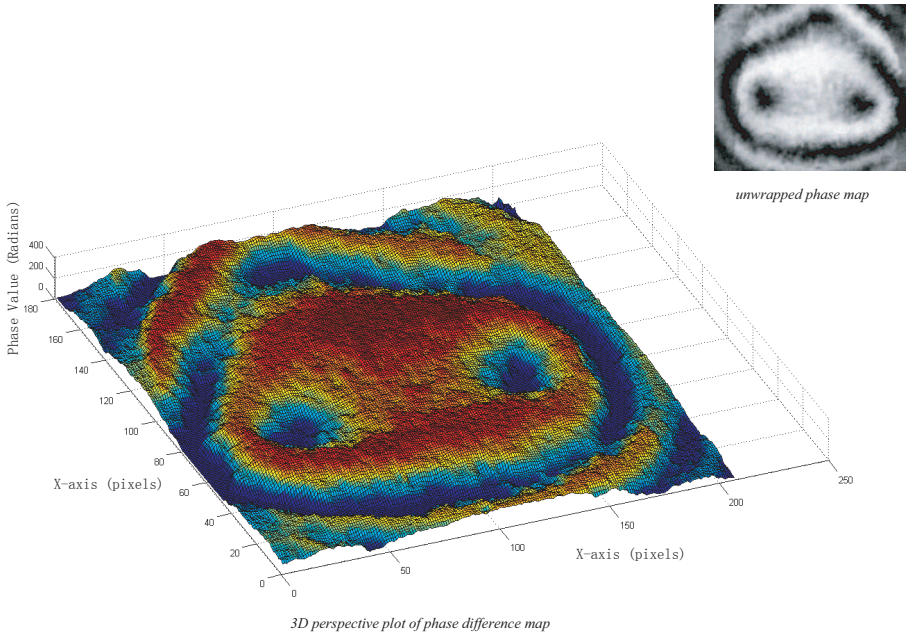

Figure 6.50 Phase map and 3D perspective plot of the phase difference map.

For high resolution data, the data are analysed by $Matlab$, which are shown in Fig.6.51:

The results obtained from $Matlab$ are quite flat. So, the centre section is an interesting location to be examined. Fig.6.52 shows the resolution and the section in the raw image which will be examined.

Fig.6.53 shows the wrapped map and unwrapped phase map. Fig.6.53(b) is the unwrapped phase map with information from the wedge, after removing the unwanted gradient, Fig.6.53(c) is the unwrapped phase map of the centre section of the cornea.

The 3D perspective plot of the phase difference map is shown in Fig.6.54, which also includes a contour map of the centre section. From the 3D shape, we can assume that the phase difference is quite similar like a saddle distribution.

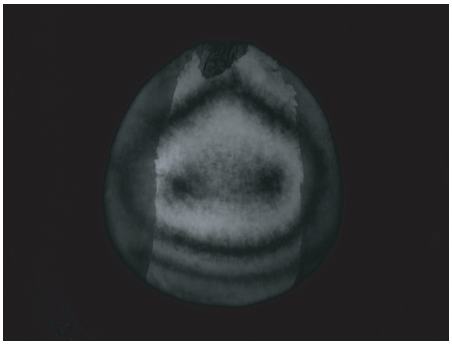

(*a*) Raw Image of cornea(resolution : 3272×2469)

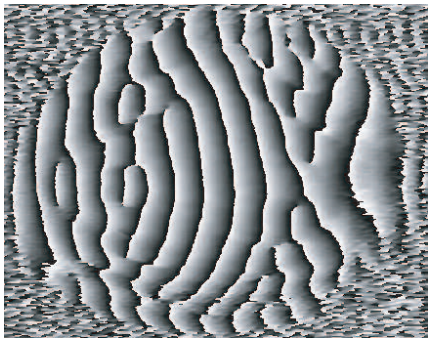

(*b*) Wrapped phase map

(*c*) *Unwrapped phase map*

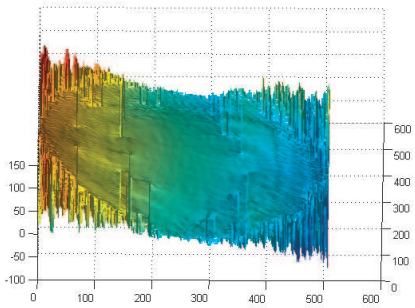

(*d*) 3D perspective plot of the phase difference map with wedge gradient

Figure 6.51 Phase map and 3D perspective plot of the phase difference map calculated with FFT algorithm by Matlab.

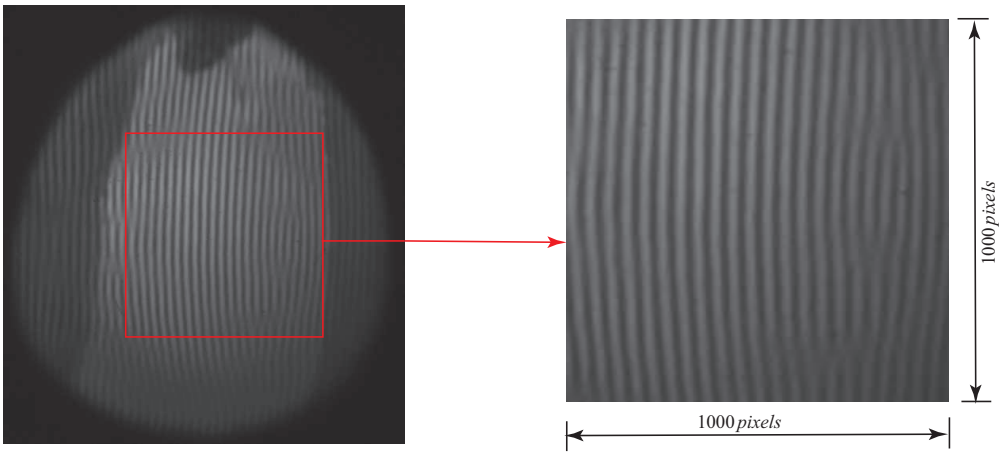

Figure 6.52 Center part of the cornea.

(*a*) wrappede phase map (*b*) unwrapped phase map with gradient (*c*) unwrapped phase map

Figure 6.53 Center part of the cornea wrapped and unwrapped phase maps.

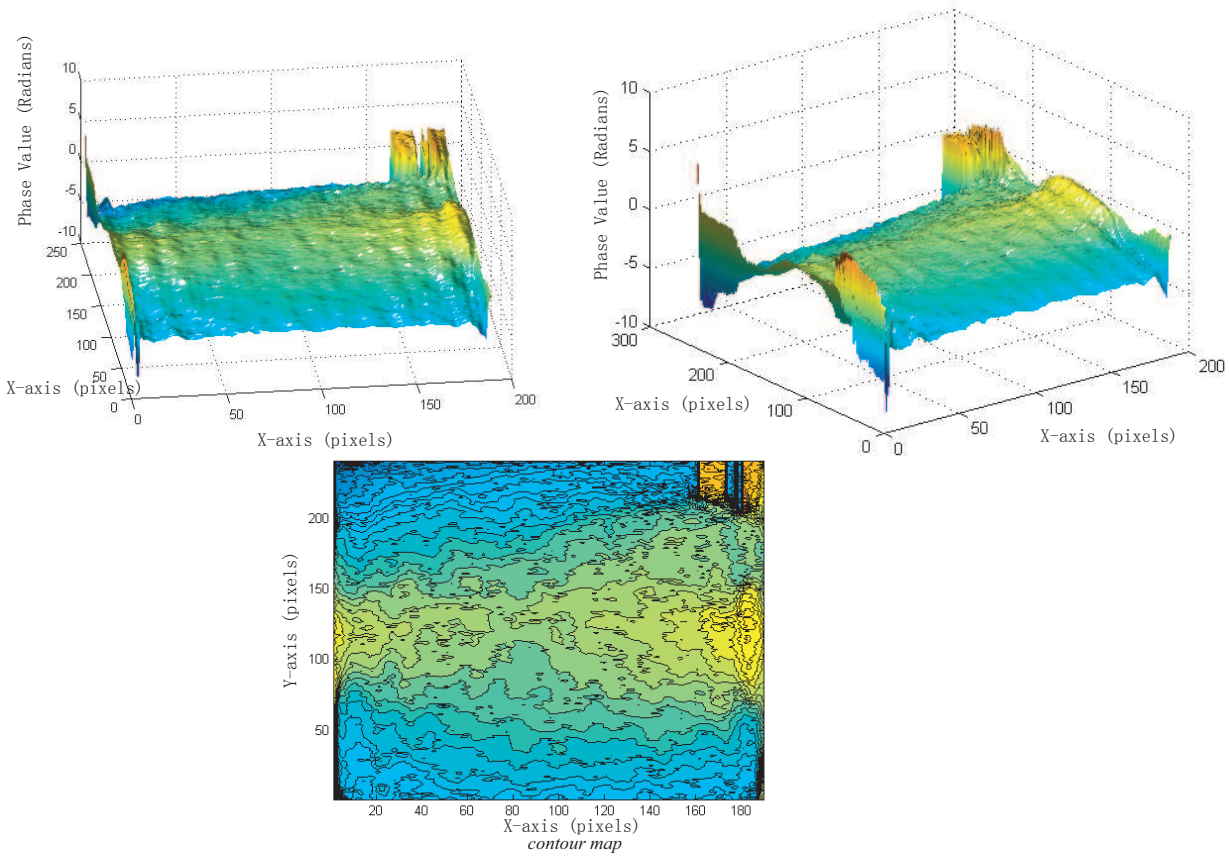

Figure 6.54 3D perspective plot of the phase difference map and contour map.

Another specimen is a cornea of a fox. In the same way, the raw image and image with the fringe are shown in Fig.6.55.

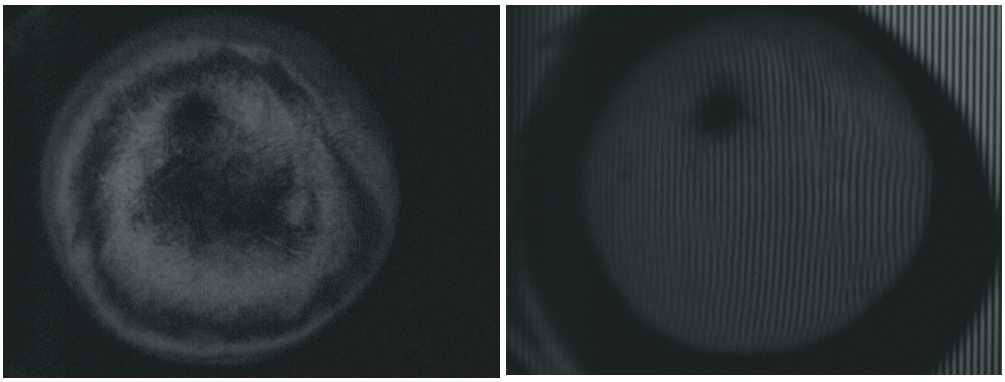

(*a*) Fox conrea raw image (*b*) Fox cornea with fringe pattern

Figure 6.55 Fox's cornea (a) cornea raw image (b) cornea with fringe.

Accordingly, the wrapped phase map and unwrapped phase map are shown in Fig.6.56.

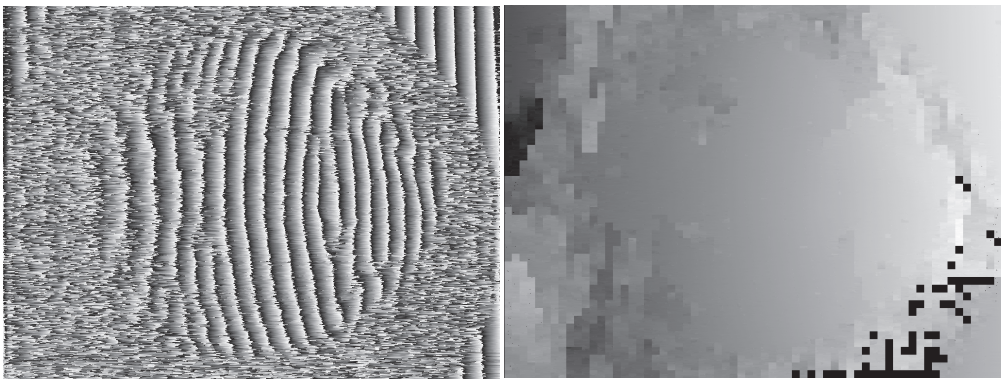

(*a*) Fox conrea wrapped phase map (*b*) Fox cornea unwrapped phase map

Figure 6.56 Fox's cornea phase map (a) wrapped phase map (b) unwrapped phase map.

The 3D perspective plot of the phase difference map is described in Fig.6.57.

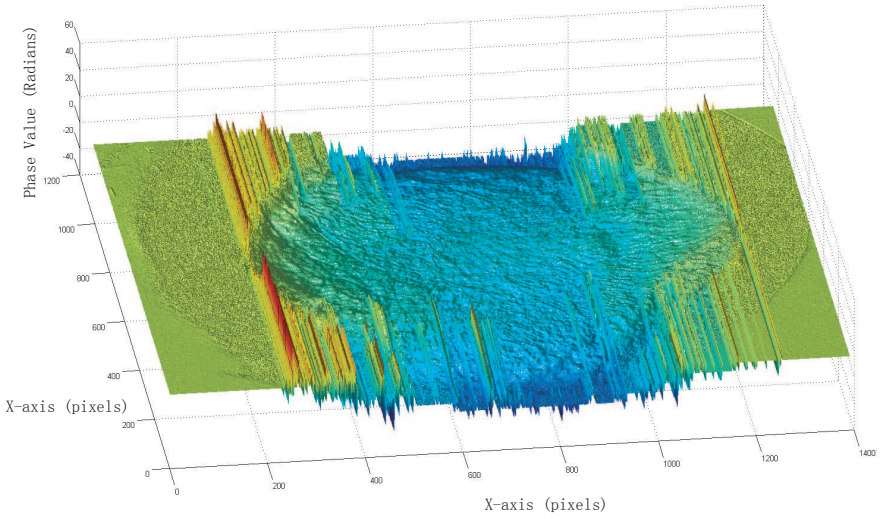

Figure 6.57 The 3D perspective plot of the phase difference map.

Fig.6.58 shows a raster centre line on the 3D phase map. There is a big curvature at the phase reverse area on both side parts. In the centre section, there is a slightly positive curvature in the middle and a structure which is similar to the porcine cornea.

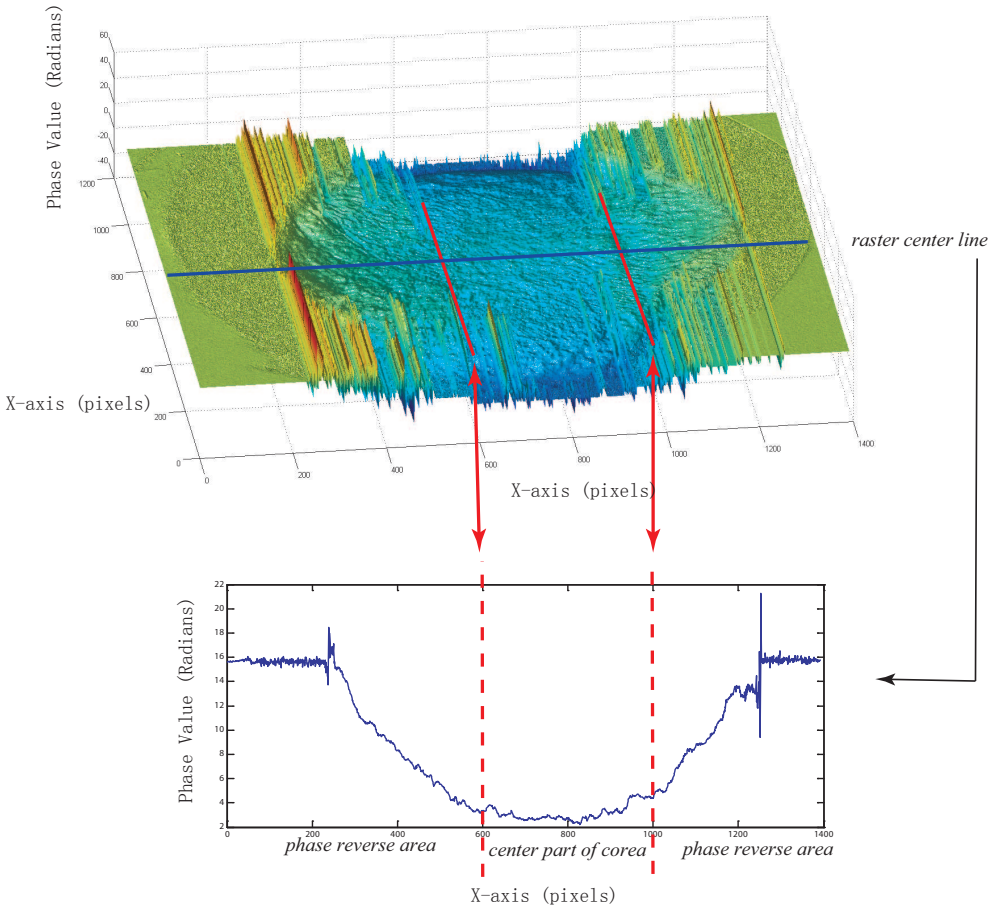

Figure 6.58 The 3D perspective plot of the phase difference map analysis.

From the Fig.6.58, the normal phase part has been extracted for separate study. In Fig.6.59, (a) repeats Fig.6.58, b is the middle part of the cornea phase map. The b area is not small enough, and is still consists of some inverse phase information. So (c) is the centre section from (b). (d) shows a centre raster line of (c). The blue line is the raster line. The red curve is curve fitting carried out an optimization curve. From the smooth red line, we can see the trend of phase distribution, but this is based on limitations due to the resolution of the data.

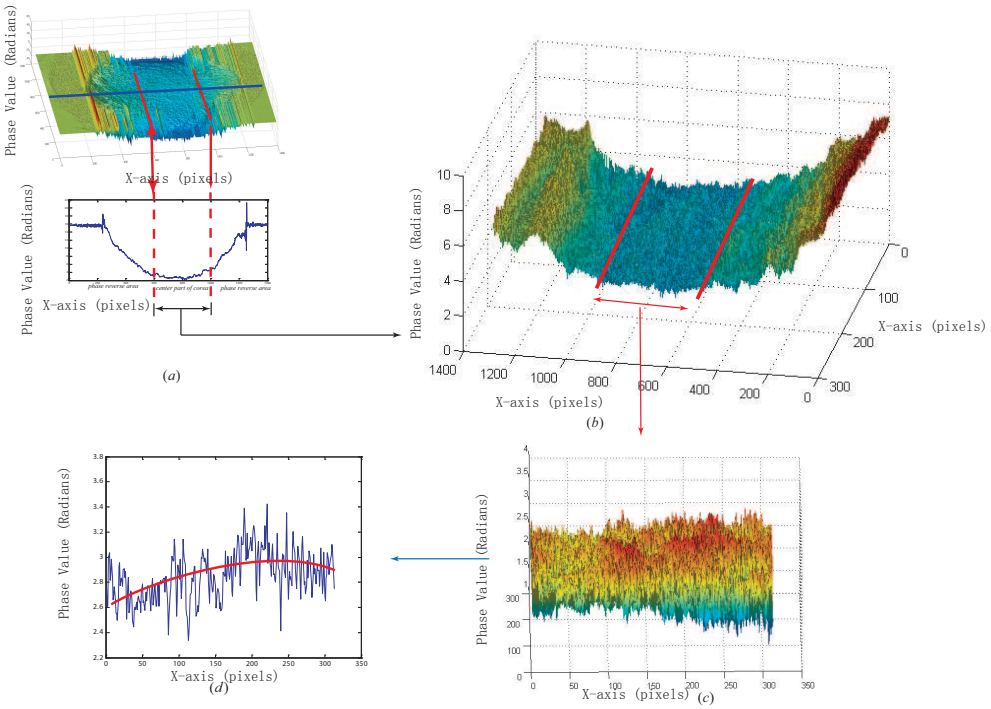

Figure 6.59 The 3D perspective plot of the phase difference map analysis.

Another example is the cornea of a cat, from Fig.6.60; we can see the raw image and phase maps. But because the sample surface folds and is not smooth when they are provided, this causes difficulties during the detection phase, and a lot of redundant information is added up. This is another kind of noise in the specimen which is unwanted information.

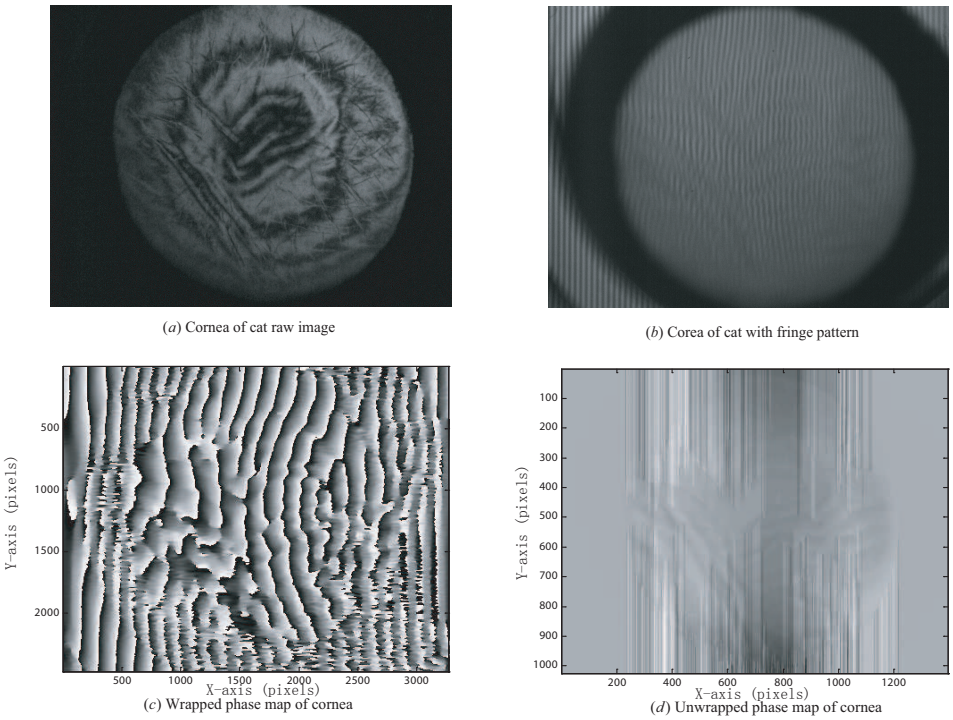

Figure 6.60 Cat cornea and phase maps.

Phase distribution is similar to previous results which is shown in Fig.6.61, although the surface is not smooth. From a selection of the best parts of the analysis, the vertical and horizontal raster line tendencies are still as expected.

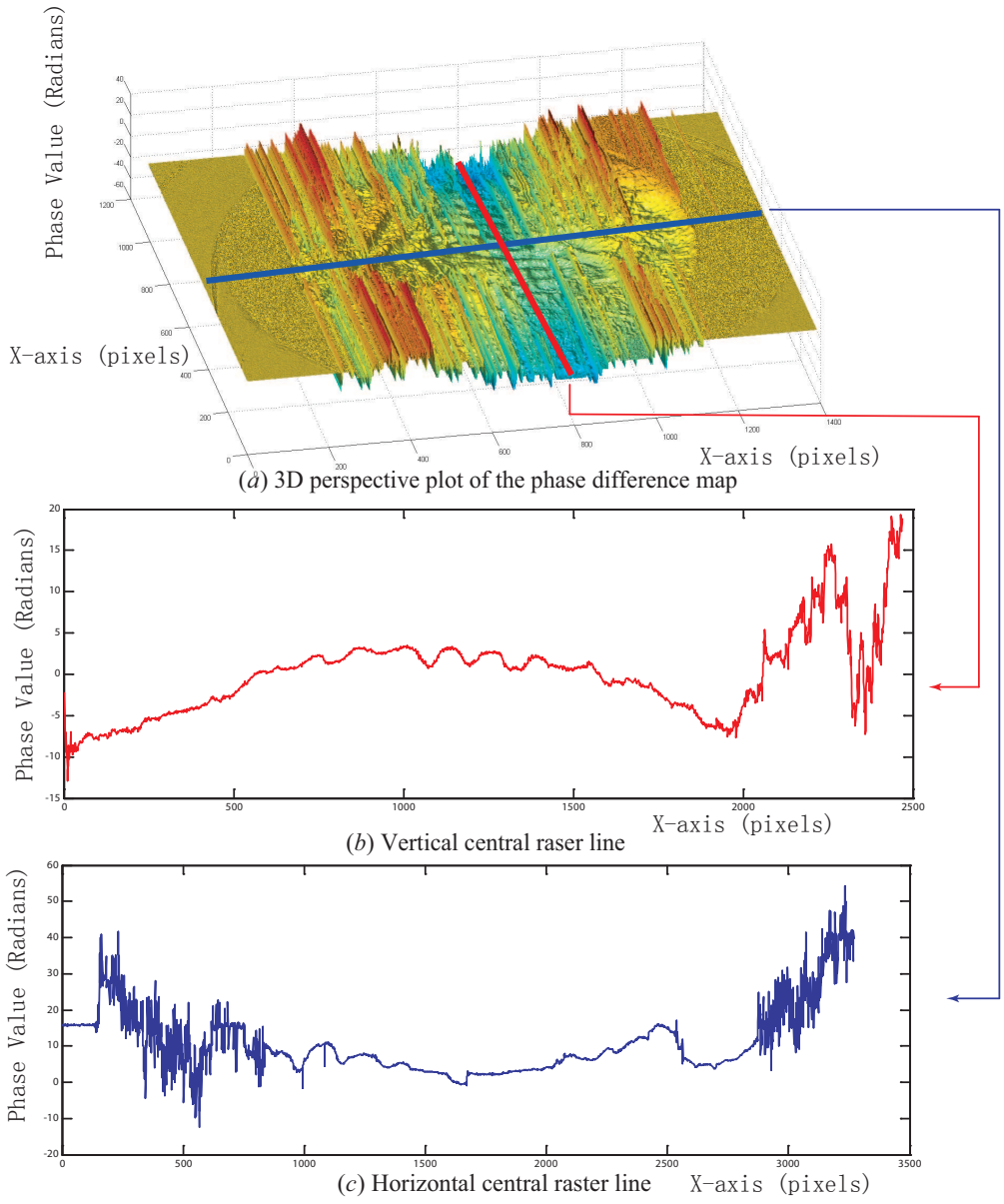

Figure 6.61 Cat cornea 3D perspective plot of the phase difference map analysis.

To summarize, maps of different parameters through the polarisation of the cornea have been calculated by using spatially resolved $Jones$ matrices. A further description of the spatial changes in this state during the polarisation of the light through the cornea has been achieved. The results show the corneal birefringence and retardation approach in the circular polarised light source. From this study, it can be concluded that the cornea contributes mostly through its birefringent structure.

6.3 K2 Long Range Microscope Study on the Cornea

According to the results described in the previous sections, the phase distribution can be detected from the cornea sample. But the results in the cornea centre location and the local collagen become ambiguous. An example result is shown in Fig.6.62. This result is obtained from a single frame. The information of the data is not enough to describe the collagen and the middle parts of the phase distribution of the cornea. The phase stepping method and Fourier transform method significantly improve the results; however, some of them are still not sufficient enough in their detail. So in this section, the K2 lens is introduced into the experiment.

When the measurement is undertaken with the polarising microscope, it is found that the retardation varies considerably according to the corneal birefringence which occurs in most parts. This is also the reason for using the lens of the microscope. For the micro structures exploration, the microscopy images are necessary for studying.

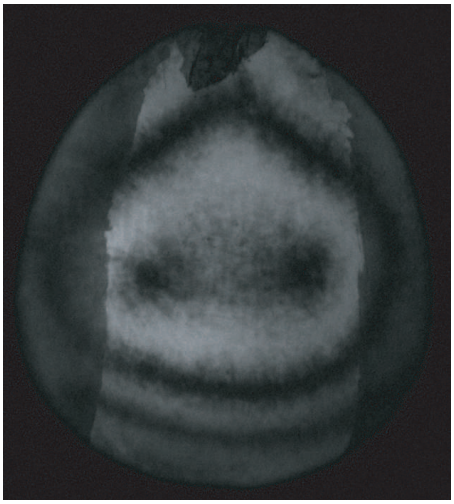

(*a*) porcine cornea raw image

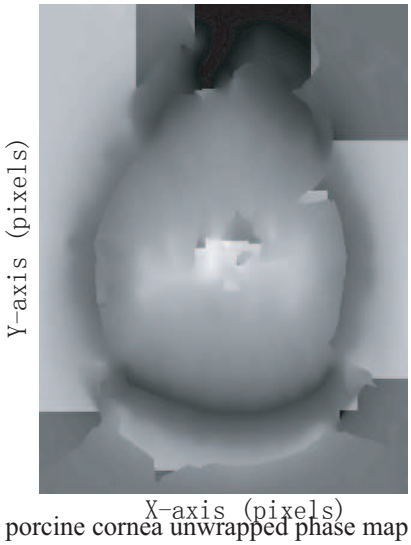

(*b*) porcine cornea unwrapped phase map

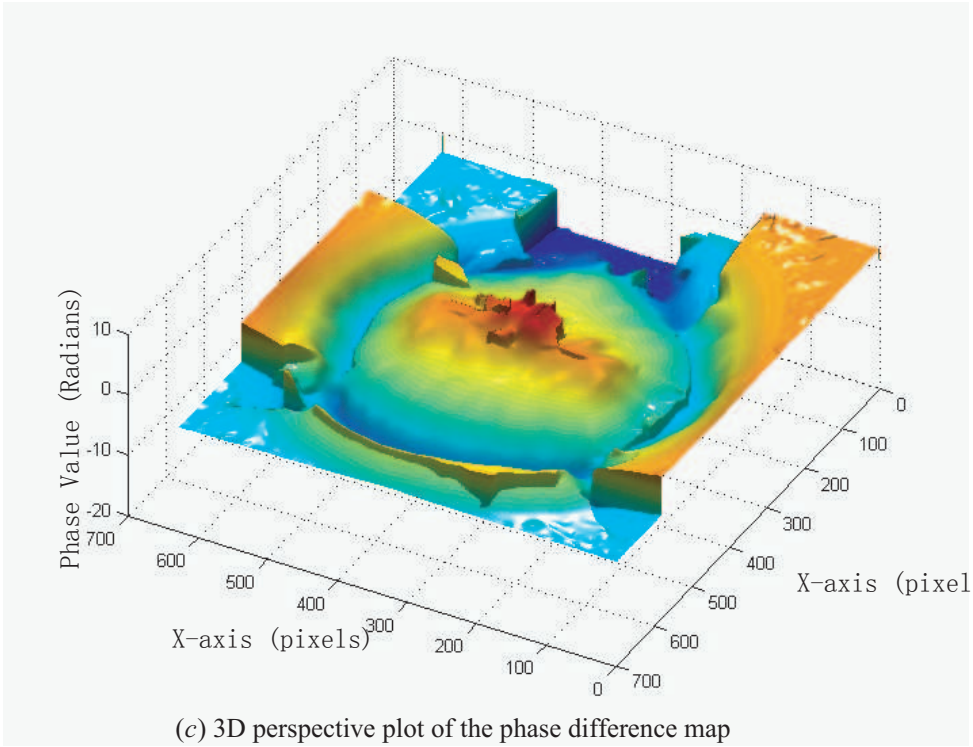

(*c*) 3D perspective plot of the phase difference map

Figure 6.62 Example of single frame of porcine cornea, phase map and 3D perspective plot of the phase difference map.

For over 20 years, the Infinity's Model K2 has been the lens in long-distance microscopes[106], which is shown in Fig.6.63. It offers micro-level images of long distance microscope. Also, it can be used with sensors up to the 35 mm format with exceptional clarity and resolution throughout the field. Its contrast levels are higher than all other competitive instruments.

Figure 6.63 Example of K2 lens.

For two of the three K2 operating ranges, a $Standard$ or $CF-Series$ Objective is directly attached to its front dovetail. The third range is obtained by attaching the Objective holder with an adapter for an infinity corrected microscope objective.

In the set up, the $Standard$ Infinity Range Objective and Close-Focus (CF) Range Objective are used in combine action. The Standard Infinity Range is the greatest offered from any long distance microscope. For a focus from infinity down to c.675 mm, the Standard Objective is used in conjunction with the internally positioned S Lens. The two lens system works harmoniously as a matched system.

By not utilizing the S Lens, $Standard$ and CF Series Objective can be used for progressive focus from 980mm down to 55mm. Depending on the chosen objective, primary magnification ranges from 0.31x to 5.33x. Additional amplifiers permit these primary magnifications to be further enlarged.

The K2 microscope lens can perform better if the objective is as brilliantly illuminated as possible. The LED units which is chosen for the experiment provide excellent characteristics. The peak wavelength is 530nm, and the bandwidth of the wavelength is around 10nm. The view angle is 85 degrees, with a parallel optical structure; the light is collimated based on the requirements of the experiment.

Output light intensity is perfectly satisfied with the K2 lens requirement which is 110 lm (lumen).

The fresh cornea is placed in formalin and mounted in a Ringer-Lock solution in a glass container when it be used in experiment. The K2 lens has a long body, and it is mounted on two standing modules on a rail. This structure ensures good stability for the k2 lens, with it and the other optical components placed in a unified optical axis, ensuring the accuracy and precision of the experiment.

The only study of the corneal ultrastructure available was undertaken by $Hertel$ in 1933, who used X-ray diffraction methods with electron microscope made by $Sebruyns$ (1950). The main problem is the statistically isotropic appearance of the cornea for normal light incidence. The birefringence is calculated by taking the measurement of retardation with light passing through the piece of cornea where the thickness is given by d. The formula is described as:

$$\omega = \frac{\theta\lambda}{\pi d \sin\alpha \tan\alpha} \tag{6.4}$$

where λ is the wavelength used, θ is the analyser shift from the normal cross position to the extinction position, and α is the angle between the optic axis and the direction of light passage.

The set up of the K2 lens is the same as the Fourier methodology set up. The sample of the cornea is shown in Fig.6.64. Compared with the previous typical system, Fig.6.64 shows the position and size of the data and a comparison with the previous whole field cornea image.

In the central area of cornea which we are interested in, the image contrast is better than those displayed through monochromatic light. Because the fluorescent light source includes different wavelength light , while the waves bandwidths are also different. Some of these are limited by a narrow bandwidth, so that they may be observed with the naked eye. The sample image is shown in Fig.6.65. The resolution of the image is 3272×2469, and file size is 20.4MB.

There are two dark patches that can be observed straddling the pupil typically aligned to the distribution of axiallity symmetry. The birefringent fringe is dis-

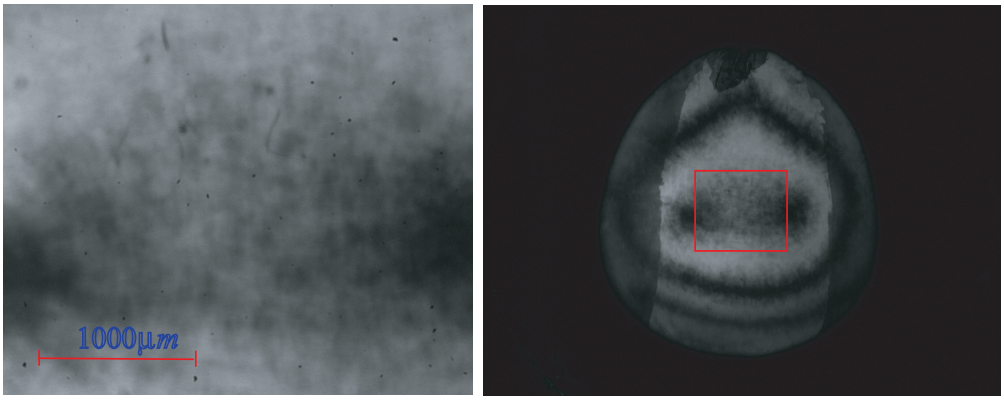

Figure 6.64 Cornea data from K2 lens and comparison with previous whole field cornea image.

tributed in a ring around the cornea. The two piece patches are like apices at the corneal centre. The centrifugal colour of the fringes matches that expected up to the second order interference colours from changes in retardation due to a graded rise in birefringence.

There is a fibrillar structure which could be visible in the central corneal area. The fibrillar pattern which has been observed is not altered by the rotation of the analyser of the polariscope although non-coaxial illumination or oblique positioning of the polarising filter affects the intensity of parts of the image[96], Fig. 6.66 which is captured by K2 lens shows the details of the fibrillar pattern. But the fibrillar structure observed by the analyser is still affected by the rotation angle of the analyser. When the analyser is between 0 degrees and 90 degrees, the fibrillar structure can be clearly observed, while from 90 degrees to 135 degrees, it can almost not be detected, an example is shown in Fig.6.67.

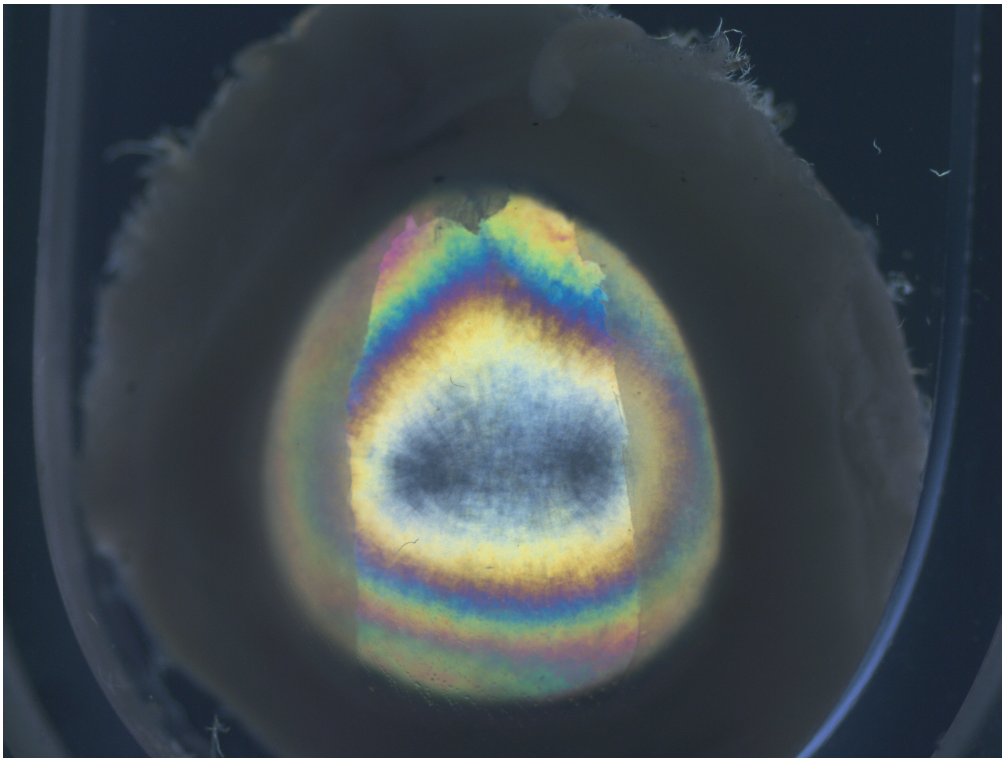

Figure 6.65 Porcine cornea in circular polariscope with high resolution color image $(resolution : 3272 \times 2469 size : 20.04MB)$.

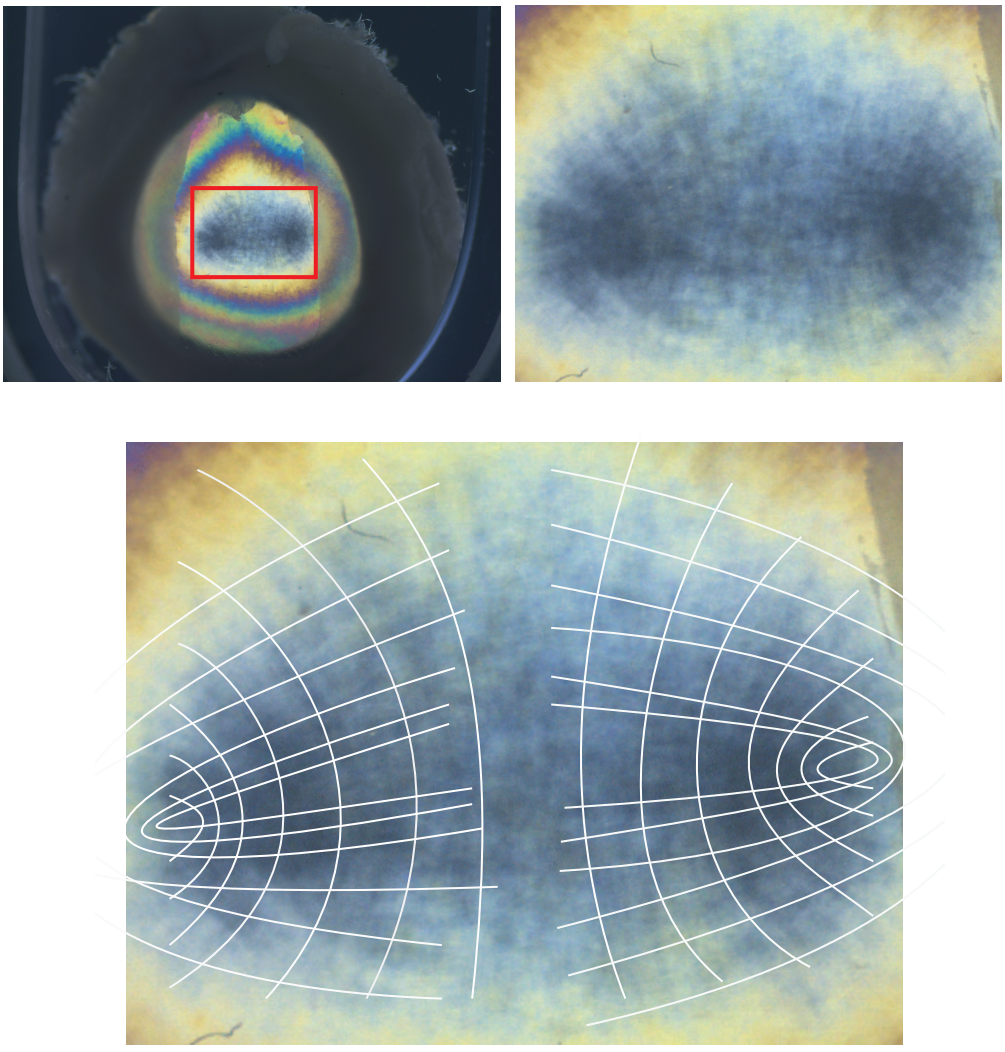

Figure 6.66 Porcine cornea in circular polariscope with high resolution color elliptical-hyperbolic distribution.

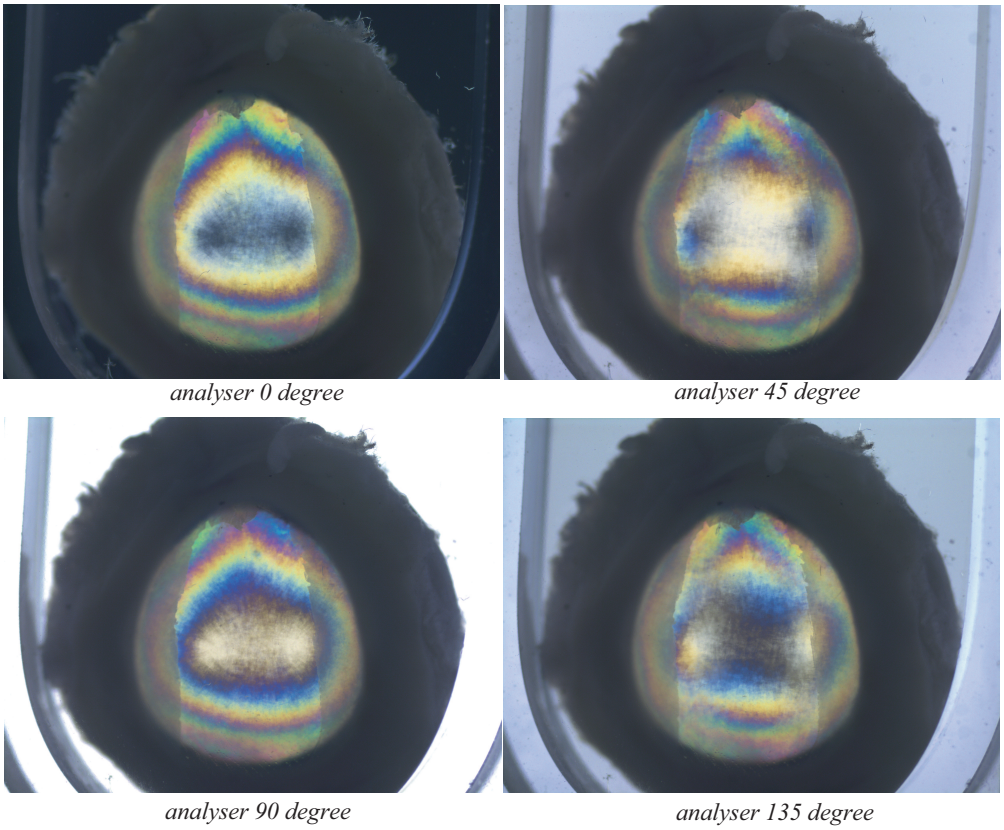

Figure 6.67 Porcine cornea in circular polariscope at four different angles.

The lens polarisation is very weak[92]. Regarding the cornea, if the polarised light passes through it, whether this is linear or circular polarised light, it will become elliptically polarised. For many technologies the light beam is roughly perpendicular to the surface of cornea. and the cornea is described as a linear retarder[94][107]. By putting this into the polariscope system, the light of one polarisation propagates through the cornea more slowly than the light of the other and thus becomes retarded in phase. The orientation of the more slowly propagating polarisation defines the slow axis of the retarder; the axis at the orthogonal will be defined as the fast axis. The retardate can be expressed as phase shifting or the difference in optical path length at a level of nanometers, a beam must travel in free space to undergo the observed phase shifting. An understanding of the corneal birefringence is the main purpose of this study.

In Fig.6.68, the K2 lens image data, the fibrillar structures are in the central and peripheral regions of the cornea. Two main areas of the fibril distribution appear

in the centre of cornea at about two foci. On the areas of the dark parts, the foci are located roughly in the middle of the corneal centre and limbus, and tend to be aligned along a nasal to temporal axis from the horizontal[96]. The temporal focus is more diffuse and gives rise to an infinite mark shape distortion of the elliptical fibrillar distribution in nearly half of the subject.

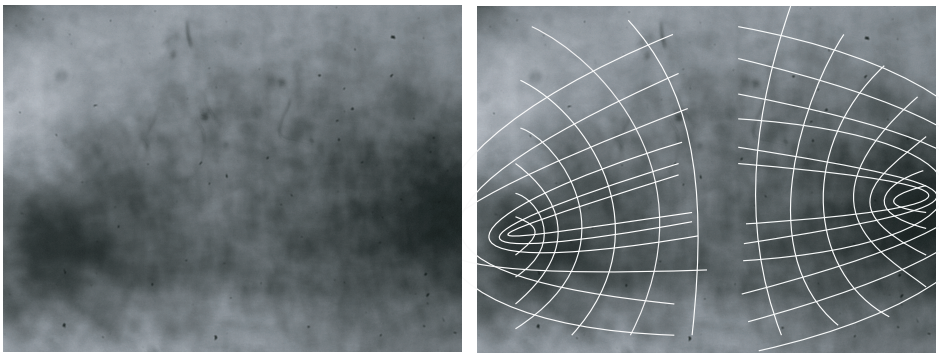

Figure 6.68 Porcine cornea with distortion and superimposed tracing of fibril distribution.

Results and Discussion

$Muller$ calculus has been implemented in the theoretical modelling of the polarised light system to measure the ocular birefringence. But in this system of describing the circular polarised system, $Jones$ calculus is preferred because it is more simplified and efficient for calculation. In the first step, the whole view of the birefringence structure of the cornea is detected. With the limitations of the hardware technique, local details can not be measured.

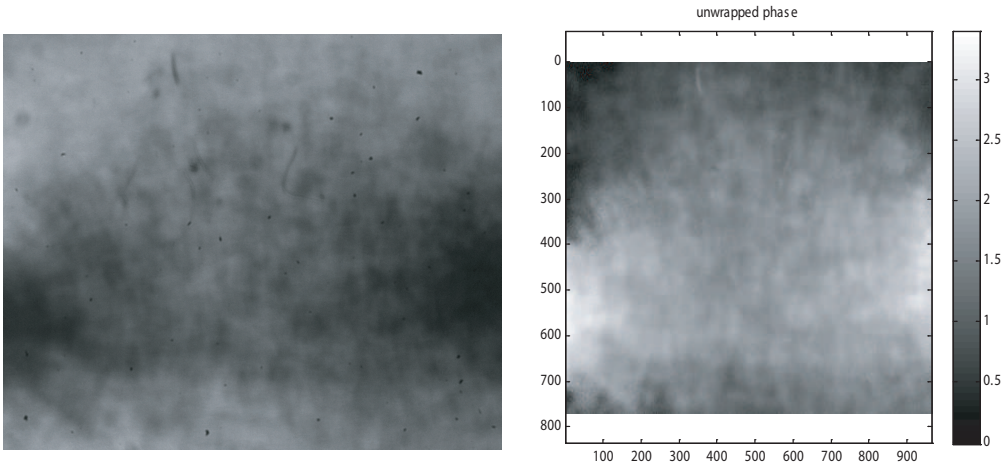

Figure 6.69 Porcine cornea center part.

The phase distribution shows in Fig. 6.69, and the 3D map of cornea central part on surface, which is the collagen, is drawn in Fig.6.70 and the contour map is shown in Fig.6.71.

From Fig.6.68, the elliptical fibrillar distribution is obtained from the raw image directly[96]. In this study, the phase stepping method and the K2 lens high resolution image data open up a new approach. The fibrillar distribution is related to the refractive index changes, and the phase changes are closely related. Fig.6.72 shows the centre phase information of the cornea, and it shows the structures on the surface, and compared with the detection in previous work, Fig.6.70 shows the 3D continuous phase changes and distribution, which is also related to the birefringent structure of the cornea.

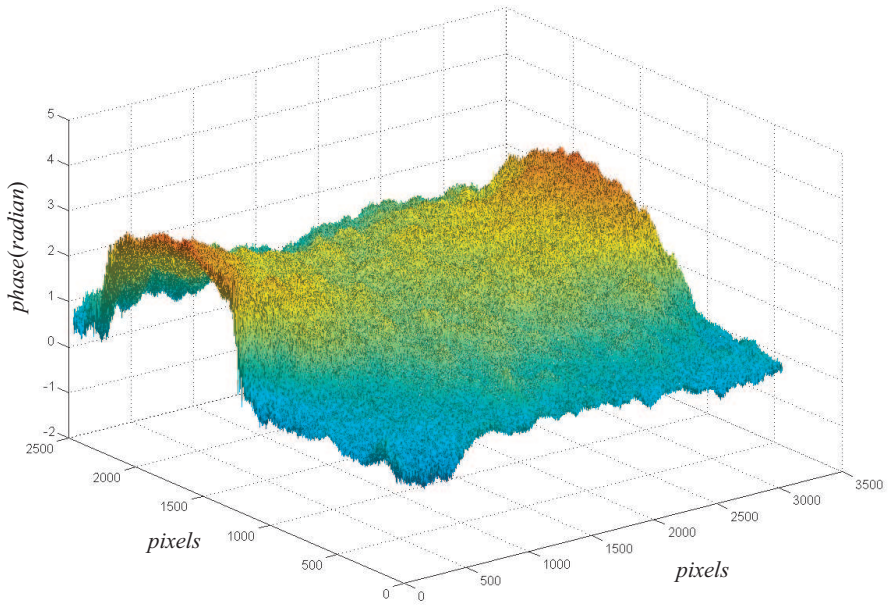

Figure 6.70 3D perspective plot of the phase difference map of the center part of porcine cornea.

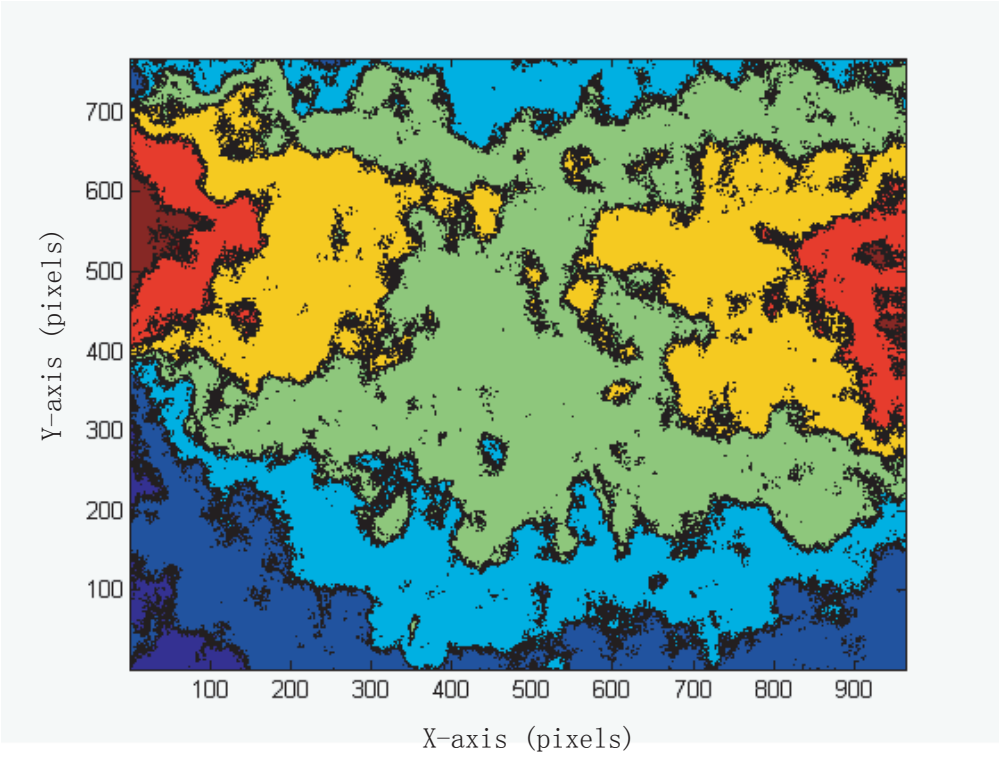

Figure 6.71 Porcine cornea center part phase contour map.

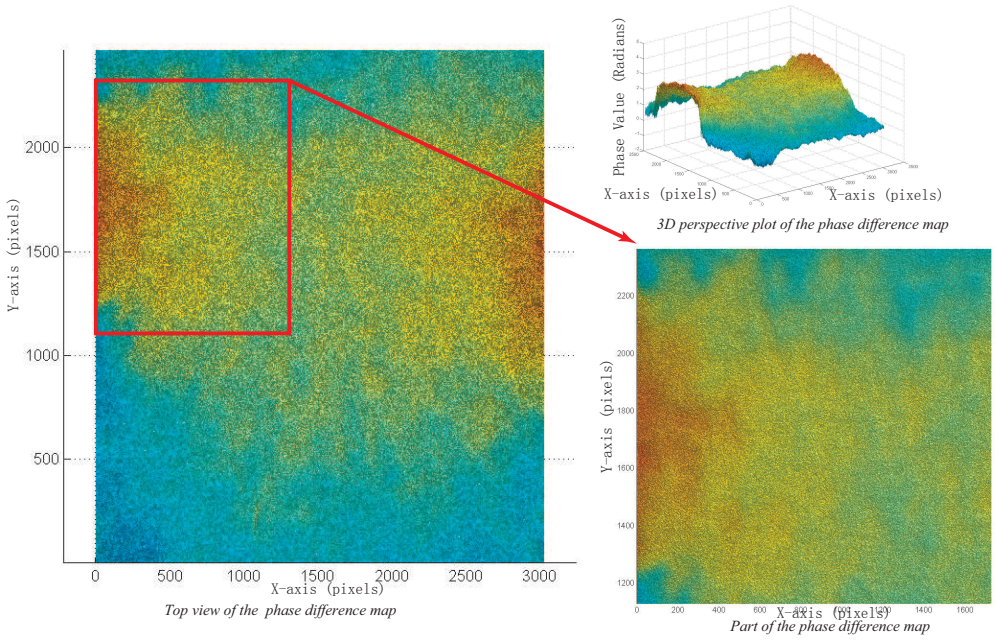

Figure 6.72 Porcine cornea phase information on surface.

The details at the two collagen areas are shown in Fig.6.73.

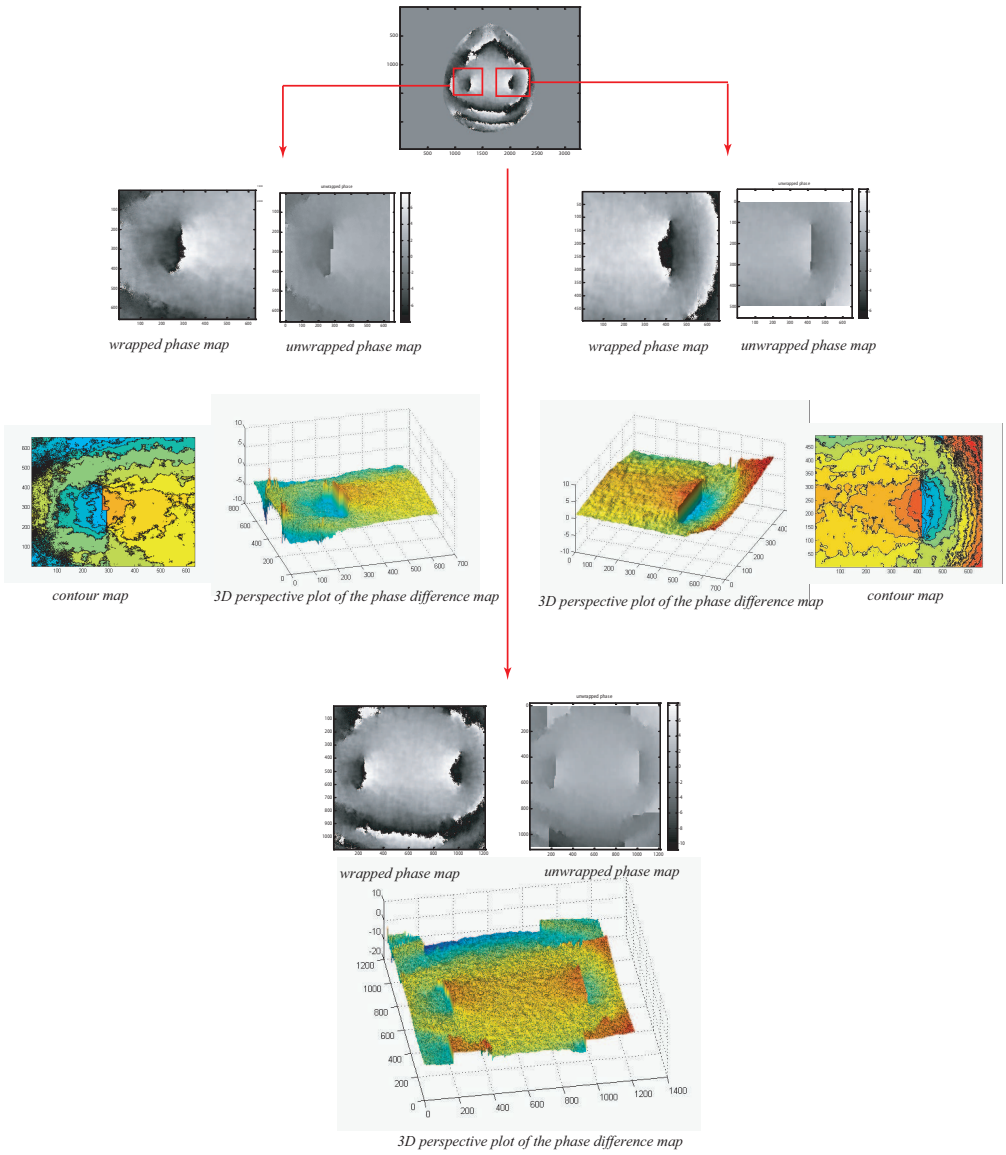

Figure 6.73 orcine cornea collagen phase information.

Last but not least, the novel and significant explore has been made with the structure of cornea. The structure was observed by our surgeon (Gary Misson, Warwick Hospital), he notice the structure from the 2D polarised pictures of cornea. The structure has been proved by the phase stepping method and polarised microscopy images, and it has been reconstructed by 3D profile.

Firstly, from the high resolution image we obtained from polariscope, we draw three lines at the axis $Y - 770pixel$, $Y - 885pixel$, and $Y - 1045pixels$, at the range between $X - 600pixels$ to $X - 1100pixels$, the intensity curve are shown

in Fig.6.74

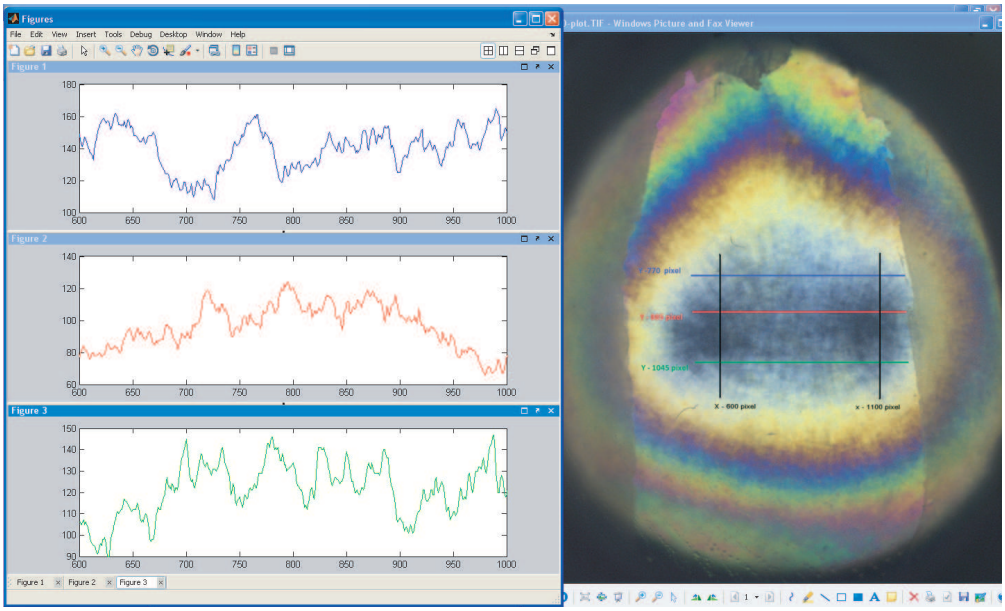

Figure 6.74 Porcine cornea phase information with three cross lines.

The three curves which include phase information are distributed regularly. We will prove it closer, as Fig.6.75 shows, we take a picture of the center part of cornea, and analyse by phase stepping method, we can see clearly about the reticular fibre curve changes regularly in Fig.6.75.

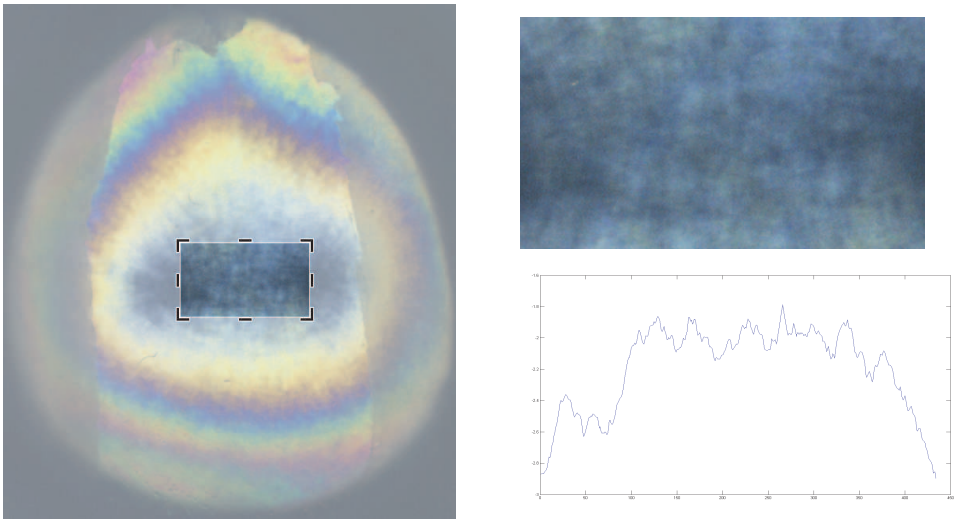

Figure 6.75 Porcine cornea phase information.

The 3D information of surface reconstructed as shown in Fig.6.76.

At the bottom part, there is another set of data shown in Fig.6.77 to prove the

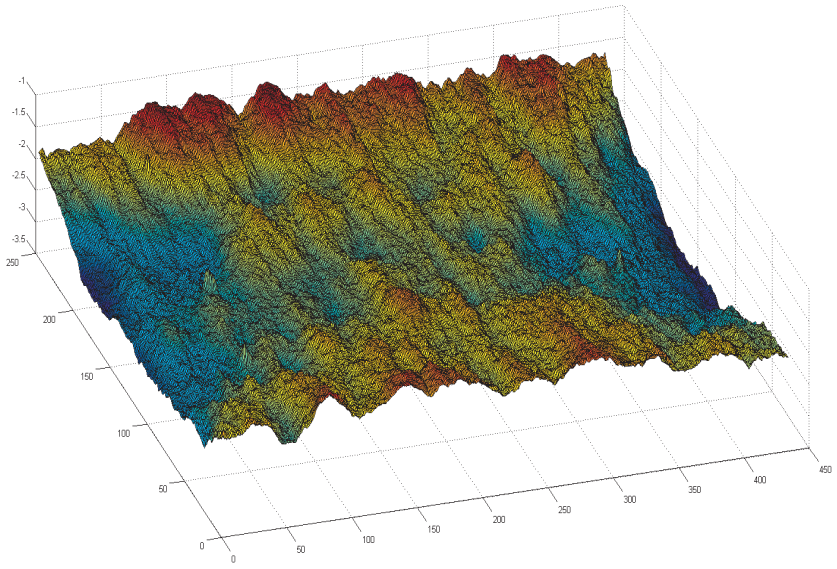

Figure 6.76 Porcine cornea phase information 3D reconstruction.

structure regulation.

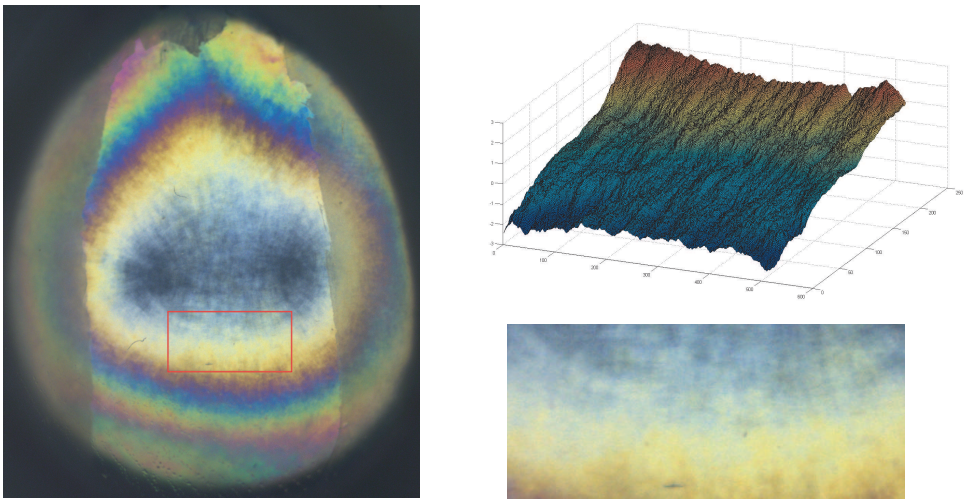

Figure 6.77 Porcine cornea phase information 3D reconstruction with bottom part.

The orientation of the circular polarised light is independent and this allows the birefringent elements of all orientations to be identified simultaneously as lighter structures against a darker background, compared with linear polarised light. Due to sensitivity of the measurements, the circular polarised system could support phase stepping and FFT methods, the techniques effective in qualitative examinations.

The study is based on an isolated model and different techniques for measuring corneal structure. Novel contributions have been shown for a confocal elliptical organization of the corneal stromal lamellar structure compatible with the results of previous investigations, and also combined with the phase stepping and Fourier transform techniques in the study. Future studies may consider the whole field phase map calibration and improve the birefringence structure.

6.4 Light Field $K2$ Microscopy

Inserting a micro-camera-array into the $K2$ microscope, this can capture the light fields and 3D information in the depth of field for biological specimens such as the cornea sample. The interest is focused on the 3D shape of the specimen. The novel methods in this section combine two techniques together for detecting not only the birefringence distribution, but also the 3D birefringence object reconstruction. We can nevertheless produce useful perspective views and focal stacks from them. Applying 3D deconvolution to these focal stacks, we can produce a set of cross sections, which can be visualized using volume rendering. For the 3D biological specimen, there is some reconstruction work that has been undertaken previously, but in the area of the reconstruction of the 3D phase object, this is absolutely an exploration of new technologies[108].

6.4.1 Introduction

Microscopes are the primary scientific instrument in many biological laboratories, but they still have some limitations. First of all, diffraction limits their spatial resolution, especially at high magnifications. And then, the object is placed and observed in the microscope system from a single direction, which makes it hard to disambiguate superimposed features. Moreover, it has a very shallow depth of field. The higher magnifications also brings more limitations. In this section, we show that by placing a micro-camera-array, which involves moving one camera on the plane a very tiny distance, at the intermediate image plane of a microscope,

we can capture a light field of the specimen in each position obtaining several photographs to satisfy the requirements of the phase stepping technique. In this case, we sacrifice spatial resolution to obtain angular resolution. Synthetic focusing can be used to produce a focal stack, with a sequence of images each focused on a different plane. In the latter, the observation is made whereby each slice in a focal stack contains blurred contributions from features off the plane on which it was focused. The number of slices in the resulting volume is limited by the axial resolution of the light field.

6.4.2 Light Field Microscope

The design for the microscope is a row of cameras placed behind the microscope lens, which is like a lenslet, as described in Fig.6.78. Then each camera records a perspective view of the scene observed from that position on the array. The spatial resolution depends on the number of cameras and the angular resolution on the number of pixels for each camera sensor.

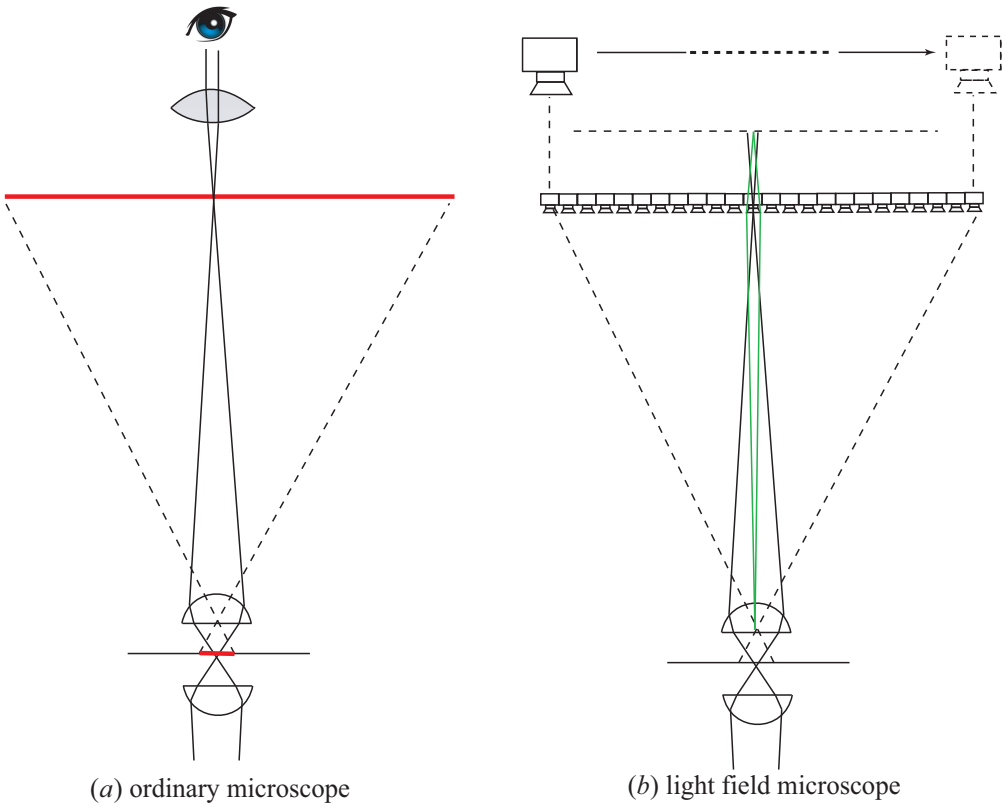

Figure 6.78 Optical layout of our light field microscope.

For a microscope, where the resolution of the image is critical, a field lens is essential. This choice also allows us to reuse the most critical and highly optimized component in a conventional microscope, which is shown in Fig.6.78(a). It would be challenging to replace this subsystem with an array of cameras to obtain good performance results. But due to hardware limitations, it is impossible to place such a micron size camera as an array in the microscope system, so a good high resolution camera takes the place of the camera array. The design is shown in Fig.6.78(b).

6.4.3 3D reconstruction

The method used to estimate and calculate the 3D shape of the specimen from the image is always a question of great interest. The common approach is through using shape stereo, which uses at least two points of the view images to build the shape of the object. On the other hand, there are other approaches to the reconstruction of images such as tomography techniques. The images are captured from the same point of view, but have different depths of field. The technique used in this study is somewhere between these two approaches. Moving the camera along its rail, we can form a sequence of images focused at different depths. This process is a convolution of the object by the point-spread-function to form a 3D image[109]. The reconstruction by 3D deconvolution needs to restore the original state for the portion of the light recorded in each pixel which is due to blurring back to the voxels from which they came.

6.4.4 Conclusion

A new kind of microscope design which used our existing techniques has been described in this thesis. It combined camera-array techniques with microscope lens to capture the 3D structure of microscopic objects in a single snapshot. In the birefringence measurement, the birefringence structure of the specimen can be detected in each frame of the depth of field. The 3D structure of the birefringence distribution may then be rebuilt.

The design does not need camera to focus perfectly before photographing each sample in a multi-well plate when using the light field microscope, leading to higher throughput.

When examining large specimens or the details of the small specimens, an appreciation of perspective is as important as lateral resolution. A light field microscope offers even more appreciation of the 3D structure, if we can devise suitable ways to present the information.

Regarding future work, the 3D reconstruction result of the birefringent structure needs to be improved. Also if the hardware is not a problem, a better understanding of the angular distribution of light in our microlens subimages would be advantageous.

6.5 Conclusion

In this Chapter, the measurement of the cornea is the main work of this study. For the material and structure that is known, firstly a software simulation was used to prove the success of the algorithm. In determining the algorithm based on the results from the simulation, this has lead to an increased general understanding and experimental reference.

To ensure the feasibility and accuracy of the experiment , and to obtain more standard reference results, we still choose materials that we were familiar with to make a copy of the cornea. The data obtained from the model in the experiment were analysed successfully.

Then some types real cornea were measured by using phase stepping and Fourier transform methods, including a study of the phase. The details around the collagen part are still ambiguous. In order to obtain the birefringence structure and details, the $K2$ microscope lens was implemented in the experiment. The results give a more clear explanation for the previous unknown area. It shows good quality results for the birefringence structure and phase distribution of the surface of the cornea.

Further efforts are being made to combine the system with camera-array technology for measuring the 3D structure of the birefringence. The camera-array was successfully set up and the data analysed as expected. The algorithm was proved and worked well with the test data. Future work may include calculating the column axis data to reconstruct the 3D results of the cornea phase map, and testing the micro-lens-array to simplify the experiment design.

The objective of this thesis has been to create a method to obtain a quantitative measurement of the cornea. Ideally this should be a system which works in reflection and has the eventual potential to be used as a medical diagnostic tool for monitoring structural changes in the human eye *in vivo*. To guarantee the system quality, the transmission system has been implemented to prove the method and define the accuracy.

A quantitative phase measuring camera which can measure the optical birefringence through a complex three dimensional object has been tested and designed successfully. Different phase measurement approaches examining the accuracy and ambiguity have been investigated. The corneas have been studied. Collagen forms an optically transparent 'rope-like' structure within the human eye to form the cornea. It presents a complex 'rough' (at the micron scale), strand-like phase structure. Thus the method of measurement required needs to provide accurate measurements, for both the phase and spatial structure. A simulation devised using transparent adhesive tape, which has a similar structure and phase shift properties, has been used to investigate different phase measurement approaches.

To investigate the cornea, it was suggested by the Hospital Consultant Mr Gary Misson (Warwick Hospital consultant eye surgeon), from his work on cornea structure that a physical simulation be used. Phase structure which is known to occur in the cornea has been detected in this experiment, and reconstructed using a 3D profile. To give a quantitative definition of the value which is related to the cornea birefringence and phase shifting, the simulation and visualization has been done to compare the results with the experiment's results. A numerical simulation of the 'test bed' model was also performed. Both to quantify the physical disc model and

to be able to calculate the type of stress loading which maybe experienced by the cornea. The model also provides the opportunity to create a more realistic three dimensional structure and the ability to model parameters such as the curvature and the varying cornea thickness.

Chapter 7

Conclusion and Future Work

7.1 Conclusion

7.1.1 Summary

The discussion and main points of this research are described in this chapter; together with some suggestions for future research.

The objective of the research has been to make a quantitative phase measurement. It purpose being to design a method of non-contacting, in vivo phase measurement of the birefringence within the cornea. The problem has been complicated because the collagen forming the cornea has a small scale irregular organic phase roughness of $10 - 50$ micrometre and a large scale regular phase structure of $30 - 50$ micrometre.

This research attempting to solve this problem has been approached in the following manner:

Firstly a review was undertaken to identify the available techniques and technology that might be applied for such measurements.

Then using the findings of this review along with the advice provided by an ophthalmic surgeon (Mr Gary Misson) a simplified numerical model was created and tested against an equivalent physical model.

Then an evaluation was undertaken to show how quantitative phase measurement

could be made of a fringe despite high levels of phase roughness.

Finally this research was combined to create the basis of a new type of ophthalmic instrument for the in-vivo measurement of corneal birefringence.

7.1.2 Contents of Chapters

The first two chapters of this research present a review of the current approaches to birefringence and phase measurement, with the purpose of the study being to review the accuracy and phase sensitivity of different available techniques. Consideration has also been given to the available cameras, and the imaging light source technology that is available. In Chapter 3 the camera characteristics are presented and compared with the phase maps of the specimens at different wavelengths. The FFT and Phase Stepping methods were then evaluated for birefringent measurement sensitivity. In Chapter 4, this sensitivity was then applied to a simulation which exhibited the specific problems associated, with the phase measurement of the cornea.

The conclusions from this stage of the research showed that the camera requires a minimum resolution of 1,000 x 1,000, pixels but that a resolution of 4,000 x 3,000 was preferable. The 4 Step Phase stepping approach from $Patternson\ and\ Wong$ was found to be the most accurate, sensitive, and quickest algorithm for this application. A successful reconstruction was achieved of a semi-random phase model simulation of the cornea.

Prior to its application to the cornea, a computer simulation was performed. The model was created based on the experience of an ophthalmic surgeon, who has developed the research as a simplified birefringent analogue of the cornea structure. The feasibility of this approach has been shown to be valid both by numerical simulation ($SolidWorks$) and by an experimental physical model. Chapter 5 also introduces the method by which the cornea can be measured by a specifically designed polariscope.

Chapter 6 concentrates on a series of animal corneas using a polariscope sys-

tem. The results show the birefringent structure of cornea. A long range microscope ($K2$ Infinity lens) was used to investigate the micro-phase structure of the cornea. This was further investigated by using both the FFT and Phase Stepping methodologies. Both techniques were applied in order to explore their accuracy and applicability to the creation of a new type of instrumentation.

Part of the research started, but as yet not completed, was to create a multi-camera, synthetic aperture phase measurement technique, with the objective being to combine phase analysis techniques with a full 3D investigation of the birefringent structure within the cornea.

The conclusions obtained from the research described in the thesis are:

- A quantitative analysis of phase accuracy in numerical analysis and experiment has been performed. The advantages and disadvantages of both *FFT* and Phase Stepping methodologies have been analysed.

- A clear phase representation of the cornea has been achieved. *FFT* and Phase Stepping reconstruction was used for such a structural visualisation of the cornea. The real physical model and numerical model of the cornea create a new approach for cornea structure research.

- A visualization of the macro/micro phase structure in the cornea was observed clearly with a polychromatic source. This can also be observed by direct imaging. Using high resolution image applied for phase activity of the cornea, the 3D properties of the cornea can be studied.

- A quantitative reflection polariscope technology for in vivo cornea measurement has been designed and developed.

- The structural visualisation has been shown not only by the *FFT* or Phase Stepping reconstruction approach, but also by using a multiple camera with synthetic aperture approach to investigate the 3D phase object.

- The accuracy of the phase encoding approaches (*FFT* and Phase Stepping) has been demonstrated with multi-wavelength monochromatic light source, and has been compared to polychromatic one.

The items above show the main contribution of my work described in the thesis. The following describe the details of each part of the work.

- Accuracy of Phase Encoding Approaches

The quantitative analysis of optical phase measurement is one of the main parts of this research. It relies on previous work, and the results are compared with different algorithms and software. Phase accuracy and error analysis were studied successfully based on both the phase stepping and Fourier transform methodologies mentioned above. The main contribution of this section was to provide a significant calibration for precision measurement with quantitative accuracy.

It is not only the basis for the application of the cornea measurement, but also provides a quantitative assessment of the existing equipment and analytical methods. On the other hand, the previous FFT software, Fran, is implemented primarily as a reference for the new phase analysis code. The new FFT code can deal with image data which have increased noise, high resolution, and different types of image formats or low contrast. The previous software Fran is no longer suitable for such complicated image data.

In the analysis of the phase stepping method, although Fran provides a simple three-step analysis, the incidence of failures and mistakes was very high. Therefore code running in $Matlab$ was created, which can be used to calculate the results of multi-step measurements with four or six steps. This is more suitable for the system set up in our lab, which is a multi-adjustable polariscope system, and helps to develop the maximum potential of the system.

Advantages and Disadvantages of both methodologies

Both Phase stepping and Fourier transform methods have their advantages and disadvantages, and have been developed and improved through my studies. The phase stepping method is widely used in phase measurement, which requires multiple interferograms taken at different times, and it is also very strict regarding the requirements for the operation of the experimental equipment. If the polariscope system can not support each optical component rotated by a precise angle; the phase stepping method can not be implemented. The multiple frames captured at different times may increase the possibility of errors occurring, especially for dynamic measurement. But the multi-camera which was improved for use with measurement may overcome this problem. The images can be captured at the same time in situations with different phase angles. It works efficiently, although calibration work is necessary. The results are more precise, and this method can avoid interference from the noise and dust of the detected objects.

The phase stepping algorithms include several schemes, one of which is the six-step. Using fewer fringe patterns for phase shifting is advantageous as this reduces the computation time and the number of phase step errors. With the comparison of the accuracy and error analysis for four and six steps undertaken in the previous chapter, the four-step method was adapted in the implementation. It produces accurate measurements even when the isoclinic component is not negligible.

The *FFT* method requires only one interferogram to extract phase information and needs a spatial wedge to generate the carrier fringe pattern, which is different to the phase stepping method which needs a phase shifting device. Image noise and ambiguity can make the *FFT* analysis fail, which means the accuracy of these algorithms in evaluating fringe order are substantially reduced when data are selected from near stress concentration areas. One of the possible reasons for this is that the intensity data may not have been recorded accurately due to inherent difficulties associated with digitization in the high density areas of the fringes. The frequency needs to be high enough to modulate the phase information, and the achievable accuracy is nearly as good as the phase stepping method. The error

of the *FFT* results is caused by frequency truncation, intensity contrast, random noise, or frequency mistake. The *FFT* method is in general more computationally intensive than the phase stepping method.

- Exploring the Structure of the Cornea

In this part, polarization light transmission measurements were made under conditions that closely approximate the physical state in order to probe the lamellar phase structure in the center of the porcine cornea. The results were interpreted with the aid of a newly developed method. The carrier fringe and phase stepping method are both considered for cornea measurement.Theory enables the predictions of the properties of the lamellar ordering, and the experimental results are consistent with the structure and phase distribution based on the transmission of the polariscope system.

The cornea is not a familiar specimen and its structure and material were introduced in Chapter five. According to the cornea's physical dimensions from medical data, a mathematical model is constructed for the 3D software simulation. Based on the study of the simulated cornea model, both the Fourier transform and phase stepping methods are evaluated. The phase stepping techniques were presented in this part and were successfully implemented to analyse the structure and optical properties of the cornea. The presence of the birefringent structures of the cornea has been used to investigate ocular optical properties and develop clinically oriented experimental and commercial devices.

The spatially resolved polarization properties of the in vitro isolated specimens were studied. These properties have been calculated from the elements of the spatially resolved Jones matrix measurements using a rotating imaging polarimeter in the transmission mode. As a result of this research a complete description of the polarization properties of the cornea are provided.

Combined with other optical elements and illuminated with a monochromatic light source, the different birefringent specimen, a cornea exhibits structural fringe patterns created by the alignment of the collagen fibers within it. The phase shifting

technique is implemented in the measurement, and an advanced digital photoelastic system is used to visualize and study the nature of the birefringent distribution of collagen fibers within the cornea. The underling structure of the cornea can be measured in a quantitative manner.

- High Resolution Image applied to the Phase Activity of the Cornea

Limited by the resolution and size of the specimen, the phase map will generate some error which may be caused by noise and ambiguity. Consequently there will be discontinuous phase distribution occurring. To solve this problem, the K2 microscope lens is introduced into the experiment. The details of the small parts of cornea can be investigated using this device. The phase discontinuous area is magnified and studied again using the phase stepping method. The phase jump occurs at the points where the collagen structure exist. On the other hand, the particulars on the peak of the central cornea were measured successfully. The birefringence map arranges the heterocoelous distribution on the top of the cornea; this structure is very tiny compared with the whole curvature of the cornea. Furthermore, the birefringent structures are also observed from the phase map results. The area of interest in the cornea which studied in the research is the center area around the collagen. The structure of the collagen fibre has been detected and the accuracy if measurement can be reached to $5-20\ micrometre$ in dimension. The structure features of the cornea which are shape, birefringent structure, curvature, and phase distribution are analysed. One object of the value in my research is to create an optical diagnosis which can measure the changes in the cornea structure.

The corneal collagen has a few of properties that allow it to fulfil its role as the main structural component within the tissue. Fibrils are narrow size, uniform in diameter and precisely organized. These properties are vital to maintaining transparency and providing biomechanical prerequisites necessary to sustain shape and provide strength. The objective of the experimental data and results is to understand the birefringence of the cornea.

The structure and organization of corneal collagen is complex compared to other tissues. The nature of the subfibrils and distribution permutation are still not fully

understood. Similarly, the organization of the fibrils requires further study. These are the main important factors regarding cornea transparency. The new technology described in this research leads to a better appreciation of high level structures and birefringence information. This is significant for understanding the cornea and devising methods for improving corneal refractive surgery.

- Exploring Multiple Cameras with Synthetic Apertures to Investigate the 3D Cornea Phase Object

A new design for the camera array technology and the microscope were implemented together. The camera array has a big aperture, which may be used for focusing change and measurement of depth of field. The focus can be moved through a family of planes by merely shifting and adding images.

For the purpose of achieving optimal focusing and the depth of field for 3D imaging, we firstly propose a setting where there are three models. The experimental results demonstrate that such parameters work in practice to successfully generate a large depth of field.

The novel hardware design and method used in this part are the K2 microscope lens and a synthetic aperture multi-camera system. By simulating the camera as a micro-lens combined with the K2 lens system, this becomes a light field polarised microscope system. Applying 3D deconvolution to these focal stacks, a set of cross sections can be produced, which can be visualized using volume rendering by capturing light fields of the cornea.

One advantage of our microscope is that it separates images captured at one selected viewpoint and focus. Thus, a specimen may be photographed and analysed at different times, or photographed in one hospital and examined in another. By using our approach the automated microscopes would not need to focus perfectly before photographing each sample in a multi-focus plate, which leads to higher throughput. This technology may be improved in future work. By considering the combining of the multi-lens device, the advantages of the completed light field polarised microscope system are:

- One shot focusing: Similar multi-cameras work together, all the features and plane of the specimen can be recorded and the most interesting and focused plane may be considered further. Also the image data will be of high resolution. - Real time focusing. - Depth of field microscope: This offers even more appreciation of the 3D structure, if suitable ways to present the information can be devised.

- The structural visualisation of the FFT and phase stepping reconstruction approach.

The technology used here for measuring the phase shifting is based on a property exhibited by most transparent models, which is the property of birefringence. Some materials naturally present double refraction, but in some applications, such as photoelasticity, the materials chosen exhibit birefringence when the specimen is loaded. The classical manual procedure of analysis is usually tedious and time consuming; and it requires skill and experience, however, with the advent of digital image processing, processing has advanced. The computer brings the development of the finite element method, while birefringence measurement and its applications have the capabilities in providing quantitative data. Phase unwrapping approaches have not fully addressed quantitative and biomaterial measurement and the success of the technique have been presented in phase stepping and fringe accuracy analysis in my work. Applications in my work have included multi-wavelength light source implementation in the phase measurement, biomedical material phase measurement, and multi-camera phase detection. The technique has been shown to be applicable to the phase maps generated by the *FFT* and phase stepping methods.

Phase stepping and *FFT* methods provide the coding of elevation and contour maps. Comparing both methods in details, the phase stepping method is adapted to non-linearities in response to the detector and the phase is computed from a series of intensity measurements. The *FFT* method depends on the deviation in the straightness of a set of fringes as a reference background. The accuracy of the *FFT* is more reliable for the spatial measurement of the fringe position than for the intensity.

However, in the case of photoelasticity, the fringe analysis approach is not straightforward. Considering the phase shifting method for the fringe pattern analysis, the method requires that the phase of an interferometer is shifted by known amounts to generate the required phase shifted images for analysis. In the birefringent measurement, the two beams travel through a common optical path, so it is difficult to phase shift one beam without introducing shift to the other beam. To overcome such problems, the multi-phase-stepping method has been evaluated and compared for accuracy.

It was found in this research that a phase shifting operation can produce phase maps from the red, green and blue components extracted from the fringe image under white light conditions. Due to the spectral characteristics of the light source and the poor quantum efficiency in the blue channel of the *CCD* sensor, the phase map of this component is noisy in regions of high fringe density. The next improvement in the normal polariscope would be the incorporation of other light sources, such as a monochromatic *LEDs*.

7.2 Future Work

There are a number of feasible extensions that may be implemented to take forward the findings from this research.

- With the application of *multi-LED*, the birefringence distribution on the specimen's surface could be detected separately at different wavelengths. The profile of the object surface could also be measured using a height resolution of microns. With the development of the *LED* manufacture, a new model of different wavelength *LEDs* could be integrated. The new hardware would improve the efficiency of the system and lower its cost. The images using broadband sources would be significantly less affected by coherent noise.

- For the phase information analysis, if when using the *FFT* method, the high stress concentration areas cannot be solved perfectly, then a high density carrier must be used. However using the phase stepping method, the resulting large amount

of high resolution image data will require a powerful computer for calculation and for the results to be displayed.

- The experiments in a lab are mainly focused on the study of the transmission system, as the cornea specimen is a transparent material. But in actual use, the transmission system would need to be changed to be a reflection based system, the feasibility of which has been demonstrated here. Because an *LED* is an incoherent light source, theoretically, it cannot be applied for diffraction and scattering. These disadvantages have been overcome and improved in experiment and we obtained very good results data, so the software will need to be improved to solve this problem.

This technology has improved not only the software but also the hardware so that the cornea measurements can be made at low cost, and by employing a simple and direct approach. This improved system is suitable for the analysis of the birefringence structures of the specimen *in vivo*.

The experimental findings of the elliptic and hyperbolic populations of collagen fibrils, may explain the optical phenomena of the central corneal retardation with biaxial-like behaviour in more peripheral areas.

The advantages of this technique over other techniques are that it is relatively simple, and there is apparatus readily available with which to implement it. It has no more risk than for conventional anterior segment photography and can be applied in vivo. Studies are currently underway to apply the technique to interferometery for comparison.

Appendix A

AVT Cameras | OSCAR F-810C / 8 MPixel

AVT Oscar F-810C

16-bit High SNR mode

Think big, when you get digital!

The AVT OSCAR F-320C, F-510C and F-810C (color) are very compact IEEE 1394 C-Mount multi-megapixel cameras, equipped with highly sensitive SONY frame readout CCD sensors. The camera offers an external asynchronous trigger shutter and operates in 12-bit mode. The AVT OSCAR family offers up to 8.13 megapixel and is thus particularly suited for use in microscopy and medical applications. A preview mode at high frame rate lets you easily position and expose the object of interest. Due to the industrial housing and additional frame grabber facilities, the camera can be perfectly used in several machine vision applications also with moving objects. The extensive built-in image processing possibilities (image pre-processing) result in outstanding image quality, reduced retouching, less load on the system and higher performance overall. The integrated smart functions take over essential functions of the frame grabber, which is compensated for use of the OSCAR. The OSCAR can be easily integrated into existing applications thanks to its powerful and flexible APIs (HALCON, DirectShow, Twain, libdc1394, etc.).

Highlights OSCAR F-810C:

- 3272 x 2469 CCD frame readout shutter
- Up to 3.1 fps at full resolution
- True partial scan
- Format_7 support (flexible AOI; flexible speed)
- Optocoupled asynchronous image trigger
- 16-bit High SNR mode (improves s/n ratio by up to factor 16 = 24 dB)
- Image pre-processing features:
  - Auto controlled gain, exposure, white balance
  - Color correction, hue, saturation
  - Real-time shading correction
  - Programmable LUT
  - And lots more ...
- Smart frame grabber features:
  - Image FIFO memory (up to 256 MB)
  - 1 trigger, multi-shot, free-run
  - 2 programmable inputs and outputs
- Color (Raw8, Raw16, RGB8, YUV 4:2:2, YUV 4:1:1, Mono8)
- Special mode for monochrome applications (Mono8)
- Super compact size
- C-Mount

ALLIED VISION TECHNOLOGIES GMBH
Taschenweg 2a | D-07646 Stadtroda | Germany
Phone: +49 (0)36428 6770 | Fax: +49 (0)36428 677-24
www.alliedvisiontec.com | info@alliedvisiontec.com

ALLIED Vision Technologies

AVT Oscar F-810C

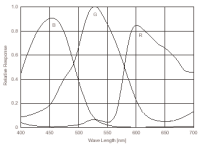

Sensor specifications (extracted from the data sheet of the sensor - excluding lens and filter)

Pin	Signal
1	External GND (RS232 and ext. power)
2	External Power (8...36 V DC)
3	
4	GP Input 1 (Default: Trigger)
5	
6	GP Output 1 (Default: IntEna)
7	GP Input GND
8	RxD (RS-232)
9	TxD (RS-232)
10	GP Output Power
11	GP Input 2 (TTL)
12	GP Output 2

Connections

Preview mode (by sub-sampling):	
548 x 410	15.0 fps
320 x 240	20.8 fps
AOI:	
3272 x 2469	3.1 fps
1600 x 1200	5.7 fps
1280 x 960	6.7 fps
800 x 600	9.2 fps
640 x 480	10.5 fps
320 x 240	14.5 fps

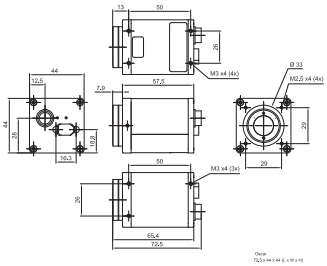

Dimensions

Camera Specifications

Image device	Type 2/3 (diag. 11.07 mm) Sony CCD frame readout (ICX-456AQ)
Effective picture elements	3288 (H) x 2470 (V)
Cell size	2.7 µm x 2.7 µm
Resolution depth	12-bit / up to 16-bit in High SNR mode
Lens mount	C-Mount
Color modes	Mono8; Y8-green, Y8-red, Y8-blue; RAW8/16; RGB8; YUV 4:2:2; YUV 4:1:1
Digital interface	IEEE 1394a; IIDC V1.3
Transfer rate	100 Mbit/s, 200 Mbit/s, 400 Mbit/s
Frame rates	Up to 3.1 fps in Format_7, up to 8.9 fps in Format_7 progressive
Image memory (FIFO)	64 MB, optional up to 256 MB
Gain control	Manual, 0 ... 20 dB (0.035 db/step); auto gain (select. AOI)
Shutter speed	20 µs ... ~67 s; auto shutter (select AOI)
External trigger shutter	Trigger_Mode_0, Trigger_Mode_1 (prog. scan, F_7 M_0); advanced feature: Trigger_Mode_15 (bulk); image transfer by command; trigger delay
Smart features	Real-time shading correction, color correction, High SNR mode (image summation); two configurable inputs, two configurable outputs, image mirror (L-R<->R-L), sub-sampling, serial port IDC V1.31
Power requirements	DC 8 V ... 36 V via IEEE 1394 cable or 12-pin HIROSE
Power consumption	3.6 watt (@ 12 V DC)
Dimensions	72.5 mm x 44 mm x 44 mm (L x W x H); w/o tripod and lens
Mass	170 g (without lens)
Operating temperature	+5 ... +45 ° Celsius
Storage temperature	-10 ... +60 ° Celsius
Regulations	EN 55022, EN 61000, EN 55024, FCC Class B; DIN ISO 9022, RoHS (2002/95/EC)
Options	Removable IR cut filter, host adapter, locking IEEE 1394 cable, AVT FirePackage/ Direct FirePackage/Fire4Linux

ALLIED VISION TECHNOLOGIES GMBH
Taschenweg 2a | D-07646 Stadtroda | Germany
Phone: +49 (0)36428 6770 | Fax: +49 (0)36428 677-24
www.alliedvisiontec.com | info@alliedvisiontec.com

www.axis.com

3316B/EN/R6/0904

Technical specifications – AXIS 206 Network Camera

Camera	
Image sensor	1/4" Progressive scan CMOS
Lens	4.0 mm, F2.0, fixed iris Horizontal angle of view: 54°
Light sensitivity	4 – 10000 lux, F2.0
Shutter time	1/10000 s to 1/2 s
Video	
Video compression	Motion JPEG
Resolutions	Up to 640x480
Frame rate Motion JPEG	Up to 30 fps at all resolutions
Video streaming	Controllable frame rate and bandwidth
Image settings	Compression, color, brightness, contrast, white balance, rotation Text overlay
Network	
Security	Password protection
Supported protocols	IPv4, HTTP, TCP, ICMP, UDP, SMTP, FTP, DHCP, UPnP™, Bonjour, ARP, DNS, DynDNS, NTP
System integration	
Application Programming Interface	Open API for software integration, including VAPIX® from Axis Communications available at www.axis.com

General	
Language support	Chinese, English, French, German, Italian, Japanese, Korean and Spanish
Processors and memory	32-bit RISC CPU Motion JPEG compression chip 16 MB RAM 4 MB Flash
Power	5.0 – 5.5 V DC, max 2.5 W
Connector	RJ-45 10BASE-T/100BASE-TX Auto-MDIX
Operating conditions	5 – 50 °C (41 – 122 °F) Humidity 20 – 80% RH (non-condensing)
Approvals	EN 55022 Class B, EN 61000-3-2, EN 61000-3-3, EN 55024, EN 61000-6-1, FCC Part 15 Subpart B Class B, ICES-003, VCCI Class B, C-tick AS/NZS 3548, EN 60950-1 Power supply: EN 60950-1, UL, CSA
Weight	180 g (0.39 lb.)
Included accessories	Power supply, stand, Installation Guide, CD with installation tool, software and User's Manual

More information is available at www.axis.com

Dimensions

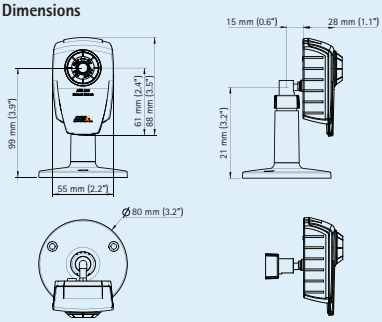

Optional accessories

Vandal-resistant housing

For information on AXIS Camera Station and video management software from Axis' Application Development Partners, see www.axis.com/products/video/software/

AXIS COMMUNICATIONS

3COM® BASELINE PLUS SWITCH 2900 GIGABIT FAMILY

Enterprise-class, Gigabit switches for small and medium businesses, voice ready with PoE and advanced features for network control and flexibility

from top to bottom: 3Com Baseline Plus, Switch 2920, Switch 2928, Switch 2952, Switch 2928 PWR, Switch 2928 HPWR

OVERVIEW

The "smart" voice-ready 3Com® Baseline Plus Switch 2900 Gigabit Family delivers Layer 2 enterprise-class Gigabit switching solutions along with layer 3 static routes, customized and priced for small and mid-sized organizations.

These managed switches offer tremendous value to small and medium businesses looking for a low cost solution who need a level of control over their network not offered by unmanaged switching products, without sacrificing the advanced functionality normally found on higher-end managed switching products.

KEY BENEFITS

LAYER 2 SWITCHING WITH ADVANCED FEATURES

The Baseline Plus Switch 2900 Gigabit Family helps build a voice ready network—with 3Com's unique auto-voice VLAN, advanced voice QoS, SNMP-based management, Power over Ethernet (PoE) and other features.

To ensure optimal use of the network bandwidth and deliver maximum voice and data quality, traffic flow can be directed according to the needs of the business using Spanning Tree and Rapid Spanning Tree, traffic prioritization, priority queuing and VLANs.

Link aggregation can be done via IEEE 802.3ad LACP or manually, allowing ports to be grouped together to form an ultra-high-bandwidth connection that greatly expands bandwidth capacity to the network core or other parts of the network.

Baseline Plus Switch 2900 models are available with 20, 28, and 52 ports; two 28 port PoE models (one with 170W budget and the other with 365W power budget) deliver data and power over the same cabling. Each switch also has four dedicated SFP ports for fiber uplinks over longer distances.

ENTERPRISE-QUALITY SECURITY

Enterprise-quality security is provided with IEEE 802.1X network login and advanced Access Control Lists (ACLs), which enable usage policies via the switch at each point of access to the network. Time based policies can also be configured on these switches. All management communications are encrypted with HTTPS.

POWER OVER ETHERNET

The Baseline Plus Switch 2928 PWR and 2928 HPWR provides inline power to attached devices—access points, Voice over IP (VoIP) phones, IP security cameras, etc.—via industry-standard IEEE 802.3af PoE over a single Ethernet cable, resulting in significant deployment cost savings. These switches also support pre-std PoE plus functionality that will enable the switch to deliver 30W of power on each port.

NO SWITCH SETUP REQUIRED

Baseline Plus Gigabit switches are operational straight out-of-the-box; as long as default settings are acceptable, there is no need to configure the switch. If desired, the switch can be configured using a web browser, console port, or SNMP management software.

ENHANCED INTUITIVE MANAGEMENT OPTIONS

For networks that require more control, the switch web management interface provides an intuitive, menu-driven process for even novice users to quickly

KEY BENEFITS (continued)

and confidently configure the switch during initial setup and manage it during normal operation. Graphical switch and port views provide a clear understanding of switch status and configuration.

In addition, the web interface features individual port-traffic monitoring (port mirroring) and diagnostic tools like ping and traceroute. A cable diagnostic tool lets users troubleshoot basic connectivity problems via the web management interface further simplifying network installation.

IMC management platform. IMC is our next generation fully integrated comprehensive management platform. It delivers full FCAPS solution as defined by ISO, among other features. IMC management software can be used to map the network topology, indicating what devices are connected, and on what ports. Switch management and software upgrades can be easily done. Other SNMP-based management tools may also be used.

The Switch family also supports a compact Command Line Interface (CLI) that is accessed via the front panel console port. Using the CLI, major switch management options can be quickly configured.

FEATURE HIGHLIGHTS

FEATURE	DESCRIPTION
Performance	
VLANs	Segment the network by grouping users based on their data or traffic exchange requirements. This ensures optimal use of available bandwidth as traffic flow is directed according to the needs of the business.
Advanced QoS and traffic limiting	Traffic prioritization, using IEEE 802.1p Quality of Service (QoS) and Type of Service (TOS) with Differentiated Services Code Point (DSCP), and ingress/egress rate limiting help ensure that critical time-sensitive traffic like voice gets the priority needed for quality communications.
Link aggregation (trunking)	Group together up to 8 ports automatically using Link Aggregation Control Protocol (LACP), or manually, to form an ultra-high-bandwidth connection to the network backbone; help prevent traffic bottlenecks.
Rapid Spanning Tree Protocol (STP/RSTP/MSTP) support	Improves network compatibility, scalability and availability.
IGMP snooping	Multicast filtering optimizes network performance, instead of flooding traffic to all ports.
Unique voice features	Automatic assignment of voice traffic to separate VLANs ("auto-voice VLAN"), advanced voice QoS, traffic limiting, multicast filtering and PoE support delivers the support necessary for quality voice communications.
Fiber uplink	Achieve greater distance connectivity using gigabit fiber uplinks.
Flexible Gigabit uplinks	Daisychain multiple units together via the built-in copper Gigabit uplink ports or connect to a network backbone via SFP-based fiber modules.
PoE support (PWR model only)	Provides power for IP phones, wireless LAN access points, and other IEEE 802.3af-compliant devices over the same cable used for data; lowers total cost of ownership since there is no need to run additional electrical wiring. Note: pre-std PoE Plus is also supported allowing the switch to deliver up to 30W of power.
Security	
IEEE 802.1X network access control	Provides standards-based security combined with local authentication.
Advanced Access Control Lists (ACLs)	MAC- and IP-based ACLs enable network traffic filtering and enhance network control. Time based ACLs allow for greater flexibiliy with managing network access.
Traffic monitoring (port mirroring)	Administrators can examine suspect data streams received on any port by mirroring the data stream to a monitoring port.
Configuration and management	
Enhanced browser-based interface	Graphical user interface allows even the most novice users to configure the switch during initial setup and monitor it during normal operation.
SNMP support	Switch can be managed with 3Com IMC, Network Supervisor, Network Director and other SNMP-compatible tools.
PoE configuration	PoE power can be enabled or disabled per unit and per port; power can also be limited per port.
Cable diagnostics	Remotely detect copper cable issues using a browser-based tool.

BASELINE PLUS SWITCH 2900 USER INTERFACE

INTUITIVE BROWSER-BASED INTERFACE

With the switch web management interface, even novice users can quickly and confidently configure the switch during initial setup and manage it during normal operation. Graphical switch and port views provide a clear understanding of switch status and configuration.

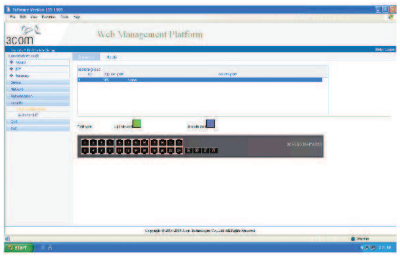

Device summary information for the Switch 2928 HPWR.

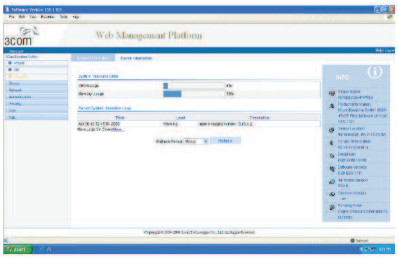

PoE summary information for the Switch 2928 HPWR.

BASELINE PLUS SWITCH 2928 PWR IN A CONVERGED NETWORK

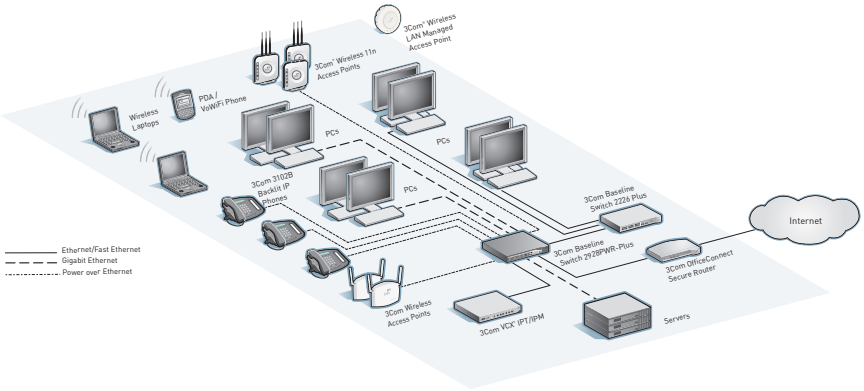

VOICE READY NETWORK

3Com Voice Ready Networks provide an innovative and holistic approach to assessing, recommending and implementing a converged network, solving the most vexing challenges that confront IT managers as they deploy Internet Protocol (IP) telephony systems. With 3Com Voice Ready Networks, organizations can optimize network infrastructure for realtime voice and video traffic, ensure secure communications and protect business assets.

The Baseline Plus Switch 2900 Gigabit Family is an integral component of this approach, offering:

- Automatic assignment of voice traffic to separate VLANs
- IEEE 802.1p prioritization and 802.1Q VLANS
- Advanced QoS and rate limiting capabilities
- IEEE 802.1X authentication
- Power over Ethernet (PWR model only)

SPECIFICATIONS

Information in this section is relevant to all members of the 3Com Baseline Plus Switch 2900 Gigabit Family, unless otherwise stated.

CONNECTORS

Switch 2920
16 10BASE-T/100BASE-X/1000BASE-T
4 Gigabit SFP ports

Switch 2928
24 10BASE-T/100BASE-T/1000BASE-T
4 Gigabit SFP ports

Switch 2928 PWR
24 10BASE-T/100BASE-T/1000BASE-T
4 Gigabit SFP ports
PoE: 170W

Switch 2928 HPWR
24 10BASE-T/100BASE-T/1000BASE-T
4 Gigabit SFP ports
PoE: 365W

Switch 2952
48 10BASE-T/100BASE-X/1000BASE-T
4 Gigabit SFP ports

All switches
All copper ports are auto MDI/MDIX, auto-negotiating RJ-45
Front-mounted console port

PERFORMANCE

Switch 2920
40 Gbps switching capacity, max.
29.8 Mpps forwarding rate, max.

Switch 2928
56 Gbps switching capacity, max.
41.7 Mpps forwarding rate, max.

Switch 2928 PWR
56 Gbps switching capacity, max.
41.7 Mpps forwarding rate, max.

Switch 2928 HPWR
56 Gbps switching capacity, max.
41.7 Mpps forwarding rate, max.

Switch 2952
104 Gbps switching capacity, max.
77.4 Mpps forwarding rate, max.

All models
Wirespeed performance
Store-and-forward switching

LAYER 2 SWITCHING

8,192 MAC addresses in address table
256 port-based VLANs (IEEE 802.1Q)
IEEE 802.3ad Link Aggregation, automated (LACP) and manual aggregation: number of ports/2 trunks, 8 ports per trunk, max.
Auto-negotiation of port speed and duplex
Auto-voice VLAN for automatic vendor-independent segregation and prioritization of VoIP traffic
IEEE 802.3x flow control (half- and full-duplex)
IEEE 802.1D Spanning Tree Protocol (STP)
IEEE 802.1w Rapid Spanning Tree Protocol (RSTP)
Internet Group Management Protocol (IGMP) v1, v2 and v3 is supported
Jumbo frames (up to 10K bytes)
Multicast filtering
Convergence
4 hardware queues per port, with IEEE 802.1p Class of Service/Quality of Service (CoS/QoS) on egress
Weighted Round Robin queuing
Traffic prioritization at Layer 2 using 802.1p QoS, and at Layer 3 using Type of Service (TOS) with Differentiated Services Code Point (DSCP)
Ingress/egress rate limiting
Auto VLAN assignment for voice traffic determined by vendor OUI
CoS remarking for prioritization of VoIP traffic

LAYER 3 SWITCHING

Static routes: 32
Virtual VLAN interface: 8
DHCP relay
ARP entry: 256

SECURITY

IEEE 802.1X Network login
Access Control Lists (ACLs)
MAC-based Layer 2 filtering rules:
- source/destination address
- Ethertype
- CoS
- VLAN

IP-based Layer 3 filtering rules:
- protocol
- source/destination address
- TCP/UDP port
- DSCP value
- IP precedence

Management communications are encrypted via HTTPS

POWER OVER ETHERNET

Switch 2928 PWR
IEEE 802.3af
170W

Switch 2928 HPWR
IEEE 802.3af
365W
Note: Both switches support pre-std IEE 802.3at std.
This enables the switch to deliver 30W per port

MANAGEMENT

Web-based configuration and management
System configuration with SNMP v1, v2c and v3
- Support Remote Monitoring (RMON) alarm, event and history recording
- Support system log
- Support hierarchical alarms
- Support NTP

Support power, fan, and temperature alarms
Support for IMC our next generation Network Management platform
CLI via console
Management communications are encrypted via HTTPS

LED INDICATORS

Module active, power, network traffic mode, link status/speed

AT-A-GLANCE TRAFFIC MONITORING

Ports: active, enabled, disabled
Modules: present, active

POWER SUPPLY

Switch 2920
Current rating: 0.8A
Voltage: 100V-240V AC, 50/60Hz
Power consumption max: 22.4W
Power dissipation: 76.43 BTU/hr max

Switch 2928
Current rating: 0.8A
Voltage: 110V-240V AC, 50/60Hz
Power consumption max: 31.5W
Power dissipation: 107.48 BTU/hr max

Switch 2952
Current rating: 1.2A
Voltage: 100V-240V AC, 50/60Hz
Power consumption max: 55.4W
Power dissipation: 189.03 BTU/hr max

Switch 2928 PWR
Current rating: 2.9A
Voltage: 100V – 240V AC, 50/60Hz
Power consumption max for Ethernet switching: 45W
PoE Budget: 170W
Power consumption for PoE: up to 170W + 25% overhead
Power dissipation: 290.08 BTU/hr max

Switch 2928 HPWR
AC source
Current rating: 8A
Voltage:100V - 240V AC, 50/60Hz
Power consumption max for Ethernet Switching: 67W
PoE Budget: 365W
Power consumption for PoE: up to 365W + 25% overhead
Power dissipation: 539.11 BTU/hr max

DC source – RPS1000-A3
Current rating: 20A
Voltage: -52V to -55V DC
PoE Budget: up to 740W
Power consumption with full PoE: 832W

All switches
Power inlet: IEC 320

DIMENSIONS

Switch 2920
Height: 4.36cm (1.72in)
Width: 44cm (17.32in)
Depth: 16cm (6.3in)
Weight: 3kg (6.61lb)

Switch 2928
Height: 4.36cm (1.72in)
Width: 44cm (17.32in)
Depth: 16cm (6.3in)
Weight: 3kg (6.61lb)

Switch 2952
Height: 4.36cm (1.72in)
Width: 44cm (17.32in)
Depth: 22cm (10.24in)
Weight: 5kg (11.02lb)

Switch 2928 PWR
Height: 4.36cm (1.72in)
Width: 44cm (17.32in)
Depth: 42cm (16.54in)
Weight: 7kg (15.43lb)

Switch 2928 HPWR
Height: 4.36cm (1.72in)
Width: 44cm (17.32in)
Depth: 42cm (16.54in)
Weight: 7kg (15.43lb)

ENVIRONMENTAL REQUIREMENTS

Operating temperature: 0° to 45°C (32° to 113°F)
Operating humidity: 10 to 90% (non-condensing)
Standard: EN 60068 (IEC 68)

REGULATORY AND AGENCY APPROVALS

Safety: UL 60950-1, EN 60950-1, CSA 22.2 60950-1, IEC 60950-1
Emissions: EN 55022 Class A, EN 61000-3-2, EN 61000-3-3, FCC Part 15 Subpart B Class A, CISPR22 Class A, ICES-003 Class A, VCCI Class A
Immunity: EN 55024

IEEE STANDARDS SUPPORTED

IEEE 802.1d Spanning Tree
IEEE 802.1p Priority Tags
IEEE 802.1Q VLANs
IEEE 802.1X Port Security
IEEE 802.1w Rapid Spanning Tree
IEEE 802.3 Ethernet
IEEE 802.3ab Gigabit Ethernet
IEEE 802.3ad Link Aggregation
IEEE 802.3af Power over Ethernet (Switch 2928 PWRand Switch 2928 HPWR only)
IEEE 802.3u Fast Ethernet
IEEE 802.3x Flow Control
IEEE 802.3z Gigabit Ethernet
ISO 8802-3

PACKAGE CONTENTS

Switch unit, power cord, self-adhesive rubber pads, console cable, rack-mount kit, product CD, warranty and safety information flyer

WARRANTY AND OTHER SERVICES

Three Year Limited Hardware Warranty
Limited Software Warranty for 90 days
Advance Hardware Replacement with Next Business Day shipment in most regions
90 days of telephone technical support
Refer to www.3com.com/warranty for details.

ORDERING INFORMATION

PRODUCT DESCRIPTION	3COM SKU
3Com Baseline Plus Switch 2920	3CRBSG2093
3Com Baseline Plus Switch 2928	3CRBSG2893
3Com Baseline Plus Switch 2928 PWR	3CRBSG28PWR93
3Com Baseline Plus Switch 2928 HPWR	3CRBSG28HPWR93
3Com Baseline Plus Switch 2952	3CRBSG5293

PRODUCT DESCRIPTION	3COM SKU
TRANSCEIVERS	
3Com 1000BASE-SX SFP	3CSFP91
3Com 1000BASE-LX SFP	3CSFP92

Visit www.3com.com for more information about 3Com network solutions.

3Com Corporation, Corporate Headquarters, 350 Campus Drive, Marlborough, MA 01752-3064
3Com is publicly traded on NASDAQ under the symbol COMS.

401206-002 08/09

Technical Datasheet DS46

LUXEON
never before possible

power light source

LUXEON® III Star

Introduction

LUXEON® III is a revolutionary, energy efficient and ultra compact new light source, combining the lifetime and reliability advantages of Light Emitting Diodes with the brightness of conventional lighting.

LUXEON III is rated for up to 1400mA operation, delivering increased lumens per package.

LUXEON Power Light Sources give you total design freedom and unmatched brightness, creating a new world of light.

For high volume applications, custom LUXEON power light source designs are available upon request, to meet your specific needs.

Features

- Highest flux per LED family in the world
- Very long operating life (up to 100k hours)
- Available in 5500K white, green, blue, royal blue, cyan
- Lambertian and side emitting radiation patterns
- More energy efficient than incandescent and most halogen lamps
- Low voltage DC operated
- Cool beam, safe to the touch
- Instant light (less than 100 ns)
- Fully dimmable
- No UV
- Superior ESD protection

Typical Applications

- Reading lights (car, bus, aircraft)
- Portable (flashlight, bicycle)
- Mini-accent/Uplighters/ Downlighters/Orientation
- Fiber optic alternative/ Decorative/Entertainment
- Bollards/Security/Garden
- Cove/Undershelf/Task
- Automotive rear combination lamps
- Traffic signaling/Beacons/ Rail crossing and Wayside
- Indoor/Outdoor Commercial and Residential Architectural
- Edge-lit signs (Exit, point of sale)
- LCD Backlights/Light Guides

PHILIPS

LUMILEDS
Light From Silicon Valley

Mechanical Dimensions

LUXEON III Star

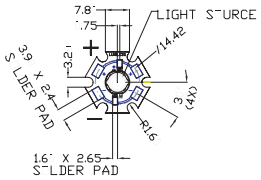

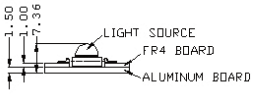

Side Emitting

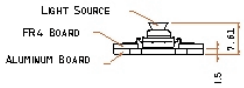

Notes:
1. Slots in aluminum-core PCB for M3 or #4 mounting screw.
2. Electrical interconnection pads labeled on the aluminum-core PCB with "+" and "-" to denote positive and negative, respectively. All positive pads are interconnected, as are all negative pads, allowing for flexibility in array interconnection.
3. Electrical insulation between neighboring Stars is required —aluminum board is not electrically neutral.
4. Drawings not to scale.
5. All dimensions are in millimeters.

Flux Characteristics at 700mA, Junction Temperature, T_J = 25ºC

Table 1.

Color	LUXEON Emitter	Minimum Luminous Flux (lm) or Radiometric Power (mW) Φ_V [1,2]	Typical Luminous Flux (lm) or Radiometric Power (mW) Φ_V [2]	Radiation Pattern
White	LXHL-LW3C	60.0	65	
Green	LXHL-LM3C	51.7	64	Lambertian
Cyan	LXHL-LE3C	51.7	64	
Blue[3]	LXHL-LB3C	13.9	23	
Royal Blue[4]	LXHL-LR3C	275 mW	340 mW	
White	LXHL-FW3C	51.7	58	
Green	LXHL-FM3C	51.7	58	Side Emitting
Blue[3]	LXHL-FB3C	13.9	21	

power light source

Luxeon® Flood

Technical Data DS24

Luxeon® is a revolutionary, energy efficient and ultra compact new light source, combining the lifetime and reliability advantages of Light Emitting Diodes with the brightness of conventional lighting.

Luxeon features one or more power light sources mounted onto an aluminum-core printed circuit board, allowing for ease of assembly, optimum cooling and accurate light center positioning.

For high volume applications, custom Luxeon power light source designs are available upon request, to meet your specific needs.

Luxeon Power Light Sources give you total design freedom and unmatched brightness, creating a new world of light.

Luxeon Flood is available in white, green, cyan, blue, red, and amber.

LUXEON®

Features

- Highest Flux per LED in the world
- Very long operating life (up to100k hours)
- Available in White, Green, Cyan, Blue, Red and Amber
- More Energy Efficient than Incandescent and most Halogen lamps
- Low voltage DC operated
- Cool beam, safe to the touch
- Instant light (less than 100 ns)
- Fully dimmable
- No UV
- Superior ESD protection

Typical Applications

- Decorative flood
- Traffic lights
- Railway crossings and wayside
- Beacons

Mechanical Dimensions

Flood 12-Up

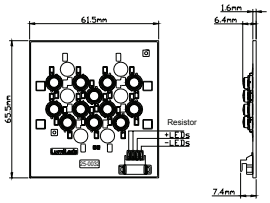

Notes:

1. Connector on board AMP type, code 2-179123-4 ; Mating connector – AMP receptacle housing assembly, code 173977-4.
2. Flood 12-Up has a resister component, 2.2k Ohm.
3. Drawing not to scale.
4. All dimensions are in millimeters.

Flood 18-Up

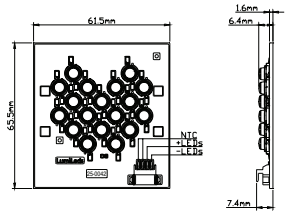

Notes:

1. Connector on board AMP type, code 2-179123-4 ; Mating connector – AMP receptacle housing assembly, code 173977-4.
2. Flood 18-Up has an NTC component, 10k Ohm.
3. Drawing not to scale.
4. All dimensions are in millimeters.

Circuit Diagram

Flood 12-Up

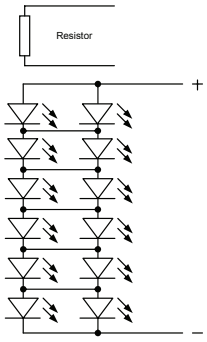

Flood 18-Up

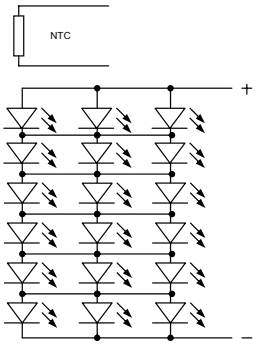

Specifications

Overview

This appendix contains information on spectrometer operation, specifications, and system compatibility. It also includes accessory connector pinout diagrams and pin-specific information.

How the HR2000+ Works

Below is a diagram of how light moves through the optical bench of an HR2000+ Spectrometer. The optical bench has no moving parts that can wear or break; all the components are fixed in place at the time of manufacture. Items with an asterisk (*) are user-specified.

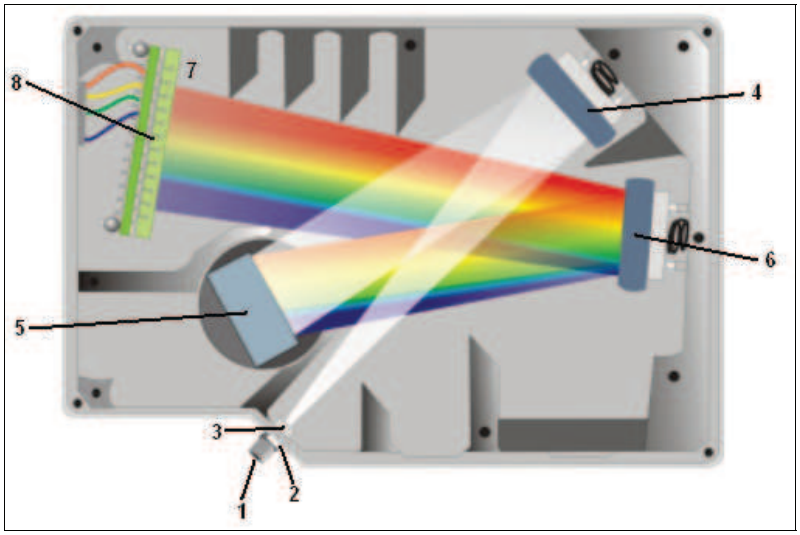

HR2000+ Spectrometer with Components

See *HR2000+ Components Table* on the following page for an explanation of the function of each numbered component in the HR2000+ Spectrometer in this diagram.

HR2000+ Specifications

The following sections provide specification information for the CCD detector in the HR2000+, as well as the HR2000+ Spectrometer itself. HR2000+CG-UV-NIR specifications are listed in *Appendix C: Error! Reference source not found.*.

CCD Detector Specifications

Specification	Value
Detector	Sony ILX-511 linear silicon CCD array
No. of elements	2048 pixels
Sensitivity	75 photons per count at 400 nm 41 photons per count at 600 nm
Pixel size	14 µm x 200 µm
Pixel well depth	62,500 electrons
Signal-to-noise ratio	250:1 (at full signal)
A/D resolution	14 bit
Dark noise	12 RMS counts
Corrected linearity	>99.8%
Maximum pixel rate	Rate at which pixels are digitized is 1 MHz

HR2000+ Spectrometer

Specification	Value
Dimensions	148.6 mm x 104.8 mm x 45.1 mm
Weight	570 g
Power consumption	220 mA @ 5 VDC
Detector	2048-element linear silicon CCD array
Detector range	200-1100 nm
Gratings	14 gratings available

Specification	Value
Entrance aperture	5, 10, 25, 50, 100 or 200 µm wide slits
Order-sorting filters	Installed longpass and bandpass filters
Focal length	f/4, 101 mm
Optical resolution	Depends on grating and size of entrance aperture
Stray light	<0.05% at 600 nm; <0.10% at 435 nm
Dynamic range	2 x 10^8 (system); 1300:1 for a single acquisition
Fiber optic connector	SMA 905 to single-strand optical fiber (0.22 NA)
Data transfer rate: USB 2.0 Port Serial Port	 Full scans into memory every 1 millisecond Full scans into memory every 600 milliseconds
Integration time	1 millisecond to 65 seconds
Interfaces	USB 2.0, 480 Mbps (USB 1.1 compatible); RS-232 (2-wire); SPI (3-wire); I^2C Inter-Integrated Circuit 2-wire serial bus
Operating systems: USB Port Serial Port	 Windows 98/Me/2000/XP, Mac OS X, and Linux Any 32-bit Windows operating system
Onboard GPIO	10 user-programmable digital I/Os
Analog channels	One 13-bit analog input and one 9-bit analog output

System Compatibility

The following sections provide information on hardware and software requirements for the HR2000+.

Compatibility for Desktop or Notebook PCs

To use the HR2000+, you must have a PC that meets the following minimum requirements:

- Operating systems: Windows 98/Me/2000/XP, Mac OS X, or Linux with USB port; any 32-bit Windows OS with serial port
- Computer interfaces: USB 2.0 @ 480 Mbps; RS-232 (2-wire) @ 115.2 K baud
- Peripheral interfaces: SPI (3-wire), I^2C inter-integrated circuit

Appendix B

ftm_carrier.m

```
%phase=ftm_carrier(imdata,carrier_freq_x,carrier_freq_y,filter_width_x,filter_width_y);
%
%This function evaluates the phase from fringe pattern with
%carrier fringes using the Fourier transform method(FTM)
%imdata: input image data
%carrier_freq_x: carrier frequency in x direction
%carrier_freq_y: carrier frequency in y direction,
%                default value is carrier_freq_x
%filter_width_x and filter_width_y:
%                widths of the filter in frequency domain
%                the default widths is 1/2*maximum(carrier_freq_x,carrier_freq_y)


function phase=ftm_carrier(imdata,carrier_freq_x,carrier_freq_y,filter_width_x,filter_width_y);

error(nargchk(2,5,nargin));

if (nargin==2)
   carrier_freq_y=carrier_freq_x;
   filter_width_x=0.5*carrier_freq_x;
   filter_width_y=0.5*carrier_freq_x;
end
if (nargin==3)
   filter_width_x=0.5*max(carrier_freq_x,carrier_freq_y);
   filter_width_y=filter_width_x;
end
if (nargin==4)
   filter_width_y=filter_width_x;
end

[M,N]=size(imdata);
temp1=fft2(imdata);
temp1=fftshift(temp1);
temp2=zeros(M,N);
temp2(M/2+1-round(filter_width_x/2):M/2+1+round(filter_width_x/2),...
     N/2+1-round(filter_width_y/2):round(N/2+1+filter_width_y/2))=...
   temp1(M/2+1+round(carrier_freq_x)-round(filter_width_x/2):...
   M/2+1+round(carrier_freq_x)+round(filter_width_x/2),...
   N/2+1+round(carrier_freq_y)-round(filter_width_y/2):...
   N/2+1+round(carrier_freq_y)+round(filter_width_y/2));
temp2=ifftshift(temp2);
temp2=ifft2(temp2);
phase=atan2(imag(temp2),real(temp2));
```

```
function [i]=franreplacement()
i=0;
imdata = imread('*.tif');

 phase=ftm_carrier(imdata,carrier_freq_x,carrier_freq_y,filter_width_x,filter_width_y);

figure, imagesc(phase), colormap gray;

unwrapped_phase=unwrapping(phase);

figure, imagesc(unwrapped_phase), colormap gray;
```

4 Phase Stepping.m

```
i1=imread('0degreeimagedata.tif');
i1= rgb2gray(i1);
i1 = double(i1);

i2=imread('45degreeimagedata.tif');
i2= rgb2gray(i2);
i2 = double(i2);

i3=imread('90degreeimagedata.tif');
i3= rgb2gray(i3);
i3 = double(i3);

i4=imread('135degreeimagedata.tif');
i4= rgb2gray(i4);
i4 = double(i4);

% m = imread('f1kmaska.tif');
% % m = rgb2gray(m);
% m = double(m);
%
% i11 = i1.*m;
% i22 = i2.*m;
% i33 = i3.*m;
% i44 = i4.*m;
%
% phase=ps(4,i11,i22,i33,i44);

phase=ps(4,i1,i2,i3,i4);


figure, imagesc(phase), colormap gray

unwrapphase=unwrapping(phase);
% m = imread('f4kmask.tif');
%  m = rgb2gray(m);
% m = double(m);
% unwrapphase2 = unwrapphase.*m;

figure, imagesc(unwrapphase), colormap gray

figure,contourf (unwrapphase,20)

figure, surf(unwrapphase)

 shading interp
lightangle(-30,45)
set(findobj(gca,'type','surface'),...
'FaceLighting','phong',...
'AmbientStrength',.3,'DiffuseStrength',.8,...
'SpecularStrength',.9,'SpecularExponent',25,...
'BackFaceLighting','unlit')
```

6 Phase Stepping.m

```
i1=imread('imagedata001.TIF');
i1 = rgb2gray(i1);
i1 = double(i1);

i2=imread('imagedata002.TIF');
i2 = rgb2gray(i2);
i2 = double(i2);

i3=imread('imagedata003.TIF');
i3 = rgb2gray(i3);
i3 = double(i3);

i4=imread('imagedata004.TIF');
i4 = rgb2gray(i4);
i4 = double(i4);

i5=imread('imagedata005.TIF');
i5 = rgb2gray(i5);
i5 = double(i5);

i6=imread('imagedata006.TIF');
i6 = rgb2gray(i6);
i6 = double(i6);

[seta,delta]=ps_al_pe(6,i1,i2,i3,i4,i5,i6);

figure, imagesc(delta);colormap gray


unwrapphase = unwrapping(delta);
unwrapphase2 = unwrapping(seta);

figure, imagesc(unwrapphase), colormap gray
figure, imagesc(unwrapphase2), colormap gray
```

normalize.m

```
function [IN, Mod]=Normalize(I, R)
%NORMALIZE  Normalize a fringe pattern or phase modulated signal
%   [IN,Mod] = Normalize(I, R) returns the normalized version of
%   the fringe pattern I. R is peak position in fringes/field of the
%   bandpass filter used to filter backgroung and noise. Mod is the
%   normalized modulation computed for IN, for regions with higher
%   fringe amplitude Mod will be closer to 1.
%   AQ, 17/9/06.
%   Copyright 2005 IOT S.L.
%   $ Revision: 1.0.104.0 $
%   $ Date: 04-09-2007.23-40 $
XFLib = actxserver('XFLib');

if nargin < 2, R=20; end
if nargin < 1, error('At least one images is necessary'); end
if R<1, error('R must be >= 1'); end

result=XFLib.Normalize(double(I), double(R));
IN=result{1};
Mod=result{2};
```

DemIQT.m

```
function [WrappedPhase, Mod]=DemIQT(IN, Mask, N, Lambda)
%DemIQT  demodulates the phase of the normalized image IN
%   [WrappedPhase, Mod]=DemIQT(IN, Mask, N, Lambda) returns the wrapped phase
%   associated with the normalized fringe pattern IN. Mask is the processing mask,
% N the neigbourhood size and
%   lambda the regularization parameter. The first input arguments are
%   required; the other three have default values. Default values for N and lambda
%   are 5 px and 1 respectively, and default value for Mask is ones(size(IN))
%   AQ, 24/10/06.
%   Copyright 2005 IOT S.L.
%   $ Revision: 1.0.104.0 $
%   $ Date: 04-09-2007.23-40 $
XFLib = actxserver('XFLib');

if nargin < 4, Lambda = 1; end
if nargin < 3, N=5; end
if nargin < 2, Mask=ones(size(IN)); end
if nargin < 1, error('At least one image is necessary'); end
if sum(abs(Mask(:)))==0, error('all Mask is set to zero') ; end
if N<1, error('N must be >= 1'); end
if Lambda<0, error('lambda must be >= 0'); end

if(max(IN(:))>1 || min(IN(:))<-1)
    error('Input image should be normalized');
end


result=XFLib.DemIQT(double(IN),double(Mask), double(N), double(Lambda));
WrappedPhase=result{1};
Mod=result{2};
```

PUMD.m

```
function Phase=PUMD(WP, Weights, Mask)
%PUMD  unwraps a wrapped phase map by the Flynn's minimum discontinuity method
%   Phase=PUMD(WP, Weights, Mask) returns the continuous phase corresponding to the
%   wrapped phase map WP. Weights are the weights assigned to each position and
%   Mask defines the processing mask.
%   AQ, 26/9/06.
%   Copyright 2005 IOT S.L.
%   $ Revision: 1.0.104.0 $
%   $ Date: 04-09-2007.23-40 $
XFLib = actxserver('XFLib');

if nargin < 3, Mask=ones(size(WP)); end
if nargin < 2, Weights=ones(size(WP)); end
if nargin < 1, error('at least a phase map is necessary') ; end
if sum(abs(Mask(:)))==0, error('all Mask is set to zero') ; end

Phase=XFLib.PUMD(double(WP), double(Weights), double(Mask));
```

The Automatic Analysis of Interferometric Data - FRAN

Description and User Guide

School of Engineering

Mark Burnett
School of Engineering
University of Warwick

Optical Engineering Laboratory 1996

FRAN - Written by T. R. Judge

7. References.

[1] C. Quan, T.R. Judge, 'The Processing of the Interference Fringe Data by FFT Method.' Handout for MSc in Optical Engineering.

[2] P.J. Bryanston-Cross, C. Quan, T.R. Judge, 'Application of the FFT method for the quantitative extraction of information from high resolution interferometric and photoelastic data.' Optics and Laser Technology, Vol. **26**, No. **3**, 1994.

[3] T.R. Judge, 'FRANSYS fringe Analysis System Documentation.' Optical Engineering Laboratory, Dept. of Eng., University of Warwick.

[4] D.P. Towers, P.J. Bryanston-Cross, C.E. Towers, 'The Automatic Quantitative Analysis of Phase Stepped Interferograms.' Optical Engineering Laboratory, Dept. of Eng., University of Warwick.

[5] D.P. Towers, T.R. Judge, P.J. Bryanston-Cross, 'Analysis of Holographic Fringe Data Using the Dual Reference Approach.' Optical Eng.,Vol. **30**, No. **4**, 1991.

Appendix C

Camera Array Collect Image Data GUI

Bibliography

[1] Oey Lee Chua. *cornea*. Website, August 2010.

[2] Dr. Murphy. *Dissection Procedure*. Website.

[3] Thomase.Furtak Miles V.Klein. Optics. Wiley, second edition, June 1986.

[4] S.Mallick M. Francon. Polarization Interferferometers. Wiley, 1971.

[5] L.S. Taylor. *An Anecdotal History of Optics from Aristophanes to Zernike - VI. WAVE OPTICS*. http://www.ece.umd.edu/ taylor/optics.htm, Electrical Engineering Dept., University of Maryland.

[6] Thomas J. Fellers Douglas B. Murphy, Kenneth R. Spring and Michael W. Davidson. *Optical Birefringence*. National High Magnetic Field Laboratory, Auguest 2003.

[7] Alfred Zajac Eugene Hecht. Optics, page 315, 1974.

[8] Chiayu Cochran, Eugene R.; Ai. *Interferometric stress birefringence measurement*. *Applied Optics*, 31(31):6702–6706, November 1992.

[9] Carole C. Montarou. Low-Level Birefringence Measurement Methods Applied to The Characterization of Optical Fibers and Interconnections. Doctor of philosophy thesis, School of Electrical and Computer Engineering, Georgia Institute of Technology, April 2005.

[10] A. E. Ennosa; D. W. Robinsona; D. C. Williams. *Automatic fringe analysis in holographic interferometry*. *Journal of Modern Optics*, 32(2):135 – 145, February 1985.

[11] *The Theory of Birefringence*. Technical Report CPGAN 014, Cambridge Polymer Group, 56 Roland Street, Suite 310, Boston MA 02129.

[12] Sanjib Chatterjee. *Measurement of surface figure of plane optical surfaces using Fizeau interferometer with wedge phase-shifter*. *Optics and Laser Technology*, 37:43–49, February 2005.

[13] Levy M. Hong Y.K. Park H.K. Moon, K.S. *Axial Displacement Measurement of a Single-Crystal Actuator Using Phase-Shift Interferometry*. *Industrial Electronics, IEEE Transactions on*, 52:953–959, 2005.

[14] P J Bryanston-Cross P H Chan and S C Parker. *Fringe-pattern analysis using a spatial phase-stepping method with automatic phase unwrapping*. *Measurement Science and Technology*, 6(9), 1995.

[15] David W. Robinson and Graeme T. Reid., editors. Interferogram analysis - digital fringe pattern measurement techniques. Bristol - Institute of Physics Pub., 1993.

[16] Herriott D. R.-Gallagher J. E. Rosenfeld D. P. White A. D. Bruning, J. H. and D. J. Brangaccio. *Digital Wavefront Measuring Interferometer for Testing Optical Surfaces and Lenses*. *Applied Optics*, 13(11):2693–2703, 1974.

[17] Daniel Malacara, editor. Optical Shop Testing. Wiley, 1992. 409-438.

[18] J. E. Greivenkamp. *Generalized data reduction for heterodyne interferometry*. *Optical Engineering*, 23:350–352, 1984.

[19] C. J. Morgan. *Least-squares estimation in phase-measurement interferometry*. *Optics Letters*, 7:368–370, 1982.

[20] Toyohiko Yatagai Guanming Lai. *Generalized phase-shifting interferometry*. *Optical Society of America*, 8(5):822–827, 1991.

[21] D. C. L. Cheung C. Y. Wu T. H. Barnes, T. Eiju. *Phase measurement accuracy of feedback interferometers*. *Optics and Lasers in Engineering*, 38(6):387–404, December 2002.

[22] Thomas Kreis. Handbook of holographic interferometry - optical and digital methods. Weinheim , [Great Britain] - Wiley-VCH, 2005.

[23] Joseph W. Goodman. Introduction to Fourier Optics. McGRAW-HILL Companies Inc., second edition, 1996.

[24] T. R. Judge. Quantitative Digital Image Processing in Fringe Analysis and Particle Image Velocimetry (PIV). PhD thesis, Department of Engineering, University of Warwick, July 1992.

[25] N. Deo. Graph Theory with Applications to Engineering and Computer Science. Number pp. 60-64. Prentice-Hall, London, May 1974.

[26] Kjell J. Gåsvik. Optical Metrology. John Wiley and Sons Ltd, third edition, 2002.

[27] Eugene A. Irene Harland G. Tompkins, editor. Handbook of Ellipsometry. William Andrew Inc., 2005.

[28] Kjell J Gasvik Neil Halliwell Katherine Creath, Kate M Crennell and Malgozata Kujawinska Toyohiko Yatagai Chris J Pickering, Parameswaran Hariharan. Interferogram Analysis - Digital Fringe Pattern Measurement Techniques. Institute of Physics Publishing, Bristol and Philadelphia, 1993.

[29] Dave Litwiller. *CCD vs. CMOS:Facts and Fiction*. *Photonics Spectra*, January 2001.

[30] G. E. Smith W. S. Boyle. *Charge coupled semiconductor devices*. *Bell Systems Tech*, 49:587–593, 1970.

[31] Goutam Kumar Sen. *Difference Between CMOS and CCD*. August 2010.

[32] Brain J. Thompson Daniel Malacara, editor. Handbook of Optical Engineering. Marcel Dekker, Inc, 2001.

[33] Jean Paul Freyssinier Ramesh Raghavan Vasudha Ramamurthy, Nadarajah Narendran and Peter Boyce. *Determining Contrast Sensitivity Functions*

for Monochromatic Light Emitted by High-Brrightness LEDs. In *Third International Conference on Solid State Lighting*, pages 294–300. SPIE, Lighting Research Center, Rensselaer Polytechnic Institute, Troy, NY, 2004.

[34] V. Ramamurthy A. Bierman J.D.Bullough N.Narendran J. P. Freyssinier, Y. Zhou. Evalution of light emitting diodes for signage applications, volume 5187, pages 5–7. International Society for Optical Engineering, Augest 2003.

[35] G. Robertson A. kuske. Photoelastic Stress Analysis. John Wiley and Sons, 1974.

[36] Z.F.Wang E.A.Patternson. *Toward Full-field Automated Photoelastic Analysis of Complex Components*. *Strain*, 1991.

[37] A. Asundi. *Phase Shifting in Photoelasticity*. *Exp Tech*, 17(1):19–23, 1993.

[38] C.G.Boay A. Asundi, L. Tong. *Phase-Shifting Method with a Normal Polariscope*. *Applied Optics*, 38:5931–5935, 1999.

[39] B.Morche F.W.Hecker. *Computer Aided Measurement of Relative Retardation in Plane Photoelasticity*. In *Experimental Stress Analysis*, pages 535–542. Proc. Of the VIIIth Int. Conf. On Exp. Stress Analysis, 1986.

[40] A.D.Nurse M.J.Ekman. *Completely Automated Determination of Two-Dimensional Photoelastic Parameters Using Load Stepping*. *Optical Engineering*, 37:1845–1851, 1998.

[41] Eino-Ville (Eddy) Talvala Emilio Antunez Bennett Wilburn Mark Horowitz Marc Levoy Vaibhav Vaish, Gaurav Garg. *Synthetic Aperture Focusing using a Shear-Warp Factorization of the Viewing Transform*. *Proc. Workshop on Advanced 3D Imaging for Safety and Security*, 2005.

[42] Keita Takahashi Yuichi Taguchi and Takeshi Naemura. *Real-Time All-in-Focus Video-Based Rendering Using a Network Camera Array*. *IEEE*, pages 28–30, May 2008.

[43] Jean-Yves Bouguet. Visual methods for three-dimensional modeling. Ph.d, California Institute of Technology, Pasadena, California, May 1999.

[44] S. Gortler A. Isaksen, L. McMillan. *Dynamically Reparametrized Light Fields*. *In Pro of ACM SIG-GRAPH*, 2000.

[45] P. Hanrahan M. Levoy. *Light Field Rendering*. *In Pro of ACM SIG-GRAPH*, 1996.

[46] Eino-Ville Talvala Emilio Antunez Bennett Wilburn Mark Horowitz Marc Levoy Vaibhav Vaish, Gaurav Garg. *Synthetic Aperture Focusing using a Shear-Warp Factorization of the Viewing Transform*. (94305).

[47] M. Speigel. Schaum's Easy Outlines Statistics. McGraw Hill, 2000.

[48] John. Taylor. An Introduction to Error Analysis. University Science Books: Sausalito, second edition, 1997.

[49] Hugh D. Young. Statistical Treatment of Data. McGraw-Hill Book Company Inc., 1962.

[50] William. Lechten. Data and Error Analysis. Prentice Hall: Upper Saddle River, NJ, second edition, 1999.

[51] D. Keith Robinson philip R. Bevington. Data Reduction and Error Analysis for the Physical Sciences. McGraw-Hill Inc., second edition, 1992.

[52] K. Ramesh. *Simulation of error in Digital Photelasticity by Jones Calculus*. *Strain*, 37:105–112, 2001.

[53] D. K.Tamrakar and K. Ramesh. *Simulation of Error in Digital Photoelasticity by Jones Calculus*. *Strain*, 37(3):105–112, August 2001.

[54] D. K. Tamrakar K. Ramesh. *Improved Determination of Retardation in Digital Photoelasticity by Load-Stepping*. *Optics and Lasers in Engineering*, 33:387–400, 2000.

[55] Judge TR. Quan. C., Peter Bryanstone-Cross. *Photoelasticity Stress Analysis Using Carrier Fringe and FFT Techniques*. *Optical Laser Engineering*, 18(2):79–108, 1993.

[56] Z. Tung M. Takeda. *Subfringe Holographic Inteferometry by Computer-based Sapatial-Carrier Fringe-Pattern Analysis*. *J. Optics*, 16(3):127–131, 1985.

[57] D. Post B. Han. *The Tilted-Plate Method for Introducing Carrier Fringes of Exension in Moire Interferometry*. *Exp. Tech.*, 13(7):25–29, 1989.

[58] L. Ramos-Izquierdo J. B. BeVelis D. C. Peirce. P. D. Hilton R. A. Mayville G. O. Reynolds, D. A. Servaes. *Holographic Fringe Linearization Interferometry for Defect Detection*. *Optical Engineering*, 24(5):757–768, 1985.

[59] J. D. Hovanesian Grant gerhart P. D. Plotkowski, Y. Y. Huang. *Improved Fringe Carrier Technique for Unambiguous Determination of Holographicly Recorded Displacements*. *Optical Engineering*, 24(5):754–756, 1985.

[60] T. D. Dudderar K. W. Koening D. R. Matthys, J. A. Gilbert. *A Windowing Techiques for the Automated Analysis of Holo-interferograms*. *Optical Laser Engineering*, 8:123–136, 1988.

[61] Ng TW. *Derivation of Retardation Phase in Computer-Aided Photoelasicity by Using Carrier Fringe Phase Shifting*. *Applied Optics*, 36(31):8259–8263, 1997.

[62] Graeme T Reid David W Robinson. *Interferogram Analysis Digital Fringe Pattern measurement techniques*. *Institute of Physics Publishing*, pages 145–166, 1993.

[63] Leslie L. Deck. *Fourier-transform phase-shifting interferometry*. *Applied Optics*, 42(13):2354–2365, May 2003.

[64] R. Fox J. Shamir and S. G. Lipson. *A Simple Method of Measuring Very Small Fringe Shifts*. *Applied Optics*, 8(1):103–106, January 1969.

[65] V.Ganapathy K.Ramesh. *Phase-shifting Methodologies in Photoelastic Analysis- the Application of Jones Calculus*. *Journal of Strain Analysis*, 31(6):423–432, 1996.

[66] Sounkalo Dembl Andr Janex Patrick Sandoz, Jean Christophe Ravassard. *Phase-Sensitive Vision Technique for High Accuracy Position Measurement of Moving Targets*. *IEEE Transactions on Instrumentation and Measurement*, 49(4):867–872, August 00.

[67] S.Yoneyama.H.Kikuta. *Phase-stepping Photoelasticity by Use of Retarders with Arbitratry Retardation*. *Experimental Mechanics*, 46:289–296, 2006.

[68] T.W.Ng. *Photoelastic Stress Analysis Using an Object Step-Loading Method*. *Experimental Mechanics*, 37(2):137–141, June 1997.

[69] Y Hu and S Chen. *The noise sensitivity of the Carr?e fringe-analysis technique*. *Meas. Sci. Technol.*, 8:871–874, 1997.

[70] P. Hariharan. *Achromatic and apochromatic halfwave and quarterwave retarders*. *Optical Engineering*, 35:3335–3337, 1996.

[71] Mahendra P. Kothiyal Basanta Bhaduri, Nandigana Krishna Mohan. *spatial phase-shifting technique in digital speckle pattern interferometry and digital shearography for nondestructive evaluation*. *Optical Engineering*, 46(5), May 2007.

[72] J Zhang Y Zhang, L Y Wu. *Study on the Phase Modulation Characteristics of Liquid Crystal Spatial Light Modulator*. *Journal of Physics: Conference Series*, 48:790–794, 2006.

[73] Peter J. Bryanston-Cross and Zuobin Wang. *Camera focusing based on fringe pattern matching*. *Applied Optics*, 36(25):6498–6502, 1997.

[74] Tomas Kegel. *Uncertainty Analysis of Turbine and Ultrasonic Meter Volume Measurements - Part 2, Advanced Topics*. Technical report, Colorado Engineering Experiment Station, Inc. Nunn, Co.

[75] Brayanston-Cross P.J. Whitehouse D.J. Wang, Z. *Phase difference determination by fringe pattern matching*. *Optics and Laser Technology*, 28:417–422, 1996.

[76] *Wavefront Distortion Interferometer Measurements*. Optics guide copyright, Melles Griot Inc., 2002.

[77] John W.O'Brynne David M.Rust. *Vector Magnetography*. *Solar Polarimetry*, pages 74–95, 1990.

[78] P J Bryanston-Cross P.H.Chan and S C Parker. *Fringe-Pattern Analysis Using a Spatial Phase-Stepping Method with Automatic Phase Unwrapping*. *Meas. Sci Technol*, pages 1250–1259, 1995.

[79] *Image Capture*. $http://www.fixingproteomics.org/docs/2D_Image_Capture.pdf$.

[80] C. M. Wang P. A. Williams, A. H. Rose. *Rotating-polarizer polarimeter for accurate retardance measurement*. *Appiled Optics*, 36(25), September 1997.

[81] David E. Birk and Mauricio A. Lande. *Corneal and scleral collagen fiber formation in vitro. Biochimica et Biophysica Acta (BBA) - Protein Structure*, 670(3):362–369, October 1981.

[82] Dr Sarbani Roy. *Normal Values in Ophthalology*. http://www.eophtha.com/eophtha/pdf

[83] Rhcastilhos. *Schematic diagram of the human eye en*. $http://en.wikipedia.org/wiki/File:Schematic_diagram_of_the_human_eye_en.svg$.

[84] Roberto Munoz. *Sobre la cornea*. Conference (talks) ppt, 2009.

[85] Ronald B. Rabbetts MSc SMSA FBCOptom DCLP. Bennett and Rabbett's Clinical Visual Optics . Butterworth-Heinemann, 4th edition, July 2007.

[86] Dr. Thomas Caceci. *Special Senses I: The Eye*. $http://education.vetmed.vt.edu/Curriculum/VM8054/Labs/Lab11/Eye/eyelab.htm$.

[87] Dr. Thomas Caceci. *Anatomy and Physiology of the Eye*. $http$: $//www.tedmontgomery.com/the_eye/$.

[88] Christopher J. Rudnisky. *Cornea of the eye*. $http$: $//www.health.com/health/library/mdp/0,,tp10754,00.html$, November 2009.

[89] *Corneal Disorders* . http://akshieyecentre.com/corneal.htm, 2006.

[90] Merindano MD; Costa J; Canals M; Potau JM and Ruano D. *A comparative study of Bowman's layer in some mammals: Relationships with other constituent corneal structures*. *European Journal of Anatomy*, 6(3), 2002.

[91] M.D. Roger F. Steinert. *Bringing a Versatile Tool To the Anterior Segment Surgeon*. The Visante OCT system provides practical information across a multitude of applications, June 2007.

[92] L. J. Bour. polarised light and the eye, chapter 1, page 13. Vision Optics and Instrumentation, CRC press Inc, Boston, MA, USA, 1991.

[93] E. Wolf M. Born. Priciples of Optics. Pergamon Press, New York, 6th edition, 1980.

[94] J. M. Bueno. *Measurment of parameters of polarisation in the Living Human Eye Using Imaging Polarimetry*. *Vision Res.*, 40:3791–3799, 2000.

[95] P. Artal J. M. Bueno. *Double-pass Imaging Polarimetry in the HUman Eye*. *opt. Lett.*, 24:64–66, 1999.

[96] Gary P. Misson. *Circular Polarisation Biomicroscopy: a Method for Determining Human Corneal Stromal Lamellar Organization in vivo*. *Ophthal Phusiol Opt.*, 27:256–264, 2007.

[97] S. Goelz J. P. Fischer R. O. W. Burk J. F. Bille B. Pelz, C. Weschenmoser. *In vivo measurement of the retinal birefringence with regard on corneal effects using an electrooptical ellipsometer*. *Proc. SPIE*, 2930:92–101, 1996.

[98] Jaroslaw Jaronski Juan M. Bueno. *Spatially Resolved Polarisation Properties for in Vitro Corneas. Phhthal Physiol Opt.*, 21(5):384–392, 2001.

[99] D. Kaplan F. A. Bettelheim. *Small Angle Light Scattering of Bovine Cornea as Affected by Birefringence. Biochim, Biophys*, (313):268–276, 1973.

[100] D. M. Maurice. The Eye, volume 1, page 525. Academic Press, second edition, 1969.

[101] Frederick A. Bettelheim Tailor J. Y. Wang. *Compartive Birefringence of Cornea. Comp. Biochem. Physiol*, 51A:89–94, 1975.

[102] Battelheim F. A. D. Kaplan. *Optico Mechanical Properties of Isolated Bovine Cornea. Biochim. Biophys. Acta*, 279:92–101, 1972.

[103] A.Asundi. *Phase Shifting in Photoelasticity. Experimental Techniques*, 17(1):19–23, January 1993.

[104] Liu Tong Anand Asundi and Chai Gin Boay. *Phase-Shifting Method with a Normal Polariscope. Applied Optics*, 38(28):5931–5935, 1999.

[105] E. J. Naylor A. Stanworth. *The Polarization Optics of the Isoclated Cornea. The British Journal of ophthalmology*, April 1950.

[106] *Model K2/SC Long-Distance Microscope The Ultimate Long-Distance Microscope.* $http : //www.infinity - usa.com/products/instruments/Model_K2.aspx.$

[107] Verhelst SC van Blokland GJ. *Corneal polarization in the living human eye explained with a baxial model. J Opt Soc Am*, (4):82–90, 1987.

[108] Marc Levoy Ren Ng Andrew Adams Matthew Footer Mark Horowitz. *Light Field Microscopy. ACM Transactions on Graphics*, 25(3), 2006.

[109] D.A. Agard J.R. Swedlow, J.W.Sedat. *Deconvolution in optical microscopy. Deconvolution of Images and Spectra*, pages 284–309, 1997.